

REPORT DOCUMENTATION PAGE

*Form Approved
OMB No. 0704-0188*

The public reporting burden for this collection of information is estimated to average 1 hour per response, including the time for reviewing instructions, searching existing data sources, gathering and maintaining the data needed, and completing and reviewing the collection of information. Send comments regarding this burden estimate or any other aspect of this collection of information, including suggestions for reducing the burden, to Department of Defense, Washington Headquarters Services, Directorate for Information Operations and Reports (0704-0188), 1215 Jefferson Davis Highway, Suite 1204, Arlington, VA 22202-4302. Respondents should be aware that notwithstanding any other provision of law, no person shall be subject to any penalty for failing to comply with a collection of information if it does not display a currently valid OMB control number.
PLEASE DO NOT RETURN YOUR FORM TO THE ABOVE ADDRESS.

1. REPORT DATE (<i>DD-MM-YYYY</i>)	2. REPORT TYPE	3. DATES COVERED (<i>From - To</i>)		
08/14/2017	Final Report	05/15/2014-05/14/2017		
4. TITLE AND SUBTITLE Passive Standoff Super Resolution Imaging using Spatial-Spectral Multiplexing		5a. CONTRACT NUMBER N00014-14-1-0515		
		5b. GRANT NUMBER		
		5c. PROGRAM ELEMENT NUMBER		
6. AUTHOR(S) Michael W. Kudenov, Ethan R. Woodard, and Zhejun Wu		5d. PROJECT NUMBER 14PR05767-00		
		5e. TASK NUMBER		
		5f. WORK UNIT NUMBER		
7. PERFORMING ORGANIZATION NAME(S) AND ADDRESS(ES) North Carolina State University, Office of Sponsored Programs, Box 7514, Raleigh, NC 27695-7514		8. PERFORMING ORGANIZATION REPORT NUMBER		
9. SPONSORING/MONITORING AGENCY NAME(S) AND ADDRESS(ES) Office of Naval Research, 875 North Randolph Street, Arlington, VA 22203-1995		10. SPONSOR/MONITOR'S ACRONYM(S) ONR		
		11. SPONSOR/MONITOR'S REPORT NUMBER(S)		
12. DISTRIBUTION/AVAILABILITY STATEMENT DISTRIBUTION A. Approved for public release: distribution unlimited.				
13. SUPPLEMENTARY NOTES				
14. ABSTRACT A summary of a new high-speed method of acquiring longitudinal spatial coherence functions is described within the context of imaging. The technique modulates incident spatial information onto spectral carrier frequencies, which can then be de-modulated in both amplitude and phase. An analysis of the technique's spatial and spectral resolution limits is also provided.				
15. SUBJECT TERMS				
16. SECURITY CLASSIFICATION OF: a. REPORT b. ABSTRACT c. THIS PAGE		17. LIMITATION OF ABSTRACT	18. NUMBER OF PAGES	19a. NAME OF RESPONSIBLE PERSON Michael Kudenov
			156	19b. TELEPHONE NUMBER (<i>Include area code</i>) (919) 515-3473

Passive Standoff Super Resolution Imaging using Spatial-Spectral Multiplexing

Final Technical/Scientific Report

Michael W. Kudenov, Principal Investigator
Ethan R. Woodard and Zhejun Wu

Optical Sensing Laboratory
North Carolina State University
Department of Electrical and Computer Engineering
2410 Campus Shore Dr.
Raleigh NC 27606

Grant Funding under Office of Naval Research
May 2014 - May 2017
Contract No. N00014-14-1-0515

Table of Contents

1.0	Introduction	3
2.0	Passive Standoff Imaging using Spatial-Spectral Multiplexing	3
2.1	Theory	3
2.2	SSM Architectures, Experimental Configurations, and Results.....	7
2.3	Reconstruction Algorithm for Nonlinear Channeled Spectra.....	29
2.4	Angular Resolution Analysis	42
2.5	Comparing Angular Resolution of Lens and General Fabry-Perot System.....	48
2.6	Tolerancing and Aberrations.....	49
2.7	4F Imaging System versus Spectrally Resolved White Light Interferometry.....	55
3.0	Snapshot Spectrally Resolved Longitudinal Spatial Coherence Interferometry.....	58
3.1	Introduction (to Spectrally Resolved Longitudinal Spatial Coherence Interferometry).....	58
3.2	Theory	60
3.3	Experimental Setup	69
3.4	Alignment of Fabry-Perot Etalon System	71
3.5	Experimental Results	75
3.6	Conclusion	83
4.0	Spectrally Resolved Longitudinal Spatial Coherence Interferometry for Channeled Spectropolarimetry	84
4.1	Introduction.....	84
4.2	Theory	86
4.3	Experimental Design and Setup	92
4.4	Results.....	94
5.0	Four-Dimensional Object-Space Data Reconstruction Using Spatial-Spectral Multiplexing	102
5.1	Introduction.....	103
5.2	Background	103
5.3	Four-dimensional scene reconstruction using SSM	106
5.4	Methodological design of the reconstruction algorithm.....	106
5.5	Experimental materials and setup	107
5.6	Non-parametric data reconstruction	113
5.7	Parametric data reconstruction	125
5.8	Conclusion and Discussion	138
6.0	Alternative Imaging Methods.....	139
6.1	Total Internal Reflection Tradespace	139
6.2	Plasmonic Angular Transmission Filter.....	143
6.3	Merit Function and Optimization (Germanium, No Dispersion)	147
6.4	Prism Specifications for Single “Knife Edge” Filter.....	149
7.0	Publications and Products.....	150
8.0	References	152

1.0 Introduction

This document serves as the final technical report for research completed under the project entitled “Passive Standoff Imaging using Spatial-spectral Multiplexing”, funded by the United States Office of Naval Research over the period of May 2014-May 2017. Organization of this document is intended to be chronological in terms of the project funding period, beginning with early research related to the theory, modeling, and design of optical systems for the spatial-spectral multiplexing technique and transitioning to systems based on spectrally resolved longitudinal spatial coherence interferometry. This document also includes research related to four-dimensional object-space reconstructions, based on the spatial-spectral multiplexing technique.

Ultimately, one of the major goals of this research was to study the resolution limits of a spatial-spectral multiplexing (SSM) technique for far-field sensing. However, the main conclusion is that far-field superresolution sensing requires phase-apertures, even with SSM, in much the same way as distributed aperture systems. This final report is organized into four main research areas, including: 1) the recovery of scene angular information using a unique SSM technique, which leverages nonlinear material dispersion; 2) spectrally resolved longitudinal spatial coherence interferometry, for encoding angular information onto the source power spectrum via. amplitude modulation; 3) an extension of the longitudinal spatial coherence interferometer system for encoding polarization information onto a source or scene’s spectral content; and 4) four-dimensional object-space reconstruction algorithms based on an optical system which leverages the spatial-spectral multiplexing technique.

2.0 Passive Standoff Imaging using Spatial-Spectral Multiplexing

2.1 Theory

The concept of the spatial-spectral multiplexing (SSM) technique, originally introduced in Ref. [1], has analogies to conventional Fourier transform spectroscopy in that information (*e.g.* angular/spatial or spectral information) is mapped onto a reciprocal optical space (*e.g.* spectral or a spatial domain) using a sinusoidal basis. In our case, we are interested in encoding angular information of a scene onto the power spectrum or spectral content of the source. This technique uses spectrally-resolved measurements generated from an interferometer, such as the tilted Michelson interferometer (MI) depicted in Fig. 1, which may be Fourier transformed to recover an incident scene’s angular information.

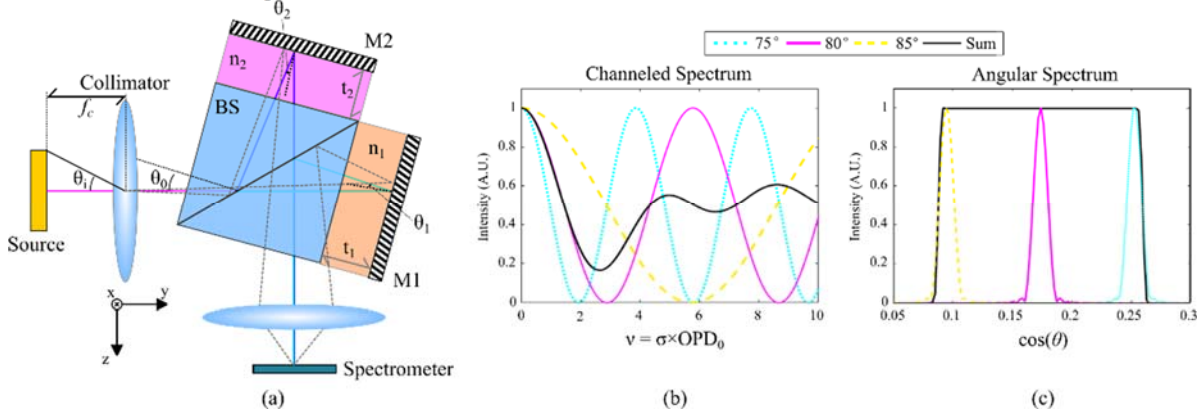


Fig. 1. Channeled SSM technique using a tilted Michelson interferometer. (a) A tilted MI accepting multiple angles from the scene. (b) The channeled spectrum created by the MI and (c) its respective angular spectrum via Fourier.

In Fig. 1 (a), a uniform broadband white light source represents a scene with an angular spectrum, $AS(\theta_i)$, where θ_i denotes the incident angles. In this example, three incident angles from the scene (e.g. $\theta_i = \{75^\circ, 80^\circ, 85^\circ\}$) are collimated into a Michelson interferometer titled at θ_0 with respect to the optical axis. Incident light from the scene undergoes two-beam interference within the interferometer after passing through each arm, which contain arbitrary materials of index of refraction $n_1(\lambda)$ and $n_2(\lambda)$. Light from the output of the interferometer is collected by a lens, and the image of the collimator (*i.e.* the exit pupil) is imaged onto a spectrometer to measure a channeled spectrum of the form

$$I(\sigma) \propto \frac{AS(\theta_i)}{2} \cos\{2\pi\sigma OPD \cos(\theta_i + \theta_0)\}, \quad (1)$$

where the intensity at the spectrometer, I , is given as a function of wavenumber, $\sigma = 1/\lambda$. The optical path difference (OPD) between each arm of the MI is, which for the situation presented in Fig. 1 (a) is given by

$$OPD(\sigma, \theta_i) = 2n_1(\sigma)t_1 \cos(\theta_1) - 2n_2(\sigma)t_2 \cos(\theta_2), \quad (2)$$

with t_1 and t_2 being the longitudinal axis displacement of M1 and M2 from the beamsplitter, respectively. Angles θ_1 and θ_2 denote the angles of refraction within the dispersive materials and are found by Snell's law to be

$$\theta_1 = \sin^{-1}\left(\frac{n_{BS}(\sigma)}{n_1(\sigma)} \sin(\theta)\right), \text{ and} \quad (3)$$

$$\theta_2 = \sin^{-1}\left(\frac{n_{BS}(\sigma)}{n_2(\sigma)} \sin(\theta)\right), \quad (4)$$

respectively, where $n_{BS}(\sigma)$ is the index of refraction of the beamsplitter and $\theta = \theta_i + \theta_0$. Note that if the interferometer is comprised of air gap arms, such that $n_1(\sigma) = n_2(\sigma) = n_0 = 1$, the OPD no longer has a wavenumber dependence, and may be written as

$$OPD(\theta) = 2n_0(t_1 - t_2) \cos(\theta). \quad (5)$$

Due to the angular dependence of the phase between the two beams in the MI, a channeled spectrum is created at the output in which each incident angle generates interference fringes with a unique frequency with respect to wavenumber (e.g. Fig. 1 (b)). The angular spectrum, AS , as a function of angle of incidence, θ_i , can be recovered from the channeled spectrum by a Fourier transform relationship. Since each angle of incidence has a unique frequency versus wavenumber in the channeled spectrum, the angular spectrum is composed of several sinc functions that represent the scene's angular information (Fig. 1 (c)). Thus, the angular spectrum representing the scene's spatial information is multiplexed onto the spectral content of the scene using wavenumber as the independent variable.

From the channeled spectrum in Fig. 1 (b), maximum coherence in the generated spectral frequencies (or interference fringes) occurs at $\sigma = 0 \text{ m}^{-1}$, which is not physically observable by a spectrometer operating in the visible region of the spectrum. However, at spectral regions where the spectrometer operates (approximately $\sigma = 1000 \text{ mm}^{-1}$ to $\sigma = 2500 \text{ mm}^{-1}$), the channeled spectrum has lost the majority of its coherence, resulting in a reduction in fringe contrast. To

illustrate this point, Fig. 2 gives a plot of a simulated channeled spectrum extended to visible wavenumbers. The simulation considers a titled Michelson interferometer ($\theta_0 = 10^\circ$) with a fixed $OPD_0 = 325 \mu\text{m}$ collecting light from an 8° field of view (FOV). The spectral resolution of the simulation is 4 cm^{-1} .

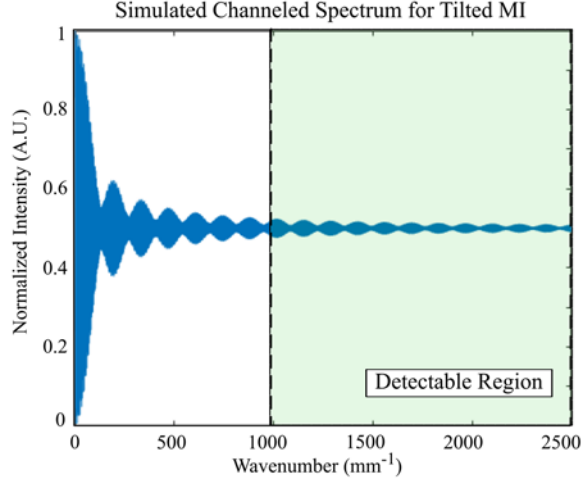


Fig. 2. Channeled spectrum generated by tilted white-light Michelson interferometer (blue curve). Region of reduced contrast at visible wavenumbers where the spectrometer operates highlighted in green.

To alleviate the issue of reduced contrast in the detectable region of the channeled spectrum, angular coherence compensation is introduced into the channeled SSM interferometer using the nonlinear dispersion properties of glass plates. Adding two dispersive glass plates into the tilted MI, as shown in Fig. 3 (a), creates a situation for which a single wavelength becomes compensated in OPD across the field of view.

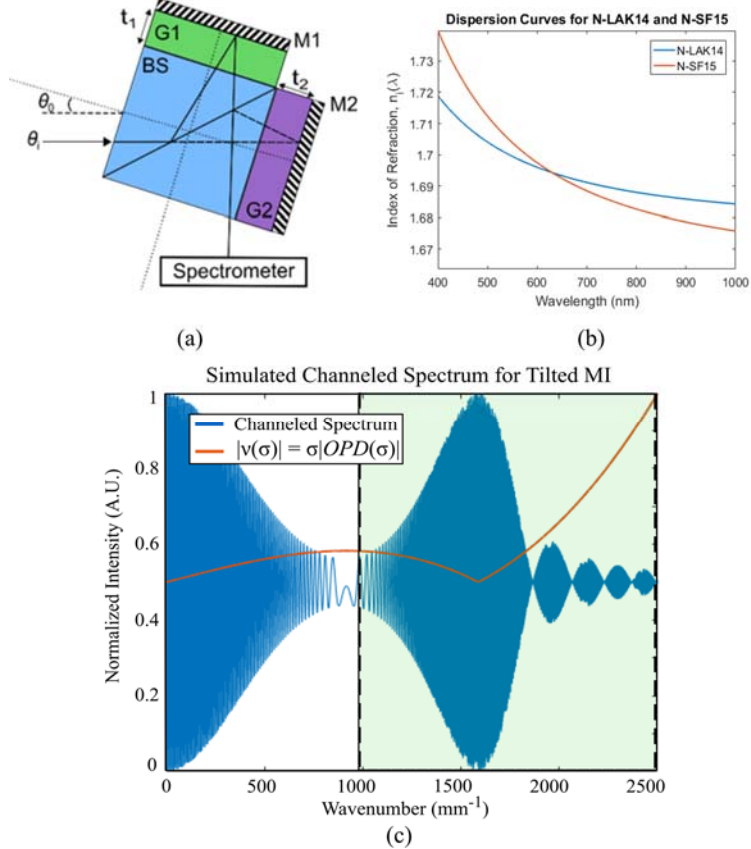


Fig. 3. Angular coherence compensation for channeled SSM. (a) A tilted MI compensated for a single wavelength defined by the intersection of the dispersion curves of the two glass plates in (b). (c) Simulated channeled spectrum generated by the MI system in (a).

The glass plates, G1 and G2, in the tilted MI from Fig. 3 (a), are strategically chosen to have indices of refraction, n_1 and n_2 , and Abbe numbers, v_1 and v_2 , such that there exists an intersection in their dispersion curves. When the thicknesses of the two glass plates, t_1 and t_2 , are equivalent, then the wavelength, λ_0 , defined by the intersection in the two dispersion curves in Fig. 3 (b), will retain a zero OPD for any given incident angle in the FOV (*i.e.* $\partial OPD / \partial \theta = 0$ at λ_0). Due to this angular compensation in OPD for a single wavelength (*e.g.* $\lambda_0 = 630.5 \text{ nm}$ ($\sigma_0 = 1586 \text{ mm}^{-1}$) for Schott [2] glass types N-LAK14 and N-SF15), the channeled spectrum exhibits an additional region of high fringe contrast in the visible region of the spectrum. The plot in Fig. 3 (c) illustrates a simulated channeled spectrum at a spectral resolution of 4 cm^{-1} for a tilted MI using glass plates of LAK14 and SF15 with thicknesses $t_1 = t_2 = 5.0 \text{ mm}$, over a FOV of $\theta_i = -4^\circ$ to $\theta_i = +4^\circ$ with $\theta_0 = +12^\circ$ of initial tilt. The new region of angular coherence is located within the detectable region of a spectrometer and centered at the design wavenumber, $\sigma_0 = 1/\lambda_0 \approx 1586 \text{ mm}^{-1}$.

Translating the channeled spectrum's region of high fringe contrast, or centerburst, to wavenumbers for visible light requires a nonlinear relationship in OPD created by the dispersion in the system. The general form for the OPD in the MI can be written as

$$v = \sigma OPD(\sigma) \cos(\theta), \quad (6)$$

where $OPD(\sigma)$ is an arbitrary wavenumber-dependent OPD and v is given in units of radians. A typical channeled spectrum, such as the one presented in Fig. 2, has an $OPD(\sigma)$ that is constant

versus wavenumber, implying that v is linear with a maximum coherence at $\sigma = 0 \text{ m}^{-1}$. However, if $OPD(\sigma)$ has a quadratic dependence with wavenumber, as presented in Fig. 3 (c), then v can be made to cross through zero-OPD at any arbitrary spectral location. Thus, high coherence regions in the channeled spectrum occur at spectral locations with $v = 0$ waves. To illustrate this point, Fig. 3 (c) shows the absolute value of the phase, $|v|$, for the center of the FOV at $\theta = 12^\circ$.

Similar to an interferogram created in Fourier transform spectroscopy⁵, the channeled spectrum (as a function of v) can be Fourier transformed to recover the angular spectrum of the scene. Due to the nonlinearity in OPD created by the dispersive glass materials in the MI, the nonlinear phase, v , must be interpolated to onto a linear v axis to create a linear phase relationship in the channeled spectrum. Once the channeled spectra have a linear phase with respect to wavenumber, the angular spectra may be recovered using direct Fourier transform algorithms. A reconstruction algorithm which leverages this linear interpolation procedure is detail in section 5.0.

The following section 3.0 will detail the modeling, design, and experimental procedures associated with multiple interferometer-based systems which were investigated to implement the SSM technique using nonlinear dispersion. These interferometer-based systems include the conventional Michelson and Mach-Zehnder interferometers, a polarization grating-based interferometer, a ‘compact’ Mach-Zehnder, and an interferometer which leverages the dispersion in a birefringent retarder. Advantages and limitations for these systems will be discussed, as well as current issues associated with tolerancing and its effects on measurement (and reconstruction), with recommendations for potential systems future systems.

2.2 SSM Architectures, Experimental Configurations, and Results

A Michelson interferometer (MI) has the capability of implementing the SSM technique, and as such was the prototype for modeling the characteristics of an interferometer-based optical system. This can be used to create a nonlinear channeled spectrum in which the angular spectrum could be multiplexed onto longitudinal carrier frequencies, such that each angle of incidence on the interferometer creates a unique frequency in the interference profile. However, limitations relating to large physical dimensions, and wavelength dependent shear between the two beams of the MI, led to the investigation of several other interferometer systems. Several systems were identified, and compared to the angular resolution of a conventional ideal lens. Various designs are shown in Fig. 4. Each optical system is comprised of two dispersive glass materials (G1 and G2) with different dispersion characteristics versus wavelength, defined by their respective indices of refraction (n_1 and n_2) and Abbe numbers (v_1 and v_2).

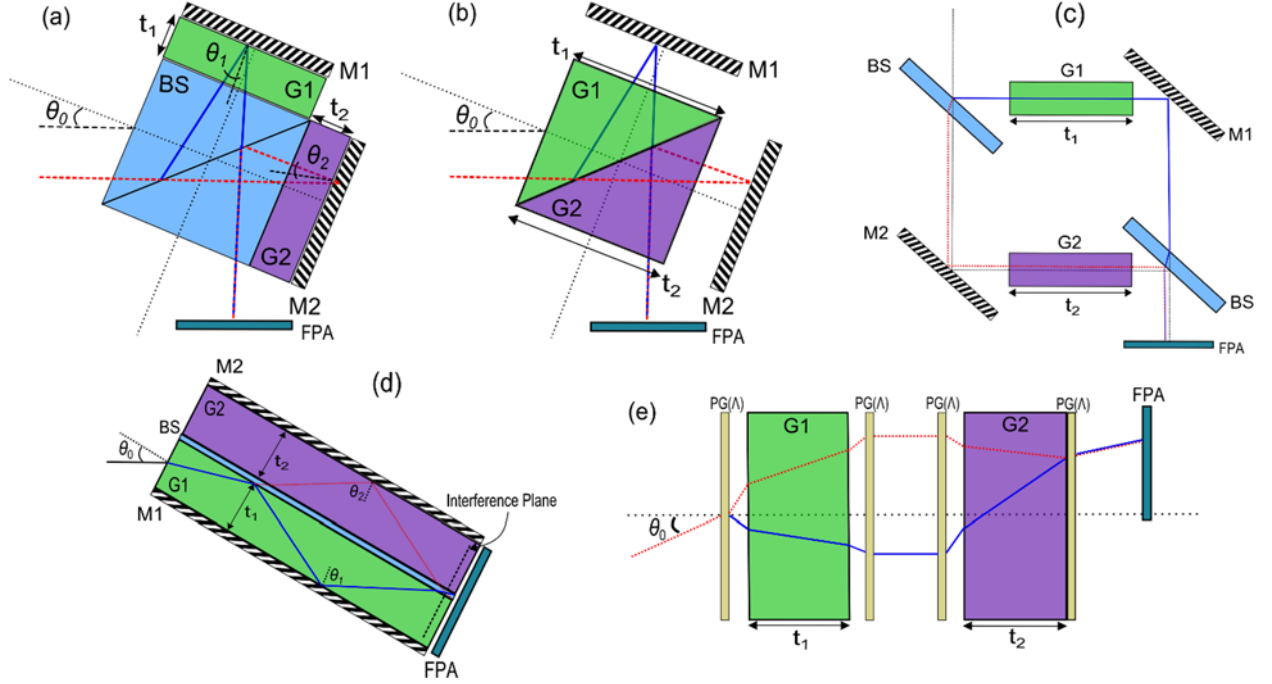


Fig. 4. Designs for the dual-glass type interferometer systems include the conventional (a) and modified (b) Michelson interferometer, the conventional (c) and modified (d) Mach-Zehnder interferometer, and the diffraction-based polarization grating (e) interferometer.

The results of the analyses performed for these systems will be presented in the following subsections.

2.2.1 Michelson Interferometer

2.2.1.1 *Modeling*

First, the Michelson interferometer (Fig. 4 (a)) was modeled. A first order SSM model for the MI was created to analyze the optical path difference (*OPD*) generation in the interferometer, maximum achievable angular resolution using the SSM technique with the MI, and the physical dimensions required to meet resolution goals. The first order model uses fundamental geometrical optics to analyze how the optical path difference varies as a function of wavelength, index of refraction of glass components, and initial angle of collimated white light incident on the beam splitter. Similar to previous methods used in the analysis of field-widened Michelson interferometers [3, 4], the technique is based primarily on the geometry and effective optical path lengths along the optical axis of the system. The OPD for a MI has been shown to be the difference in optical path lengths of beams traveling through two different arms of the system. Consider the MI as shown in Fig. 5, with two glass plates (or dispersion fluid), one in each arm of the interferometer.

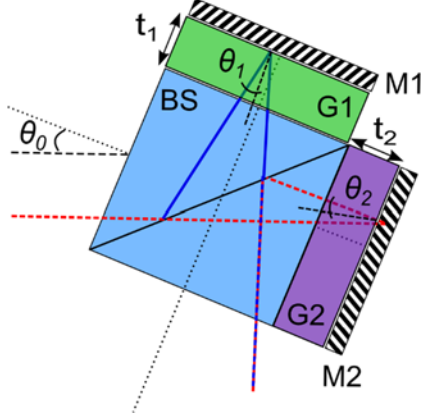


Fig. 5. A Michelson interferometer with a plate of glass (or dispersion fluid) in each arm. One plate has a higher relative dispersion (lower Abbe number) than its counterpart.

In Fig. 5, G1 and G2 are markers of the two glass plates, each having an index of refraction of $n_1(\lambda)$ and $n_2(\lambda)$, and thicknesses t_1 and t_2 , respectively. The two plates are mounted (with negligible air gaps) between mirrors M1 and M2, and a 50/50 beam splitter that has a wavelength dependent index of refraction of $n_{BS}(\lambda)$. Collimated light is directed into the system at an initial angular offset of θ_{tilt} , such that every angle of incidence is unique during validation. The OPD of the ideal MI interferometer, depicted in Fig. 1, may be represented as

$$OPD = OPL_1 - OPL_2, \text{ and} \quad (7)$$

$$OPD = 2n_1 t_1 \cos(\theta_1) - 2n_2 t_2 \cos(\theta_2). \quad (8)$$

It may be shown that (2) [3] can be rewritten in terms of the angle of incidence, θ_i , of the collimated source as

$$OPD = 2n_1 t_1 \left(1 - \frac{\sin^2(\theta_i)}{n_1^2} \right)^{1/2} - 2n_2 t_2 \left(1 - \frac{\sin^2(\theta_i)}{n_2^2} \right)^{1/2}. \quad (9)$$

By Taylor series expansion, the expression of (9) may be expanded about the argument θ_i to identify the higher order behavior of the system as

$$OPD = 2(n_1 t_1 - n_2 t_2) - \sin^2(\theta_i) \left(\frac{t_1}{n_1} - \frac{t_2}{n_2} \right) - \frac{\sin^4(\theta_i)}{4} \left(\frac{t_1}{n_1^3} - \frac{t_2}{n_2^3} \right) - \frac{\sin^6(\theta_i)}{8} \left(\frac{t_1}{n_1^5} - \frac{t_2}{n_2^5} \right) - \dots \quad (10)$$

From (10), it is clear that the MI's OPD is mainly influenced by the indices of refraction and thicknesses for the two glass plates/fluids (n_1/t_1 and n_2/t_2) and the angle of incidence, θ_i , of the collimated light source.

2.2.1.2 Experimental Design

After analysis of several combinations of flint (higher dispersion) and crown (lower dispersion) glass types, N-LAK33A (G1) and N-SF14 (G2) were chosen as the two dispersive materials to be used in proof of concept experiments for the SSM technique. The dispersion curves for N-LAK33A ($n_d = 1.7539$, $v_d = 52.27$) and N-SF14 ($n_d = 1.7618$, $v_d = 26.53$) materials are depicted in Fig. 6 (a), giving a dispersion intersection at $\lambda_0 = 736.4$ nm. The thickness of the glass plates was

specified at $t = 10$ mm, with dial indicator measurements (after manufacturing) indicating thicknesses for the N-LAK33A and N-SF14 of $t_1 = 10.205$ mm and $t_2 = 10.182$ mm, respectively. Simulation of the channeled spectra generated for a $\theta \sim 7^\circ$ FOV at $\theta_0 = 10^\circ$ for ideal (equal) and actual glass thicknesses is presented in Fig. 6 (b). A proof of concept experimental setup for the MI-based system is presented in Fig. 7. In this situation, the spectrometer is used to sample across the exit pupil of the system.

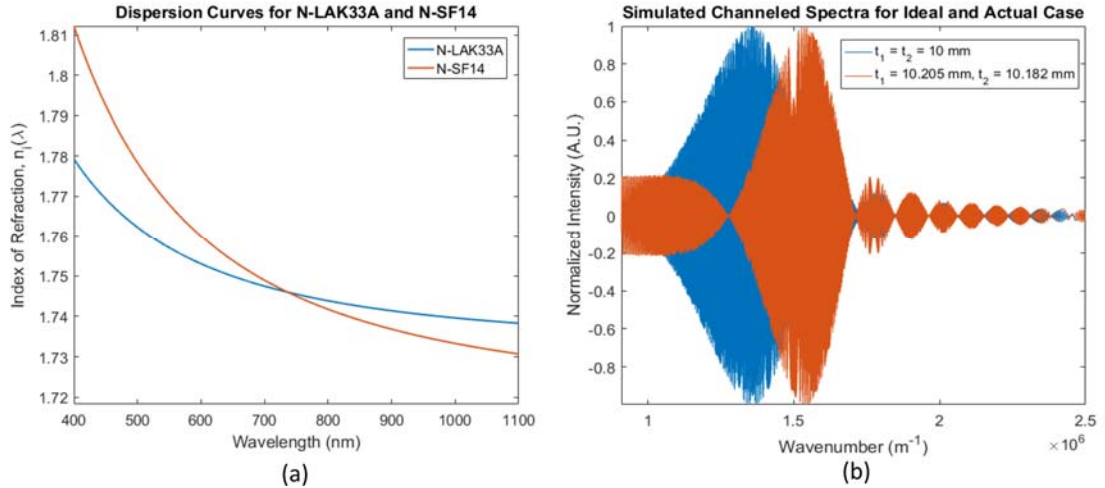


Fig. 6 (a) Dispersion curves for glass windows N-LAK33A and N-SF14. (b) Simulations of channeled spectra for the ideal case ($t_1 = t_2$) and the actual case ($t_1 \neq t_2$).

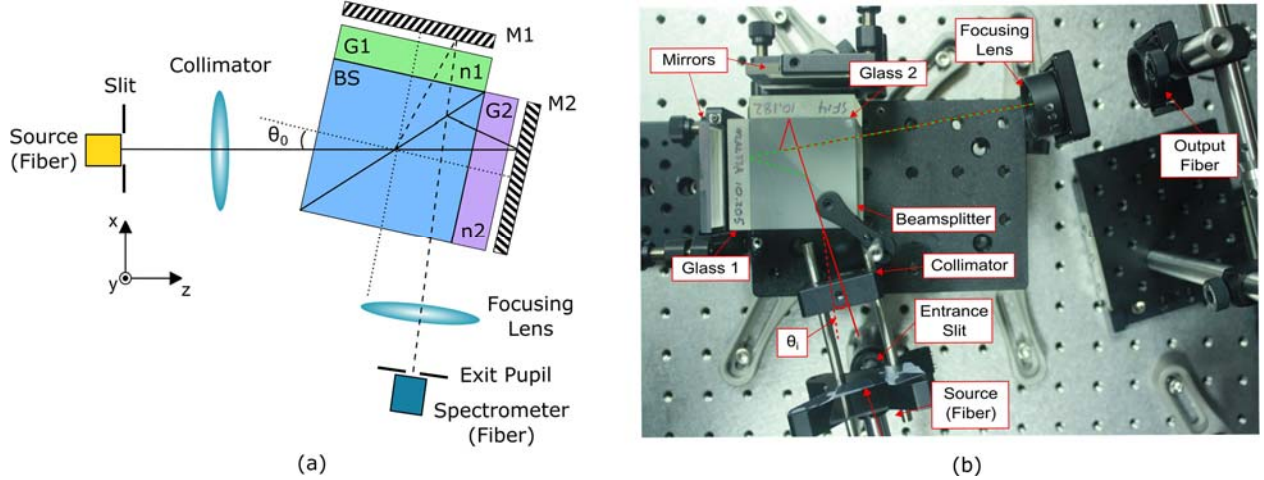


Fig. 7. (a) Schematic of MI system for SSM proof of concept experiment. (b) Optical table setup for SSM experiment, sampling the (exit) pupil plane of the collimator.

In the schematic of the experimental setup in Fig. 7, a tungsten halogen lamp is used as the broadband white light power spectrum. Light from the lamp is propagated by a fiber optic microscope light guide to illuminate a 7 mm long slit which acts as the incident uniform angular spectrum. The entrance slit is collimated by an F/2 achromat ($f = 50$ mm) into the MI at an angle of $\theta_0 = 10^\circ$ with respect the normal axis of the beamsplitter's (BS) front surface. A 50" non-polarizing N-BK7 cube beamsplitter with $\sim 50/50$ R/T is used to reflect/transmit the two beams into the corresponding arms. Each beam propagates through one of the glass plates, N-LAK33A (G1) and N-SF14 (G2), with thicknesses $t_1 = 10.205$ mm and $t_2 = 10.182$ mm, respectively. After

reflection at dielectric mirrors M1 and M2, the two beams recombine to interfere at the BS interface. The collimated output of the MI is collected by another F/2 achromat ($f = 50$ mm), and an image of the collimator (*i.e.* exit pupil) is sampled using a 300 μm fiber. Light from the fiber is measured using a Thorlabs Optical Spectrum Analyzer (Thorlabs OSA201C) with a spectral response of $\lambda \approx 350\text{-}1100$ nm and maximum spectral resolution of 0.25 cm^{-1} .

2.2.1.3 Results

The preliminary experiment using the MI interferometer was designed to interrogate several factors related to the measured channeled spectrum. This included: (1) centerburst spectral location; (2) interference fringe frequency (compared with simulation); (3) contrast of centerburst; and (4) phase variations across the pupil. The experimental setup in Fig. 7 allows for sampling different positions across the pupil by translating the 300 μm fiber orthogonal to the optical axis, across the defocused image of the scene's slit. In this situation, we can measure the amplitude and phase across the slit, giving an idea of the centerburst's location and fringe frequency, as well as any phase variations across the measurable spectral band. In Fig. 8, the normalized, mean centered spectra for 3 slit positions (at $x = \{-3.5\text{ mm}, 0\text{ mm}, \text{ and } 3.5\text{ mm}\}$) are plotted versus wavelength. The spectra were acquired at a spectral resolution of 2 cm^{-1} with the OSA with maximum gain and 40 rolling averages. The raw channeled spectral measurement were flat field corrected by

$$b'(\nu) = \frac{b_M(\nu) - b_D(\nu)}{b_X(\nu)}, \quad (11)$$

where b' is the processed spectrum, b_M is the measured spectrum, b_D is a dark frame, and b_X is the spectrum of the unmodulated lamp. Additional Fourier filtering was strategically applied to remove additional noise components and background modulations.

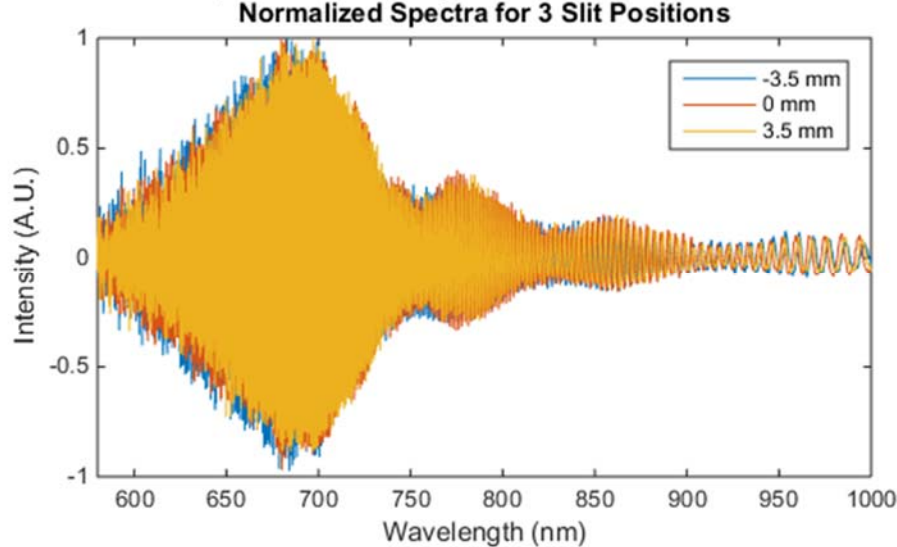


Fig. 8. Flat field corrected channeled spectra for 3 positions across the defocused image of the scene slit (*i.e.* exit pupil).

The normalized channeled spectra in Fig. 8 clearly show a peak in contrast (*i.e.* centerburst) at a spectral location of $\lambda_0 \approx 682.1$ nm. Dispersion in the system produced by the glass materials is evident from the nonlinearity in fringe frequency across the spectral band, as well as the expansion of the centerburst. A comparison of the measured experimental data with a simulation of the

experimental design is presented in Fig. 9, with both spectra sampled at a spectral resolution of 2 cm^{-1} .

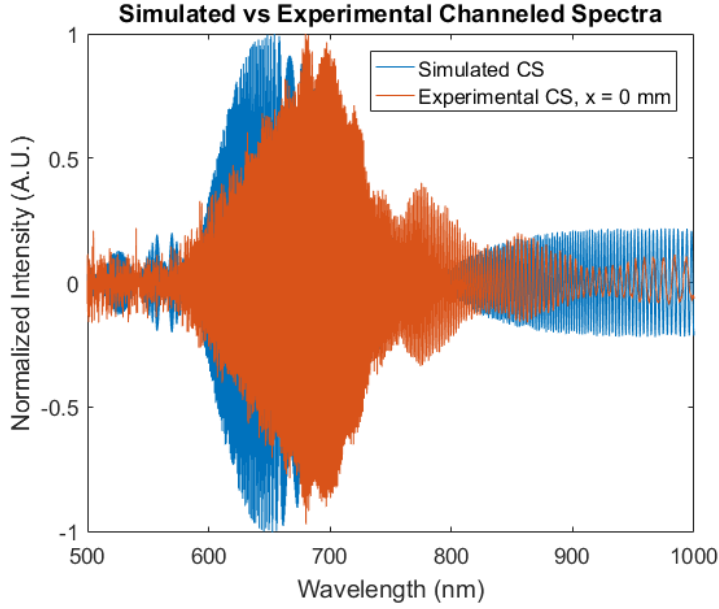


Fig. 9. Simulated (blue curve) versus experimental (red curve) channeled spectra for the proof of concept MI system.

Centerburst locations in Fig. 9 for the simulated and experimental data were found to be $\lambda_0 \approx 658.1 \text{ nm}$ and $\lambda_0 \approx 682.1 \text{ nm}$, respectively, with differences most likely attributed to beamsplitter terminus or small displacements from zero-OPD in the experimental MI. Fringe frequencies near the centerbursts are approximately equal (fringe period $\sim 0.75 \text{ nm}$), however, differences in fringe frequency are evident at longer wavelengths which may be caused by lower spectral resolution at the edge of the detectors spectral range.

To investigate phase variations across the pupil, the fiber is translated across the defocused image of the scene slit. Fig. 10 depicts a magnified view of the processed experimental data near the centerburst (a) and at longer wavelengths (b) to demonstrate that sampling at different locations across the pupil exhibit similar amplitude, but different phase information.

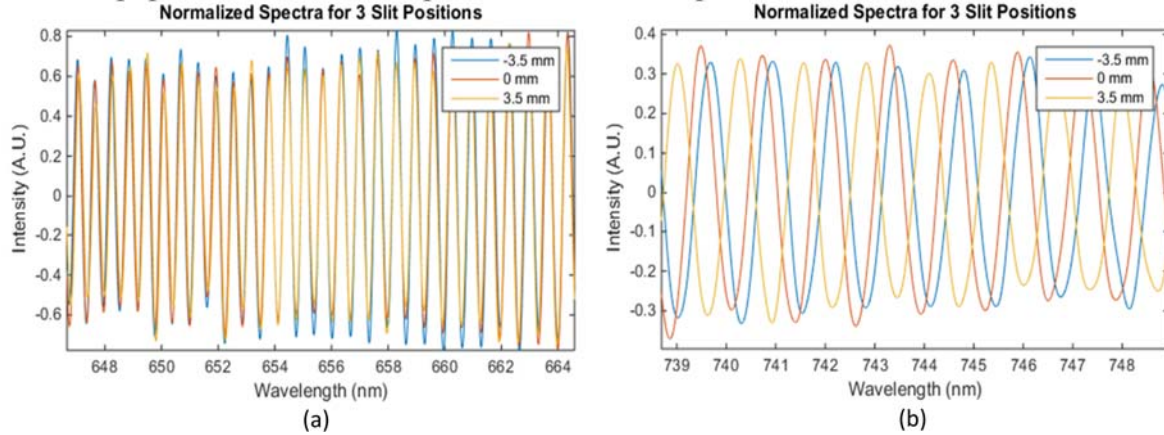


Fig. 10. Magnified view of the processed experimental data near the centerburst (a) and at longer wavelengths (b).

From Fig. 10 (a) it is evident that the 3 angular positions across the slit coherently match near the centerburst, and that the interferometer is stable under the experimental integration times. In Fig. 10 (b), the fringe frequencies of the 3 incident angle ‘bands’ are no longer coherently match as expected, demonstrating that each incident angle is given a unique frequency component in the measured spectrum.. A superposition of these 3 spectra would be closer to the ideal measurement for the system, in which all amplitude and phase information from the scene is collected in the pupil.

2.2.2 Mach-Zehnder Interferometer

2.2.2.1 *Modeling*

The conventional Mach-Zehnder (MZ, Fig. 4 (c)) interferometer setup with a different glass plate in each path gives an on-axis OPD (by phase arguments) of

$$OPD_{TMZ} = n_1 t_1 - n_2 t_2. \quad (12)$$

Off-axis angles of incidence that are much smaller or larger than the usual 45° of the first beamsplitter would potentially have problems staying confined to the system (e.g. oblique angles may not be able to enter the glass type, let alone propagate on the normal path). To alleviate this situation, the modified Mach-Zehnder (MMZ, Fig. 4 (d)) fully encapsulates the two beams at a larger range of incident angles by extending the beamsplitter and filling the two optical paths with the glass plates. The MMZ is similar to a coupled waveguide in which each beam propagates through a different material (experiences a different optical path length) before “recombining” further down the system. Several issues arise with this setup including, how light is collected into the system ($\theta_0 = 0^\circ$ would only propagate through one glass plate with the shown setup), how the interference is to be detected since it occurs inside the beamsplitter (possibly similar to lateral shearing interferometer at output in which the two beams cross), multiple internal reflections will increase the dispersion at wavelengths other than the design wavelength (to reduce this effect the system would need to be shortened in the longitudinal direction). By phase accumulation and geometrical ray tracing arguments, the OPD for the MMZ appears to be proportional to $1/\cos(\theta)$, but treating the MMZ similar to a two plane-parallel plate (Fabry-Perot cavity) system gives the usual $\cos(\theta)$ proportionality if the two beams are compared relative to an incident ray being reflected at the surface of G1. The model for this two plane-parallel plate situation is presented in Fig. 11.

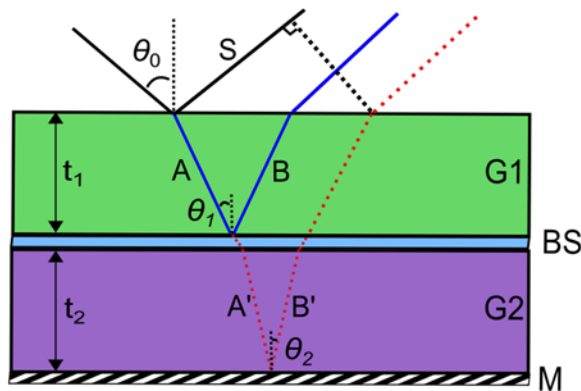


Fig. 11. Two plane-parallel plate model of MMZ interferometer system.

To define the OPD in terms of the difference between optical path lengths, the two ray paths in Fig. 11 are labeled with uppercase A/B and A'/B' such that

$$OPD = OPL_1 - OPL_2 = (A + B) - (A' + B') - S, \quad (13)$$

where S denotes the optical path as seen by a ray that is reflected by the surface of G1. In this situation, since the beamsplitter (BS) acts a mirror to optical path 1, and is transparent to optical path 2, we can write $A = B$ and $A' = B'$ to give

$$OPD = \frac{2n_1 t_1}{\cos(\theta_1)} - \frac{2n_2 t_2}{\cos(\theta_2)} - S. \quad (14)$$

By observation of the MMZ system it would appear that the S term would not be needed since rays reflected at the first surface would not be relevant to the interference produced at the output. This leaves the $1/\cos(\theta)$ dependence mentioned before. If S is to be taken into consideration, geometric arguments show that it is equal to

$$S = [2t_1 \tan(\theta_1) + 2t_2 \tan(\theta_2)] \sin(\theta_0), \quad (15)$$

which when substituted into equation (14) with the of Snell's law relations and a trigonometric identity reduces the OPD to

$$OPD = 2n_1 t_1 \cos(\theta_1) - 2n_2 t_2 \cos(\theta_2), \quad (16)$$

which is identical to the OPD for a traditional MI.

2.2.2.2 Experimental Design

Similar to the MI detailed in section 3.1.2, the experimental design of the MZ interferometer incorporates the two glass windows, N-LAK33A and N-SF14 with indices of refraction denoted n_1 and n_2 , respectively. This design was implemented to allow for larger off-axis angles (larger potential θ_0 compared with MI), which would reduce the measured spectral frequencies and loosen the restraint on high spectral resolution, as well as increase the maximum experimental angular resolution. A schematic and table top experimental setup for the MZ is presented in Fig. 12.

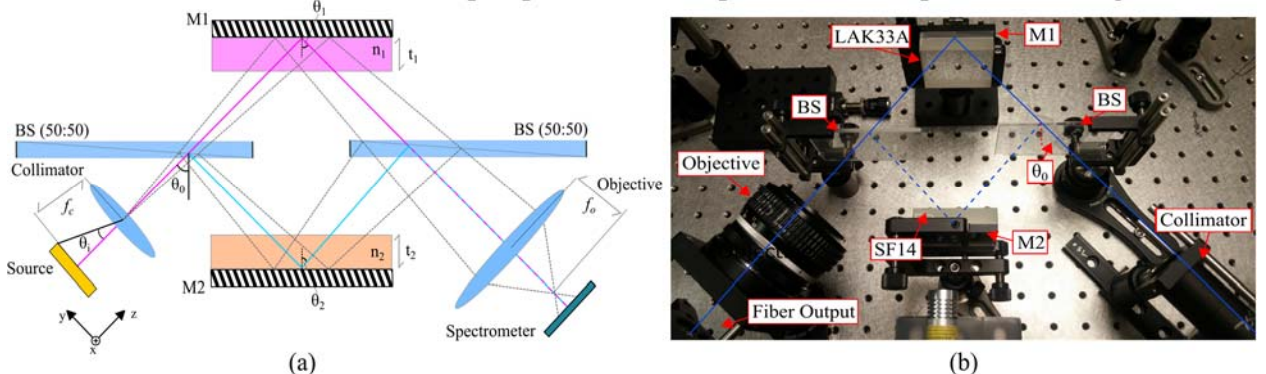


Fig. 12. (a) Schematic and (b) optical table setup for a proof of concept experiment using a MZ interferometer.

Referring to Fig. 12 (a), the experimental proof of concept for the SSM technique uses a 150 W halogen source (work light bulb) as the broadband white light source. The filament of the halogen lamp acts as the scene's 'slit', and is further stopped down by a one-dimensional 15 mm long slit. The scene's slit is collimated into the system and split into two beams at the first of two 3 mm thick, N-BK7 visible ($\lambda = 400-700$ nm) plate BS (Edmund Optics #62-882). Each of the two beams propagates through one of the two dispersive materials, which are mounted onto a dielectric mirror.

The reflected beams recombine at the second plate BS to interfere, and light at the output is collected with an F/1.8 Nikon lens. A 1000 μm aperture VIS-NIR fiber is used to sample the pupil plane of the system and propagate the light to the spectrometer.

2.2.2.3 Alignment

The alignment procedure for the MZ interferometer relies on balancing the interference of both planar and spherical wavefronts at the sampling plane of the system. The basic procedure is illustrated in FIG 13.

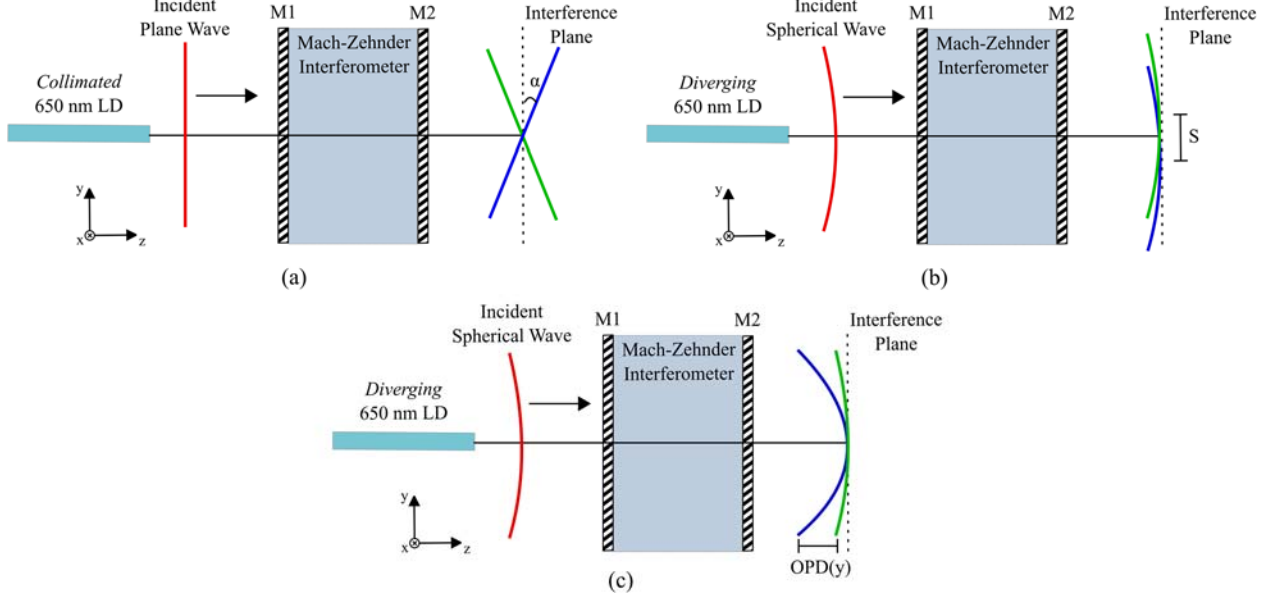


Fig. 13. Illustrations of the three techniques used for aligning the MZ interferometer for proof of concept experiments.

The first step in the procedure is to propagate a collimated monochromatic source (*e.g.* laser diode, $\lambda = 650 \text{ nm}$) into the interferometer as in Fig. 13 (a). As the planar wavefronts interfere at the output of the interferometer, it is possible to use the tip-tilt on the plate BS mounts to adjust the angle between the two interfering beams. This angular shear may produce additional spatial frequencies across the pupil, and must be eliminated before measurement. The second and third step in Fig. 13 (b) and (c) rely on a diverging laser diode to correct for lateral shear between the two spherical wavefronts and tune the interferometer to zero-OPD (for which all incident wavelengths interfere constructively). By using the tip-tilt mounts of the plate BS and the longitudinal translation stage mount for one of the mirrors, it is possible to align the system to zero-OPD. As with the relative angle between planar wavefronts in Fig. 13 (a), the lateral shear removed in order to eliminate unwanted spatial frequencies across the pupil, which ultimately reduce the contrast in the measured channeled spectra due to fringe incoherence.

2.2.2.4 Results

Experimental channeled spectra measurements for the SSM technique using the MZ interferometer were acquired using two detectors, the Thorlabs Optical Spectrum Analyzer (OSA) and an Oriel MIR8035 Fourier transform infrared (FTIR) spectrometer. Both scanning Michelson-based Fourier transform spectrometers have similar maximum spectral resolution ($\Delta\sigma \sim 1 \text{ cm}^{-1}$), with the OSA operating in the visible ($\lambda = 350\text{-}1100 \text{ nm}$) and the FTIR with a silicon detector (Newport 80019) operating in the NIR ($\lambda = 700\text{-}1000 \text{ nm}$). These spectrometers were used in conjunction with the MZ experimental setup to determine if the centerburst (*i.e.* maximum contrast, or spectral

location where phase is constant across the pupil) location was distinguishable in the measured spectra. A typical measurement with the OSA is presented in Fig. 14, plotting signal intensity (W) versus wavelength. The plot is magnified over the range of $\lambda \sim 545$ - 670 nm to examine spectral regions near the location identified by the ideal simulations (see Fig. 9).

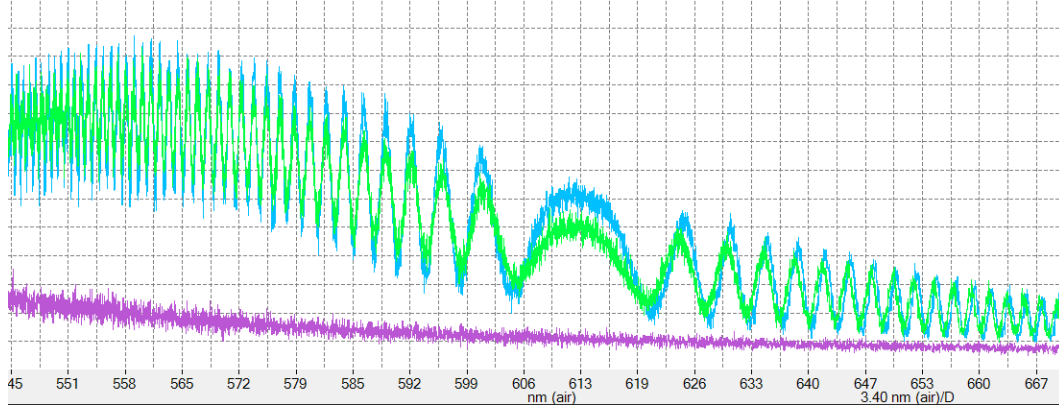


Fig. 14. Channeled spectrum acquired by the OSA spectrometer from interference generated in the dispersive MZ interferometer.

The measured spectrum in Fig. 14 demonstrates that the dispersive MZ interferometer indeed generates a sinusoidally modulated white light spectrum. However, due to the nonlinear dispersion associated with the glass materials, the spectral location of the centerburst is not readily apparent. One drawback to the OSA is the limited signal-to-noise ratio (SNR), where the blue curve represents a spectral measurements and the purple curve a dark frame. To operate the system with sufficient SNR, a high intensity light source was needed as the broadband white light source (e.g. 150 W tungsten lamp or 75 W xenon arc lamp). One prominent feature in the measured spectrum is the static phase point located at $\lambda \sim 613$ nm. This region of the spectrum is related to the $\partial OPD / \partial \sigma = 0$ condition, however, and not the $\partial OPD / \partial \theta = 0$ associated with the centerburst. It may be possible in the future to use this point as a reference to determining the location of the centerburst, which is why measurements with the FTIR were also investigated.

Since the contrast of the interference fringes measured by the OSA were relatively low for longer wavelengths ($\lambda > 800$ nm), spectral measurements with the FTIR were acquired to analyze the spectrum in the NIR. Fig. 15 plots the channeled spectrum versus wavenumber acquired from the same MZ interferometer setup in Fig. 14 using the FTIR with a spectral resolution of 8 cm^{-1} . Again, the interference fringes generated by the MZ interferometer are present from $\lambda \sim 700$ nm to 1050 nm, with reduced contrast near the edges of the silicon detector's spectral responsivity. Calculation of the contrast (or visibility) as defined by

$$V = \frac{I_{\max} - I_{\min}}{I_{\max} + I_{\min}}, \quad (17)$$

found that, at the simulated wavenumber of maximum coherence, $\sigma = 1357\text{ mm}^{-1}$, $V = 0.1477$. Whereas the maximum contrast in the channeled spectrum in Fig. 15 located at $\sigma = 1291\text{ mm}^{-1}$ was calculated at $V = 0.2140$. This result shows that additional tolerancing errors may be present in the system, making it difficult to determine the exact location of the centerburst. Improvements to the system would need to be made in order to lead to successful reconstruction of incident angular spectra using the SSM technique, primarily relating to consistently referencing the phase

of the interference fringes to the zero phase point (*i.e.* $\nu = 0$) by determining the spectral location of the centerburst.

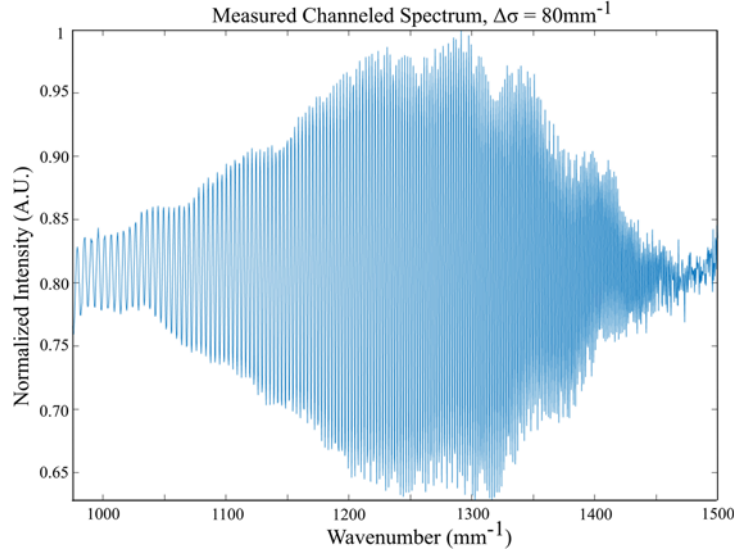


Fig. 15. Channeled spectrum acquired by the FTIR spectrometer from interference generated in the dispersive MZ interferometer.

2.2.3 Polarization Grating-based Interferometer

2.2.3.1 *Modeling*

Another potential system for the channeled SSM system (Fig. 4 (e)) is based on placing the dispersive glass materials between polarization gratings. A schematic for such a system is shown in Fig. 16.

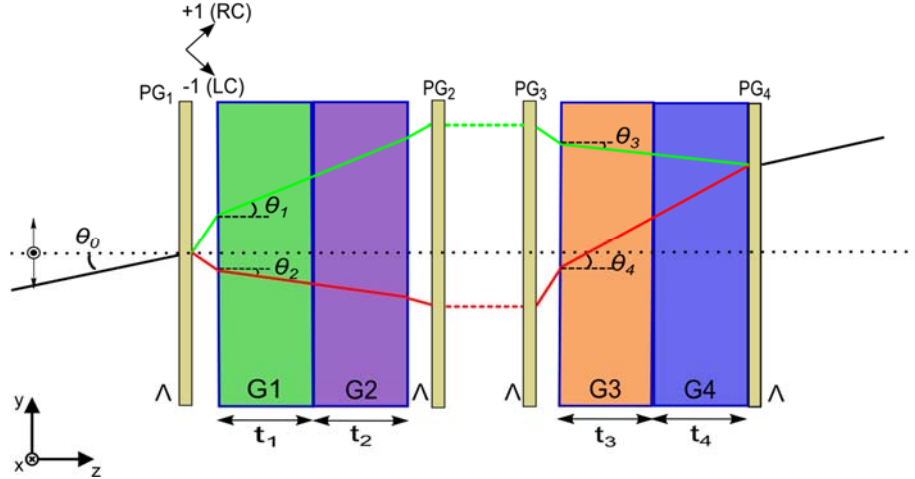


Fig. 16. Design of a PG-based channeled SSM system containing four dispersive materials and four polarization gratings.

The design of a PG system shown in Fig. 16 shows the general case of four dispersive glass plates or fluids (G₁, G₂, G₃ and G₄) and four polarization gratings, each taken to have the same period, Λ . Note that dispersion characteristics (as a function of wavelength) and thicknesses of the dispersive materials need not be the same and that the number of dispersive materials may differ from four depending on the tradespace analysis. The ‘best’ system for the system could contain

less than four glass plates (or more) and need not be symmetric (i.e. two plates between two PGs). The ideal scenario will be tackled by the tradespace analysis and the optical and geometrical breakdown of the system. Also, note that refraction will occur between the surfaces of G1 and G2, as well as G3 and G4, assuming they are determined to be of different dispersive characteristics. The last polarization grating in the system (i.e. PG₄) is placed directly on the surface of G4 for both ease of depiction here as well as to note the possibility of attaching PGs directly to glass surfaces when the system is built.

The main benefit behind the alternative PG system, compared a tilted MI system, is that it may be designed to eliminate wavelength dependent shear within the system (or more precisely, the dispersive shear becomes constant with respect to wavelength), as the materials (e.g. PG periods) may be chosen to make the system more robust to incident angle θ_0 . Another benefit being that the system containing PGs demonstrates lower spectral frequencies in interferograms due to lower OPDs. The first PG of period A , splits the incident electromagnetic radiation (which is given an initial angle of incidence of θ_i) into the +1 and -1 orders of right circular (RC) and left circular (LC) polarizations, respectively. The two orders then travel through the system, propagating through a different optical path length determined by the thicknesses and dispersive characteristics of the materials. Because of the geometry of the system, the fourth PG recombines the two orders (with a slight shear) into the output of the system. Due to the fact that the +1 and -1 orders are subject to different optical path lengths, an optical path difference (OPD) is created within the system.

Analyzing the simple case of two dispersive materials (glass plates), each between a set of two PGs with period A , will give an initial idea of the OPD of the system. The parameters of this system are depicted in Fig. 17.

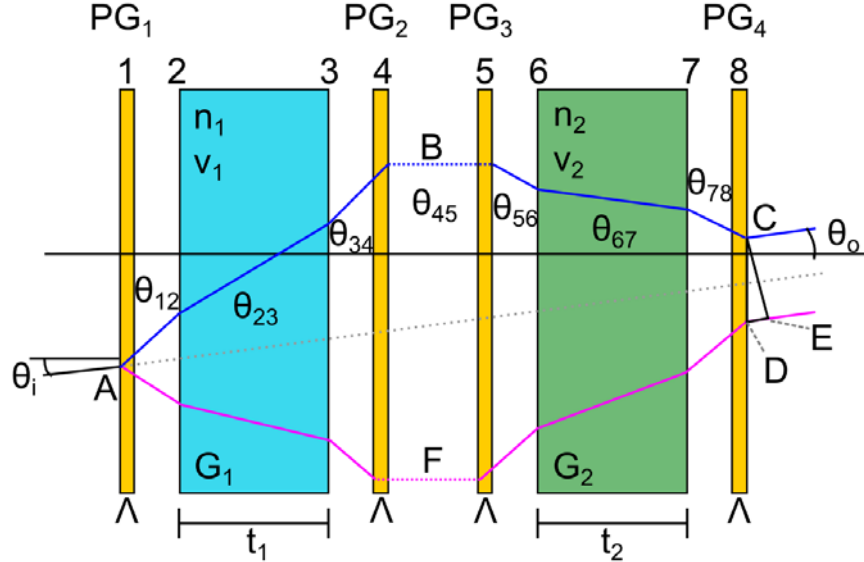


Fig. 17. Design of PG-based system with two dispersive materials between respective sets of PGs with period A . The rays are shown for an unbalanced system at a wavelength for which the refractive indices of glasses G1 and G2 are unequal.

In this situation, the two materials are G₁ and G₂ with indices of refraction and thicknesses of n_1 and t_1 , and n_2 and t_2 , respectively. While it is drawn explicitly in Fig. 17 with an air gap, the axial spacing between PG₁ and G₁, G₁ and PG₂, PG₂ and PG₃, PG₃ and G₂, and G₂ and PG₄ are

assumed zero (e.g., they are in perfect contact). In this configuration, the optical path difference can be calculated using the ray geometry of Fig. 17, such that

$$OPD = (AB + BC) - (AF + FD) - DE. \quad (18)$$

The optical path length of the interferometer's modes can be established as

$$OPL_1 = AB + BC, \text{ and} \quad (19)$$

$$OPL_2 = AF + FD + DE, \quad (20)$$

where OPL_1 and OPL_2 are the optical path lengths of the top and bottom ray paths, respectively. Using ray tracing, the optical paths for each ray can be calculated through a series of refraction and transfer procedures. This yields the values for the intervening angles, as well as the offset positions along the x axis for the various rays. Ray tracing produces the following (exact) relationships:

$$\theta_{12} = \sin^{-1} \left(\frac{m\lambda}{\Lambda} - \sin \theta_i \right), \quad (21)$$

$$\theta_{23} = \sin^{-1} (\sin \theta_{12} / n_1), \quad (22)$$

$$\theta_{34} = \sin^{-1} (n_1 \sin \theta_{23}), \quad (23)$$

$$\theta_{45} = \sin^{-1} \left(\frac{-m\lambda}{\Lambda} - \sin \theta_{34} \right), \quad (24)$$

$$\theta_{56} = \sin^{-1} \left(\frac{-m\lambda}{\Lambda} - \sin \theta_{45} \right), \quad (25)$$

$$\theta_{67} = \sin^{-1} (\sin \theta_{56} / n_2), \quad (26)$$

$$\theta_{78} = \sin^{-1} (n_2 \sin \theta_{67}), \text{ and} \quad (27)$$

$$\theta_0 = \sin^{-1} \left(\frac{m\lambda}{\Lambda} - \sin \theta_{78} \right). \quad (28)$$

Meanwhile, the offsets, assuming that the x intercept of the incident ray is equal to x_1 , yields

$$x_3 = t_1 \tan \theta_{23} + x_1, \quad (29)$$

$$x_3 = x_6, \text{ and} \quad (30)$$

$$x_7 = t_2 \tan \theta_{67} + x_6. \quad (31)$$

With these calculations, OPL_1 or OPL_2 can be calculated by substituting a diffraction order $m = +1$ or $m = -1$, respectively. Ultimately, the shear between the two beams is small, but it is present, and it represents an identical effect to that which occurs in a Fabry Perot Etalon or Michelson Interferometer. A view of a real ray trace for such a PG-based system is depicted in Fig. 18. In this

case, the system consists of two 100 mm thick pieces of model glass with refractive indices $n_d = 1.7$ and Abbe numbers $v = 20$ and $v = 80$ for glasses G1 and G2, respectively, and each of the four PGs has a grating period $\Lambda = 4$ microns. For this example, the optical path difference between the right circular and left circular beams can be calculated as $OPL_1 = 347.818$ mm and $OPL_2 = 347.817$ mm. This yields a relatively small OPD of $OPD = 0.95$ microns. Ultimately, this is a much smaller OPD than what is achievable in a Fabry Perot Etalon given a similar aperture size.

For instance, in this system, a separation between the two beams at surface 4 and 5 is calculated to be 20 mm, whereas an FPE could achieve a 0.95 micron OPD at an incidence angle of 20 degrees with a cavity thickness of 0.5 microns. This would translate into a spatial separation of

$$D = 2d \tan \theta, \quad (32)$$

where d is the FPE thickness and D is the spatial separation between the two interfering rays, and corresponds to the aperture size required by the FPE when the beam diameter is infinitely small. In this case, $D = 2 * 0.5e-6 * \tan(20) = 0.36$ microns, a factor of 55E3 times smaller than the PG interferometer. Thus, it is likely that either (a) other methods of heterodyning are required or (b) an alternative interferometer or technique will be necessary.

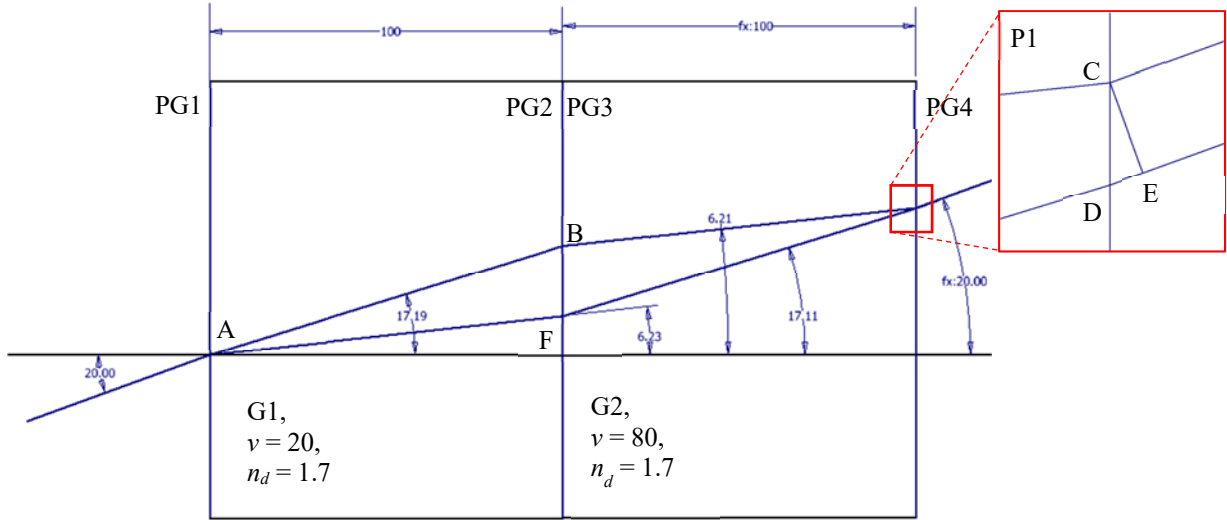


Fig. 18. PG-based system, depicted for a 20 degree angle of incidence at 633 nm. The PG grating periods are all equal to $\Lambda = 4$ microns. All dimensions in mm or degrees. A zoomed in region of the two exiting rays is displayed in panel (P1).

2.2.3.2 Experimental Design for a PG-based Interferometer System

A basic schematic for the PG-based interferometer system for proof of concept experiments is shown in Fig. 19.

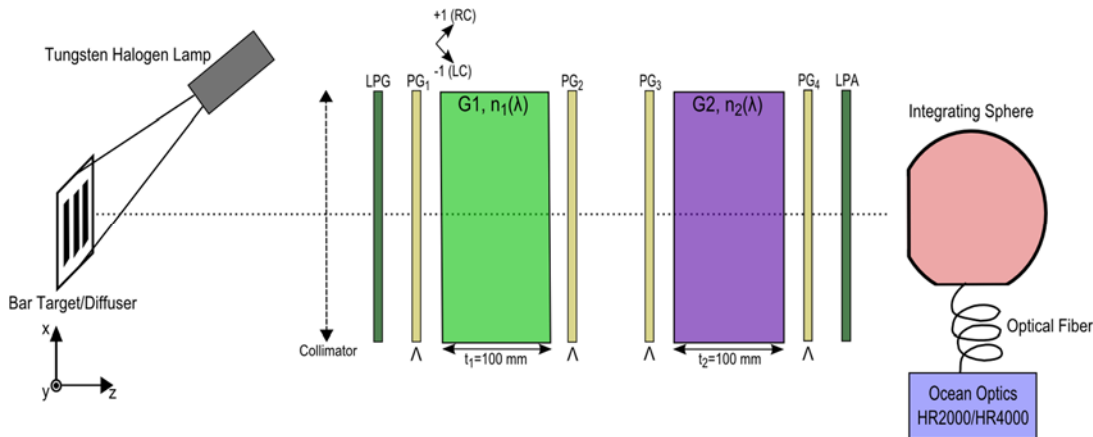


Fig. 19. Experimental setup for establishing proof of concept results for the SSM technique and resolution data using a PG-based interferometer.

Light from a tungsten halogen lamp (or similar spectrally broadband visible source) illuminates a diffuse surface or bar target creating the scene for the imaging system in object space (which may be used to measure spatial resolution). The source light is collimated (or in the far field) before entering the interferometer through a linear polarizer (LPG). This acts as the polarization generator to ensure linear polarized light enters the system. The first polarization grating, PG₁, with grating period Λ , diffracts the incident linearly polarized from the scene into the $m = +1$ and $m = -1$ first orders that correspond to right circular (RC) and left circular (LC) light. As shown in previous works and discussions, the nonlinear dispersion characteristics of the two glass plates enables the maximum coherence of a generated channeled spectrum to be arbitrarily shifted to a wavelength in the visible region of the spectrum where the intersection of the two glass dispersion curves occurs. The two different optical path lengths (OPLs) corresponding to RC and LC, dependent on both incidence angle and wavelength, are recombined at PG₄ to create an interference profile in which the scene's angular spectrum is modulated onto the power spectrum. A linear polarization analyzer is placed in the system to selectively filter certain polarization states of interest before the modulated light enters an integrating sphere that homogenizes the signal and makes the system more robust to large off-axis angles. An optical fiber carries the integrated light to the Ocean Optics HR2000 (or HR4000) spectrometer to measure the power (and multiplexed angular) spectrum. Materials that were identified for the construction of the proof on concept (POC) included:

- Glass plates – Two dispersion characteristics (one high, one low) that (for now) have the dispersion intersection in the visible. Would like the pair of materials to maximize OPD as well as keep the frequency content of the channeled spectrum in resolvable ranges for the Ocean Optics HR2000/4000. Compensation across the field of view (FOV) for the design wavelength is also critical. Thus, the 1) materials/glass types need to be identified, 2) the physical dimensions (thickness, width, surface flatness, etc.) of the plates, 3) vendors need to be identified.
- Polarization gratings – the period(s) Λ and physical dimensions (related to size and placement) need to be determined based on the outcome of the meeting with Dr. Escuti.
- Spectrometer – the HR2000 and HR4000 could potentially be used for the experiment with “maximum” optical resolutions of 0.035 – 6.8 nm and 0.02 – 8.4 nm full-width half-maximum (FWHM), respectively (listed under Ocean Optics product specifications, <http://oceanoptics.com/product/hr2000-custom/>). Other spectrometers (e.g. echelle spec.) could be pursued depending on funding.

- Sources and light collecting/guiding optics – the sources currently available in the lab (tungsten lamp, argon lamp) could be used as well as the integrating sphere and optical fibers currently available. A source monochromator and/or another integrating sphere could potentially be looked into.
- Bar target – may or may not be needed depending on experiments.

2.2.3.3 Glass Selection Process and Results

A list of potential glass pairs was used, in conjunction with two-plate analysis, to determine the capabilities and performance of different materials in the PG-based interferometer. The main properties that were analyzed were the maximum OPD, the maximum absolute difference in OPD across the FOV, and the highest spectral frequency content of a basic channeled spectrum generated using the OPD in the system model. Glass dispersion, with respect to wavelength, was modeled using the general Sellmeier equation (coefficients from Schott Glass data sheet), and used as the index of refraction for glass 1 (G1) and glass 2 (G2) in the optical path length calculations. Pairs of glass materials were matched based on similar indices of refraction at n_d ($\lambda_d = 587.6$ nm) from the glass map in Zemax, with dispersion curve intersections occurring in the visible spectrum.

The spectral range of the calculations was 400 nm to 800 nm at 1,000 samples, with a 5,000 samples FOV ranging from 5° to 25° . The thicknesses of both glass plates, G1 and G2, were chosen to be 100 mm (semi-arbitrary values) with a PG period of 5.0 μm (which determines the incident angle in the system). Table 1 shows data from the glass analysis with pairs grouped by ranges of indices of refraction at n_d . Results include the (Schott) glass tag, dispersion intersection (λ_0), index of refraction at intersection (n_0), maximum, minimum and absolute difference of OPD, and the calculation of an approximate value for the maximum angular resolution for a PG-interferometer using the two glass types.

Table 1. Glass analysis data for several pairs of potential glass materials for the PG-interferometer.

	Glass 1	Glass 2	λ_0 (μm)	n0	max OPD (mm)	min OPD (mm)	max ΔOPD (m)	approx. min $d\theta$ (rads)	min $d\theta$ (degrees)
Group 1 ($nd = 1.65$)									
	LAK7	SF2	0.5116	1.6570	0.1335	-0.0994	0.1086	0.0071	0.4063
	LAK22	SF2	0.5156	1.6565	0.1219	-0.0952	0.0991	0.0078	0.4450
Group 2 ($nd = 1.69$)									
	LAK12	SF5	0.4983	1.6852	0.1587	-0.0994	0.1291	0.0060	0.3417
	LAK9	SF8	0.5481	1.6939	0.1161	-0.1364	0.1109	0.0082	0.4672
	PLAK35	SF8	0.5092	1.7000	0.1513	-0.1114	0.1231	0.0063	0.3585
	LAK14	SF8	0.4765	1.7067	0.2043	-0.0942	0.1662	0.0046	0.2654
	LAK14	SF15	0.6354	1.6940	0.0631	-0.1877	0.1525	0.0050	0.2889
	PLAK35	SF15	0.7626	1.6853	0.0100	-0.2049	0.1665	0.0046	0.2647
Group 3 ($nd = 1.72$)									
	LAK34	SF1	0.4564	1.7425	0.2771	-0.0879	0.2255	0.0034	0.1957
	LAK34	PSF69	0.5004	1.7368	0.2037	-0.1346	0.1658	0.0046	0.2662
	LAK34	SF10	0.5733	1.7302	0.1232	-0.1905	0.1548	0.0050	0.2846
	LAK8	SF1	0.7005	1.7069	0.0327	-0.2106	0.1711	0.0045	0.2575
Group 4 ($nd = 1.75$)									
	LAK33A	LAF7	0.4966	1.7627	0.1314	-0.0819	0.1069	0.0072	0.4126
	LAK33B	LAF7	0.4817	1.7656	0.1475	-0.0737	0.1200	0.0064	0.3676
	LAK33A	SF4	0.6076	1.7525	0.1004	-0.2234	0.1816	0.0042	0.2427
	LAK33B	SF4	0.5897	1.7548	0.1165	-0.2153	0.1749	0.0044	0.2519
	LAK33A	SF14	0.7743	1.7444	0.0092	-0.2921	0.2374	0.0032	0.1856
	LAK33B	SF14	0.7356	1.7469	0.0253	-0.2839	0.2307	0.0033	0.1910
Group 5 ($nd = 1.78$)									
	LAF33	SF56	0.5698	1.7875	0.1269	0.1913	0.1555	0.0049	0.2835
	LAF33	SF11	0.5706	1.7874	0.1314	-0.2030	0.1649	0.0047	0.2672

As expected, the higher the maximum absolute OPD in the system the lower the minimum resolvable angular separation, $d\theta$ (i.e., better resolution). This concludes that glass pairs with relatively high *absolute* values in the “max OPD” or “min OPD” columns would be best (e.g. LAK33A/SF14, LAK8/SF1, etc.) in order to maximize the angular resolution. However, this term is also directly related to the highest frequency content in the generated channeled spectrum. If the channel spectrum requires a higher spectral resolution than what is offered by the HR2000 or HR4000, then other glass types with lower maximum OPDs may need to be selected, or other spectrometer outlets will need to be pursued.

To determine the required spectral resolution for a given maximum OPD, we looked at four glass pairs with varying maximum OPD values. The maximum OPD for these pairs was used as the (spectral) frequency for a sinusoidal curve that approximated the highest frequency content across the entire spectrum as a function of wavenumber. In other words, given the value of OPD_{\max} calculated for a pair of glass types,

$$I(\sigma) \propto \cos(2\pi\sigma|\text{OPD}_{\max}|). \quad (33)$$

The glass pairs of interest and their related data are shown in Table 2. Spectral resolutions are denoted $\Delta\lambda$, with the subscripts F ($\lambda_F = 486.1$ nm), d ($\lambda_d = 587.6$ nm), and C ($\lambda_C = 656.3$ nm) representing the Fraunhofer spectral lines where the spectral resolutions were determined.

Table 2. Spectral resolutions required to resolve maximum frequencies in channeled spectrum, related to magnitude of OPD for four glass pairs.

Glass 1	Glass 2	λ_0 (μm)	max OPD (mm)	approx. min $d\theta$ (rads)	$\Delta\lambda_F$ (nm)	$\Delta\lambda_d$ (nm)	$\Delta\lambda_C$ (nm)
LAK33A	SF14	0.7743	0.2921	0.0033	0.4080	0.5880	0.7240
LAK8	SF1	0.7005	0.2106	0.0045	0.5640	0.8600	1.0720
LAK12	SF5	0.4983	0.1587	0.0060	0.7640	1.1080	1.3960
LAK22	SF2	0.5116	0.1219	0.0078	0.9760	0.1452	1.7560

Note that the combination of LAK22 and SF2, which represents the lowest maximum absolute OPD ($\text{OPD}_{\text{max}} = 0.1219 \text{ mm}$) of the glass pairs analyzed, requires a spectral resolution of $\Delta\lambda_F = 0.9760 \text{ nm}$ in the blue and $\Delta\lambda_C = 1.7560 \text{ nm}$ of resolution in the red. If the HR4000 can produce a reliable spectral resolution of approximately 2.0 nm, then an alternative detector or glass pair may need to be found. Also, it is important to note that many of these values for spectral resolution are only approximations, and the method and results are susceptible to error on the part of the investigator. The process of determining the required spectral resolutions used the OPD_{max} to generate a sinusoidal approximation for the channeled spectrum, which was then plotted in regions of interest with respect to wavenumber (inverse wavelength). Plots of this process for the LAK8/SF1 pair are shown in Fig. 20.

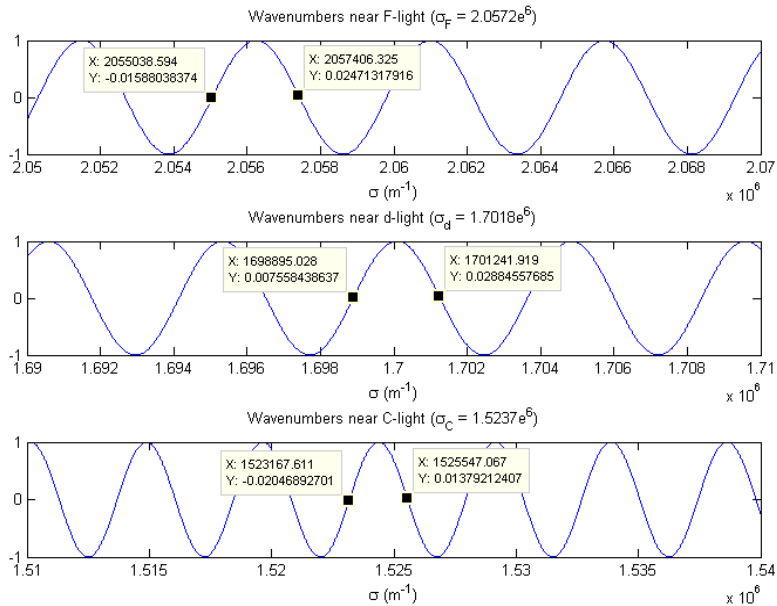


Fig. 20. Analysis of spectral content for the LAK8/SF1 glass pair at wavenumbers near the Fraunhofer spectral lines. Separation of the data cursors is an approximation of the spectral resolution needed to resolve the frequency content.

The difference of the inverses of the data cursor values (in wavenumber) give an approximation for the spectral separation in wavelength, *i.e.*

$$\Delta\lambda \approx \left| \frac{1}{\sigma_1} - \frac{1}{\sigma_2} \right|, \quad (34)$$

where σ_1 and σ_2 are the data cursor values in inverse meters. Obviously, this is not the most accurate process since values for $\Delta\lambda$ will statistically change every time the data cursor point is chosen. The data cursor values were chosen at the intensity value (arbitrary units) of 0 to represent the FWHM for that half-period in the channeled spectrum.

2.2.3.4 PG-interferometer as a Shearing Interferometer

Under further analysis, the PG-based interferometer acts as a shearing interferometer with 0 shear (displacement CE in Fig. 17 and Fig. 18) at $i = 0$ degrees for all wavelengths. Interference fringes have 0 spatial (angular) frequency versus wavenumber at incident angle $\theta_i = 0$ degrees and are in phase at λ_0 (based on the dispersion intersection of the two glass plates). This is a shearing interferometer, with interference behaving identical to a common-path Sagnac interferometer. However, it was determined that the shear is less efficient (compared to Sagnac interferometer). To demonstrate this point, the simulation in Fig. 21 plots the interference fringes generated at the CE plane of the PG-based interferometer. The main drawback for such a shearing interferometer is that the simulation required glass thicknesses of $t_1 = t_2 = 200$ mm to provide 0.22 nm of shear at 500 nm.

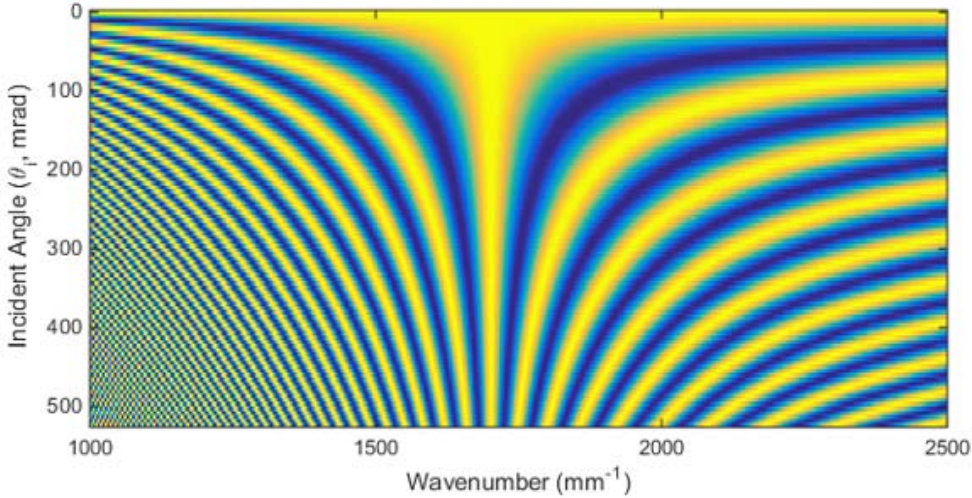


Fig. 21. Simulation of the interference fringes generated at the output of the PG-based interferometer, plotting angle of incidence θ_i versus wavenumber, σ .

2.2.4 Miscellaneous System Architectures

Other interferometer architectures which leveraged nonlinear dispersion, or more accurately systems which exhibited the necessary $\partial OPD / \partial \theta = 0$ at λ_0 for the SSM technique were also investigated. Two of these systems were a 1) ‘compact’ Mach-Zehnder interferometer and 2) an interferometer based on a birefringent retarder. The model designs and findings are presented in the following sections.

2.2.4.1 Compact Mach-Zehnder

Due to tolerancing concerns with the aforementioned systems (i.e. the MI and MZ interferometers) primarily relating to non-ideal effects from beamsplitter termini, mirror flatness, and aberrations, a compact MZ as shown in Fig. 22 was constructed and tested. In this design, the plate or cube beamsplitter and dielectric mirrors of conventional interferometers are replaced with gold thin film layers. To achieve the same functionality of a MZ interferometer, two layers of gold thin film are adhered to the outside surface of our two respective glass plates (N-SF14 and N-LAK33A). These gold layers are designed with a thickness sufficient to act as reflective surfaces as seen in the left-hand image of Fig. 22. The inside surface of one of the glass plates was also coated with a thin (~ 40 μm) layer of gold, which effectively acts as a beamsplitter at the center of the module.



Fig. 22. (left) A compact Mach-Zehnder interferometer with visible white light interference fringes visible and (right) the preliminary setup for measuring a channeled spectra from the compact Mach-Zehnder.

A preliminary experimental setup of the compact MZ is depicted in the right-hand image of Fig. 22. In this test, a slit is illuminated by a halogen tungsten lamp before collimation with a 50 mm focal length lens into the compact MZ. The collimated beam incident on the interferometer propagates through the first glass plate before splitting at the thin gold layer, which acts as the beamsplitter. The two respective beams reflect from the gold layers on the outside surface and recombine at the central gold layer to interfere. Light at the output is collected with a 50 mm focal length lens and sampled (within the pupil plane) by a fiber-coupled spectrometer.

In the preliminary experiment it was found that the interferometer was successful in generating a sinusoidally modulated white light spectrum. It was also noted that the device could be capable of operating at higher maximum angles of incidence ($\theta \sim 65^\circ\text{-}70^\circ$) compared to the previous interferometers ($\theta_0 \sim 10^\circ\text{-}15^\circ$ for the MI, $\theta_0 \sim 45^\circ\text{-}50^\circ$ for the MZ), which has the benefits of reducing the required spectral resolution of the detector and increasing the experimental angular resolution of the system. However, the compact design limits the FOV in this particular setup, and more design considerations would need to be taken into account to optimize the system. Alignment of the compact MZ was also limited due to the monolithic design. For instance, the left-hand image of Fig. 22 demonstrates the existence of white light fringes necessary for the SSM technique, but it is difficult to ensure that the light from the source is propagating through the zero order fringe with this setup. With further improvements to the fore optics and alignment techniques, this device offers a potential compact interferometer design for the SSM technique, while removing tolerancing and vibrational issues associated with using beamsplitters and mirrors.

2.2.4.2 Birefringent Retarder with Dichroism

Another approach to the SSM technique was to use the nonlinear dispersion of the ordinary and extraordinary rays within a birefringent retarder. Based on the physics of birefringent retarders, incident unpolarized light propagating through the material will experience two different phase velocities associated with the ordinary, o, and extraordinary, e, rays. These velocities are correlated to the indices of refraction of the two rays denoted n_o and n_e , respectively. An example of the dispersion curves for the o and e rays of the positive uniaxial birefringent crystal cadmium sulfide (CdS) are plotted in Fig. 23 versus wavelength in microns.

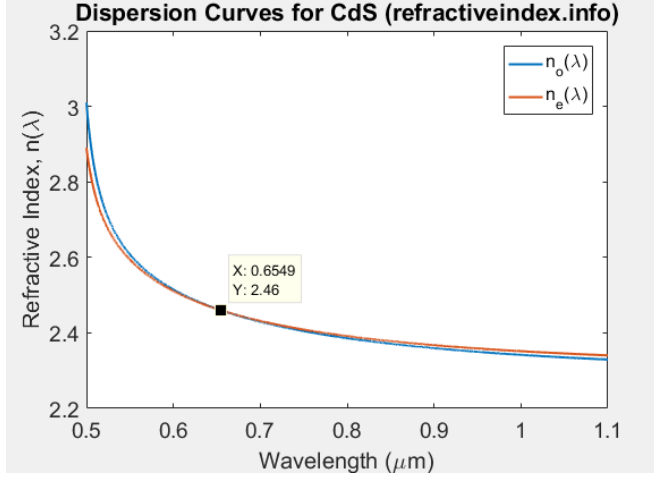


Fig. 23. Dispersion curves for the ordinary and extraordinary rays of CdS.

From the data in Fig. 23, the indices of refraction $n_o(\lambda)$ and $n_e(\lambda)$ exhibit an intersection at $\lambda \sim 655 \text{ nm}$, a condition similar to the dispersion crossings in the previous system. A simulation of the channeled spectrum generated by an interference between the two rays is illustrated in Fig. 24. The plots of the channeled spectrum and phase variable $v = \sigma \text{OPD}(\sigma)$ are simulated for an 11° FOV at $\theta_0 = 15^\circ$ for a CdS retarder of thickness $t = 10 \text{ mm}$.

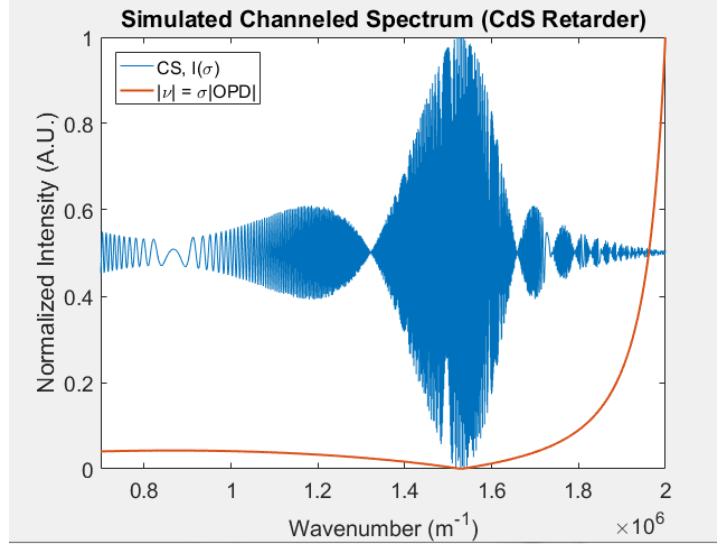


Fig. 24. Simulation of the channeled spectrum and phase, $v = \sigma \text{OPD}(\sigma)$, generated by the o and e rays of a CdS retarder based on the relationship in the dispersion curves between $n_o(\lambda)$ and $n_e(\lambda)$

Thus, it was hypothesized that a birefringent crystal such as CdS may be used as the single dispersive material in the SSM technique. As such, a schematic of the potential experimental setup for the SSM technique is presented in Fig. 25 (a), followed by a preliminary table top system for investigating the concept in Fig. 25 (b).

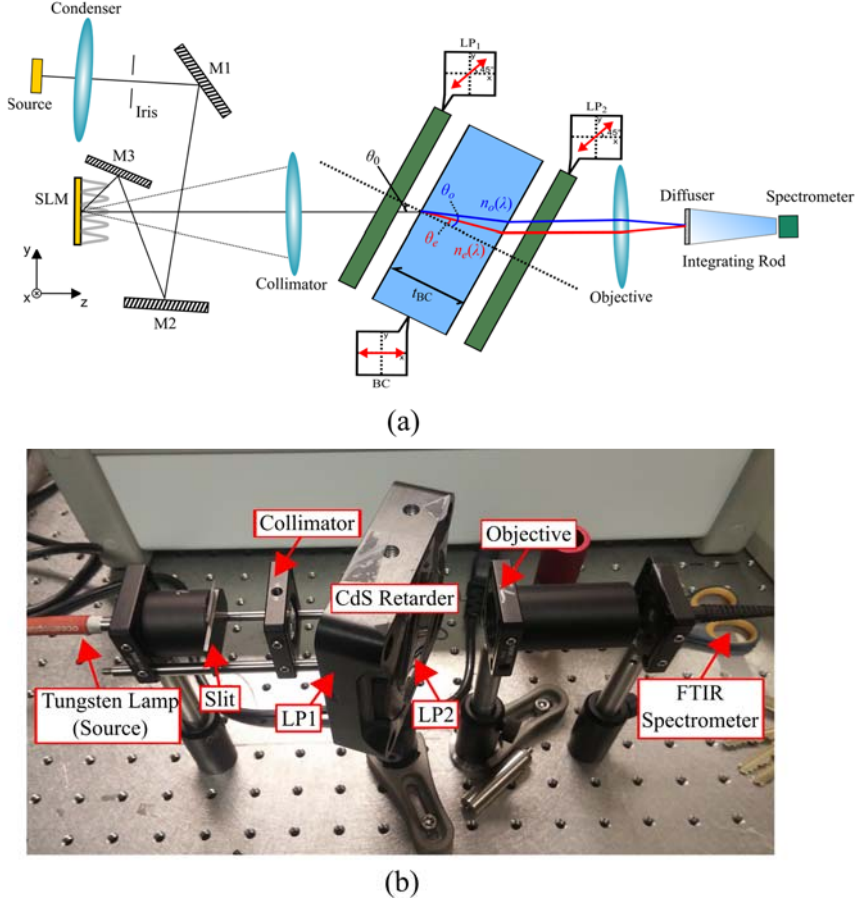


Fig. 25. (a) Schematic of potential proof of concept SSM system using a birefringent crystal. (b) Preliminary experiment of birefringent system using a CdS retarder as the dispersive material.

In order to generate interference between the o and e ray, it is necessary that polarized light is incident on the birefringent retarder. To this end, Fig. 25 (a) illustrates how the concept would be implemented experimental, in which light from a broadband white light source is relayed onto a spatial light modulator (SLM) which acts as the scene to be reconstructed via the SSM technique. Light form the SLM is then collimated into the birefringent interferometer. The collimated beam first passes through a polarization generator (LP₁) oriented at 45° before passing through the CdS birefringent crystal (BC) oriented at 0°. The o and e rays undergo different velocities (or indices of refraction) within the crystal to create a shear between the two beams. At the output of the CdS is a polarization analyzer (LP₂) oriented at 45° which allows the two states to interfere with each other. A lens is used to collect the interfering beams and a pseudo-pupil plane generated by a diffuser and integrating homogenizes the output which is then sampled using a spectrometer.

In the preliminary setup depicted in Fig. 25, a tungsten halogen lamp is used to illuminate a 15 mm slit which acts as a uniform angular spectrum. The scene is then collimated into the interferometer composed of generator LP₁, a $t = 10$ mm thick CdS retarder, and analyzer LP₂. The light is collected with a 50 mm focal length (F/2) lens and sampled by a spectrometer at the pupil plane of the system. In the preliminary experiment, it was determined that interference between the two rays does indeed generate a sinusoidally modulated white light spectrum, including evidence of the static phase point for which $\partial OPD / \partial \sigma = 0$ (as seen in Fig. 24 near $\lambda \sim 0.9 \mu\text{m}$). The angular sensitivity of the device was also higher than the previous interferometer systems based on phase

variations caused by tilting the CdS retarder (varying θ_0) However, the centerburst of the channeled spectrum was not evident in the measured spectra. This was due to the fact that the CdS retarder is dichroic in nature, meaning that one of the polarization states becomes fully absorbed at certain wavelengths. In our CdS interferometer system, the dichroism occurs at the wavelength associated with the centerburst, and thus no interference between the two states exists to implement the SSM technique. Though unfortunate, this investigation leads to an interesting concept of using birefringent materials to create the needed dispersion relationship in the SSM technique. Future research could be dedicated to investigating other birefringent materials (e.g. TiO₂ (triaxial) and AgGaS₂/AgGaSe₂), liquid crystals, or the coupling of the o and e states under stress or by applying an electric or magnetic field [5]

2.3 Reconstruction Algorithm for Nonlinear Channeled Spectra

Due to the dispersive nature of the materials used in the channeled SSM interferometer systems, the OPD becomes nonlinear with wavenumber. Or more precisely, the general OPD, given by

$$v = \sigma OPD(\sigma) \cos(\theta), \quad (35)$$

has a nonlinear dependence with wavenumber, with $OPD(\sigma)$ being a wavenumber-dependent OPD (v in waves). The benefit for the nonlinear characteristics in OPD, and thus the channeled spectrum, is that the zero-OPD crossing can be chosen for any arbitrary wavelength. The drawback is that the nonlinear channeled spectrum must be interpolated (sampled) onto a linear axis in order to accomplish the signal processing (e.g. Fourier transformations) required to reconstruct the incident angular spectrum with greater accuracy. The plot in Fig. 26 shows a simple example of this nonlinear dependence compared to a linear dependence,

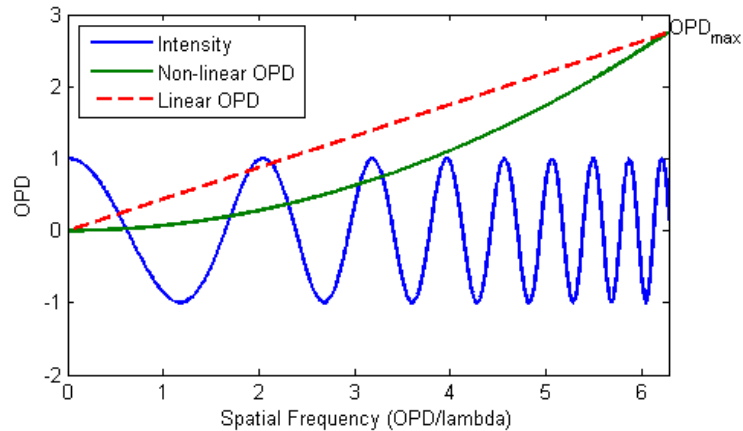


Fig. 26. Example of a general situation for a channeled spectrum (blue spectrum) with a nonlinear OPD dependence (green line) versus a linear OPD dependence (red line).

The linearization process to reconstruct the incident angular spectrum begins by resampling or interpolating the nonlinear samples onto a linear axis, such that the v dependence becomes linear, allowing for a Fourier transform algorithm to be implemented. Research towards this intermediate goal has been in investigating and creating algorithms to convert nonlinear interferograms into angular spectra. Techniques that have been considered and may need further investigation include

deconvolution, wavelet transforms, Gabor-Wigner transform, and neural networks combined with empirical calibration procedures [6-9].

2.3.1 Simulations of Linear and Nonlinear Optical Path Differences

The OPD is always of interest in an interferometer since it determines the phase and interference of the light in the system. For our purposes, the OPD could potentially be altered in such a way to increase (or decrease) certain parameters related to the operation of the device. Two parameters of particular interest are the increase in spatial resolution (related to $1/\text{OPD}$) and the decrease in spectral bandwidth needed to perform a measurement. Both of these operating parameters are affected by the functional form of the OPD (e.g. linear, quadratic, cubic, quartic) and the physical geometry of the system (i.e. tilt angle and dimensions), and the sampling size of the measurement. The questions then becomes, what OPD is required for the system to obtain maximum spatial resolution and minimize the bandwidth for the measurement, and what tradeoffs make arise from these two situations.

This project has investigated a system that was modeled using a constant OPD versus wavenumber, which creates a linear phase factor v versus wavenumber given by

$$v = \sigma \text{OPD}(\sigma) \cos(\theta_i - \theta_0) \quad (36)$$

where σ represents wavenumber of light, θ_i and θ_0 are the incidence and tilt angles of the interferometer, respectively. Note that for the case when v is linear with wavenumber, OPD becomes constant with respect to wavenumber and can be written simply as OPD_0 . Though the linear case has been developed, the spatial-spectral multiplexing system will require a nonlinear phase with wavenumber to relocate the zero crossing wavenumber, or maximum coherence wavenumber, into a detectable region (constant OPD requires zero crossing at $\sigma = 0$). However, the linear case is by no means trivial for the reason that if nonlinear phase can be converted onto a linear axis, then the same processing techniques (fast-Fourier transform and/or short-time Fourier transform [10]) that are used for the linear case can then be applied to the nonlinear case. If this is not the case, in other words if the nonlinear phase cannot be converted to linear phase due to some circumstance (e.g. wavelength dependent shear factor in the interferometer), then other techniques will need to be implemented.

As this method attempts to analyze higher orders wavenumber dependence in OPD, we start by simulating the linear v case (constant OPD with wavenumber) for reference and later comparisons. Given some arbitrary tilt angle ($\theta_0 = 25^\circ$) and constant OPD related to the resolution needed to be competitive with F/1 lens ($\text{OPD}_0 = 8.60 \text{ mm}$), scanning over a small field of view (FOV) of -2° to $+2^\circ$ and a spectral range of $\sigma = 0 \text{ m}^{-1}$ to $\sigma = 2.2 \times 10^6 \text{ m}^{-1}$. The channeled spectrum and linear v are plotted against wavenumber in Fig. 27.

It is important to mention the effects of under sampling of both plane waves (incident angles) and wavenumbers in the OPD simulations. This under sampling causes issues due to the fact that we are investigating a discrete simulation of OPD. If the sampling of wavenumbers is too small, the angular spectrum will become aliased and will not localize in the frequency domain. For sufficiently large spectral samples ($\approx 50,000$ wavenumbers for the linear v case), the spectrum will have a constant frequency bandwidth without aliasing (become localized). For the sampling of planes waves, the number of incident angles will affect the repetitions of areas of constructive interference. For a small number of samples in the FOV, the channeled spectrum shows multiple regions of relatively high coherence (which should only exist at $\sigma = 0$ for the linear case). As the number of sampled plane waves is increased, these regions move out towards large wavenumbers until they eventually exit the spectral range of interest. When simulating channeled spectra (and

angular spectra) it is important to keep aliasing out of the simulation or the results will be insufficient (the spectra will still be “real”, but not sufficient for our modeling purposes, since a spectrometer cannot sample with aliasing). Thus, for the channeled spectrum presented in Fig. 27 we choose a sufficiently large number of spectral samples (100,000 wavenumbers) and a relatively large number of plane waves (1,000 incident angles in the FOV) to remove the extra regions of coherence from the spectral range of interest.

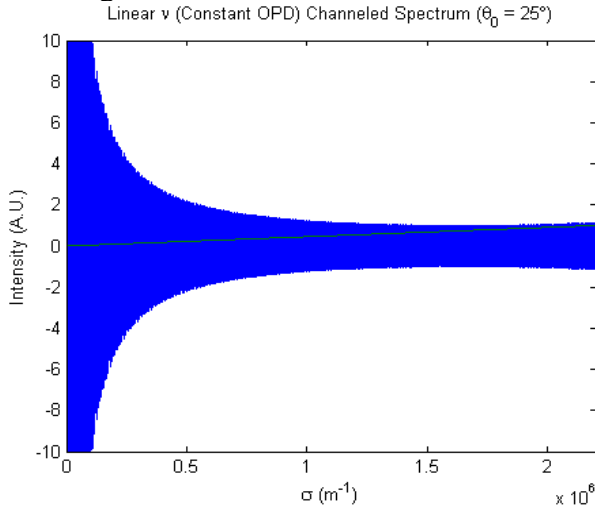


Fig. 27. Linear v (constant OPD) channeled spectrum (blue) plotted with the linear v (green) against wavenumber from, $\sigma = 0 \text{ m}^{-1}$ to $\sigma = 2.2 \times 10^6 \text{ m}^{-1}$. Channeled spectrum is samples with 100,000 wavenumbers and 1,000 planes waves in the FOV from -2° to $+2^\circ$.

In this particular case maximum phase coherence occurs only at $\sigma = 0 \text{ m}^{-1}$, while regions of lower visibility occur at larger wavenumbers. Because the phase information is linear with respect to wavenumber, having the form

$$v = \sigma OPD_0 \cos(\theta_i - \theta_0), \quad (37)$$

an ideal reconstruction can theoretically be created using a Fourier transform (FT) of the channeled spectrum to acquire a representation of the angular spectrum. Note here that v for this case is linear in as much as σOPD_0 is linear across the entire spectrum. However, this is under the assumption that the $\cos(\theta_i - \theta_0)$ term modulates the phase in such a way as to be constant for all wavenumbers. In other words, the sinusoidal term is just a constant for a given incident angle. Continuing the reconstruction procedure under the constant angle dependence assumption will lead to a Fourier transform that has the form presented in Fig. 28.

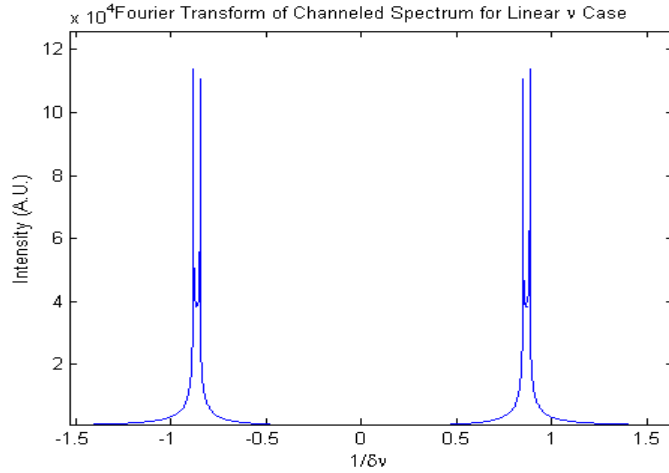


Fig. 28. Fourier transform of a single-sided ($\sigma = 0 \text{ m}^{-1}$ to $\sigma = 2.2 \times 10^6 \text{ m}^{-1}$) channeled spectrum formed by a linear v plotted with respect to $1/\delta v$.

At this level of wavenumber sampling the frequency content in the FT of the channeled spectrum (or angular spectrum) is stationary with respect to the x-axis (i.e. enough wavenumber samples to localize the spectrum). However, due to the large amount of sampled angles of incidence, the individual plane wave components of the angular spectrum cannot be resolved. Another interesting point to mention in Fig. 28 is the “two peak” nature of each of the symmetric angular spectra, which may be caused by a loss of visibility for plane waves near $\theta_i = 0^\circ$.

To show an example of a situation in which the individual plane waves may be resolved (by eye, not necessarily by a detector) from the angular spectrum, Fig. 29 depicts the reconstructed angular spectrum for a channeled spectrum sampled at only 10,000 wavenumber samples and 10 angles of incidence in the FOV. Again, this plot is only meant to show areas of particular interest in the angular spectrum and is not meant as an actual model for the linear v simulation.

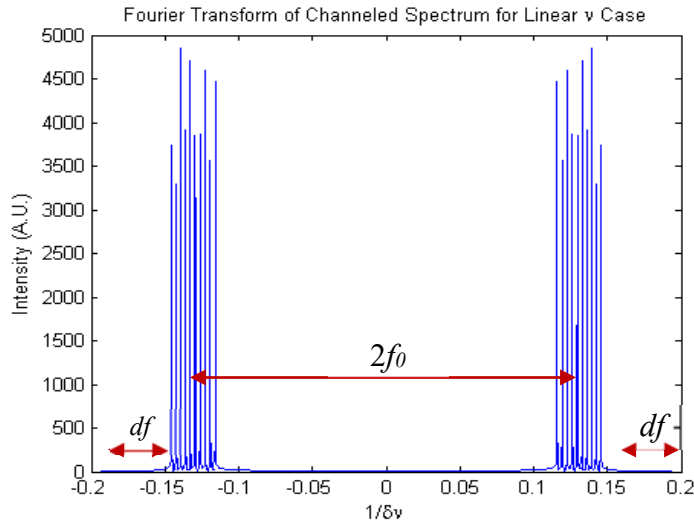


Fig. 29. Fourier transform of a double-sided channeled spectrum formed by a linear v plotted with respect to $1/\delta v$. Important ranges in frequency bandwidth are represented on the graph.

From Fig. 29 it can be shown that all 10 sampled incident angles from $\theta_i = -2^\circ$ to $\theta_i = +2^\circ$ can be reconstructed using an FT of a channeled spectrum for cases of linear v . The spectral sampling of wavenumbers for the FT was increased over the range of $\sigma = -2.2 \times 10^6 \text{ m}^{-1}$ to $\sigma = +2.2 \times 10^6 \text{ m}^{-1}$

(for channeled spectra centered at $\sigma = 0 \text{ m}^{-1}$, still 10,000 wavenumber samples) in order to increase the resolution of the FT (i.e. double-sided interferogram gives better image resolution or $\sqrt{2}$ -fold improvement in SNR, not an actual increase in spectral resolution since information is redundant to a single-sided interferogram).

Also represented in Fig. 29 are bandwidth frequencies of interest that must be addressed in the larger scheme of the project. The FT of the channeled spectrum is plotted with respect to the Nyquist frequency, $\pm F_N = \pm F_s/2$, where F_s is the sampling frequency of the channeled spectrum, and f_0 represents the frequency bandwidth of the measured spectrum, and df represents frequency components that do not contain spectral information (i.e. wasted frequency content). Because the Nyquist frequency is related to $1/\delta\nu$, or the sampling frequency of the linear ν , then f_0 must also be related to this relationship. The values of df can be decreased by altering the sampling frequency of the wavenumber spectrum. On the other hand, the bandwidth f_0 (for single-sided interferograms) and $2f_0$ (for double-sided interferograms) can only effectively be altered by changing the tilt angle of the MI, implying the bandwidth is related to the sinusoidal dependence on angles (incident and tilt) in the linear ν term. This component of the frequency domain needs to be reduced for more effective measurements, but changing tilt angle during measurements or finding the optimal tilt angle may be impractical (as the first is mechanically complex, and the second will most likely change for various scenes, spectrally and spatially). Thus, it is necessary to minimize this frequency bandwidth in the angular spectrum without altering a set tilt angle. One proposed method is by changing the OPD dependence of ν to higher powers (e.g. linear, quadratic, cubic, etc.) to find the optimal OPD, then determine if the OPD is physically realizable in an optical system.

The next step would be to advance to a linear OPD from a constant OPD, thus giving ν a quadratic dependence with wavenumber. This gives rise to the first nonlinear phase situation that could be implemented in a MI system for the SSM technique. Letting ν take on an arbitrary functional form, we may represent ν as

$$\nu_{\text{quad}} = (a\sigma^2 + b\sigma + c)\cos(\theta_i - \theta_0). \quad (38)$$

where we will represent a quadratic wavenumber dependent ν as ν_{quad} . Note that the sinusoidal angle dependence is still present, but the first term has now taken on a quadratic functional form with respect to wavenumber. Making parallels to the linear case we see that

$$(a\sigma^2 + b\sigma + c) \propto \sigma \text{OPD}(\sigma). \quad (39)$$

Factoring and dividing by wavenumber gives

$$\text{OPD}(\sigma) = m_{\text{OPD}}\sigma + b', \quad (40)$$

where m and b' are scalar quantities that represent the slope and y-intercept of a linear OPD relation with wavenumber. The slope can be somewhat arbitrarily chosen, with steeper slopes relating to higher spectral frequencies, however the method used in the simulation was

$$m_{\text{OPD}} = \frac{\Delta \text{OPD}}{\Delta \sigma} = \frac{\text{OPD}_{\max} - \text{OPD}_{\min}}{\sigma_{\max} - \sigma_{\min}}, \quad (41)$$

where the maximum OPD was chosen for the same constant OPD that gives competitive spatial resolution and minimum OPD was taken to be zero over the spectral range of $\sigma_{\min} = 0$ to

$\sigma_{\max} = 2.2 \times 10^6 \text{ m}^{-1}$. The value of b' defines the zero crossing for the linear OPD and can be chosen arbitrarily, though in the range of an appropriate detector is best. The zero crossing here is chosen for typical d-light wavelength of $\lambda_d = 587.6 \text{ nm}$ or $\sigma_d = 1.7018 \times 10^6 \text{ m}^{-1}$. A plot of the channeled spectrum formed by the quadratic v of the form

$$v_{\text{quad}} = \sigma \text{OPD}(\sigma) \cos(\theta_i - \theta_0) = \sigma(m_{\text{OPD}}\sigma + b') \cos(\theta_i - \theta_0), \quad (42)$$

is shown in Fig. 30, with the absolute magnitude of the quadratic v function superimposed with respect to wavenumber. The FOV is taken to be the same range of incident angles as the linear case (i.e. $\theta_i = -2^\circ$ to $\theta_i = +2^\circ$, however, plane wave sampling was increased to 1000 in order to remove repetitions of constructive interference, 200 samples was sufficient as well) over a spectral range of $\sigma = 0 \text{ m}^{-1}$ to $\sigma = 2.2 \times 10^6 \text{ m}^{-1}$ of 100,000 samples, with an initial interferometer tilt of $\theta_0 = 25^\circ$.

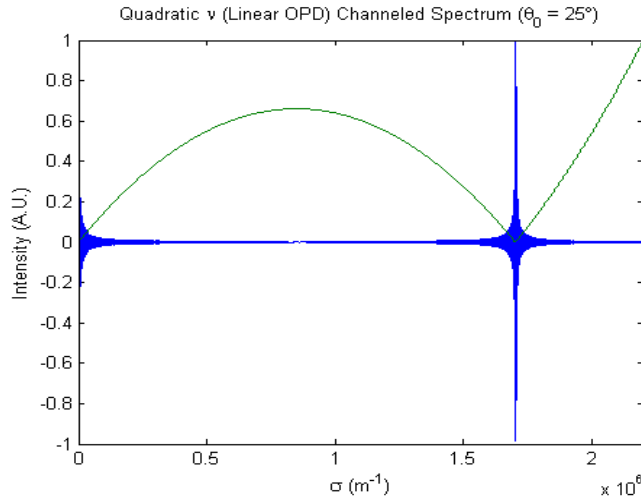


Fig. 30. Normalized quadratic v (Linear OPD) channeled spectrum (blue) plotted with the normalized absolute magnitude of the quadratic v (green) with respect to wavenumber.

The plot of the quadratic v channeled spectrum has some notable points of interest. First, the zero crossings of the quadratic v occur at both $\sigma = 0 \text{ m}^{-1}$ and at $\sigma = \sigma_0 = 1.7018 \times 10^6 \text{ m}^{-1}$ (i.e. where we defined the quadratic v to take on zero values). As seen in the linear case, maximum coherence of phase occurs at the zero crossings (part of the benefit of nonlinear phase is we can obtain coherence in detectable regions), with lower regions of coherence occurring at other wavenumbers. For the arbitrary maximum OPD of 8.60 mm, the spatial frequency of the channeled spectrum's fringes are relatively high, which will be difficult to resolve by a standard detector or Fourier transform spectrometer (FTS). A second point worth considering is the low spectral frequency region that is located between the two zero crossings (in Fig. 30 the location is near $\sigma = 0.85 \times 10^6 \text{ m}^{-1}$) where the absolute magnitude of the quadratic phase factor has a slope of zero (i.e. at local maxima or local minima in phase). This area may be of interest due to the lower spectral frequencies being easier to resolve with a detector (i.e. measurements do not require as high a spectral resolution) and could possibly be addressed with heterodyning of the wavefronts. A close up of this aspect is shown in Fig. 31 for the wavenumber range of $\sigma = 0.70 \times 10^6 \text{ m}^{-1}$ to $\sigma = 1.00 \times 10^6 \text{ m}^{-1}$, which encapsulates the region of low spatial frequency where the slope of the phase factor v becomes zero. This portion of the channeled spectrum is generally associated with the zero-phase point for which $\partial \text{OPD} / \partial \sigma = 0$ and is often seen in dichroic materials.

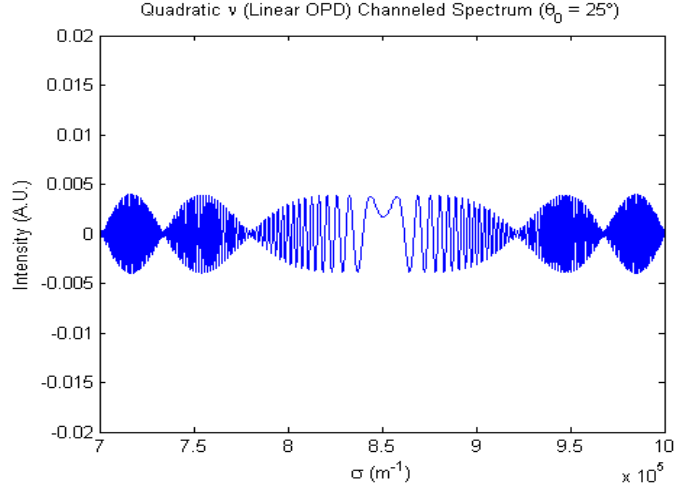


Fig. 31. Close up of the quadratic v channeled spectrum for the spectral range of $\sigma = .70 \times 10^6 \text{ m}^{-1}$ to $\sigma = 1.0 \times 10^6 \text{ m}^{-1}$. Shows that there exists a region near local maxima (or minima) of the quadratic v phase factor that exhibit fringes of lower frequency.

Continuing with our analysis of the quadratic v channeled spectrum, we would like to reconstruct the angular spectrum via some type of Fourier transform. However, a direct FT (using the MATLAB routine “fft”) of the 100,000 wavenumber, 1,000 plane wave nonlinear channeled spectrum data results in an incorrect representation of the angular spectrum, shown for reference in Fig. 32, and is not meant to express the actual method for reconstruction.

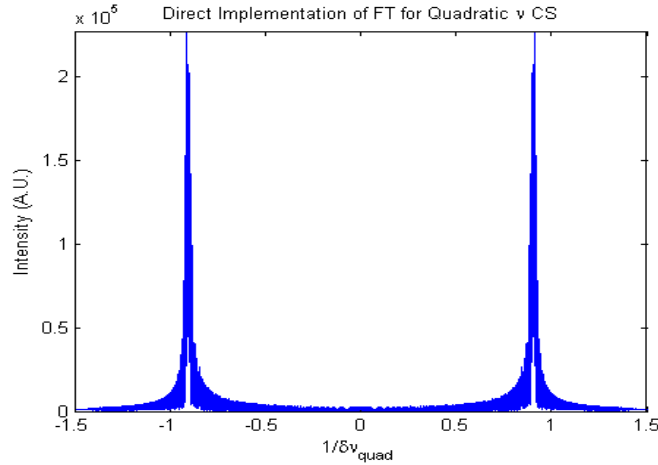


Fig. 32. Direct implementation of a fast Fourier transform of a quadratic v channeled spectrum before preprocessing (interpolation).

Obviously, from Fig. 32 we can see that the sampled incident angles (i.e. plane waves) are unresolvable due to the incompatibility of the nonlinear nature of the channeled spectrum data and the linear nature of the FT. Thus, to resolve this issue, measures (e.g. preprocessing, linear interpolation, etc.) need to be taken in order to convert the nonlinear data of the quadratic v channeled spectrum into a manageable form for a direct FT implementation.

Returning to Fig. 30, we note that for wavenumbers greater than σ_0 , the absolute magnitude of v takes on a pseudo-linear form that although functionally quadratic, could be approximated as linear. The spectral range of interest is shown in Fig. 33 for reference.

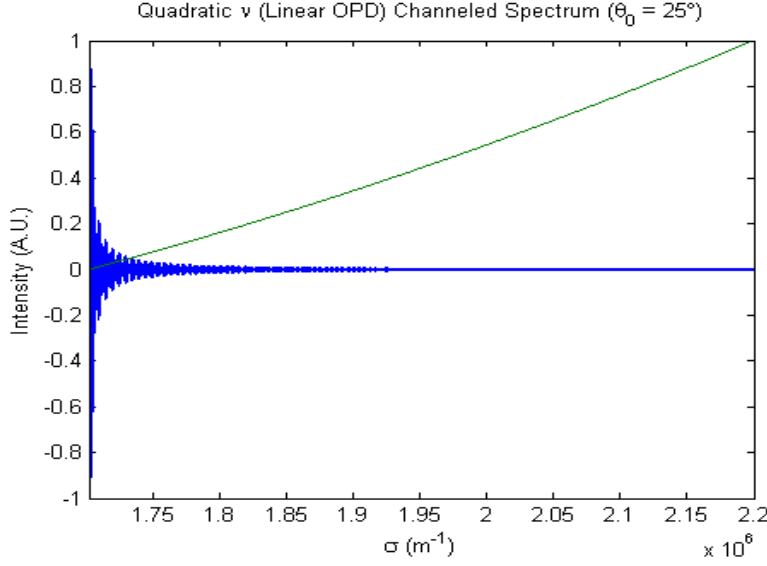


Fig. 33. Quadratic v channeled spectrum over the spectral range $\sigma = 1.7018 \times 10^6 \text{ m}^{-1}$ to $\sigma = 2.2 \times 10^6 \text{ m}^{-1}$.

The spectral range highlighted in Fig. 33 may be of particular interest since the nonlinear phase represented by v may be interpolated onto a linear axis before implementation of an appropriate transform.

2.3.2 Linear Interpolation Algorithm for Angular Spectra Reconstruction

Interpolation of data points often requires the use of techniques or algorithms related to curve fitting or regression analysis. For our purposes, interpolation will be used to convert nonlinear data onto a linear axis, effectively making the data linear. Choice of the algorithm dictates how much distortion is introduced to the resultant interpolated spectra.

Continuing the reconstruction simulation with the channeled spectrum presented in Fig. 33, to reconstruct an angular spectrum from the quadratic v dependence, the data would first need to be interpolated from a nonlinear axis onto a linear axis. One method for this process is applied here to test its validity for modeled channeled spectra with higher order OPD functional forms. First, the channeled spectrum with quadratic phase dependence is extracted with the respective values of v from the OPD Simulations model. The functional form of the channeled spectrum is defined as

$$I(\sigma, \theta) = 2I_0 [1 + \cos(2\pi v(\sigma, \theta))], \text{ with} \quad (43)$$

$$v(\sigma, \theta) = v_{\text{quad}} = \sigma \text{OPD}(\sigma) \cos(\theta_i - \theta_0) = \sigma(m_{\text{OPD}}\sigma + b') \cos(\theta_i - \theta_0). \quad (44)$$

The value of the initial intensity of the scene's spectrum, I_0 , is chosen to be unity for this example, but will be changed to investigate the effects of non-uniform spectral content on reconstruction of spatial information. Since the channeled spectrum is defined from $\sigma = 0 \text{ m}^{-1}$ to $\sigma = 2.2 \times 10^6 \text{ m}^{-1}$ (with 100,000 samples) and the zero crossing exists at $\sigma_0 = 1.7018 \times 10^6 \text{ m}^{-1}$, it is impossible to perfectly fit a linear curve to the quadratic phase curve because the linear curve cannot have both the same maximum and minimum OPDs and zero crossings as the quadratic curve. Thus, the channeled spectrum must be initially truncated before interpolation can occur, which may lead to some potential loss of information depending on the detector range and how much of the spectral range of the channeled spectrum needs to be omitted. Different truncation schemes (i.e. how many

data points to leave out of the interpolation data) give different final results for the linearized channel spectrum and the reconstructed angular spectrum. The degree of these differences may need to be further analyzed to determine how much truncation can occur before the data becomes distorted. The example presented here chooses the truncated data to range from the minimum value of ν to the maximum value of ν in the original nonlinear phase data (which approximately corresponds to $\sigma = 0.851 \times 10^6 \text{ m}^{-1}$ to $\sigma = 2.2 \times 10^6 \text{ m}^{-1}$). Note that both the nonlinear ν and the linear space that defines the spectral range in MATLAB must both be truncated to keep arrays of equal length. A plot of the channeled spectrum and nonlinear ν over the truncated spectral range is shown in Fig. 34.

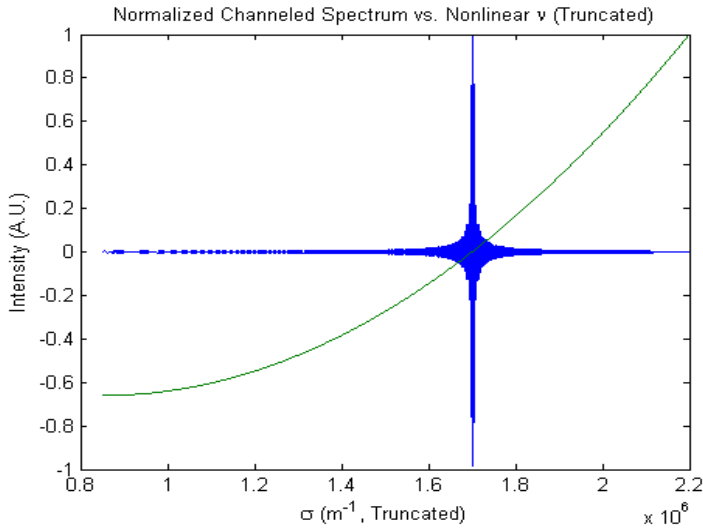


Fig. 34. Normalized channeled spectrum and nonlinear (quadratic) ν over the truncated spectral range of $\sigma = 0.851 \times 10^6 \text{ m}^{-1}$ to $\sigma = 2.2 \times 10^6 \text{ m}^{-1}$.

Next, a polynomial fit was applied to the truncated nonlinear ν data to determine the coefficients for an N^{th} order polynomial. Choosing the order of the fitting polynomial is somewhat arbitrary (as higher order coefficients become redundant); however, since ν is quadratic for the simulation, a value of $N = 3$ was chosen as the order of the polynomial. Depicted below in Fig. 35 is a plot of the truncated version of the original nonlinear phase ν versus the third-order polynomial fitting of the nonlinear data.

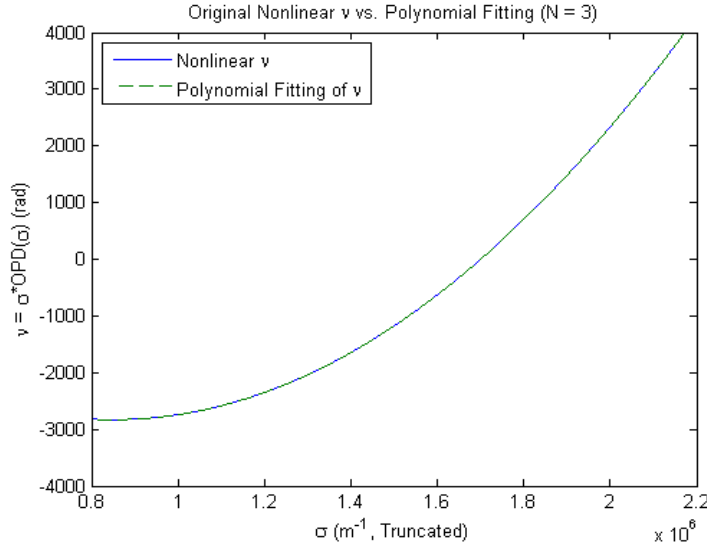


Fig. 35. Plot of the original nonlinear phase v versus the third-order polynomial fitting of the truncated data.

From Fig. 35, the polynomial fit appears to sufficiently match the functional form of the nonlinear phase data (as the data has the same values for all σ in the defined spectral range). The coefficients for the third-order fitting polynomial of the form

$$p(\sigma) = p_3\sigma^3 + p_2\sigma^2 + p_1\sigma + p_0, \quad (45)$$

were calculated, for this example, to be

$$p_3 = -1.263 \times 10^{-28}, p_2 = 3.9091 \times 10^{-9}, p_1 = -0.0067, \text{ and } p_0 = 2.9984 \times 10^{-10}. \quad (46)$$

Note that the coefficient for the term related to σ^3 can be approximated as zero, and the value for the slope of the linear OPD, m , has the same value for p_2 in the polynomial fit as it did when calculating the slope by the method used in equation . With a sufficient fit of the nonlinear phase, the next step located the value(s) of the zero crossings by calculating the polynomial's roots. For the 3rd order polynomial, we can calculate three roots as

$$r_1 = 3.0951 \times 10^{19}, r_2 = 1.7018 \times 10^6, \text{ and } r_3 = 4.5071 \times 10^{-8}, \quad (47)$$

where r_2 is the value of the defined zero crossing at $\sigma_0 = \sigma_d = 1.7018 \times 10^6 \text{ m}^{-1}$. The other two roots, r_1 and r_3 , are located outside the spectral range of interest and must be removed by taking real values for the roots and determines which root is located within the range of interest. For our example, the loop successfully determined r_2 to be the correct root. This process may need to be revisited for higher order OPDs where a larger number of roots are located within the spectral range of interest, or for situations in which the truncation may clip the data at values of σ that are themselves roots.

Now that the functional form and zero crossing have been determined, the next step in the interpolation process is to create a new linear wavenumber axis that shifts the nonlinear data points onto a linear axis. This can be accomplished by finding the relationship between the original nonlinear data and a linear approximation for the nonlinear data using values obtained from the simulation. For starters, the linear approximation for v can be obtained using the equation

$$v_{\text{linear}} = m_v(\sigma - r), \quad (48)$$

where v_{linear} represents the linear approximation of v , r is the root or zero crossing for the linear function, (*i.e.*, the value of r_2 from (47)), and m_v can be found by

$$m_v = \frac{\Delta v}{\Delta \sigma} = \frac{v_{\max} - v_{\min}}{\sigma_{\max} - \sigma_{\min}}. \quad (49)$$

The maximum and minimum values for both v and σ for the linear approximation are obtained from the truncated version of the original nonlinear v . Fig. 36 shows a plot of the truncated nonlinear phase v from Fig. 35 versus the linear approximation of v obtained from equations (48) and (49).

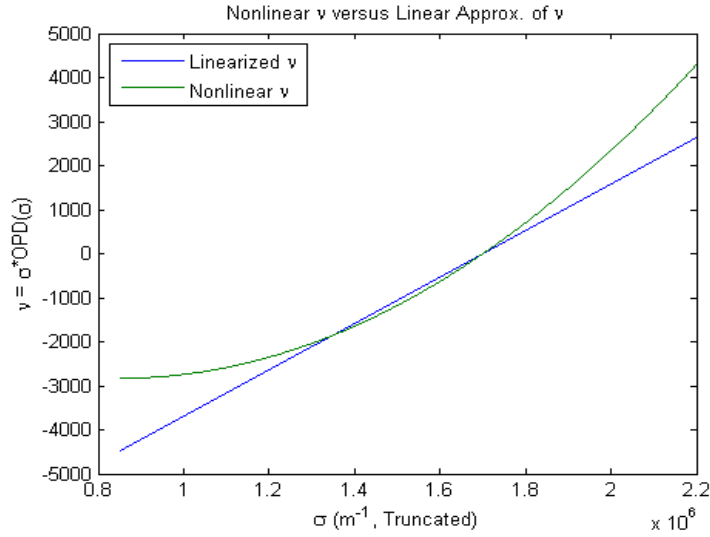


Fig. 36. Plot of the truncated nonlinear v versus the linear approximation of v from obtained via the zero crossing and the maximum and minimum values of the nonlinear v .

Though the linear approximation for v , the relative difference between the nonlinear data and a linear representation of v can be calculated. This relationship will be useful in interpolation of the nonlinear data onto a linear axis. We define this relationship to be the ratio of the nonlinear curve in equation (45) to the linear approximation found in equation (48), such that

$$R = \frac{v_{\text{nonlinear}}}{v_{\text{linear}}} = \frac{p_2 \sigma^2 + p_1 \sigma + p_0}{m_v(\sigma - r)}, \quad (50)$$

where R represents the normalization ratio and the value of p_3 is taken to be zero. Using the relationships for nonlinear v found in equation (42) and the linear OPD found in equation (48), R can be reexpressed as

$$R = \frac{\sigma(m_{\text{OPD}}(\sigma - b'))}{m_v(\sigma - r)}. \quad (51)$$

Since the zero crossing values of both the linear OPD and linear v are taken to occur at

$$r = b' = \sigma_0 = 1.7018 \times 10^6 \text{ m}^{-1}, \quad (52)$$

the normalization ratio R can be further reduced to

$$R = \left(\frac{m_{OPD}}{m_v} \right) \sigma, \quad (53)$$

which represents the relationship of a nonlinear phase (defined by a linear OPD of slope m_{OPD}) to a linear phase (defined by a linear v of slope m_v) with respect to wavenumber, σ . This relationship can be used to find the relative difference between nonlinear data and linear data in terms of wavenumber. Another N^{th} order polynomial ($N = 3$) is used to fit the normalization ratio R onto the truncated wavenumber axis to create a linear axis that will be used for interpolation. Here, the third-order polynomial fit of the normalization ratio returns the coefficient values

$$p_3^R = 1.6901 \times 10^{-31}, p_2^R = -8.3736 \times 10^{-25}, p_1^R = 7.4125 \times 10^{-7}, \text{ and } p_0^R = -6.0795 \times 10^{-13} \quad (54)$$

where again we may opt to take coefficients of relatively high powers of negative integers to be zero (i.e. p_3 and p_2 of the R polynomial fitting, note the superscript R is only for identifying the different coefficients). In this case, the polynomial fit returns a linear curve with respect to wavenumber that can be represented by

$$R' = p_1^R \sigma + p_0^R. \quad (55)$$

To interpolate the nonlinear channeled spectrum onto the linear axis, we must define a linearized σ axis that is taken to be the polynomial fit R' multiplied by the truncated wavenumber axis, i.e.

$$\sigma_{\text{linear}} = \sigma R' = \sigma(p_1^R \sigma + p_0^R). \quad (56)$$

Thus, the linearized wavenumber axis, σ_{linear} , is the original wavenumber axis weighted by a linear function that represents the relative difference between the nonlinear phase and the linearized phase. The measured channeled spectrum may now be interpolated onto the linear axis in equation (56) using the MATLAB routine “interp1”, which interpolates the truncated channeled spectrum at the query points of the original wavenumber axis onto the linearized wavenumber axis using a cubic interpolation. We now have a representation of the nonlinear data interpolated onto a linear wavenumber axis, which can be transformed via a Fourier transform to reconstruct the scene’s angular spectrum.

If we continue to process the channeled spectrum, presented in Fig. 34, we note that truncation (from $\sigma = 0.851 \times 10^6 \text{ m}^{-1}$ to $\sigma = 2.2 \times 10^6 \text{ m}^{-1}$) effectively removes 38.6% of the channeled spectrum based on where we have located the maximum and minimum values of the quadratic phase term, v . Thus, it may require an increase in the number of wavenumber samples to reconstruct the spectrum. There exists a trade-off here due to the fact that increasing the wavenumber samples also increases the need for a higher spectral resolution.

A simulation of this interpolation procedure was performed. The spectral sampling included 100,000 wavenumbers, spanning $\sigma = 0 \text{ m}^{-1}$ to $\sigma = 2.2 \times 10^6 \text{ m}^{-1}$, and plane wave sampling of 1,000 plane waves spanning an FOV of $\theta = -2^\circ$ to $\theta = +2^\circ$. The truncated channeled spectrum (from Fig. 34) was interpolated onto a linear wavenumber axis to obtain the result shown in Fig. 37. The reconstruction of the angular spectrum of the linearly interpolated channeled spectrum via a direct Fourier transform implementation is presented Fig. 38.

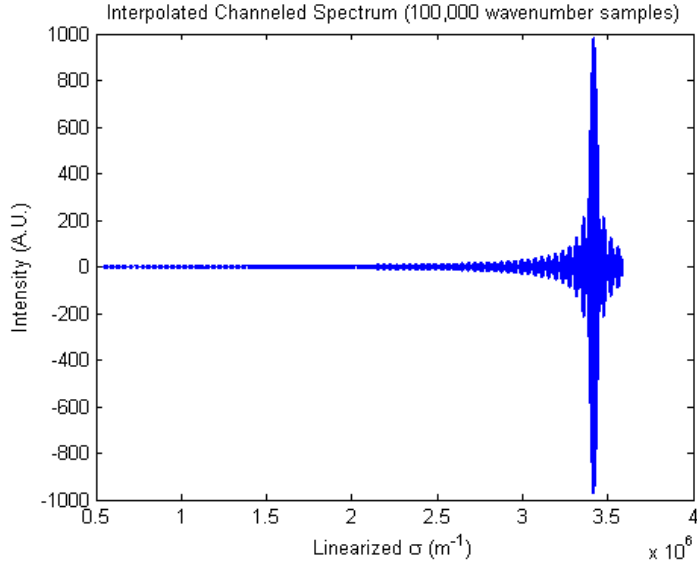


Fig. 37. Plot of the linearly interpolated channeled spectrum after truncation of wavenumbers to obtain the content between maximum and minimum values of the nonlinear v . Channeled spectrum initially contained 100,000 wavenumber samples before truncation.

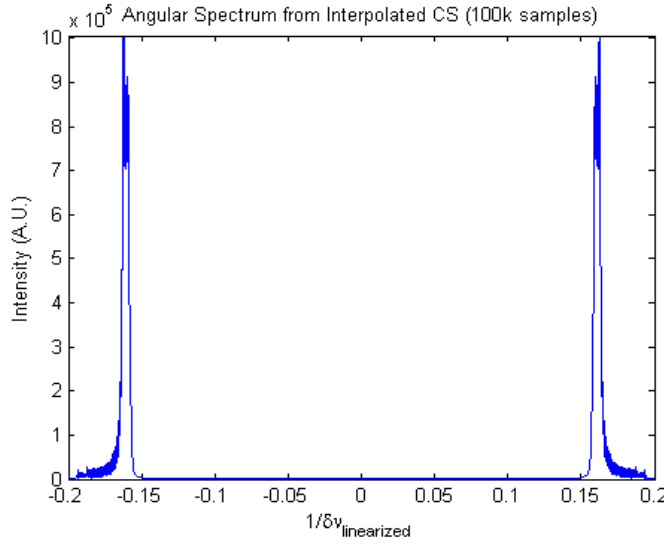


Fig. 38. Reconstructed angular spectrum from direct FFT implementation of the linearly interpolated channeled spectrum of 100,000 wavenumber samples before truncation.

From the linearly interpolated channeled spectrum shown in Fig. 37, it is first apparent that the interpolated spectrum is more symmetric around the centerburst than the original nonlinear spectrum in Fig. 34. The maximum coherence region related to the zero crossing wavenumber has been interpolated to the far right side of the linearized axis corresponding to larger wavenumbers, while regions of relatively low coherence comprise the majority of the spectrum.

The reconstruction of the angular spectrum via a direct Fourier transform implementation, shown in Fig. 38, appears to be implemented successfully. The sampling of wavenumbers is high enough to localize the bandwidth in the frequency domain, but the sampling of such a relatively small FOV may be the cause of the jaggedness seen at the peaks of the bandwidth. For reference of this effect, Fig. 39 shows a close up of a single-side of the angular spectrum shown in Fig. 38.

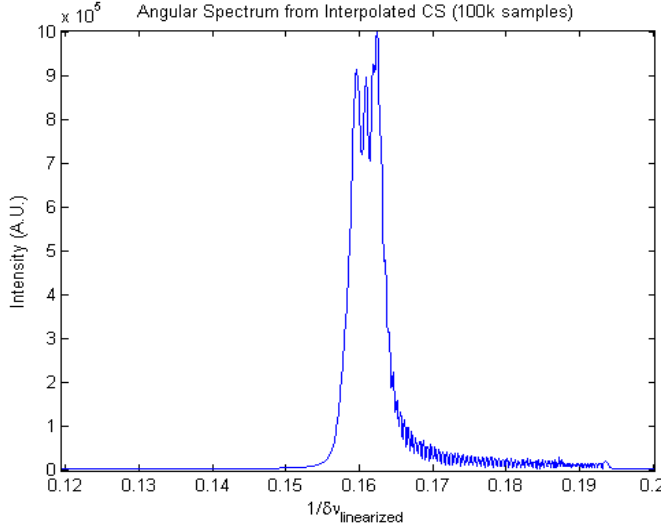


Fig. 39. Close up of a single side of the reconstructed angular spectrum. Note the jagged sampling at the peaks of the bandwidth.

2.4 Angular Resolution Analysis

A major focus for the researchers is the potential spatial resolution tradespace of the channeled SSM system, especially when compared to conventional imaging systems that use lenses. A conventional lens will image a scene by transforming the scene's angular spectrum into two-dimensional spatial information that can be detected at the focal plane of the lens. The scene's angular information is effectively “encoded” onto the two-dimensional transverse interference fringes created by the lens. This transverse interference creates a fundamental limitation in the maximum realizable angular resolution for a lens, which is determined by the wavelength of light and the physical dimensions (i.e. the diameter) of the lens.

To analyze the spatial resolution capabilities of the channeled SSM interferometer, we make an analogy to the Fourier transform spectrometer (FTS), whose maximum spectral resolution, $\Delta\lambda$, is related to the maximum phase imparted by the scanning MI within the FTS. The spectral resolution of the FTS [11] is given by

$$\Delta\lambda \propto \frac{1}{OPD_{\max}}. \quad (57)$$

Since the maximum OPD within a MI could theoretically be increased to arbitrarily high values by translating one of the mirrors a larger distance, the FTS has the capability of having very high spectral resolution. By similar arguments, the maximum angular resolution, $\Delta\theta$, in the channeled SSM interferometer is also related to the maximum phase imparted by the optical system such that

$$\Delta\theta \propto \frac{1}{v_{\max} \sin(\theta_i - \theta_0)} = \frac{1}{\sigma_{\max} OPD_{\max} \sin(\theta_i - \theta_0)}, \quad (58)$$

where we have made use of the definition for the maximum phase v in the interferometer from Eq. (6). The value σ_{\max} defines the maximum wavenumber in the spectral range of the source and OPD_{\max} is the largest OPD versus wavenumber in the tilted MI system. Since the angular resolution is set by the maximum phase, whose value can be chosen arbitrarily high, the resolution of the angular spectrum in the channeled SSM interferometer is limited by materials and physical size.

An analysis of the tilted MI [12] in Fig. 1 (a) reveals that the OPD within the interferometer has the form

$$OPD = 2n_1 t_1 \cos(\theta_1) - 2n_2 t_2 \cos(\theta_2), \quad (59)$$

where θ_1 and θ_2 represent the refracted angles into the glass plates G1 and G2, respectively, and can be calculated from Snell's law. Thus, it would appear that the interferometer has an extra degree of freedom in manipulating angular resolution that the lens does not have: namely index of refraction. The thickness of the plates provides the other degree of freedom which represents a physical dimension of the interferometer, similar to the diameter of a lens. To determine the behavior of the OPD as a function of index of refraction, we analyze the simpler case of a Fabry-Perot etalon.

A tilted Fabry-Perot etalon (FPE) can serve as a simplification to the tilted MI model due to similar relationships between the OPD and both index of refraction and angle of incidence. The rotating FPE system in Fig. 40 is comprised of a glass plate of index and thickness, n_1 and t_1 , which forms a cavity between two mirrors, M1 and M2, which can be tilted at an angle, θ_0 , with respect to the optical axis. The FPE, which is assumed to have an infinite extent along the mirrors in the xy -plane, is illuminated by a monochromatic point source, S, that is far enough away from the first surface of the cavity that the incident wavefronts are assumed planar. A lens would be placed after the system to focus rays onto the observation plane located behind the cavity.

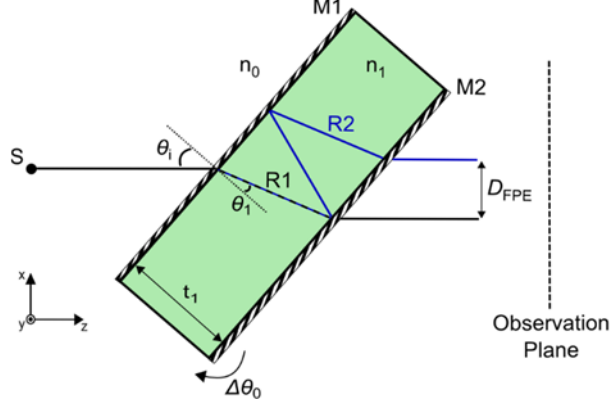


Fig. 40. Rotation Fabry-Perot cavity illuminated by a point source creating two-beam interference at the observation plane. The optical paths of the two interfering rays are represented as R1 (black line) and R2 (blue line).

If we consider the case of two-beam interference in which only two rays (the first transmitted beam and the beam transmitted after its first round trip), are allowed to interfere at the output plane. In this case, the FPE's OPD can be calculated as

$$OPD_{FPE} = OPL_{R1} - OPL_{R2} = \frac{2n_1 t_1}{n_0} \cos(\theta_1), \quad (60)$$

with θ_1 being the internally refracted angle into the plate, and the index of the ambient medium, n_0 , taken as the index of air. By Snell's law, the OPD of the FPE can be written in terms of the angle of incidence, θ_i , as

$$OPD_{FPE} = 2n_1 t_1 \cos\left(\sin^{-1}\left(\frac{1}{n_1} \sin(\theta_i)\right)\right). \quad (61)$$

To determine the FPE's angular resolution as a function of OPD, we consider the change in angle of incidence required to shift the interference fringes at the observation plane by a single order. The condition for a bright fringe in the interference profile for transmitted rays can be shown to be

$$OPD_{FPE} = m\lambda; \quad m \in \mathbb{Z}, \quad (62)$$

implying that OPDs that are an integer number of wavelengths produce maxima in intensity at the observation plane [13]. Taking the derivative of the bright fringe condition reveals how the order in the fringe pattern shifts with small changes in angle of incidence.

$$\frac{d}{d\theta_i}(OPD_{FPE}) = \frac{d}{d\theta_i}(2n_1 t_1 \cos(\theta_i)) = \frac{d}{d\theta_i}(m\lambda). \quad (63)$$

Using the relation between angle of incidence and the refracted angle from (61), the derivative from (63) can be written as

$$2n_1 t_1 \left(\frac{-\frac{1}{2n_1} \sin(2\theta_i)}{\sqrt{n_1^2 - \sin^2(\theta_i)}} \right) = \lambda \frac{dm}{d\theta_i}. \quad (64)$$

Defining the maximum angular resolution, $d\theta_i$, for a change in fringe order of $m = \pm 1$ and maximum wavenumber, σ_{\max} , equation (64) reduces to

$$d\theta_i = \frac{\lambda_{\min}}{t_1 \sin(2\theta_i)} \sqrt{n_1^2 - \sin^2(\theta_i)} = \frac{1}{\sigma_{\max} t_1 \sin(2\theta_i)} \sqrt{n_1^2 - \sin^2(\theta_i)}. \quad (65)$$

The plots in Fig. 41 are the angular resolution from (65) for three different values of the index of refraction of the plate, $n_1 = \{1.5, 1.6, \text{ and } 1.7\}$. The maximum wavenumber is chosen at

$\sigma_{\max} = 2.5 \times 10^6 \text{ m}^{-1}$ and the plate thickness is taken to be $t_1 = 10 \text{ mm}$, with an incident FOV over the angles $\theta_i = 10^\circ$ to $\theta_i = 20^\circ$.

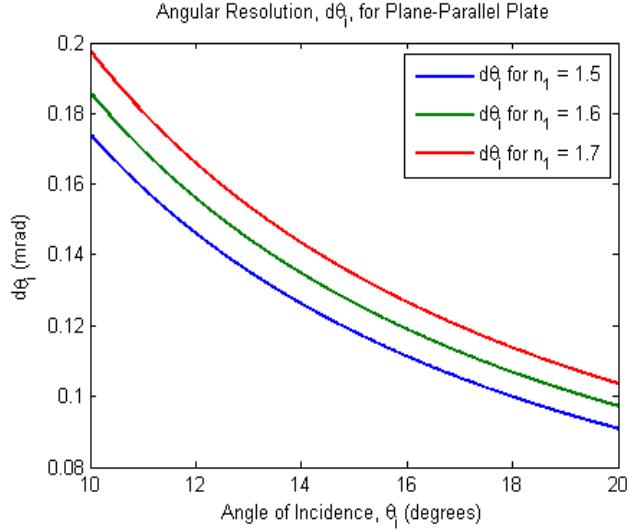


Fig. 41. Angular resolution, $d\theta_i$, for an FPE for three different indices of refraction, $n_1 = \{1.5, 1.6, \text{ and } 1.7\}$.

From Fig. 41, it can be seen that increases in the index of refraction of the plate decreases the maximum angular resolution of the system. Since the OPD is dependent on the angles of refraction into the cavity, as opposed to angles incident at the surface of the cavity, increasing the index of refraction of the plate leads to an FPE that is less sensitive to angle. This behavior effectively removes the index of refraction as an extra degree of freedom in increasing the OPD to achieve larger angular resolutions, leaving only the physical dimension of plate thickness.

The “maximum” angular resolution (or more specifically, the minimum resolvable angular separation of two point sources) of an ideal lens can be calculated from the well-known equation

$$d\theta_{lens} = 1.22 \frac{\lambda}{D}, \quad (66)$$

which relates the angular resolution to the wavelength of light, λ , and the diameter of the lens, D (defined as a circular aperture). This equation is derived from Fraunhofer diffraction of light at a circular aperture and falls under the small angle approximation. Fraunhofer diffraction at a circular aperture leads to the equation for the PSF of a lens (circular) given by

$$I(\theta) = I(0) \left[\frac{2J_1(ka \sin \theta)}{ka \sin \theta} \right]^2, \quad (67)$$

where k is the wavenumber ($2\pi/\lambda$), a is the radius of the circular aperture of the lens, θ is the angle that the diffracted ray makes with the optical axis towards the image plane, and J_1 is the first order Bessel function of the first kind. It can be seen that the PSF of a lens is determined by the argument of the Bessel function and is a function of the wavelength (λ), size of the lens (radius, a , or the diameter, D) and the extent of the angles allowed to propagate from the lens (θ).

An important detail to note is where the ‘1.22’ scalar quantity in the lens’ angular resolution equation comes from and how it changes with the aforementioned parameters (λ , D , and θ). For

reference, the plot in Fig. 42 shows the normalized PSF of an F/1 lens ($f = D = 100$ mm) for a single wavelength, $\lambda = 500$ nm, and a range of angles of $\theta = -10^\circ$ to $\theta = 10^\circ$.

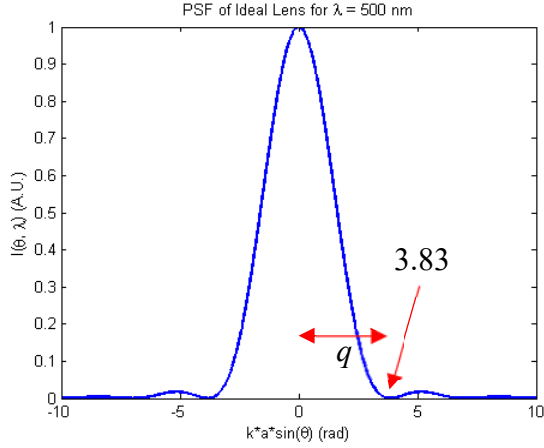


Fig. 42. PSF of an ideal lens for a single wavelength, $\lambda = 500$ nm.

From Fig. 42, we can define the radius of the PSF, q , as the spatial distance between the maximum and first zero-crossing of the intensity profile which occurs at the value 3.83 rad (and -3.83 rad). From here we can show that an analytic form of q has the form

$$ka \sin(\theta) = \frac{kaq}{R} = 3.83 \quad (68)$$

$$\Rightarrow q = 1.22 \frac{R\lambda}{2a} = 1.22 \frac{R\lambda}{D}, \quad (69)$$

with R being the ray path distance from the center of the circular aperture of the lens. Assuming the lens is focused onto the image plane such that the focal length, f , is approximately equal to the distance R gives

$$q \approx 1.22 \frac{\lambda f}{D} = 1.22 \lambda (F/\#). \quad (70)$$

Now, applying the small angle approximation (which may have major implications, since it is derived for two equal-irradiance, incoherent, distant point sources) yields

$$\frac{q}{f} = \sin(d\theta) \approx d\theta. \quad (71)$$

The angular resolution, calculated previously, yields

$$d\theta_{lens} \approx 1.22 \frac{\lambda}{D}. \quad (72)$$

Thus, the value ‘1.22’ in both equations (66) and (72) is derived from the zero-crossings of the first order Bessel function and the use of the small angle approximation with respect to distant point sources. However, it is of interest here to determine whether the ‘1.22’ value (and thus, zero-crossings) will change for broadband light containing multiple wavelengths.

Fig. 42 depicts the PSF of an ideal lens versus the argument of the Bessel function (i.e. $k \times a \times \sin \theta$). Thus, plotting the lens PSF with respect to any arbitrary wavelength for the given

argument will always give a zero-crossing at the 3.83 rad value. In order to compare the PSFs of several wavelengths, you could either 1) take the average wavenumber, k_{avg} , value across the spectral range, or 2) take the maximum wavenumber, k_{max} , related to the minimum wavelength in the spectrum. For the latter case 2), it is as if the smallest wavelength in the spectrum sets the maximum angular resolution by having the smallest PSF bandwidth. Thus, we will use this value (for now) to calculate the polychromatic angular resolution of the lens. If we consider the visible spectrum over the wavelengths $\lambda = 400$ nm to $\lambda = 800$ nm with the smallest wavelength (400 nm) setting the maximum angular resolution for this spectral range, then we get several lens PSFs, one for each wavelength (assume five wavelengths here, shown in Fig. 43).

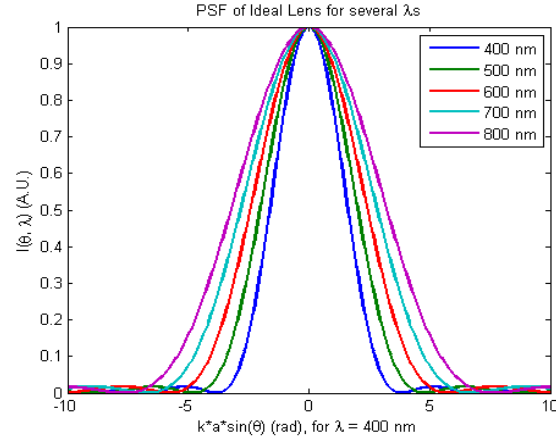


Fig. 43. PSF of lens plotted for five values of λ in the visible range with $\lambda = 400$ nm setting the lower bound of the angular resolution.

The overall PSF is approximated as the summation of all the component PSFs for each wavelength in the spectrum. For 50 wavelengths in the range of $\lambda = 400$ nm to $\lambda = 800$ nm, the total unscaled intensity is plotted in Fig. 44.

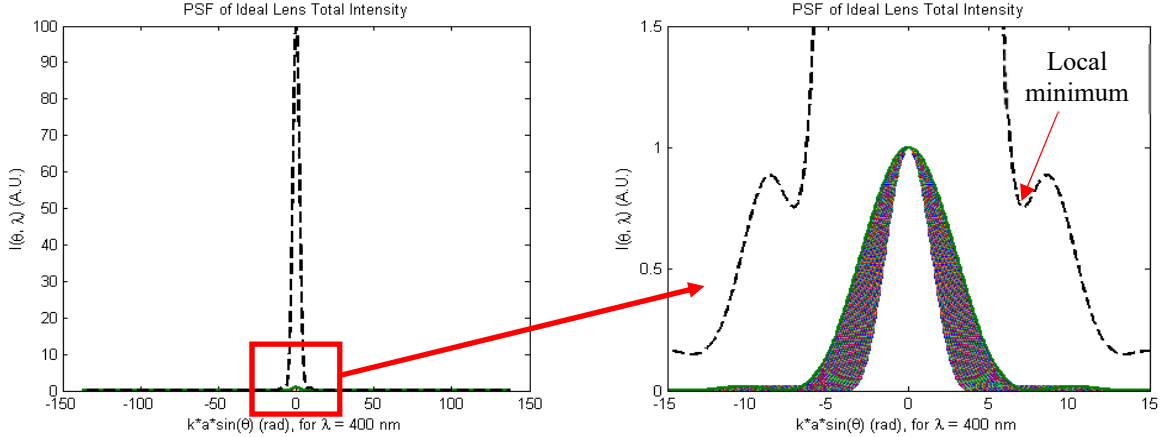


Fig. 44. Polychromatic lens PSF (black dashed line) represented as the summation of all the component wavelengths of the spectrum, unscaled version to show relative magnitude on left and zoomed-in version to show minima on right.

From Fig. 44 we see that the summation of all PSFs over the spectrum of 100 wavelengths gives an overall PSF that does not have a zero-crossings like to the constituent PSFs. However, the local minima in the polychromatic PSF occur at approximately ± 7.16 rad with a relative intensity of $I = 0.754$; roughly twice the value of the diffraction-limited PSF (3.83 rad) at $\lambda = 400$ nm. If we

were to repeat the same process in equations (68) through (72), then the angular resolution of an ideal lens with a polychromatic source over the spectral range $\lambda = 400$ nm to $\lambda = 800$ nm could be approximated as

$$d\theta_{lens,poly} \approx \frac{7.157}{\pi} \frac{\lambda}{D} = 2.28 \frac{\lambda}{D} \quad (73)$$

This approximation for angular resolution of an ideal lens for a polychromatic source could then be used to compare the resolutions of other imaging systems with polychromatic sources.

2.5 Comparing Angular Resolution of Lens and General Fabry-Perot System

Now that an approximation for the angular resolution of an ideal lens imaging a polychromatic source has been established, we can compare this result to the angular resolution of an SSM's FPE. Given a fixed mirror separation, the angular resolution of this system can be expressed as

$$d\theta_{FP} = \frac{1}{\sigma_{max} OPD_{max} \sin(\theta_0)} = \frac{1}{v_{max}}, \quad (74)$$

where θ_0 is the angle incident on the FP with initial tilt included. We must determine what value of v_{max} (or more specifically OPD_{max} , since σ_{max} is determined/set by the spectrum and θ_0 can only range over certain realistic values) creates an angular resolution, $d\theta$, which surpasses that of a lens.

From the above analysis, we can calculate the angular resolution of the lens imaging a polychromatic point source, and using the relationship to the numerical aperture relate the angle of incidence to the lens's diameter. Thus, we may write

$$NA = n_0 \sin(\theta_0) = n_0 \sin\left(\arctan\left(\frac{D}{2f}\right)\right) \approx n_0 \frac{D}{2f}, \quad (75)$$

$$\Rightarrow D = 2f \sin(\theta_0). \quad (76)$$

Now, the diameter of a lens can be represented as a function of the allowable angles of incidence and it can be used to calculate the angular resolution from equation (73). Similarly, for the general FP system, the angular resolution can be calculated for a set of incident angles, and by manipulating the value of OPD_{max} , will eventually lead to a value of v_{max} that creates a higher angular resolution than the lens system.

For example, Fig. 45 illustrates the polychromatic angular resolution of a lens with a focal length, $f = 50$ mm, over a range of angles from $\theta_0 = 5^\circ$ to $\theta_0 = 45^\circ$. This lens is compared to the general FP for values of $OPD_{max} = \{10 \text{ mm}, 20 \text{ mm}, 30 \text{ mm}\}$ over the same FOV (with 5° of initial tilt). Both system angular resolutions are calculated for $\lambda_{min} = 400$ nm, or $\sigma_{max} = 2.50 \times 10^6 \text{ m}^{-1}$.

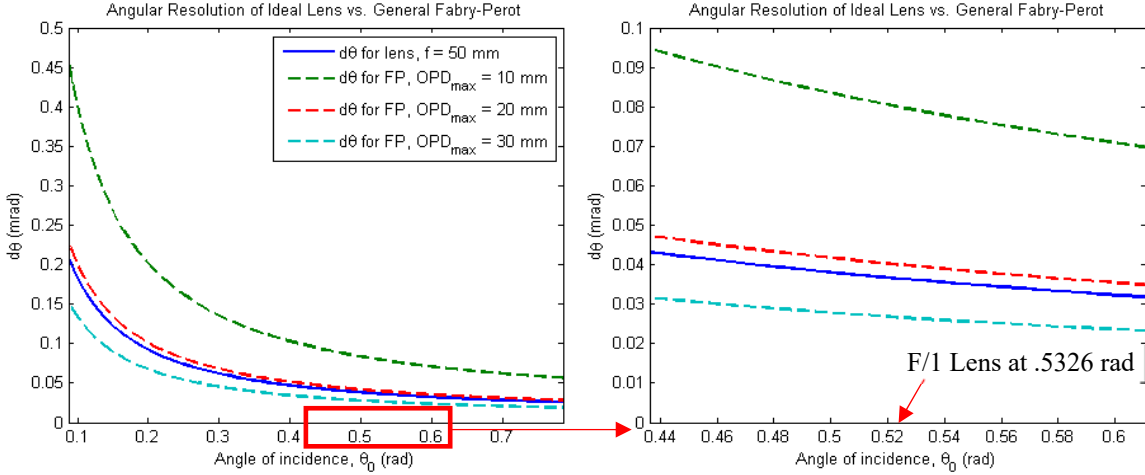


Fig. 45. Angular resolution of ideal lens and general FP versus angle of incidence ($\theta_0 = 5^\circ$ to $\theta_0 = 45^\circ$) for $\sigma_{\max} = 2.50 \times 10^6 \text{ m}^{-1}$ for multiple values of OPD_{\max} (top). Zoomed-in version of the same plot around the angles of incidence for which $f = D$ for the lens (bottom).

From the plot in Fig. 45, it would appear that relatively large values of OPD_{\max} ($\approx 22 \text{ mm}$) would be needed to surpass the angular resolution of a lens for these sets of calculations. The computation for the angle of incidence by way of the lens diameter may not be the best way to go about the problem, but it seems to give expected results. Now the question becomes can OPD_{\max} values of this magnitude be reached in the FP interferometer system and for what physical parameters is that possible.

2.6 Tolerancing and Aberrations

2.6.1 Tolerancing of Beamsplitter Terminus

One major issue with using interferometers for the SSM technique is related to tolerancing of the system. These tolerancing issues are primarily related to (but not limited to) the beamsplitter terminus, surface flatness, wedge angles and parallelism, transverse angles of the optics (which can cause shear), or any surface nonuniformities in the interferometer that can add additional wavefront aberrations to the interfering beams. To analyze the effect of some of these issues, models in MATLAB and Zemax were created to investigate the effect of different glass plate thicknesses, different relative angles between the plates, and the effects that various aberrations (e.g. coma, spherical, astigmatism) had on the channeled spectrum. The MATLAB modeling technique first defines a range of wavelengths (or wavenumbers) of interest for the system (e.g. $\lambda = 400 \text{ nm}$ to $\lambda = 2 \mu\text{m}$). Using the Cauchy equations

$$n(\lambda) = A + \frac{B}{\lambda^2}, \text{ with} \quad (77)$$

$$A = n_d - \frac{B}{L_d^2}, \text{ and} \quad (78)$$

$$B = \frac{(n_d - 1)}{\nu_d \left[(L_c^2 - L_f^2)(L_c^2 \times L_f^2) \right]}, \quad (79)$$

where n_d and ν_d represent the index of refraction and Abbe number of the glass material and L_f , L_d , L_c denote the major Fraunhofer lines for 486.1 nm, 587.6 nm, and 656.3 nm, respectively. An

example of the dispersion curves for two glass types, Schott N-LAK8 and N-SF1, are illustrated in Fig. 46. The intersection of the dispersion curves is meant to represent the “design wavelength”, λ_0 , for which the system has zero OPD regardless of angle of incidence such that

$$\frac{\partial}{\partial \theta} OPD = 0 . \quad (80)$$

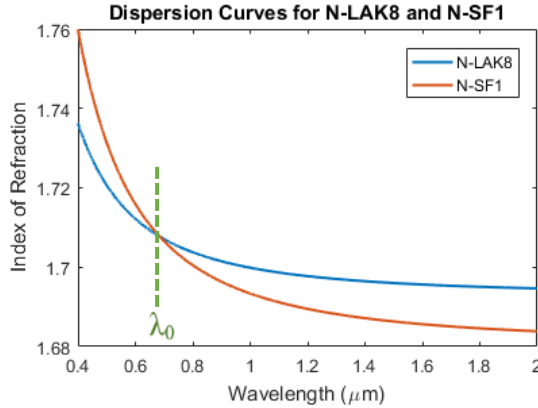


Fig. 46. Dispersion curves of potential glass options (N-LAK8 and N-SF1) based on Sellmeier equations and known coefficients. Intersection represents design wavelength of the MI system.

Similarly, the dispersion of the beamsplitter’s material must be incorporated to model the effects of the terminus on the system’s phase. The beamsplitter’s terminus is depicted in Fig. 47, and is an error created by an offset in the two 45° prisms used to form the beam splitter. The terminus was measured to be approximately 1 mm in the current MI system and assumed to be of the same material as the beamsplitter, namely N-BK7 glass.

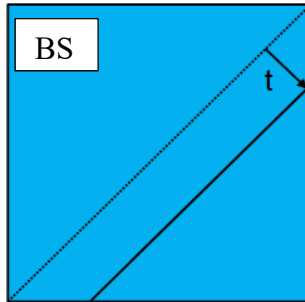


Fig. 47. Depiction of beamsplitter terminus, with t representing the thickness of the offset.

In the MATLAB model, the terminus was considered as a plate of N-BK7 with thickness, t_{terminus} , which adds to the optical path length of a single arm of the beamsplitter. Air gaps were also considered in the model, one for each arm of the beamsplitter, with a constant index of refraction, $n_{\text{air}} = 1.00027$, and thicknesses $t_{1,\text{air}}$ and $t_{2,\text{air}}$, respectively. Thus, equation (8) can be generalized to take the form

$$OPD = \left[2n_1 t_1 \cos(\theta_1) + 2n_{1,air} t_{1,air} \cos(\theta_1) + 2n_{\text{terminus}} t_{\text{terminus}} \cos(\theta_1) \right] - \left[2n_2 t_2 \cos(\theta_2) + 2n_{2,air} t_{2,air} \cos(\theta_2) \right] \quad (81)$$

The expression represented above can be expanded in the same manner as in (9) and (10) to represent the OPD in terms of the angle of incidence on the beamsplitter. After defining a range of incidence angles (e.g. $\theta_i = 0^\circ$ to 10° , with an initial offset of 10°), the model sums all output intensities to generate a channeled spectrum (CS) over the range of incidence angles with respect to wavenumber. Intensity calculations are made using the form

$$I(\sigma, \theta) = 2I_0 [1 + \cos(2\pi\nu(\sigma, \theta))] \quad (82)$$

where I_0 is calculated as unity (for simplicity) and $\nu(\sigma, \theta)$ is defined as

$$\nu(\sigma, \theta) = \sigma OPD(\sigma) \cos(\theta), \quad (83)$$

where the OPD is given in (81). An example of an ideal model with a uniform broadband white light illumination is shown in Fig. 48, where parameters are chosen to be n_1 (N-LAK8); n_2 (N-SF1); n_{terminus} (N-BK7), $t_1 = t_2 = 2$ mm; $t_{1,air} = t_{2,air} = t_{\text{terminus}} = 0$ mm. The OPD is calculated over a range of incidence angles from $\theta_i = 0^\circ$ to $\theta_i = 10^\circ$ with an initial MI tilt angle of $\theta_0 = 10^\circ$, with an angular spectrum magnitude of unity. To compare with the ideal case, a channeled spectra is simulated with a beamsplitter terminus of $t_{\text{terminus}} = 5$ μm . Both simulations are generated over the spectral range of $\sigma = 0.5 \times 10^6$ to $\sigma = 2.5 \times 10^6$ ($\lambda = 400$ nm to $\lambda = 2$ μm) at a spectral resolution of 8 cm^{-1} .

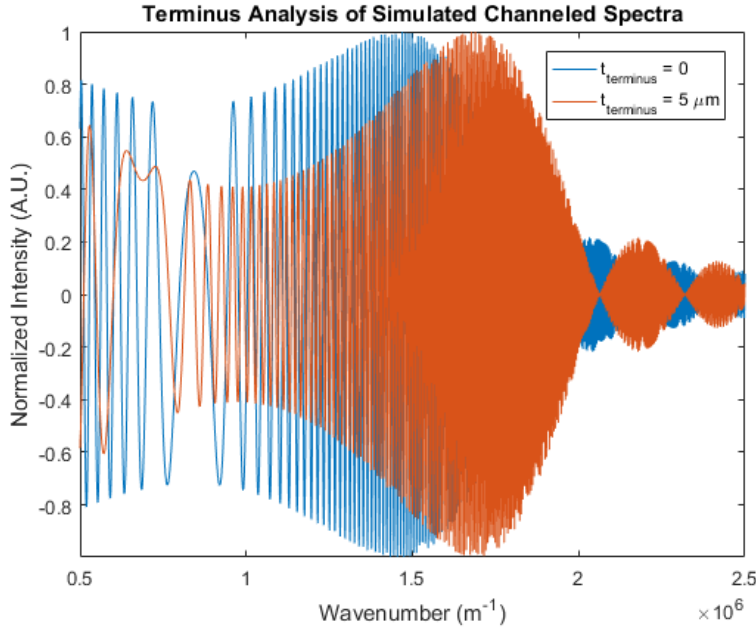


Fig. 48. Simulations of channeled spectra generated by a Michelson interferometer for equal path lengths ($t_1 = t_2 = 2$ mm) with (red curve) and without (blue curve) a beamsplitter terminus.

Phase variations and amplitude modulations are apparent when a terminus of thickness $t_{\text{terminus}} = 5$ μm is added to the system. In the situation presented in Fig. 48, the addition of a beamsplitter terminus shifts the region of maximum contrast (i.e. centerburst) from $\sigma \approx 1.470\text{E}6$ to $\sigma \approx 1.689\text{E}6$. In practice this would make determining the location of the centerburst difficult if

the terminus was not known *a priori*. Also, note that the fringe contrast will be reduced for increasing thickness of the beamsplitter terminus, ultimately resulting in an overall reduced signal to noise ratio.

One additional issue in the dispersive-based SSM systems could be caused by nonuniformities in the surface flatness of the beamsplitter(s) or mirrors, which can add additional aberration to the system. As an example, Fig. 49 depicts images of the white light interference patterns (localized at infinity) within the Michelson interferometer. The left and right figure were taken when the MI was aligned to zero OPD for two different sets of mirror. In the left figure, a large amount of astigmatism is present, whereas in the right figure the amount of aberration is reduced. However, the right figure demonstrates the white light interference pattern for the ‘best’ experimental case, which is not ideal. In the ideal experiment, the interferometer would generate a single fringe across the FOV, as sampling across multiple fringes implies portions of the scene will not be aligned to zero OPD and create incoherence and different spectral powers within the measured channeled spectra.

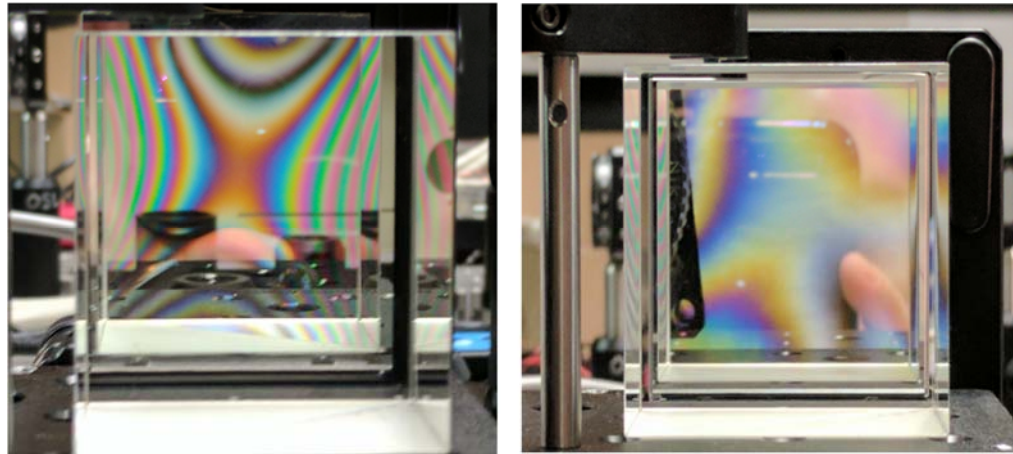


Fig. 49. Images of the white light interference patterns generated by a Michelson interferometer for two different sets of dielectric mirrors.

2.6.2 Wavefront Aberrations in Interferometers

While the MI system can offer robust compensation for phase errors, it will be important to model various sources of these phase errors at varying magnitudes, keeping in mind that these effects will eventually determine the specifications of optical components (*e.g.*, material/index/dispersion, thickness, surface flatness, etc.) for a proof of concept system. Phase errors are analogous to non-planar wavefronts, which will diminish the spatial resolution of the Spatial-Spectral multiplexing (SSM) technique, since these rays would correspond to a source point at many angles on the image plane. The current approach to modeling phase errors is to use the MZDDE application of MATLAB and Zemax to change various parameters within the lens prescription defined in Zemax. For wavefront aberrations, this involves defining a “Zernike Standard Phase” surface in the Zemax lens prescription and alternating the Zernike surfaces properties through MZDDE. This enables arbitrary wavefront aberrations to be simulated on every surface. A Zemax ray trace of the MI that was used, in conjunction with the MATLAB model, is presented in Fig. 50.

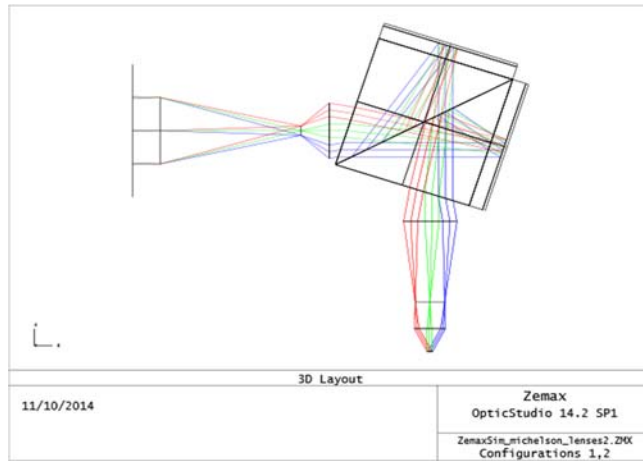


Fig. 50. Zemax ray trace of MI used with MZDDE and the MATLAB modeling routine.

When considering wavefront aberrations in the MI system, there are two primary situations to be concerned with: 1) the same wavefront error is imparted in both arms of the MI beamsplitter; and 2) wavefront error is only imparted to a single arm. The first situation is hypothesized to have negligible effects on transmitted wavefront error since both arms of the MI will see the same initial phase error, and modulate that phase error in similar ways. The second situation, which can be caused by any variation of parameters between the two arms, will have more apparent effects. Once the two situations are modeled, the MATLAB/Zemax script can evaluate the OPD across an arbitrary pupil plane, field of view, and spectra by using the merit function generator in Zemax. The general models for the two different cases of wavefront error in the system are presented in Fig. 51, where the location of the Zernike Standard Phase surface is shown in a relative location to the MI system.

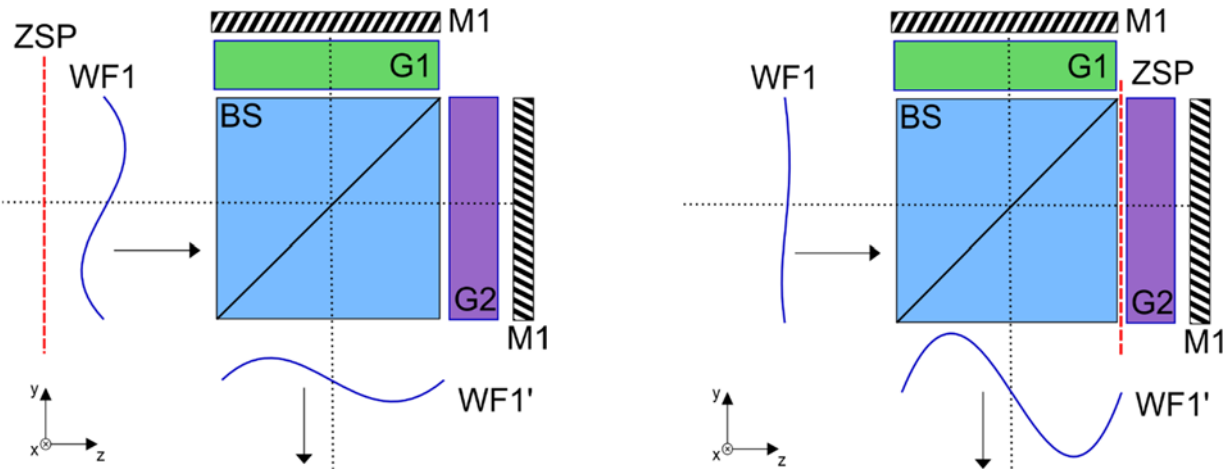


Fig. 51. Diagrams of two different scenarios for modeling the effect(s) of wavefront aberrations in the MI system. (Left) Both arms of the MI experience the same added wavefront error. (Right) Same initial wavefront error, but one arm has more wavefront error added.

The diagrams in Fig. 51 show the two situations for modeling wavefront aberrations in the MI system in Zemax. Zernike Standard Phase (ZSP) is denoted by the relative location of the surface in the system, on the left diagram this surface is placed in front of a collimating lens, before the beamsplitter (BS) such that both arms (defined by glass plates G1, G2 and mirrors, M1 and M2,

respectively) experience the same wavefront error which could be related to the scene or initial imaging lenses. The diagram on the right has the surface placed only for one path of the MI, right after the beamsplitter to simulate wavefront error that could be created on the surfaces of the glass plate (or prisms), surface of the mirror, or surface of the beamsplitter cube. Again, this situation (right) models the effect of a varying degree of relative wavefront error between the two arms of the beamsplitter. The diagrams also show hypothetical wavefronts, WF1 and WF1', which illustrate possible outcomes for each scenario. For the left diagram, the degree of wavefront error is hypothesized to be minimal, while on the right diagram the transmitted wavefront error could potentially be more severe since the relative phase error will be much larger.

The situation on the right of Fig. 51 will be further expanded to analyze the individual optical components and their contributions to the wavefront error for a single arm of the beamsplitter. These results will be essential to evaluating how much tolerance is on the various components.

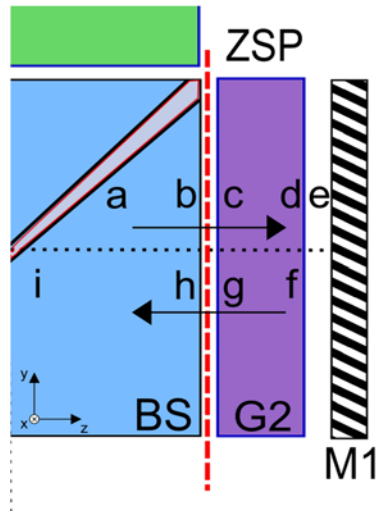


Fig. 52. Schematic of the breakdown evaluation of the wavefront error contributed by each surface of a single arm of the MI system.

The diagram presented in Fig. 52 shows one potential method to evaluate the root-mean-square (RMS, defined below) contribution of wavefront error made by each surface of an arm in the MI system. The variables $\{a, b, \dots, i\}$ in the diagram represent the coefficients for RMS wavefront error for each surface, such as beamsplitter wedge (a and i), beamsplitter surface (b and h), plate surfaces and/or surface flatness (c, g and d, f), and mirror surface and flatness (e). Note that some coefficients, such as b and h will be approximately equivalent since they represent the same surface in different directions of propagation. Wavefront aberrations in this case are the measure of how much deviation from perfect spherical occurs, averaged over the entire wavefront. We may define the RMS wavefront error as our metric to calculate the amount of this deviation versus a system without aberrations as

$$\sigma^2 = \frac{1}{\pi} \int_0^{2\pi} \int_0^1 [\Delta W(\rho, \theta) - \overline{\Delta W}]^2 \rho d\rho d\theta = \overline{\Delta W^2} - (\overline{\Delta W})^2, \text{ and} \quad (84)$$

$$\sigma = \sqrt{\overline{\Delta W^2} - (\overline{\Delta W})^2}. \quad (85)$$

Equations (84) and (85) define the variance σ^2 and the RMS wavefront error σ for a normalized circular pupil. The values for $\Delta W(\rho, \theta)$ are measured relative to the best fit spherical wave, or the mean wavefront OPD, and are given in units of waves. For the purpose of tolerancing the system the RMS wavefront error can be considered a sum of the individual contributions from each surface in the optical path, i.e.

$$(0.5)RMS = \sum_i a_i \sigma_{total} = \sigma_{total} (a + b + \dots + i). \quad (86)$$

In Eq. (86) σ_{total} represents the total RMS wavefront error for a given optical path (beamsplitter arm), multiplied by the coefficients for each surface. Initially, the values of the coefficients will be based on the degree of the potential contribution for a given surface (e.g. beamsplitter wedge will most likely have a higher RMS contribution than the mirror, and will therefore be weighted larger). The 0.5 multiplicative factor in front of the calculation is another arbitrary value that sets the limit on how much wavefront error is acceptable, as well as a reasonable approximation for what can be manufactured.

The effects of the various sources of wavefront error will be measured by the spot size of the point spread function (PSF) and the visibility (related to coherence) of the channeled spectrum. The PSF is created by linearizing the nonlinear OPD versus wavenumber and acts as a reconstruction of a scene's input angular spectrum in the form of a point source. Initially, the input spectrum can be point sources (approximate delta functions after reconstruction), but will eventually need to be expanded to any arbitrary spectrum at varying angles of incidence. The metric for spot size is the full-width half maximum (FWHM) of the delta function which is determined by fitting a Gaussian distribution function to one of the two-sided delta functions and finding the value for

$$FWHM = 2\sqrt{2 \ln 2}\sigma \approx 2.355\sigma, \quad (87)$$

where σ is defined here as the standard deviation of the Gaussian function.

2.7 4F Imaging System versus Spectrally Resolved White Light Interferometry

One potential advantage of the SSM technique, over conventional imaging with lenses, is the ability to directly access or manipulate the spatial Fourier domain of the incident angular spectrum. Since the SSM technique uses two-beam interference to modulate the angular spectrum onto carrier frequencies, the channeled spectrum has both amplitude and phase information. Conversely, the output of a lens only contains the spatial amplitude with no phase information of the scene that can be demodulated from within the Fourier plane (lens pupil). The distinction between the outputs of the two optical systems is illustrated in Fig. 53 and Fig. 54, with a conventional 4F system and the tilted MI both imaging an infinite cosinusoidal grating of period A in object space.

The 4F imaging system in Fig. 53 (a) is comprised of two imaging lenses of focal length f imaging a cosinusoidal grating of infinite extent in the x -dimension in object space. The cosinusoidal grating of period A is illuminated by on-axis monochromatic plane waves, which are diffracted into the $m = 0, \pm 1$ orders of the grating only before being collected by the first imaging

lens. Each diffraction order represents a plane wave of unique angular or spatial frequency, which considered together make up the angular spectrum. The first lens transforms each plane wave into a converging spherical wave that creates a point image at the Fourier plane located one focal length away from the lens. Because of the limited spatial extent created by the circular aperture of the lens, the point images in the Fourier plane broaden to create the conventional diffraction-limited point spread function. Since the scene's angular spectrum is comprised of only the three spatial frequencies corresponding to the diffraction orders of the grating (i.e. $m = 0, \pm 1$), the Fourier plane consists of three point spread functions (Fig. 53 (c)). Though the Fourier plane contains the amplitude of each spatial frequency from the grating, there exists no measurable phase information at this location. In other words, if a conventional square law detector were placed in the Fourier plane, it would only be able to measure information related to amplitude and phase could not be calculated. Thus, in order to retrieve the angular spectrum's phase information and reconstruct the scene, another imaging lens would need to be placed one focal length (f) behind the Fourier plane (Fig. 53 (d)).

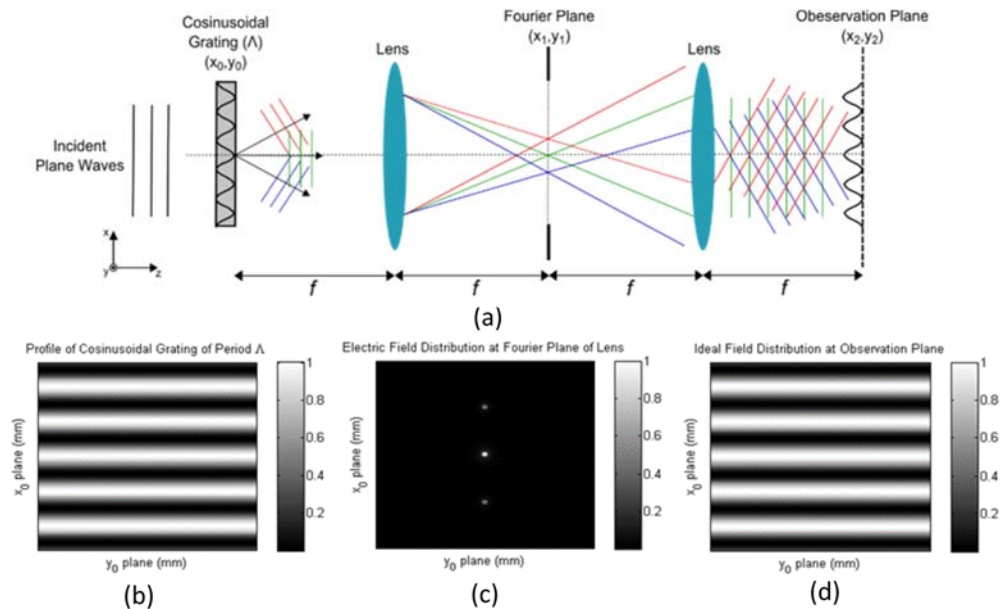


Fig. 53. Illustrations of a 4F imaging system (a) imaging an infinite extent cosinusoidal grating of period Λ in object space. The electric field distribution of the cosinusoidal grating (b) is imaged by a lens in the 4F system to create the field distribution at the Fourier plane of the lens (c). The second lens in the 4F system reconstructs the cosinusoidal grating (d).

Meanwhile, the tilted MI depicted in Fig. 54 (a) is related to the Fourier plane of the 4F system at resolving the spatial frequencies created by a grating. By using two-beam interference, the fixed OPD MI modulates the incident spatial frequencies (which are directly related to the angle of incidence, θ_i , on the interferometer) after multiplication with the cosinusoidal grating onto the spectral information of the scene.

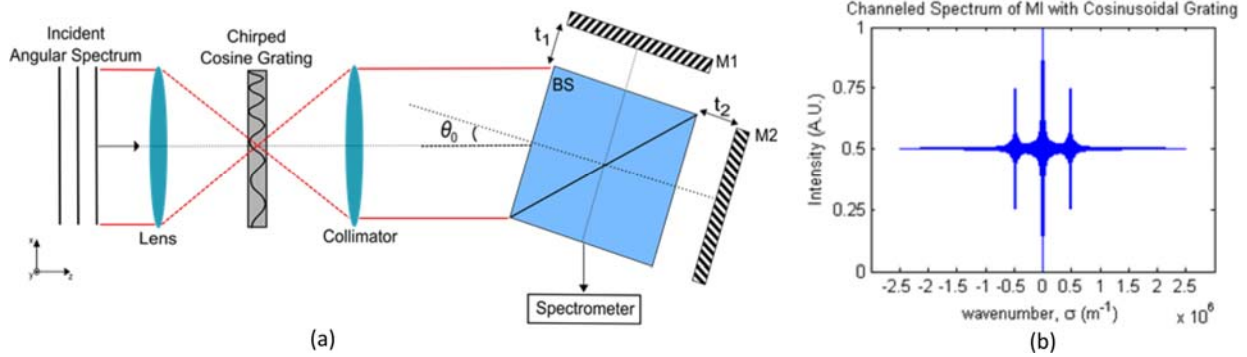


Fig. 54. A tilted MI (a) imaging a chirped cosinusoidal grating in object space. The channeled MI modulates the multiplication of the incident angular spectrum and cosinusoidal grating using two-beam interference to create a channeled spectrum (b) as a function of wavenumber at the observation plane.

The tilted MI depicted in Fig. 54 (a) is fundamentally different from the 4F system at resolving the spatial frequencies created by a grating. By using two-beam interference, the fixed OPD MI modulates the incident spatial frequencies (which are directly related to the angle of incidence, θ_i , on the interferometer) after multiplication with the cosinusoidal grating onto the spectral information of the scene. If a spectrally broadband source of arbitrary angular spectrum (e.g. a uniform spectrum as illustrated in Fig. 54 (a)) illuminates a chirped cosinusoidal grating, then the interference profile of the MI takes the form of a channeled spectrum, similar to the one in Fig. 54 (b), in which “channels” at higher spectral frequencies form from coherence between the diffraction orders of the grating. The difference between the observation plane of the MI and the 4F lens system being that spatial amplitude and phase can be recovered from the channeled spectrum, whereas the Fourier plane of the lens only contains amplitude information. Thus, a MI using the SSM technique could recover both amplitude and phase information of the spatial frequencies of the scene at the output plane at the spatial resolution set by the maximum OPD in the interferometer.

If a spectrally broadband source with an arbitrary angular spectrum is spatially modulated by a chirped cosinusoidal grating, then the interference profile of the MI takes the form of a channeled spectrum, similar to the one in Fig. 54 (b), in which “channels” at higher spectral frequencies form from coherence between the diffraction orders of the grating. The difference between the 4F imaging system’s Fourier plane and the MI’s channeled spectrum is that, in the MI, both spatial amplitude and phase can be recovered, whereas the lens’s Fourier plane only contains amplitude information. Thus, a MI using the SSM technique could recover both amplitude and phase information of the scene’s spatial frequencies at the output plane at the spatial resolution set by the maximum OPD in the interferometer.

3.0 Snapshot Spectrally Resolved Longitudinal Spatial Coherence Interferometry

3.1 *Introduction (to Spectrally Resolved Longitudinal Spatial Coherence Interferometry)*

Encoding information onto different dimensions has been investigated in the fields of fiber optics and communication [14-18], medical imaging [19,20], microscopy [21-23], and remote sensing [24,25]. Techniques presented in the past have relied on an analog of Hadamard multiplexing to encode spatial information onto the incident power spectrum; *e.g.*, by use of filter arrays or masks onto which an object is imaged. In this work, we focus on encoding of a scene's angular spectrum onto a broadband power spectrum by use of phase-based multiplexing. This is achieved by leveraging longitudinal spatial coherence and the angular sensitivity of a Fabry-Perot etalon to modulate incident angular information onto the coherence of the source power spectrum. In this way, each spatial component of the angular spectrum has a unique frequency in the measured channeled spectrum [26]. The proposed technique has parallels to Fourier transform spectroscopy [27] in which interferometric systems are used to modulate the source's power spectrum onto an angular spectrum (or spatial axis). Similar to Fourier transform spectroscopy, reconstructing the angular spectrum can be achieved using a Fourier transform relationship.

In the field of fiber optics and communication a different approach to spatial-spectral encoding or multiplexing is used to increase the amount of information that can be transmitted along the fiber. Since fibers have low spatial resolution and complex transfer functions versus angle, incident spatial information is encoded onto a different space, such as wavelength [16] or time [17]. In many cases, the spatial-spectral encoding and decoding processes are accomplished using diffractive optical elements or prisms. For example, Armitage *et. al.* [15] proposed a technique for wavelength multiplexing using dispersive prisms to encode a one-dimensional object onto the spectrum of a white-light point source. The prisms served to disperse the white light spectrum across a one-dimensional slit along the object such that each spatial point was encoded onto a different wavelength before propagating through a non-imaging light pipe. Meanwhile, Mendlovic *et. al.* [18] devised a wavelength multiplexing technique which relied on diffractive structures to create the spectral spreading across both one- and two-dimensional objects. In this instance, the diffraction gratings were designed such that each spatial location or pixel across the object was mapped to a specific wavelength before transmitting through a single-mode fiber. The decoding process, used to reconstruct the object, also relied on diffractive elements to convert the individual wavelengths back into their corresponding spatial components. More recently the research of Barankov and Mertz [20] has demonstrated the use of spread-spectrum encoding to create high-throughput two-dimensional images of broadband white-light illuminated sources through single-mode fibers. By using low-finesse Fabry-Perot etalons as the spread-spectrum encoder, incident ray angles from an extended spatial distribution are given a unique spectral code across the full spectrum of the source. Reconstructing the object requires numerical decoding, rather than optical decoding, as seen in the prism and diffraction grating systems.

Unlike the wavelength multiplexing created using dispersive prisms or diffractive optical elements, our proposed system relies on interferometric techniques to encode the angular information onto the power spectrum. In this way, individual components of the angular spectrum

are not mapped to specific wavelengths, but are instead given unique frequencies or phases across the entire spectral range of the source. Our technique is more similar to the work of Barankov and Mertz; however, the basis of our encoding procedure relies on Dirac delta functions in the spatial domain being related to sinusoids in the spectral domain, rather than pseudo-random but unique spectral codes used in their spread-spectral encoder. This allows for a direct Fourier transformation relationship between the measured channeled spectrum and the reconstruction of the incident angular spectrum.

Longitudinal spatial coherence is used here to refer to coherence between two points along the optical axis as derived by interpretation of the Van Cittert-Zernike Theorem [0]. Many researchers have studied the application of longitudinal spatial coherence to the fields of optical coherence profilometry and tomography [29-33]. Rosen and Takeda [30] demonstrated the use of longitudinal spatial coherence for surface profilometry by shifting the degree of spatial coherence with modulations of the source's intensity distribution. The researchers used a Michelson interferometer illuminated with quasi-monochromatic spatially incoherent light to measure the gap between a reference and test mirror. However, instead of translating one of the mirrors along the longitudinal axis to determine peaks in coherence, spatial masks, defined by Fresnel zone plates, were used to modulate the source distribution. The height of the mirrors was thus determined by a relationship between peaks in spatial coherence and the grating constant or fringe frequency of the zone plates. Similarly, Wang *et. al.* [31] continued the preceding work to demonstrate an interferometric system for tomographic applications. Using a spatial light modulator to create angular spectra, it was shown that high-contrast fringes were only evident at surface heights which were spatially coherent with Fresnel zone plate-like sources.

In our interferometric technique, the concept of longitudinal spatial coherence is used to maximize the contrast in fringes observed within the measured channeled spectrum. The spatial frequencies of a source's angular spectra are coherently matched to the transmission peaks of monochromatic Haidinger fringes generated within a Fabry-Perot etalon. When a spectrometer is used to measure the channeled spectrum, maximum coherence occurs at a wavelength which observes resonance along the longitudinal axis of the cavity. A channeled spectrum refers to a sinusoidally modulated white-light spectrum and forms the basis for the measured output of the proposed technique. An example of the use of a channeled spectrum to recover information is presented by Oka and Kato [24], in which the state of polarization of a scene is modulated onto the power spectrum of the source. Using birefringent retarders to create phase retardations along the longitudinal axis as a function of wavenumber, three quasi-cosinusoidal components are generated which carry information about the polarization state of the scene. These components appear as discrete channels along the axis of path difference for the system, and are readily accessible to demodulate the polarization information of interest. To create discrete channels within the spectrally resolved measured signal of our system, a cosinusoidal spatial carrier frequency is used to shift a coherence into the detectable region of the spectrum. The carrier frequency is then amplitude modulated with a spatial envelope to encode angular information into the channeled spectrum's coherence. Recovery of the envelope is readily achieved by a Fourier transformation of the measured channeled spectrum.

In section 2, we present the theory of the proposed interferometric technique for angular-spectral encoding and derive parallels to Fourier transform spectroscopy. Details of the experimental design and procedures for validation of the technique are presented in section 3. Results from experimental validation for the reconstruction of sinusoidal and random angular spectra are offered in section 4, followed by a discussion of the results.

3.2 Theory

In a conventional Fourier transform spectrometer, or as we will refer to it as a Fourier Transform Power Spectrometer (FTPS), incident frequency components of the power spectrum are represented as unique spatial frequencies after two-beam interference. A view of a typical FTPS is illustrated in Fig. 55 (a), in which a Michelson interferometer (MI), with tilted mirrors, is used to create a spatially varying optical path difference (OPD) on a focal plane array (FPA). In this system, light from a source is collimated through a collimator into a beamsplitter (BS). This redirects the light onto two mirrors, M1 and M2, which are tilted by an angle α . Light is reflected from these tilted mirrors into an objective lens, which focuses the mirrors onto a focal plane array (FPA).

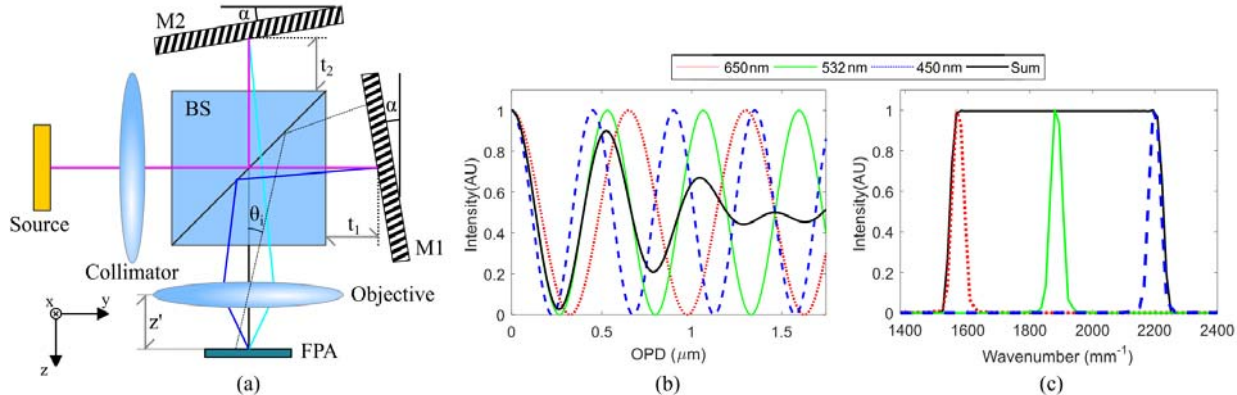


Fig. 55. (a) Michelson interferometer configured to measure the spectrum of a source. (b) Interference pattern, measured on the FPA as a function of OPD; (c) Fourier transform of the data in (b), yielding the source's power spectrum.

The OPD, as a function of FPA spatial position, can be represented [34] as

$$OPD(y) = 4y \tan \alpha. \quad (88)$$

The detected interference pattern, measured by the FPA, can be calculated [35] as

$$b[OPD(y)] = \text{rect}\left(\frac{OPD(y)}{OPD_{\max}}\right) \int_0^{\infty} \tau_p(\sigma_0) \rho(\sigma_0) \{I(\sigma_0) + I(\sigma_0) \cos[2\pi OPD(y)\sigma_0]\} d\sigma_0, \quad (89)$$

where b is the measured photogenerated current, ρ represents the detector's responsivity in A/W, I is the incident intensity in W, τ_p is the optics' power spectrum transmission function, rect is a uniform rectangular apodization function of width OPD_{\max} [36], and σ_0 is the incident wavenumber in units of inverse length. Assuming an ideal 50:50 BS and mirror reflectivity, the transmittance is

$$\tau_p(\sigma) = \frac{1}{2} \tau_c(\sigma) \tau_o(\sigma), \quad (90)$$

where τ_c and τ_o are the transmittances of the collimator and objective lenses, respectively. A view of the interference pattern is illustrated in Fig. 55 (b) versus OPD for 450 nm, 532 nm, and 650 nm visible light, as well as a continuous superposition given a uniform power spectrum. Fourier transformation of Eq. (89) with respect to $OPD(y)$ yields the detected power spectrum as

$$B(\sigma) = \int_0^\infty \left\{ \tau_p(\sigma_0) \rho(\sigma_0) I(\sigma_0) \left[\delta(\sigma) + \frac{1}{2} \delta(\sigma - \sigma_0) + \frac{1}{2} \delta(\sigma + \sigma_0) \right] * \text{sinc}(OPD_{\max} \sigma) \right\} d\sigma_0. \quad (91)$$

where $*$ represents the convolution operator, σ is the Fourier transform variable of OPD in cycles per unit length, and the constant term from Eq. (89) has been removed for clarity. The full width spectral resolution of the measured spectrum is then related to the interferogram's maximum OPD, such that

$$\Delta\sigma = 1/OPD_{\max}, \quad (92)$$

where OPD_{\max} is the maximum OPD sampled in Eq. (89). Thus, the Fourier transform of the interferogram yields the power spectrum $I(\sigma)$, weighted by the responsivity and transmission functions. Fig. 55 (c) illustrates the Fourier transformation of the interference data in Fig. 55 (b), illustrating that the individual spectral components are present within the recovered source spectrum. An FTPS configured in this way assumes that the source light's spatial distribution is uniform (or slowly varying) across the mirrors. If it is not, it creates an additional, spatially dependent modulation term in Eq. (89) that can be represented as

$$b(OPD(y)) = \text{rect}\left(\frac{OPD(y)}{OPD_{\max}}\right) \int_0^\infty \tau_A(\theta_i) \tau_p(\sigma_0) \rho(\sigma_0) \{I(\sigma_0) + I(\sigma_0) \cos[2\pi OPD(y) \sigma_0]\} d\sigma_0, \quad (93)$$

where $\tau_A(\theta_i)$ defines the spatial modulation that appears across the mirror's surface, $\theta_i = y/z'$ is the viewing angle between a position on the mirror's surface and its conjugate position on the FPA, and z' is the distance between the objective lens and FPA. It should be mentioned that spatial modulations across the mirror can be caused by, *e.g.*, inhomogeneity in the source, cosine falloff from the collimator and objective lenses, and angular transmission of antireflection coatings or etalon resonances. Fourier transformation with this spatial dependence yields

$$B(\sigma) = \int_0^\infty \left\{ \tau_p(\sigma_0) \rho(\sigma_0) I(\sigma_0) \left[\delta(\sigma) + \frac{1}{2} \delta(\sigma - \sigma_0) + \frac{1}{2} \delta(\sigma + \sigma_0) \right] * \text{sinc}(OPD_{\max} \sigma) * \mathcal{F}\{\tau_A[OPD(y)]\} \right\} d\sigma_0. \quad (94)$$

where \mathcal{F} represents the Fourier transform and the OPD dependence in τ_A can be calculated using Eq. (88) given $y = \theta_i z'$. If $\tau_A(\theta_i)$ does not contain the same spatial frequencies as the modulated power spectrum, then the effect of not having a spatially uniform source would appear at spatial frequencies outside of the spectrum after Fourier transformation. Conversely, if it contains similar spatial frequencies as the data, then crosstalk can occur. Thus, it is best to ensure no spatial modulation is present or to measure $\tau_A(\theta_i)$ separately from the spectral modulation; *e.g.*, nonuniformity or flatfield correction [37]. Thus, this interferometer is used to measure an arbitrary power spectrum assuming that the scene has a uniform angular spectrum.

We will now formulate the theory of spectrally resolved longitudinal spatial coherence interference within the context of the FTPS described above, which we will refer to as a Fourier Transform Angular Spectrometer (FTAS). What will be demonstrated is that using a tilted

interferometer, with spectrally resolved interferometry, is directly analogous to the FTPS but for measuring arbitrary angular spectra across one dimension. A view of our concept interferometer is illustrated below in Fig. 56 (a). It consists of the same MI, except it applies parallel (non-tilted) mirrors. However, the interferometer itself is tilted with respect to the incident light's optical axis. Light from a spatially and spectrally uniform source is first collimated into the MI, which is tilted with respect to the incident optical axis (or global y -axis) by an angle θ_0 . The light is split by a BS into two glass plates, with refractive indices n_1 and n_2 and thicknesses t_1 and t_2 , respectively. Light then reflects off mirrors M1 and M2 before recombining at the BS. Finally, light transmits through a relay lens, which images the collimator's pupil into the entrance aperture of a spectrometer (*e.g.*, a dispersive spectrometer's entrance slit or fiber, or a Fourier transform spectrometer's entrance pupil). Note that a refractive glass has been included between the BS and mirrors M1 and M2 for generality.

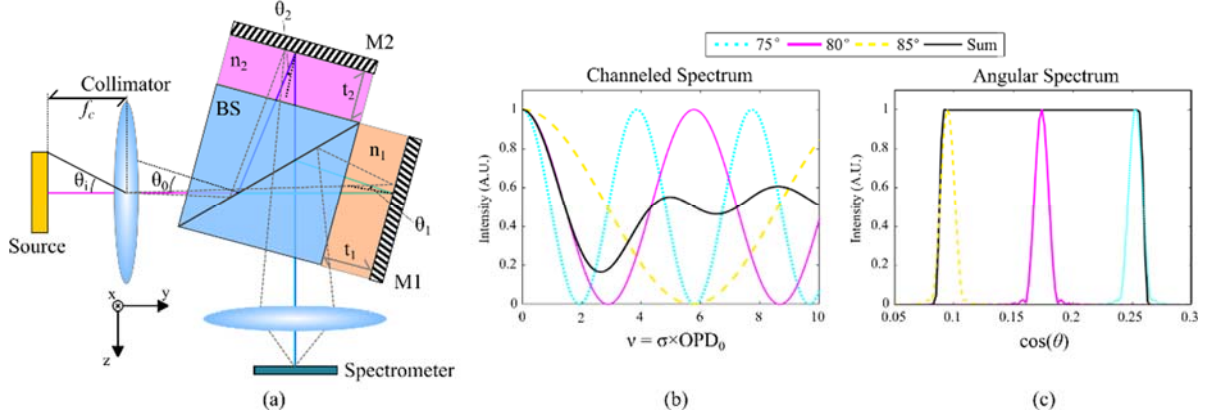


Fig. 56. (a) Michelson interferometer configured to measure the angular spectrum of a uniform source. (b) Spectrally resolved interference pattern, measured on the spectrometer, as a function of a measurement variable v that depends on wavenumber σ ; (c) Fourier transform of the data in (b), yielding the source's angular spectrum.

The OPD of the MI interferometer of Fig. 56 (a) may be represented as [38]

$$OPD(\sigma) = 2n_1(\sigma)t_1\cos(\theta_1) - 2n_2(\sigma)t_2\cos(\theta_2), \quad (95)$$

where θ_1 and θ_2 are the light's propagation angles inside the glass plates. Often, a MI is “field-widened” by optimizing the refractive indices in such a way as to make the interferometer less sensitive to OPD changes as a function of incidence angle. However, in the FTAS, the goal is to maximize the change in OPD versus incidence angle to maximize spatial resolution. To quantify this, the interference pattern can be calculated assuming $n_1 = n_2 = 1$ such that $\theta_i + \theta_0 = \theta_1 = \theta_2$ and

$$OPD(\theta) = 2(t_1 - t_2)\cos(\theta) = OPD_0\cos(\theta), \quad (96)$$

where $\theta = \theta_i + \theta_0$ and OPD_0 is the MI's optical path difference at normal incidence. The two beam spectrally resolved interference, calculated for a single incident planewave, can be expressed as

$$b(v, \theta_i) = \frac{A(\theta)}{2} \left\{ 1 + \cos[2\pi v(\sigma)\cos(\theta)] \right\}, \quad (97)$$

where $A(\theta)$ is the incident and offset (in angle) angular spectrum and,

$$v(\sigma) = \sigma OPD_0. \quad (98)$$

In this case, the Fourier transform variable of the incident angular spectrum is a dimensionless quantity v . Note that for a MI with $n_1 = n_2 = 1$, the OPD is constant versus wavenumber. However, the quantity v still spans a range of values from $v = 0$ at $\sigma = 0 \text{ m}^{-1}$ to some maximum value v_{\max} at σ_{\max} . A depiction of a channeled spectrum, which was simulated with $OPD_0 = 4.0 \mu\text{m}$ for wavenumbers spanning $\sigma = 0 \text{ cm}^{-1}$ to 25000 cm^{-1} , is illustrated in Fig. 56 (b). Fourier transformation of Eq. (97), taken with respect to the measurement variable v , yields

$$B(q) = \frac{A(\theta)}{2} \left\{ \delta(q) + \frac{1}{2} \delta[q - \cos(\theta)] + \frac{1}{2} \delta[q + \cos(\theta)] \right\}, \quad (99)$$

where q is the transform variable. Eqns. (97) and (99) are expressed for a single incident plane wave component. For a superposition of plane waves given an arbitrary $A(\theta)$, these expressions can be represented in integral form. Additionally, the optics' spectral and angular transmission functions, the intensity of the incident power spectrum, and the detector's responsivity, can be included such that

$$b(v) = I(\sigma) \tau_p(\sigma) \rho(\sigma) \operatorname{rect}\left(\frac{v}{v_{\max}}\right) \int_{-\pi/2}^{\pi/2} \left\{ A[\arccos(q_0)] \tau_A[\arccos(q_0)] * \left\{ 1 + \cos[2\pi v(\sigma) q_0] \right\} \right\} dq_0, \quad (100)$$

where $q_0 = \cos(\theta)$ and v_{\max} is the maximum value of Eq. (98) for a particular instrument or channeled spectrum. Defining the Fourier transformation variables as $v(\sigma)$ (unitless) and q (reciprocal space) yields the Fourier transformation of Eq. (13) as

$$B(q) = \int_{-\pi/2}^{\pi/2} \left\{ A[\arccos(q_0)] \tau_A[\arccos(q_0)] \left[\delta(q) + \frac{1}{2} \delta(q - q_0) + \frac{1}{2} \delta(q + q_0) \right] * \operatorname{sinc}(v_{\max} q) * \mathcal{F}\left[g\left(\frac{v}{OPD_0}\right)\right] \right\} dq_0, \quad (101)$$

where

$$g\left(\frac{v}{OPD_0}\right) = I\left(\frac{v}{OPD_0}\right) \tau_p\left(\frac{v}{OPD_0}\right) \rho\left(\frac{v}{OPD_0}\right), \quad (102)$$

is the source's power spectrum, optics' transmittance, and detector responsivity contributions. Similar to the previous spatial modulation across the FTPS's mirrors, if either I , τ , or ρ have angular frequencies that overlap with $A(\theta)$, then crosstalk can occur between the measured angular spectrum and these power spectrum terms. Ultimately, in a similar process to Refs. [39,40] for channeled spectropolarimetry, these contributions can be measured separately and accounted for to remove crosstalk. Finally, the angular transmittance of the system $\tau_A(\theta)$ is multiplicative with the incident power spectrum, and behave similarly to the spectral transmittance term in the FTPS.

Since the frequency of the channeled spectrum components are linear with $\cos(\theta)$, Eq. (101) demonstrates that the angular spectrum component corresponding to $A(\theta)$ will be located in the reciprocal space at a position equal to $\cos(\theta)$. A view of this is provided in Fig. 56 (c), which illustrates that the Fourier transformation of a channeled spectrum, taken with respect to v , with $OPD_0 = 4.0 \mu\text{m}$ and wavenumbers spanning $\sigma = 0 \text{ cm}^{-1}$ to 25000 cm^{-1} . To properly configure the frequency axis, the inverse cosine must be taken of q . Finally, the interferometer's angular offset θ_0 should be subtracted to properly relate incident angles to object space angles.

Similar to an FTPS, the angular resolution of the FTAS can be related by the Fourier transform relationship between the windowing function in Eq. (13) and the Fourier transform's output in Eq. (101). From the convolved sinc function, the full width angular resolution is related to

$$\Delta q = 1/v_{\max}. \quad (103)$$

Relating this to the angular resolution in object space can be achieved by substituting the value of q such that

$$\Delta q = \sin(\theta) \Delta \theta = 1/v_{\max}. \quad (104)$$

The angular resolution is equal to

$$\Delta \theta = [v_{\max} \sin(\theta)]^{-1}. \quad (105)$$

For the MI described previously, assuming a system in air

$$v_{\max} = \sigma_{\max} OPD_0, \quad (106)$$

and therefore

$$\Delta \theta = [\sigma_{\max} OPD_0 \sin(\theta)]^{-1}. \quad (107)$$

Thus, the angular resolution can be increased by increasing OPD_0 , increasing the maximum wavenumber observed in the channeled spectrum, or operating the system at $\theta = \pi/2$ radians. It should be mentioned that when $\theta = \pi/2$ radians, this is most analogous to operating a Young's Double Pinhole Interferometer (YDPI) viewing linear straight-line fringes, whereas when $\theta = 0$ radians, the interference pattern is centered on Haidinger fringes.

3.2.1 Cohherence

As mentioned previously, the measurement variable v ranges from $v = 0$ to $v = v_{\max}$ over the spectral range $\sigma = 0 \text{ m}^{-1}$ to $\sigma = \sigma_{\max}$. For the MI in Fig. 1 (a), the OPD is constant versus wavenumber, thus v is linear with respect to wavenumber over the spectral range of the optical system. In this situation, the region of maximum coherence for which the unique spectral frequencies of the individual incident angles are in phase occurs at $v = 0$ ($\sigma = 0 \text{ m}^{-1}$). This is illustrated by the simulation of a MI channeled spectrum in Fig. 57.

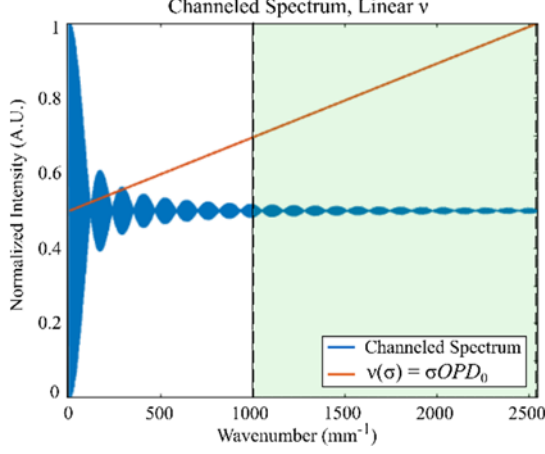


Fig. 57. Channeled spectrum simulated for MI with linear v (red line) relationship, illustrating low coherence in the detectable region of the spectrum (green shading).

The channeled spectrum in Fig. 57 was simulated from $\sigma = 0 \text{ mm}^{-1}$ to $\sigma = 2875 \text{ mm}^{-1}$ for a MI with an $OPD_0 = 200 \mu\text{m}$. The angular spectrum is a uniform one-dimensional source with a field of view (FOV) from $\theta = 43^\circ$ to $\theta = 47^\circ$. Maximum coherence occurs at $\sigma = 0 \text{ mm}^{-1}$, however, in the detectable region of the spectrum represented by green shading (*e.g.* responsivity of a silicon detector), the measured fringe contrast in the channeled spectrum is minimal. To remedy this situation by heterodyning coherence to the measurable region of the spectrum, our technique modulates the incident angular spectrum with a fixed spatial carrier before directing the light into the interferometer. The configuration required for this is provided in Fig. 58, in which a digital light projector (DLP) based spatial light modulator (SLM) is positioned in front of the FTAS. Light from an arbitrary object's angular spectrum is first relayed onto an SLM with a 1:1 afocal relay for simplicity. The SLM's transmittance is configured to be a chirped sinusoidal angular spectrum such that

$$\tau_s(\theta) = \frac{1}{2} + \frac{1}{2} \cos[2\pi\nu_0 q_0], \quad (108)$$

where ν_0 represents the rate of change in q_0 . It should be mentioned that for small tilt angles θ_0 , the angular spectrum defined by Eq. (108) is highly chirped (as with Haidinger fringes), and approaches a constant frequency for larger values of θ_0 (as with YDPI fringes). Light transmitted by the SLM is then incident into the rest of the previously described MI through a collimator lens of focal length f , such that the ratio between object space and the interferometer's angles remains 1:1 for simplicity.

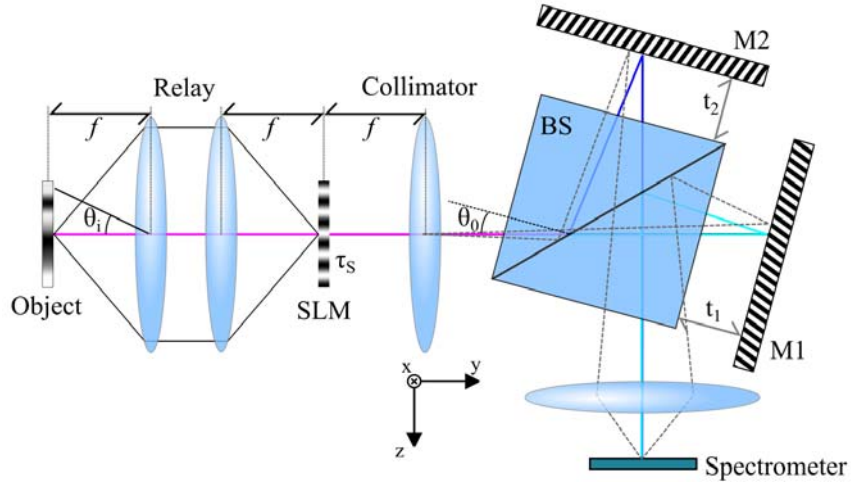


Fig. 58. FTAS which relays an arbitrary object's angular spectrum onto an SLM with transmittance τ_s . Light is then collimated into the tilted MI, where the spectrally resolved interference is detected using a spectrometer.

The SLM's transmittance can be included directly in Eq. (13) as a part of the angular transmittance τ_A as

$$\tau_A(\theta) = \tau_O(\theta)\tau_S(\theta), \quad (109)$$

where τ_O is the angular transmittance of the lenses, BS, and other optics in the system and are generally of low angular frequency. Given this, assuming τ_O is constant yields the detected current as

$$b(\nu) = I(\sigma)\tau_P(\sigma)\rho(\sigma)\text{rect}\left(\frac{\nu}{\nu_{\max}}\right) \int_{-\pi/2}^{\pi/2} \left\{ A[\arccos(q_0)]\tau_s[\arccos(q_0)] * \left\{ 1 + \cos[2\pi\nu(\sigma)q_0] \right\} \right\} dq_0. \quad (110)$$

Substituting τ_s into the integral yields

$$b(\nu) = \Gamma \int_{-\pi/2}^{\pi/2} \frac{A[\arccos(q_0)]}{4} [1 + \cos(2\pi\nu_0 q_0)] \{1 + \cos[2\pi\nu(\sigma)q_0]\} dq_0, \quad (111)$$

where

$$\Gamma = I(\sigma)\tau_P(\sigma)\rho(\sigma)\text{rect}\left(\frac{\nu}{\nu_{\max}}\right). \quad (112)$$

Expanding yields

$$b(\nu) = \frac{\Gamma}{4} \int_{-\pi/2}^{\pi/2} A[\arccos(q_0)] \left\{ \begin{aligned} & 2 + 2\cos(2\pi\nu_0 q_0) + 2\cos[2\pi\nu(\sigma)q_0] \\ & + \cos\{2\pi q_0 [\nu(\sigma) - \nu_0]\} + \cos\{2\pi q_0 [\nu(\sigma) + \nu_0]\} \end{aligned} \right\} dq_0. \quad (113)$$

From this result, there exists a sum and difference term which re-localizes the coherence maximum, with reduced contrast, at $\nu = \pm v_0$. Provided the value of v_0 is selected such that this secondary coherence exists within the desired spectral passband, the angular spectrum can be measured and reconstructed. For a given wavenumber of secondary coherence, σ_m , the spatial frequency term must be selected such that

$$v_0 = \sigma_m OPD_0. \quad (114)$$

To further discuss how v_0 allows access to the information contained within the incident angular spectrum, a simulation of Eq. (113) was conducted for $OPD_0 = 200 \mu\text{m}$, wavenumbers spanning $\sigma = 0 \text{ mm}^{-1}$ to $\sigma = 2857 \text{ mm}^{-1}$, incidence angles θ spanning 75° to 85° , and a secondary coherence wavenumber $\sigma_m = 1751 \text{ mm}^{-1}$ ($\lambda = 571 \text{ nm}$). For this value of σ_m , Eq. (114) yields $v_0 = 350$. A depiction of the channeled spectrum for these specifications is illustrated in Fig. 59 (a) for $A[\arccos(q_0)] = 1$. In this figure, the spectrometer's spectral responsivity $\rho(\sigma)$ is assumed to have non-zero values for wavenumbers spanning $\sigma = 1000 \text{ mm}^{-1}$ to $\sigma = 2500 \text{ mm}^{-1}$ (λ spanning 1000 to 400 nm). Thus, the responsivity acts as a windowing filter, only permitting a certain region of the channeled spectrum to be sampled within the immediate vicinity of v_0 .

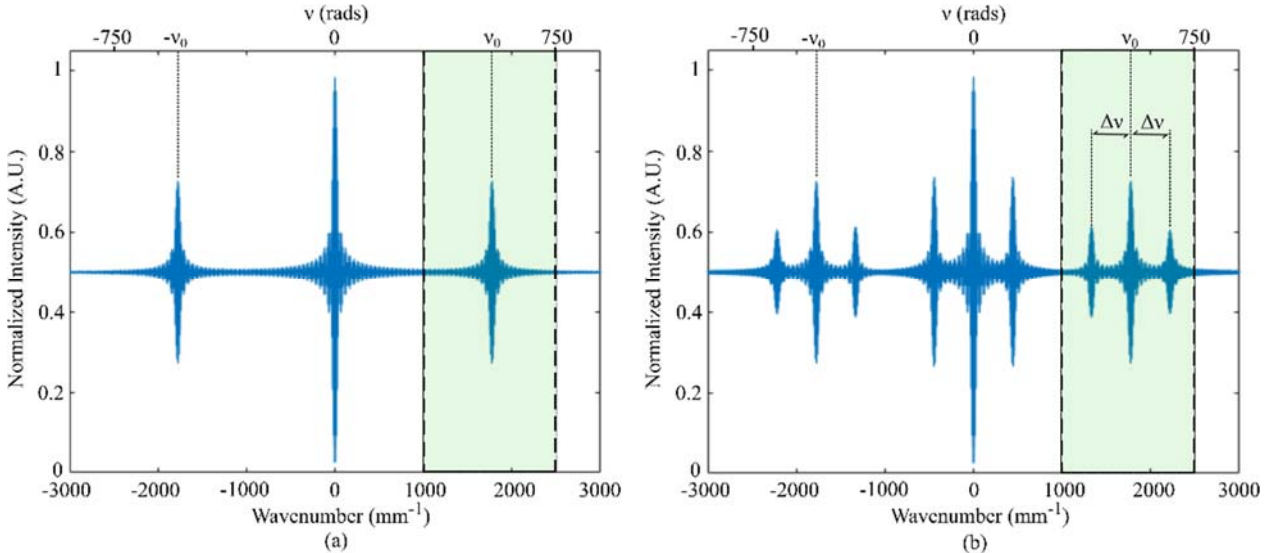


Fig. 59. Channeled spectrum for wavenumbers spanning 0 mm^{-1} ($\lambda = \infty \text{ nm}$) to 2857 mm^{-1} ($\lambda = 350 \text{ nm}$). The highlighted region signifies wavenumbers spanning 1000 to 2500 mm^{-1} (λ spanning 1000 to 400 nm). Measurement of (a) the cosine carrier frequency v_0 and (b) an additional modulation on v_0 with a frequency Δv .

Simulating now a non-uniform angular spectrum with a single frequency component yields

$$A[\arccos(q_0)] = \frac{1}{2} + \frac{1}{2} \cos(2\pi\Delta\nu q_0), \quad (115)$$

where $\Delta\nu$ is the envelope's rate of change on the carrier defined by frequency v_0 previously. Substituting Eq. (115) into Eq. (113) for $\Delta\nu = 100$ yields the channeled spectrum depicted in Fig. 59 (b). The addition of this new frequency component expresses itself as an additional 'channel' within the spectrum, centered about both the primary carrier at $v = 0$ and the secondary carriers at $v = \pm v_0$. Since the spectrometer already behaves as a rectangular windowing filter for the $v = -v_0$

component, the detected channeled spectrum b_D only contains the carrier plus its side bands such that

$$b_D(\nu) = \frac{\Gamma}{4} \int_{-\pi/2}^{\pi/2} A[\arccos(q_0)] \left\{ 2 + 2 \cos(2\pi\nu_0 q_0) + \cos[2\pi q_0(\nu(\sigma) - \nu_0)] \right\} dq_0, \quad (116)$$

where it is assumed that $\rho(\sigma)$ in Γ has

$$\begin{aligned} 0 < \rho(\sigma) &\leq 1; \quad 1000 \leq \sigma \leq 2500, \\ \rho(\sigma) &= 0; \quad 1000 > \sigma \text{ and } \sigma > 2500. \end{aligned} \quad (117)$$

Mapping $\nu = 0$ at σ_m yields the demodulated sampling axis such that

$$\nu'(\sigma) = (\sigma - \sigma_m) OPD_0 = \nu(\sigma) - \nu_0. \quad (118)$$

Substituting Eq. (118) into Eq. (116) and taking the Fourier transformation with respect to $\nu'(\sigma)$ yields

$$B_D(q) = \int_{-\pi/2}^{\pi/2} \left\{ A[\arccos(q_0)] \left\{ [1 + 2 \cos(2\pi\nu_0 q_0)] \delta(q) + \frac{1}{2} \delta(q - q_0) + \frac{1}{2} \delta(q + q_0) \right\} \right. \right. \\ \left. \left. * \text{sinc}(\nu_{\max} q) * F\left[g\left(\frac{\nu}{OPD_0}\right)\right] \right\} dq_0. \quad (119) \right.$$

This makes the Fourier transformation of the demodulated channel per Eq. (116) equal to the transformation illustrated previously in Eq. (101) with the exception of a larger magnitude component at $q = 0$. This is a consequence of the channels' reduced contrast compared to the original component.

3.2.2 Spectrally Resolved Longitudinal Spatial Coherence Interferometry

To advance the technique of longitudinal spatial coherence interferometry, we use a spectrometer to spectrally resolve the output of an interferometer. To demonstrate this concept, an example taken from Ref. [31] is used, in which the researchers controlled longitudinal coherence by manipulating the source profile to determine the mirror displacement in a MI. This was accomplished by using a spatial light modulator to generate a quasi-monochromatic extended source in the form of a Fresnel zone plate (FZP), given by intensity distribution

$$I_{FZP}(r) = \left(\frac{1}{2} \right) \left[1 + \cos(2\pi\gamma r^2 + \beta) \right], \text{ where} \quad (120)$$

$$\gamma = \frac{\Delta z}{\lambda_0 f^2}, \text{ and} \quad (121)$$

$$\beta = \frac{4\pi\Delta z}{\lambda_0}. \quad (122)$$

Here, r is used to define the radius along the circular source, f is the focal length of the collimating lens, and Δz is the path displacement along the propagation axis between the two mirrors in a MI. Note that Δz is related to the previously defined OPD_0 by $OPD_0 = 2\Delta z$, due to the double pass in the MI. From Eq. (120), a spatially incoherent source illuminating the FZP would produce high coherence peaks at the optical path differences $2\Delta z = 0, \pm 2\lambda f^2 \gamma_0$. Simulating the FZP for $\lambda_0 = 633$ nm, $f = 300$ mm, and an optical displacement of $\Delta z = 2.0$ mm indeed shows visibility peaks located at their corresponding locations as shown in Fig. 60 (a). In other words, high contrast fringes would be recorded using a CCD for $\lambda_0 = 633$ nm when the mirrors are displaced by $\Delta z = 2$ mm.

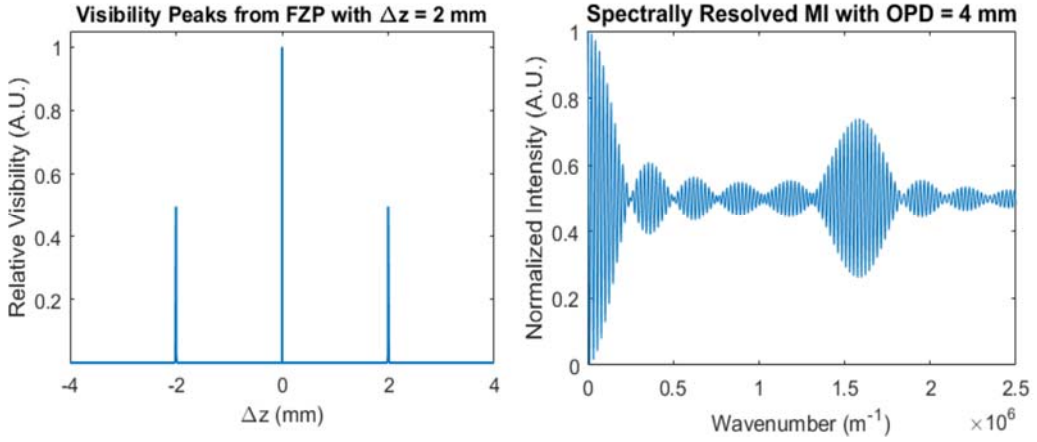


Fig. 60. (a) Visibility peaks simulated for a FZP designed for $\lambda_0 = 633$ nm and high coherence at $\Delta z = 2$ mm. (b) Simulated spectrally resolved channeled spectrum for $2\Delta z = 4$ mm.

To simulate the spectrally resolved output of the MI, we define the variable $v(\sigma)$ from Eq. (98) in terms of the FZP parameters such that

$$v(\sigma) = \sigma OPD_0 = \sigma(2\lambda_0 f^2 \gamma). \quad (123)$$

In this way, the linear phase term $v(\sigma)$ will be coherently matched for $\lambda_0 = 633$ nm ($\sigma_0 = 1.579E6$ m $^{-1}$) to the FZP source and thus, the monochromatic Haidinger fringes of the MI. The channeled spectrum in Fig. 60 (b) generated from $\sigma_0 = 0$ m $^{-1}$ to $\sigma_0 = 2.5E6$ m $^{-1}$ using Eq. (111) assumes a uniform power spectrum, with $A(\theta)$ being defined by Eq. (120) for $\Delta z = 2$ mm. The simulation samples the FZP source angular spectrum across a 3 mm slit at an incident angle of $\theta_0 = 12^\circ$. Evident from Fig. 60 (b) is the region of coherence located at the designed wavenumber $\sigma_0 = 1.579E6$ m $^{-1}$. Noting that the secondary coherence peak in the channeled spectrum is analogous to the two side visibility peaks of FZP in Fig. 60 (a). Thus, by spectrally resolving the output of the interferometer it is possible to determine the longitudinal coherence in a snapshot measurement, without modulating the source's spatial profile.

3.3 Experimental Setup

Any interferometer that has an angularly dependent interference effect can be used to modulate the angular spectrum onto its incident power spectrum in this fashion. However, some interferometers are mechanically easier to interface to than others. Consider the spatial resolution of the FTAS per Eq. (107). This resolution can be maximized when $\theta_0 = \pi/2$ rad. In this case, we are close to the maximum slope of the cosine given in Eq. (96). Additionally, the frequency of the

channeled spectrum's oscillations is also a minimum when $\theta_0 = \pi/2$ rad for a given OPD_0 , meaning a spectrometer with a lower spectral resolution is required to resolve the channeled spectrum.

Initially, we implemented a version of the MI, depicted previously, to perform our experimental validations [41]. However, due to the aforementioned reasons – primarily the requirement for high spectral resolution (and thus, signal intensity) – we opted to implement a Fabry Perot Etalon (FPE) multiple-beam interferometer. The parameters of the FPE were selected such that it approximated a two-beam interferometer, with most of the power contained exclusively within the first order. A schematic of the interferometer's configuration is depicted in Fig. 61 (a). A Texas Instruments DLP LightCrafter Evaluation Module is illuminated by a xenon arc lamp through a series of three mirrors (M1 through M3). These mirrors optimally couple the light into the DLP-based SLM, which contains the angular spectrum under measurement. Reflected light is then collimated by a collimation lens (50 mm focal length) into a two-mirror (M4 and M5) FPE, which consists of two 10:90 (R:T) dielectric plate beamsplitters from Thorlabs (BSN16) with reflectance magnitudes of R_1 and R_2 , respectively. Mirror M4 is placed on a translation stage, which allows tuning the etalon's thickness t . An objective lens (50 mm focal length) focuses the FPE's reflected light onto a ground glass diffuser and integrating rod, where the spatial information is homogenized. Homogenization ensures both a uniform spatial and spectral angular spectrum across the measured beam, which is often inhomogeneous due to diffraction from the SLM. Finally, the light is measured by a spectrometer at the homogenized output. A photo of the experimental setup is presented in Fig. 61 (b).

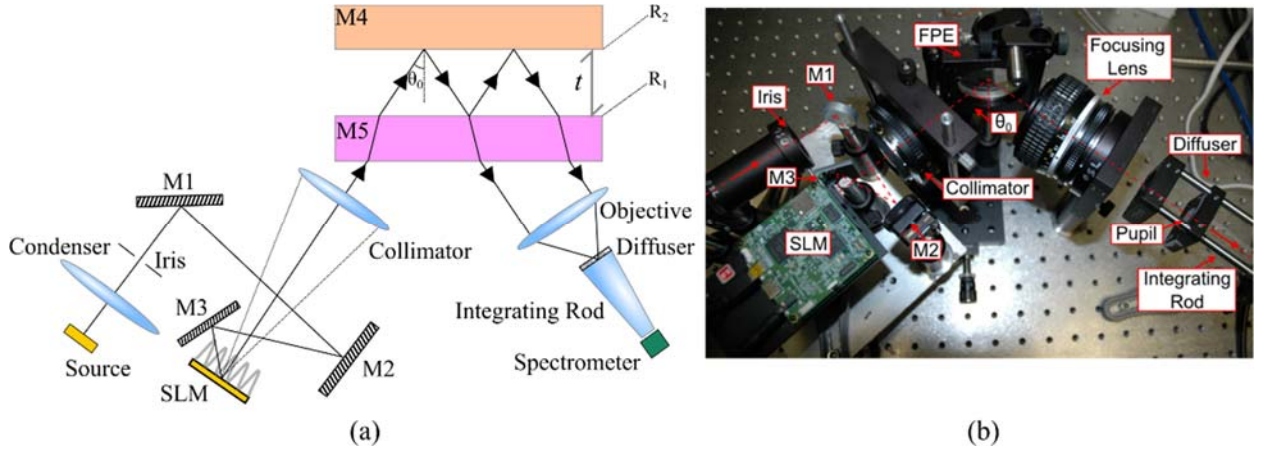


Fig. 61. (a) Schematic of the experimental configuration for the FPE-based interferometer; (b) photo of the setup on the benchtop.

The spectrometer that was implemented for measuring the channeled spectra is illustrated in Fig. 62 (a). Light from the output fiber illuminates a 20 μm slit, which is then collimated by a 50 mm focal length Nikon Nikkor F/1.8D lens. Collimated light from the slit illuminates a 1200 lines/mm diffraction grating (Thorlabs GR50-1205) placed on a rotating platform which enables tilt control within the xz plane. Diffracted light is then imaged by an 85 mm focal length Nikon Nikkor F/1.8D objective lens onto a Thorlabs LC1-USB 3,000 pixel linear silicon CCD array. By rotating the grating in the xz plane, the measured spectral band can be changed to coincide with the measured channeled spectra. This spectrometer was calibrated using known spectral lines within low pressure mercury and oxygen gas discharge lamps. All experimental data were acquired across wavelengths spanning 515–652 nm at a spectral resolution of $\Delta\lambda \sim 0.06$ nm.

Measurements of the channeled spectra were acquired using the Thorlabs *SPLICCO* GUI and were calibrated in *MATLAB*.

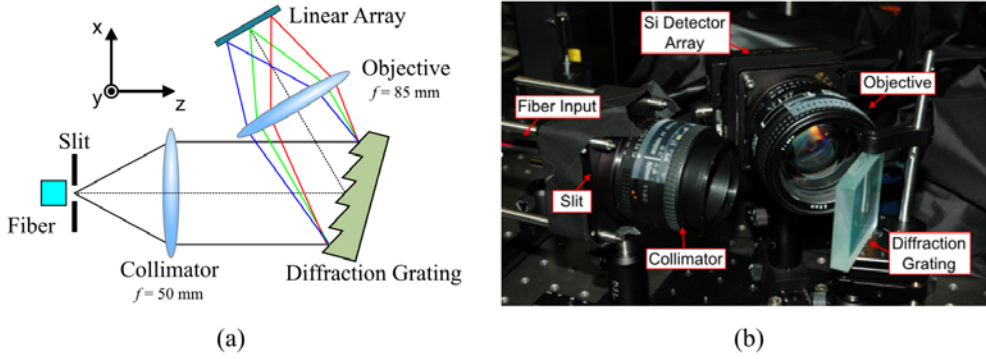


Fig. 62. (a) Schematic of the spectrometer that was used for our experiments; (b) photo of the spectrometer on the benchtop.

3.3.1 FPE Simulation

Using data available from Thorlabs, the FPE's reflectance was calculated [42]. The results of this calculation are illustrated in Fig. 63 (a) for a thickness $t = 14 \mu\text{m}$ and an angle of incidence $\theta_0 = 52^\circ$. Additionally, the coating's reflectance, provided by the manufacturer, is also illustrated for reference. Fourier transformation of these reflectance spectra, calculated for a cavity thickness $t = 100 \mu\text{m}$ and incidence angle of $\theta_0 = 52^\circ$, demonstrates that the first order resonance has a magnitude 5 times higher than the second. Additionally, since the FTAS is operated at channeled spectrum frequencies close to the resolution of the spectrometer, these higher order effects are not observed in the spectra.

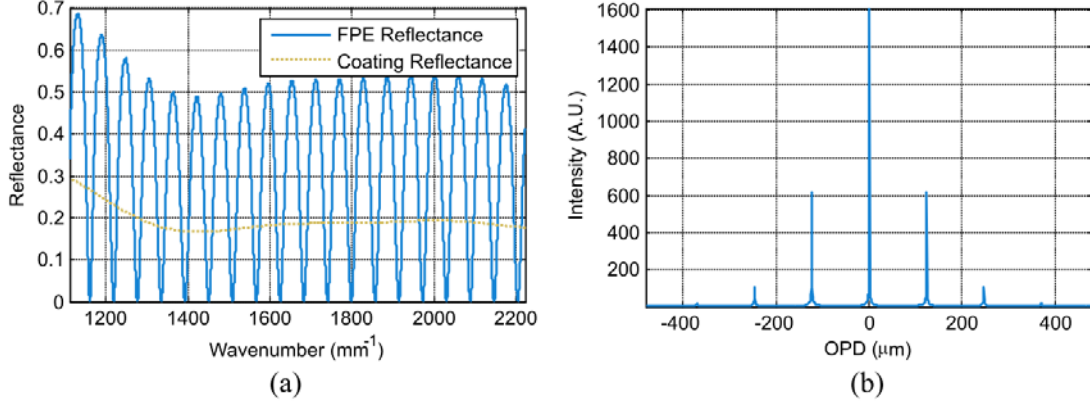


Fig. 63. (a) Calculation of FPE reflectance vs. wavelength (solid blue line), for $t = 14 \mu\text{m}$ and an angle of incidence of 52° , and the coating reflectance (dashed orange line), as obtained from Thorlabs at an incidence angle of 45° [0]. (b) Fourier transform of the FPE reflectance spectrum of (a), but for a $t = 100 \mu\text{m}$ cavity.

3.4 Alignment of Fabry-Perot Etalon System

High contrast of the channeled spectra's fringes is essential to maintain high signal to noise ratio (SNR) after Fourier transformation. To optimize contrast, an alignment procedure was developed. The central purpose of this procedure is to maximize the centerburst's coherence at a single wavelength within the spectrometer's spectral passband. This was achieved by tuning the etalon's

thickness, such that the observed Haidinger fringes are coherently matched to the SLM's carrier frequency.

A schematic of the alignment setup is illustrated in Fig. 64 (a). While it is similar to the experimental configuration presented in Fig. 61 (a), the xenon arc lamp and spectrometer are replaced by a neon gas discharge lamp and a camera, respectively. Light from the gas lamp illuminates the SLM along the same path as the xenon arc lamp. The SLM is loaded with the desired carrier frequency, which is collimated and transmitted through the FPE. An objective (12.5 mm focal length) focuses the reflected light onto a 648x480 pixel element CCD Array, creating an image of the illuminated SLM carrier angular spectrum superimposed onto a background of neon Haidinger fringes, which is generated by the etalon. A narrowband filter, with a 633 nm center wavelength at 3 nm full-width at half maximum spectral bandwidth, is placed before the objective such that only the fringes associated with the 632.8, 633.08, and 633.44 nm transitions of the neon gas discharge lamp are transmitted to the camera [43]. Fig. 64 (b) depicts an image, measured by the camera, of the off-axis Haidinger fringes superimposed onto the SLM's carrier frequency. Due to a difference in frequency between the carrier frequency and the monochromatic Haidinger fringes, a beat frequency is observed. In this case, the Haidinger fringes have a higher frequency than the carrier. To correct this frequency misalignment, the etalon thickness is tuned such that the Haidinger fringes align coherently with the carrier frequency. As depicted in Fig. 64 (c), the carrier frequency matches the Haidinger fringes. At this point, the channeled spectrum's maximum coherence will occur at the alignment wavelength of $\lambda \sim 633$ nm.

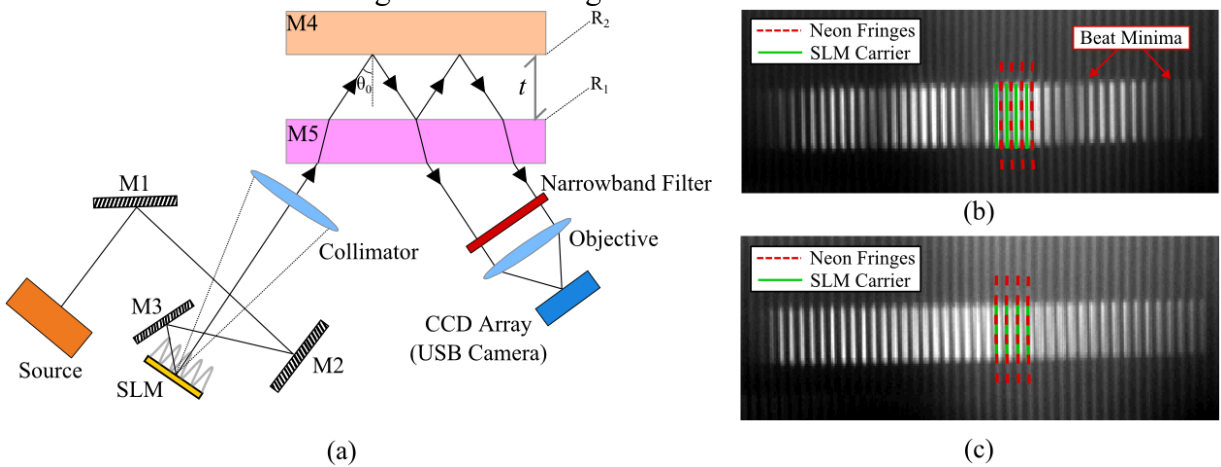


Fig. 64. (a) Schematic for FPE alignment configuration, in which the xenon arc lamp source was replaced with a low pressure neon gas discharge lamp. A camera is also used to directly observe the light from the SLM and source. (b) Image of the SLM's carrier fringe superimposed onto the fringe, observed by residual spectrally narrow band light reflected off the SLM's surface. A spatial beat frequency is observed when the FPE's thickness is not ideal. (c) Image of an aligned system. In this case, maximum coherence would occur at a wavelength equal to the neon gas lamp's filtered emission wavelength at 633 nm.

3.4.1 Alignment Procedure

The first step in the alignment procedure is to ensure that the Haidinger fringes generated by interference within the etalon are centered within the Fabry-Perot etalon. This allows for the spatial pattern of the carrier frequency to align with Haidinger fringes with the least amount of curvature. Alignment of the etalon is achieved first by using white light within the room, assuring that the double reflections of an object on the optical table overlap. Cavity alignment may then be fine tuned with a spatially incoherent monochromatic source. By placing the monochromatic source,

in our case a mercury lamp filtered to emit only the 546.1 nm line, and looking directly on through the axis normal to the etalon's front surface, the Haidinger fringes are generally visible. At this point, adjusting the tip-tilt mount will allow for the fringes to be centered along the normal axis of the etalon.

To optimize the alignment of the etalon, a USB camera is placed normal to the front beamsplitter surface and images light emitted from the monochromatic source (*e.g.* filtered mercury gas discharge lamp, $\lambda \sim 546.1$ nm) located on the opposite side of the Fabry-Perot. This allows for images of the Haidinger fringes to be acquired and the contrast of the fringes to be maximized further. The USB camera lens are adjusted such that the Haidinger fringes, located at infinity, are focused. An alignment setup and example of the imaged Haidinger fringes is depicted in Fig. 65 (a) and Fig. 65 (b), respectively.

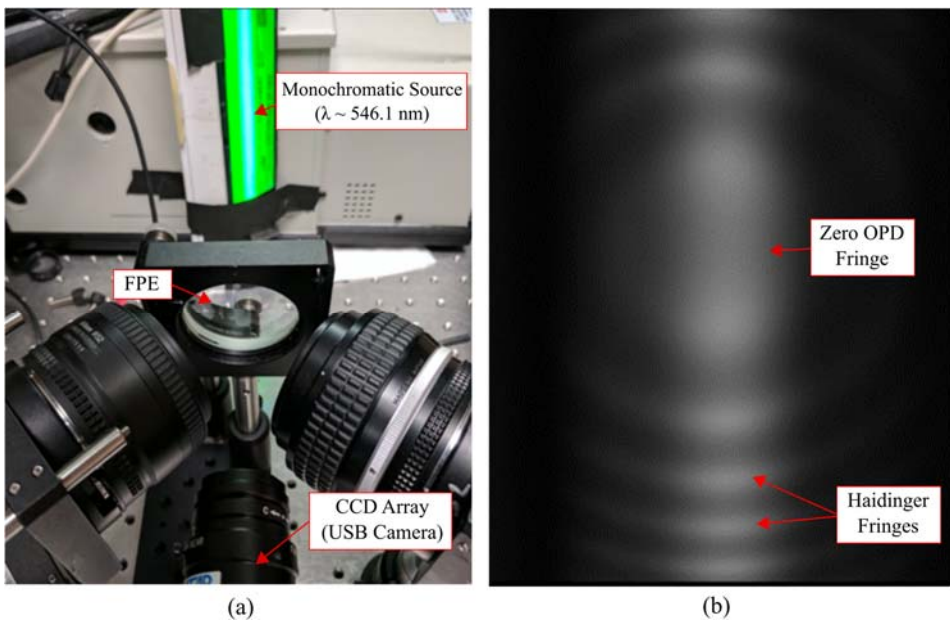


Fig. 65. (a) Setup for aligning the FPE for maximum contrast. A USB camera focused at infinity is used to image the Haidinger fringes generated by a monochromatic source. (b) Image of the Haidinger fringes generated by the etalon.

The second step in the alignment procedure is to 1) ensure collimation of the SLM pattern from the relay optics and 2) match the SLM carrier frequency to the frequency of the Haidinger fringes within the etalon. The step begins with illuminating the SLM with reflected light from a neon gas discharge lamp as shown in FIG 13.

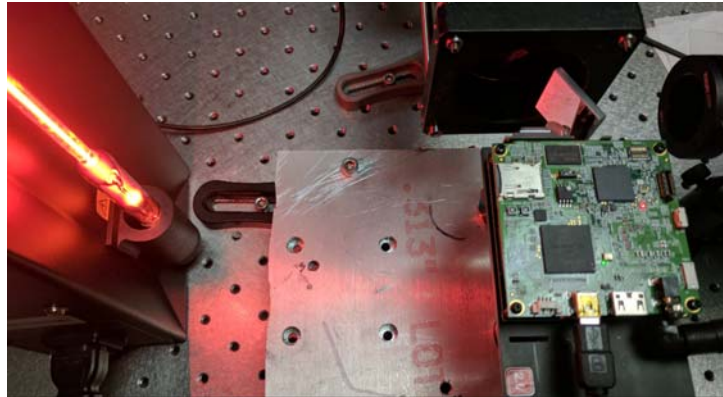


Fig. 66. Image of the illumination setup for collimation and alignment of the SLM carrier frequency to the Haidinger fringes within the etalon.

As light from the neon discharge lamp is reflected onto the SLM to illuminate the micromirror display, the first lens (Nikon F/1.8) of a 1:1 relay collimates the light, which is then focused into an intermediate image plane by a second lens. This intermediate image of the SLM carrier frequency is then collimated into the FPE. To align the carrier frequency to the Haidinger fringes within the etalon, a USB camera is placed in transmission of the interferometer to image both the SLM pattern and the etalon's fringes. The setup and example image of this is shown in FIG 4.

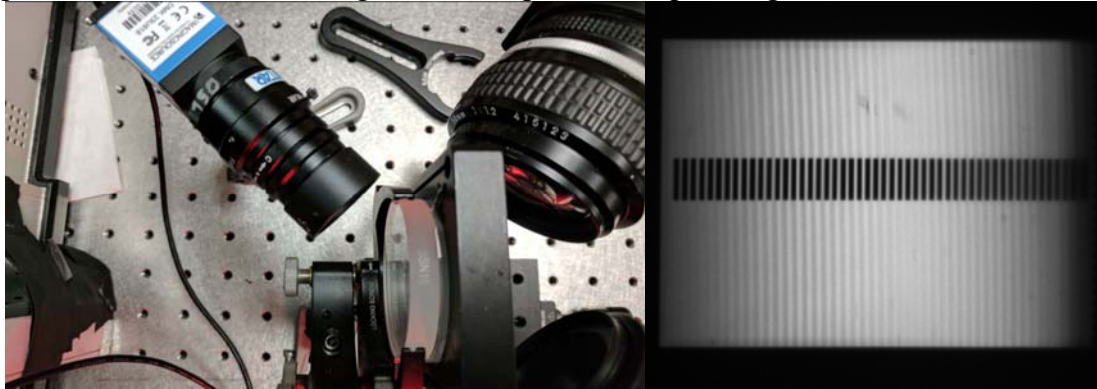


Fig. 67. Images of (left) the setup for ensuring collimation of the carrier frequency and (b) an acquired image from the SLM carrier frequency pattern superimposed on Haidinger fringes generated by monochromatic light.

For the sinusoidal and random angular spectra, *MATLAB* was used to create bitmap images which could be loaded onto the SLM. The characteristics of these angular spectra were dependent on the size of the SLM's micromirror display, dimensions of the micromirrors, angle of incidence for the center of the angular spectrum on the interferometer, and the frequency of the carrier and modulations. All angular spectra were chirped as a function of angle by sampling them linearly with respect to $\cos(\theta)$, thus compensating for the nonlinear angular frequency of the Haidinger fringes. The angular spectra were limited to a 100 pixel tall band, across the SLM's vertical axis, to eliminate complications relating to the curvature of the Haidinger fringes.

3.5 Experimental Results

3.5.1 Sinusoidal Angular Spectra

In order to quantify the angular spectra with respect to the previous model, sinusoidal envelopes were used to modulate the SLM's carrier frequency. The chirped carrier frequency has an average spatial period of $145.8 \mu\text{m}$, which corresponds to an average spatial frequency of $f_c = 6.87$ cycles/mm across the SLM. This carrier was modulated with an envelope function, which took the form of a sinusoid with a spatial frequency of $f_m = N \times f_c$, where $N \in [0.200, 0.450]$.

Measurements were conducted in increments of $\Delta N = 0.025$. A one-dimensional view of the sinusoidal angular spectra, loaded onto the SLM, are illustrated in Fig. 68. In this figure, each angular spectrum is labeled by its corresponding spatial frequency factor N .

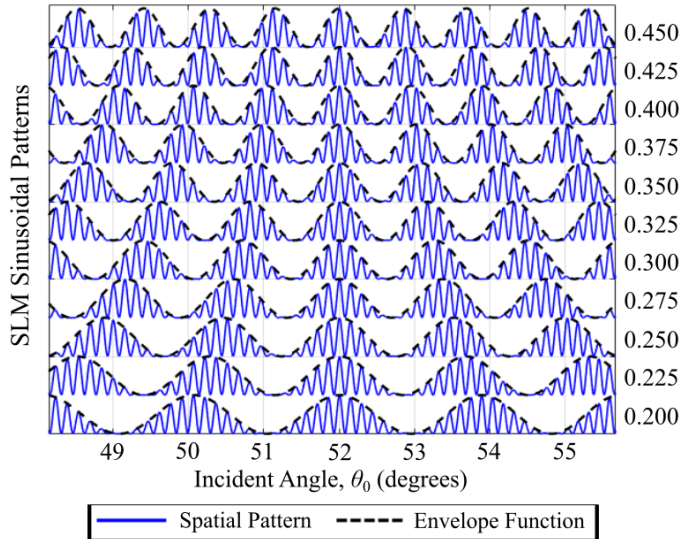


Fig. 68. Sinusoidal angular spectra that were loaded onto the SLM (solid blue line) and the associated envelope function (black dashed line) that corresponds to the spatial information being measured.

After light was reflected from the FPE, it was detected using a spectrometer ($\Delta\lambda \sim 0.06 \text{ nm}$ resolution), which measured wavelengths spanning 515-652 nm (or wavenumbers spanning $1533\text{-}1941 \text{ mm}^{-1}$). For our measurements the centerburst wavelength was set at $\lambda = 619.5 \text{ nm}$, by varying the FPE's thickness, to include both sides of the centerburst within the spectrometer's spectral range. The raw data were processed by

$$b'(\nu) = \frac{b_M(\nu) - b_D(\nu)}{b_X(\nu)}, \quad (124)$$

where b' is the processed spectrum, b_M is the measured spectrum, b_D is a dark frame, and b_X is the spectrum of the unmodulated lamp. Note that in this case, b_X acts as a spectral 'flat field' for all measurements. Filtering in the Fourier domain was used to remove additional background components in the data, which exist beyond the spatial resolution of the FPE (approximately $f_c/2$). To calibrate the measurements' ν axis, OPD_0 was calculated using Eq. (96) and a measurement of the incidence angle ($\theta_0 = 52 \pm 1^\circ$) using a protractor, as determined by the geometry of our

experimental setup. The processed channeled spectra were also normalized to the magnitude of the centerburst, $b'(0)$.

Measured channeled spectra are illustrated in Fig. 69 (a) for values of N spanning $0.200 \times f_c$ to $0.450 \times f_c$. Notable is the increased separation between the centerburst and the peak of the envelope's coherence maxima, denoted as Δv previously in Fig. 59 (b). Fourier transformation of these channeled spectra, followed by Mertz phase correction [44], yielded the results depicted in Fig. 69 (b), which illustrates the envelopes' reconstructions and those of the sinusoidal angular spectra versus the arccosine of the Fourier transform variable q . Mertz phase correction was applied to correct for asymmetries in the centerburst of the channeled spectra. Given our SLM and collimator, the incident FOV was approximately 7.52° . Despite this, only $\sim 6^\circ$ is illustrated due to errors on the edges of the FOV. These are caused by the Gibbs phenomenon, and relates to the rectangular apodization function that was used when processing the channeled spectra. Additionally, a shift in the angular spectrums' centration is evident when comparing Fig. 68 to Fig. 69 (b). Specifically, angular spectra were generated with a common phase-reference that was centered at the measured incidence angle, $\theta_0 = 52 \pm 1^\circ$. However, reconstructions appear centered near $\theta_0 = 52.6^\circ$. Since this was within experimental error, the incident angular spectra were all offset by 0.6° to align to the known center. This is analogous to offsetting the spectral axis of a spectrometer after measuring a light source with a known emission wavelength.

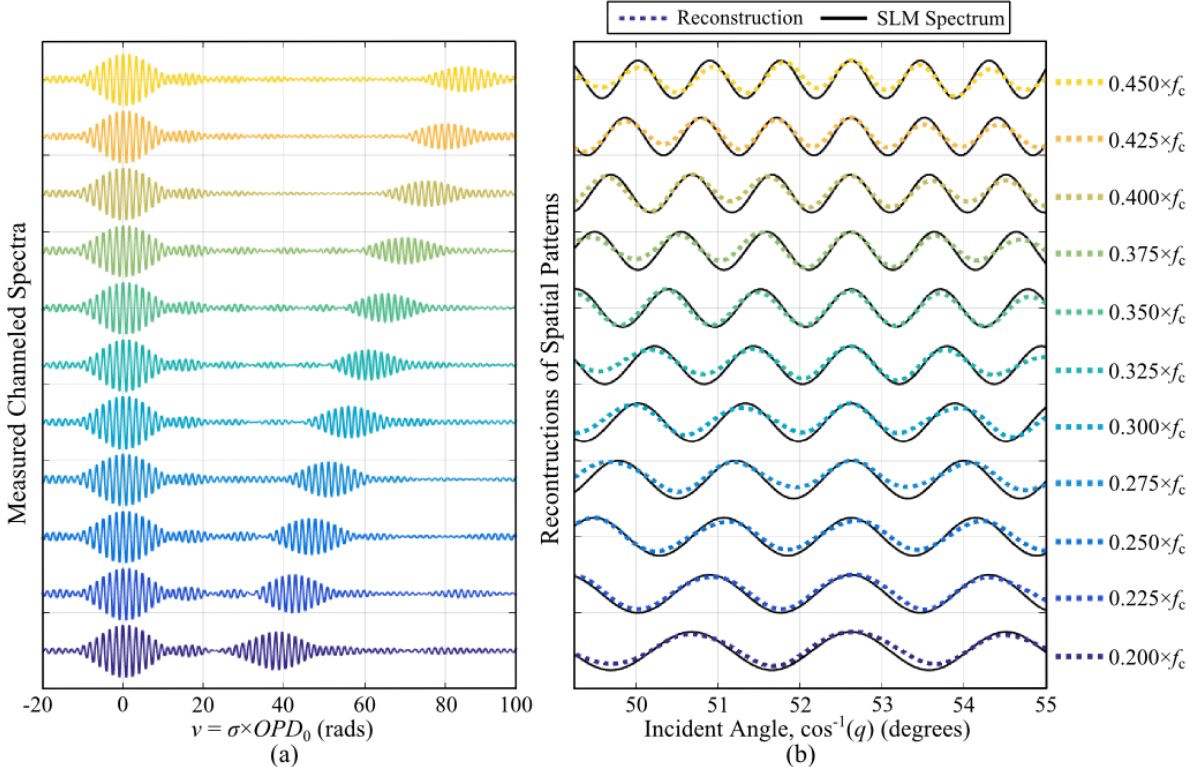


Fig. 69. Measured results. (a) Channeled spectra. The spectra are illustrated from highest to lowest spatial frequency from top to bottom. (b) The reconstructed results (dotted colored lines), after Fourier transformation and Mertz phase correction, plotted with the sinusoidal angular spectra (solid black lines).

3.5.2 Random Angular Spectra

In addition to sinusoidal angular spectra, spatially smooth, random angular spectra were also modulated onto the source's white light spectrum. Similar to the sinusoidal angular spectra, a chirped sinusoidal carrier, with an average frequency of $f_c = 6.87$ cycles/mm, was modulated with randomly generated envelopes. Random angular spectra were generated in *MATLAB* as bitmap images by interpolating 20 random points onto a spatially smooth axis across the SLM's horizontal dimension. To ensure accurate measurements, spatial frequencies within the random spectra were band-limited to a spatial frequency of 3.2 cycles/mm. 100 random spectra were generated and used for experimental validation. Fig. 70 illustrates seven of the spatially smooth, random spectra, which were randomly selected from the 100 spectra using *MATLAB*. The experimental measurements and reconstructions presented here are based on these seven random angular spectra.

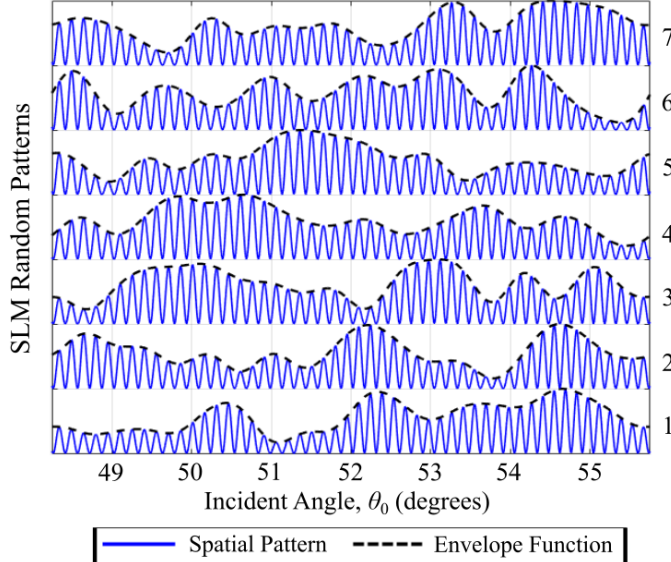


Fig. 70. Random angular spectra that were loaded onto the SLM (solid blue line) and the associated envelope function (black dashed line) that corresponds to the spatial information being measured.

Similar to the sinusoidal angular spectra presented in section 4.1, measurements of the channeled spectra for the random angular spectra were acquired using the Thorlabs *SPLICCO* program for 30 rolling averages at an integration time of 75 ms. The channeled spectra of the seven random spectra, depicted in Fig. 71 (a), were measured immediately following the measurements of the sinusoidal angular spectra to minimize any environmental variations (*e.g.*, vibration and temperature) in the etalon's thickness between experiments. An additional measurement of the carrier frequency was taken after every tenth measurement to ensure that the centerburst did not drift significantly from $v = 0$.

Fourier transformation of the channeled spectra, with Mertz phase correction, produced the results presented in Fig. 71 (b), which plots the random envelope reconstructions alongside the SLM's input. Since the random angular spectra are not limited to a single modulation frequency, as in the previous sinusoidal case, the measured channeled spectra from Fig. 71 (a) contains an arbitrary envelope. Fourier transformation, followed by Mertz phase correction, yielded the angular spectra per Fig. 71 (b). Visually comparing the reconstructed envelopes and the random SLM angular spectra demonstrates that prominent peaks and valleys are recovered after Fourier transformation.

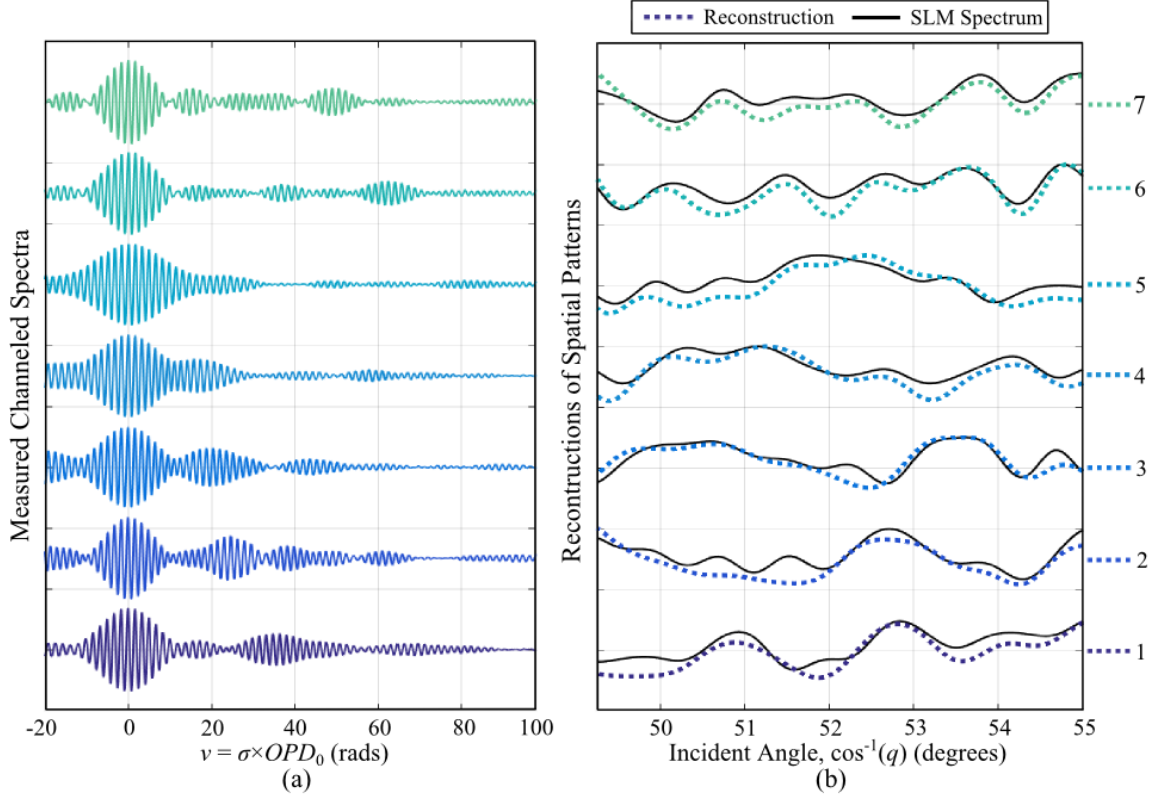


Fig. 71. Measured results for random spectra. (a) Channeled spectra. The spectra were randomly selected from an experiment containing 100 different random spectra. (b) The reconstructed results (dotted colored lines), after Fourier transformation and Mertz phase correction, plotted with the randomly generated angular spectra (solid black lines).

3.5.3 Error Analysis

To quantify the system's accuracy, the root-mean-square (RMS) error was calculated for both the sinusoidal and random angular spectra. The method used calculates error between the reconstructions and the SLM's angular spectra over the field of view $\theta_0 \in [50.0^\circ, 55.0^\circ]$. This range was determined based on the carrier frequency's uniformity. Additionally, RMS error was calculated after removing the aforementioned 0.6° offset between the measured and incident angular spectra by

$$RMS = \sqrt{\frac{\sum_{m=1}^M (\hat{y} - y)^2}{M}}, \quad (125)$$

where M is the number of samples across the field of view (*i.e.* 455 samples over the range $\theta_0 \in [50.0^\circ, 55.0^\circ]$) and \hat{y}, y represent the normalized values for the reconstruction and SLM's angular spectra, respectively.

Fig. 72 (a) depicts the RMS error of the sinusoidal angular spectra for each modulation frequency factor N from Fig. 69 (b). RMS errors range from 0.082 to 0.157, with a mean of 0.127. Meanwhile, Fig. 72 (b) depicts the RMS error of each of the 7 random angular spectra depicted previously in Fig. 71 (b). RMS error calculations between the reconstruction of the random envelopes and their corresponding SLM spectra range from 0.096 to 0.153, with a mean

of 0.123 for the seven randomly selected spectra presented here. Across the entire sample population of 100 random spectra, the minimum error was 0.075 and the maximum was 0.235, with a mean value of 0.136.

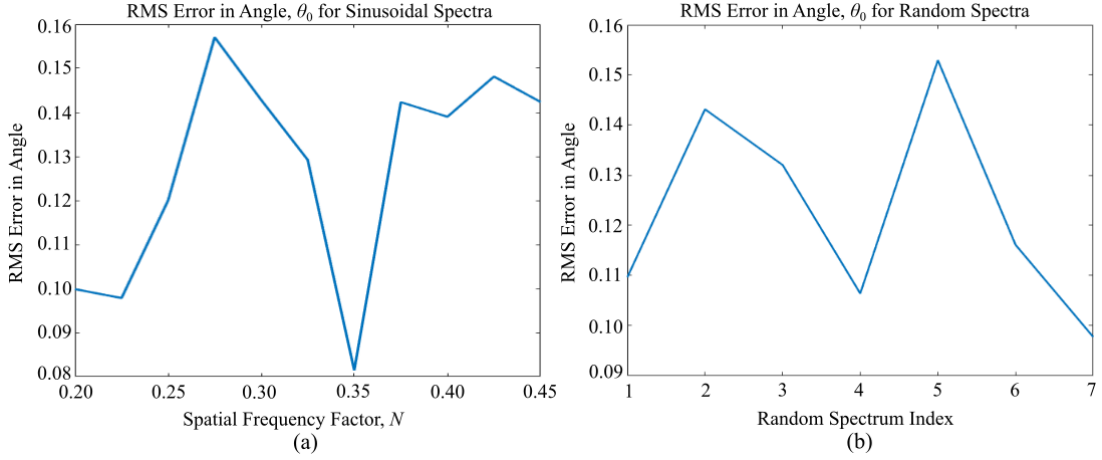


Fig. 72. (a) RMS error versus spatial frequency factor N for the sinusoidal angular spectra and (b) (a) RMS error versus spectrum index for the band-limited random angular spectra.

It is expected that higher RMS errors, such as the peak at $N = 0.275$ in Fig. 72 (a), are primarily related to changes in the etalon's thickness between measurements. While precautions were taken to reduce vibrations by mechanically coupling the two mirrors of the etalon, there were still residual vibrations present in the environment. From observing gas discharge interference fringes (see Fig. 64) we estimate that the residual vibration caused random variations in the cavity's thickness of approximately 0.06 microns. Despite this, the RMS error does not increase significantly over time, where index 1 of the random angular spectra corresponds to the 16th measurement and index 7 to the 91st measurement. We may therefore infer that even if there are variations in the etalon's thickness from one measurement to the next, the etalon remained in a similar state across all 100 random measurements (~ 275 seconds total, with spectra uploading and saving). Additional error sources could come from the optical coupling between the SLM and FPE. This was achieved using the 50 mm focal length commercially available lens from Nikon. The modulation transfer function (MTF) of this lens was not deconvolved from the measured data before calculating the RMS error. Despite this, the predominant features within the input and output angular spectra are still evident.

3.5.4 6.4 Angular Resolution Analysis

The angular resolution for the FTAS is set by the maximum phase, v_{\max} , within the interferometer. This is analogous to how the windowing function created by maximum OPD sets the spectral resolution for conventional FTS. From the Fourier transform relationship in equation (107), the theoretical maximum angular resolution in object space for the system is

$$\Delta\theta = \frac{1}{v_{\max} \sin(\theta)} = 1.87 \text{ mrad} = 0.107^\circ, \quad (126)$$

for $v_{\max} = \sigma_{\max} OPD_0 = 584.4$, with $\sigma_{\max} = 1942 \text{ mm}^{-1}$ ($\lambda_{\min} = 515 \text{ nm}$) and $OPD_0 = 301 \mu\text{m}$. The angular resolution was calculated for the center of the FOV, $\theta = \theta_0 = 52.0^\circ$. Noting that steeper incidence angles onto the interferometer increase the angular resolution of the system. The angular

resolution calculated in equation (126) corresponds to a spatial resolution of $\Delta y = 93.7 \mu\text{m}$, or 8.68 pixels across the SLM with a $10.8 \mu\text{m}$ mirror pitch.

In practice, the angular resolution of the FTAS is limited by the spectral range of the detector. Though the maximum wavenumber sets the theoretical angular resolution, we observe from Fig. 69 (a) that channels containing information with higher spatial frequencies (*i.e.* larger Δv) shift outside of the spectral region of detection. For the system presented in this paper, the spectral region from 515-652 nm creates a maximum angular resolution more in line with

$$\Delta\theta_{\text{system}} = \frac{1}{\Delta v_{\text{spec}} \sin(\theta)} = 8.90 \text{ mrad} = 0.51^\circ, \quad (127)$$

where $\Delta v_{\text{spec}} = (\sigma_{\text{max}} - \sigma_{\text{min}})OPD_0 = 123.0$ is the rectangular window which defines the resolution of the system.

From the reconstructions of sinusoidal angular spectra in Fig. 69 (b), the system is able to recover one period of the sinusoidal target with the highest spatial frequency ($f_m = 0.450 \times f_c$) at an angular subtense of $\Delta\theta_{\text{SLM}} = 15.0 \text{ mrad}$, corresponding to 69.5 pixels on the SLM. However, in the reconstruction of angular spectra in Fig. 71 (b), the angular spectrum corresponding to the second channeled spectrum fails to recover the two peaks around $\theta = 51^\circ$. Upon inspection, the adjacent peaks subtend angles $\Delta\theta_{\text{SLM}} = 13.8 \text{ mrad}$ and $\Delta\theta_{\text{SLM}} = 14.3 \text{ mrad}$, respectively, implying experimental system resolution is $\Delta\theta_{\text{system}} \approx 14.5\text{-}15.0 \text{ mrad}$ using the grating spectrometer spanning 515-652 nm at $\Delta\lambda \sim 0.06 \text{ nm}$.

3.5.5 Radiometric Analysis

Experimental results for the reconstruction of sinusoidal and random angular spectra, presented previously in sections 4.1 and 4.2, respectively, were acquired from the FTAS system illuminated with a 75 W xenon arc lamp source. From this incident optical power illuminating the SLM, the reconstructions appear smooth due to the high signal-to-noise ratio (SNR) at the spectrometer. For a discussion of the system's potential for remote sensing applications, a radiometric analyses of both the experimental and optimal configurations were made. An optimal and an (unfolded) experimental configuration is presented in Fig. 73 (a) and (b), respectively.

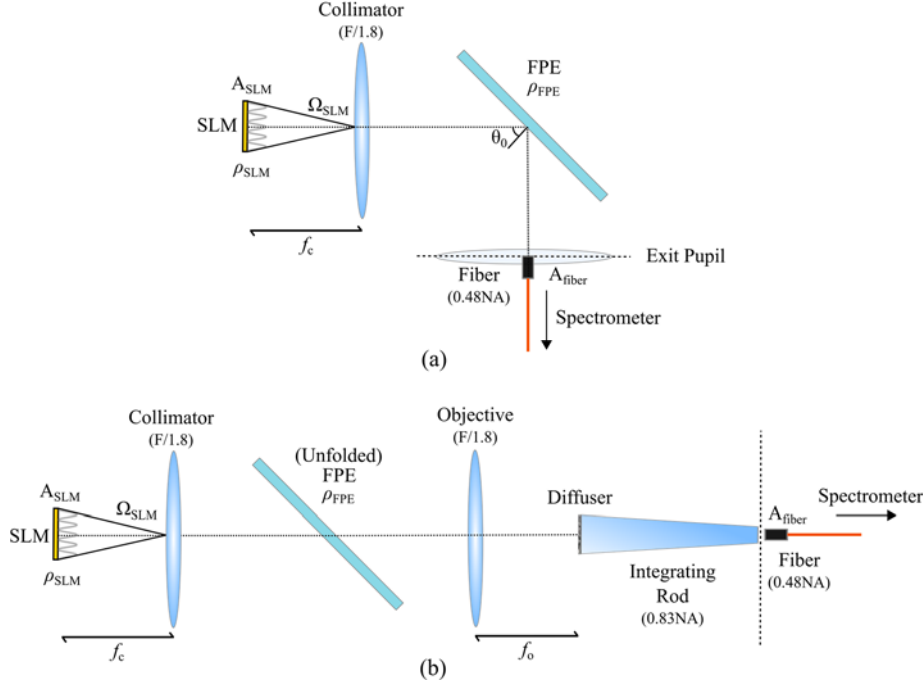


Fig. 73. Schematic used for radiometric and SNR calculations for (b) the optimal system setup, sampling within the exit pupil of the objective, and (b) the ‘unfolded’ experimental setup, in which an integrating rod is used to homogenize the source light.

In the optimal setup, the fiber directly samples source radiance within the system’s exit pupil. The SLM underfills the optical fiber’s numerical aperture and the optical power collected by the fiber, Φ_{fiber} (W), is set by the fiber’s core area, A_{fiber} , and the solid angle subtended by the SLM, Ω_{SLM} , by

$$\Phi_{fiber,optimal} = (\rho_{SLM} \tau_{optics} \rho_{FPE} L_{SLM}) (A_{fiber} \Omega_{SLM}), \quad (128)$$

where

$$\Omega_{SLM} = A_{SLM} / f_c^2. \quad (129)$$

The SLM’s reflected radiance, L_{SLM} (in W/m²/sr), is calculated based on the power incident on the system, Φ_{source} . The reflectivity of the SLM and FPE, ρ_{SLM} and ρ_{FPE} , as well as the transmittance of the collimator of focal length f_c , are included. In the case of the experimental setup from Fig. 73 (b), the SLM’s solid angle underfills the solid angle of the fiber. However, a fraction of the radiance is lost due to a mismatch between the numerical apertures (NA) of the fiber and the integrating rod. The optical power collected by the fiber in the experimental setup is calculated as

$$\Phi_{fiber,exp} = \Phi_{fiber,optimal} \times \left(\frac{\Omega_{fiber}}{\Omega_{rod}} \right), \quad (130)$$

where the ratio between the solid angles is 0.3318 for a 0.48 NA fiber and 0.83 NA integrating rod with 3× magnification. Thus, 66.8% of the power from the SLM is lost in the experimental setup’s integrating rod.

For radiometric analysis of the FTAS systems, we first considered an agnostic spectrometer by calculating the signal-to-noise ratio (SNR), in photon flux, across a single spectral resolution

element. To calculate the FTAS's SNR, a single spectral band ($\Delta\lambda = 0.06$ nm at $\lambda_0 = 584$ nm) is propagated through the system. Values for the SNR were calculated for both the optimal and experimental setups, for laboratory conditions using a xenon lamp source and a passively illuminated target which overfills the optical system. A summary of the relevant source parameters, transmittance and reflectance coefficients, and detector characteristics for the SNR calculations are presented in Table 1.

Table 1. Parameters for Radiometric Calculations for the FPE system

Source		Optics		Detector	
Parameter	Comment	Coefficient	Comment	Parameter	Comment
$\Delta\lambda = 0.06$ nm	Spectral band	$\tau_{\text{collimator}} = 0.9$	Transmittance of collimators	$R = 0.83$	Responsivity of CCD at λ_0
$\lambda_0 = 584$ nm	Center wavelength for the system	$\tau_{\text{objective}} = 0.9$	Transmittance for objectives	$\eta = 0.9$	Quantum efficiency
$\Phi_{\text{xenon}} = 75$ W	Electrical power of lamp used in experiment	$\rho_{\text{SLM}} = 0.25$	Duty cycle of SLM and sinusoidal pattern	$\text{Dark} = 0.0001$	Dark Noise (electrons/sec/pixel)
$T_{\text{sun}} = 5777$ K	Temperature of the sun	$\rho_{\text{FPE}} = 0.25$	Reflectance of FPE	$\text{Read} = 2.3$	Read Noise (electrons/sec)
$R_{\text{sun}} = 695.8\text{E}6$ m	Radius of the sun	$\rho_{\text{grating}} = 0.65$	Reflectance of grating at λ_0	$N = 3000$	Number of pixels on CCD
$S_{\text{sun}} = 149.6\text{E}9$ m	Earth-sun distance	$\alpha_{\text{fiber}} = 20$ dB/km	Attenuation of optical fiber		
$\tau_{\text{atmo}} = 0.9$	Transmittance of atmosphere				
$\rho_{\text{target}} = 0.5$	Reflectance of target				

A 75 W xenon arc lamp was used as the source under laboratory conditions, which corresponds to a source exitance of 1.554 W/m^2 ($\Phi_{\text{band}} \approx 5.15 \text{ mW}$) over the single spectral band [32]. The xenon lamp source was focused directly onto the SLM with an elliptical mirror of $f_{\text{lamp}} = 180$ mm. For the simulated scene, a target with an average reflectance of $\rho_{\text{target}} = 0.5$ is assumed to overfill the optical system. The target is illuminated by the single spectral band ($\Delta\lambda$) from the sun with an irradiance of 0.1019 W/m^2 , which is then focused onto the SLM using an F/2 objective lens. SNR is calculated by converting the optical power incident on the fiber from equations (128) and (130) to photon flux (photons/second), while assuming the system is shot noise limited under Poisson statistics. Fig. 74 presents the calculated SNR values versus integration time (in seconds) for the optimal and experimental setups under the laboratory and overfilled target conditions.

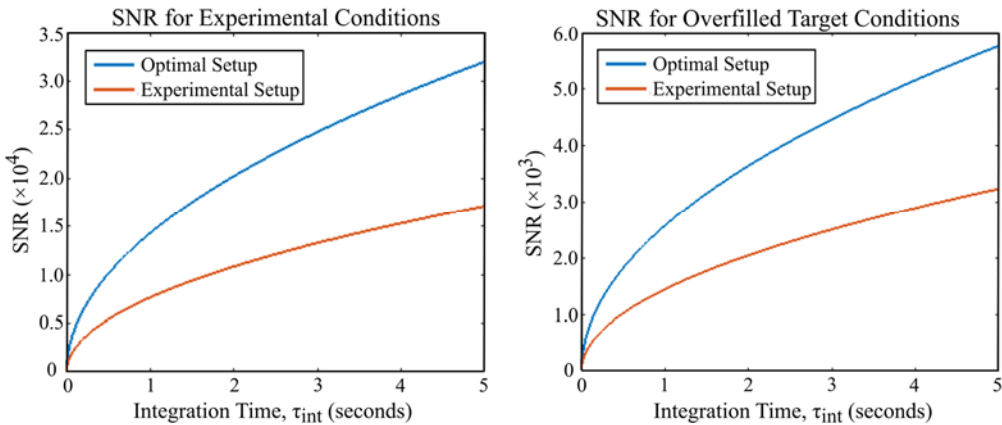


Fig. 74. SNR versus integration time calculated based on the optical power collected at the aperture of the fiber for the optimal and experimental FTAS systems under (a) laboratory conditions and (b) a simulated overfilled target under passive solar illumination.

SNR curves from Fig. 74 demonstrate the light-gathering potential of the FTAS system when losses and noise sources from the spectrometer are not considered. However, SNR values may be calculated for the optimal and experimental FTAS systems using a grating-based spectrometer, as in the experimental setup from section 3. We include the optical fiber's attenuation, the grating's spectral reflectance, and the spectral responsivity of the silicon CCD array for the single spectral band of $\Delta\lambda = 0.06$ nm at $\lambda_0 = 584$ nm. Detector quantum efficiency and noise sources are also taken into account with the values listed in Table 1. To calculate the SNR of the FTAS system with a spectrometer, the optical power incident on the aperture of the fiber is propagated through the spectrometer and imaged onto a single pixel of the CCD array. The incident optical power on the pixel is converted from photon flux to detected electron flux. Fig. 75 presents the SNR curves for the optimal and experimental setups with the grating spectrometer under identical laboratory and simulated conditions as in Fig. 74.

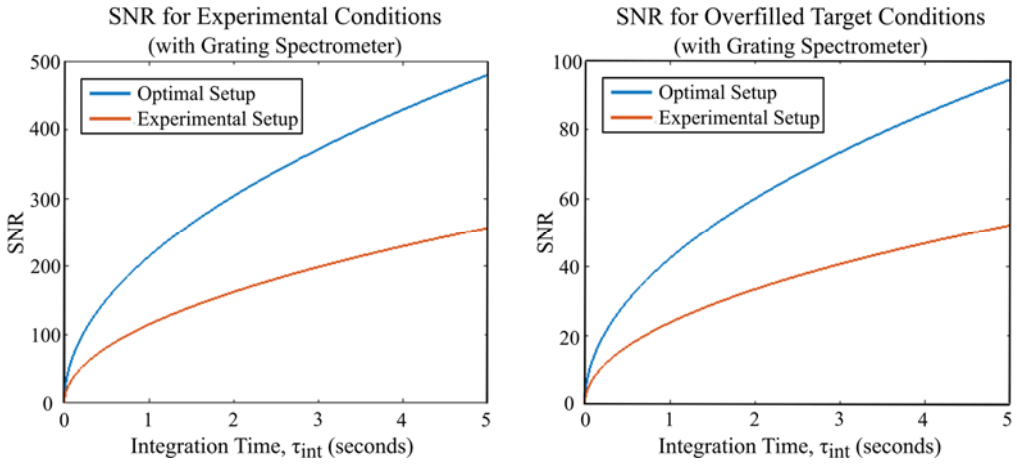


Fig. 75. SNR versus integration time calculated for the optimal and experimental setups of the FTAS systems using the grating spectrometer under (a) laboratory conditions and (b) a simulated overfilled target under passive solar illumination.

The SNR curves in Fig. 75 demonstrate the throughput disadvantage associated with using a grating-based spectrometer. However, with the experimental integration time of $\tau_{int} = 75$ ms with 30 averages from section 4, the SNR values for a single channeled spectrum measurement using the experimental FTAS setup are 172.53 and 29.58 for the laboratory and simulated overfilled target, respectively. An approximate SNR for experimental data presented in section 4 was made by calculating the ratio of the RMS signal to RMS noise in the frequency domain for a measurement of the channeled spectrum generated by the SLM's carrier frequency. With an integration of $\tau_{int} = 75$ ms at 30 averages for the SLM's carrier frequency, an SNR of ~ 146.5 is calculated. Improvements to the current FTAS system may include anti-reflection coatings on the optics, however, the primary limiting factor for throughput of the system is the spectrometer. The grating-based spectrometer may potentially be replaced with a Fourier transform spectrometer, requiring the FTAS system to operate in the near-infrared, which need only effect the coatings and FPE alignment, since coherence may be located at any arbitrary spectral location.

3.6 Conclusion

We have demonstrated the use of longitudinal spatial coherence interferometry to encode a scene's angular spectrum onto the source's power spectrum. By modulating the scene's angular spectrum with a sinusoidal carrier, a channeled spectrum with a high degree of coherence was generated. In the experimental setup, an SLM was coupled into a Fabry-Perot etalon and spectrometer.

Reconstructing the angular spectrum was achieved by Fourier transformation of the channeled spectrum, using techniques common to Fourier transform spectroscopy of the power spectrum. RMS error calculations were based on direct comparisons between the measured and incident angular spectra. RMS errors for sinusoidal and random spectra were measured to be 12.7% and 13.6%, respectively. Error sources are primarily attributed to the collimator's MTF and vibration in the FPE. Future work will be focused on reducing these errors, as well as expanding the technique to enable measurement of angular spectra within 2D and 3D scenes. Angular resolution analysis of the system showed the system recovered angular information within experimental error at $\Delta\theta = 15$ mrad for the sinusoidal and random angular spectra. Finally, as part of our current work, we assumed that each point contains the same spectra. We will also work towards removing this assumption such that each point in the scene can have an arbitrary spectrum with spectral smoothness.

4.0 Spectrally Resolved Longitudinal Spatial Coherence Interferometry for Channeled Spectropolarimetry

4.1 Introduction

In this section we introduce an extension of the snapshot spectrally resolved longitudinal spatial coherence interferometry technique from Ref. [45] to operate as a channeled spectropolarimeter. In channeled spectropolarimetry (CP), polarization information, defined by the Stokes vector of the scene, is typically modulated onto the source's power spectrum. In many cases [47-49], a

Fourier transform relationship exists between the measurement domain (*e.g.* wavenumber σ) and its reciprocal domain (*e.g.* OPD) which allows for recovery of the incident Stokes parameters via Fourier transform reconstruction algorithms and calibration techniques.

An example of the use of a channeled spectrum (CS) to recover polarization information is presented by Oka and Kato [46], in which the state of polarization of a scene is encoded within the incident spectral information. Using two high-order birefringent retarders (simple schematic from the researchers presented in Fig. 76) to create phase retardations along the longitudinal axis as a function of wavenumber, three quasi-cosinusoidal components are generated which carry information about the polarization state of the scene in the measured spectrum. These components appear as discrete channels in the Fourier domain (*i.e.* along the axis of optical path difference for the system), and are readily accessible to demodulate the polarization information of interest.

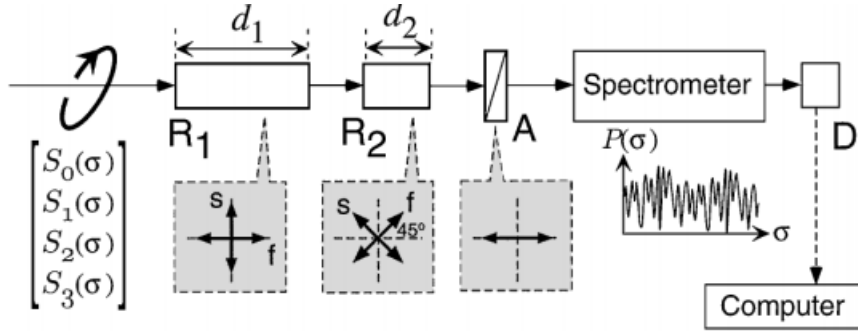


Fig. 76. Model of the CP technique used by Oka and Kato [46], in which high order retarders are used to generate cosinusoidal carrier frequencies which encode the incident state of polarization onto the source power spectrum as a function of wavenumber, σ .

For our purposes, we intend to leverage the analogous Fourier transform relationships detailed in section 3.2 to recover one-dimensional angular distribution of the Stokes parameters given by the Stokes vector

$$S(\theta) = \begin{bmatrix} S_0(\theta) \\ S_1(\theta) \\ S_2(\theta) \\ S_3(\theta) \end{bmatrix} = \begin{bmatrix} I_0(\theta) + I_{90}(\theta) \\ I_0(\theta) - I_{90}(\theta) \\ I_{45}(\theta) - I_{135}(\theta) \\ I_R(\theta) - I_L(\theta) \end{bmatrix}, \quad (131)$$

where S_0 is the total intensity of the incident light, S_1 denotes polarization preference for linear 0° over 90°, S_2 for linear 45° over 135°, and S_3 for circular-right over circular-left polarization states. Our technique is based on the simple model in Fig. 77, in which the incident angularly dependent Stokes parameters are amplitude modulated by a combination of a carrier frequency generated by a spatial light modulator (SLM) and a sinusoidal patterned polarization grating (PG). By using a linear CS modulator with an angularly dependent phase, the Stokes parameters (as a function of incidence angle) may be encoded onto the source's power spectrum. Spectrally resolving the CS modulator's output enables a measurement of the incident polarization state in the form of discrete channels. These channels are readily extracted, and recovery of the incident Stokes parameters may be achieved using Fourier transform reconstruction algorithms in conjunction with calibration techniques.

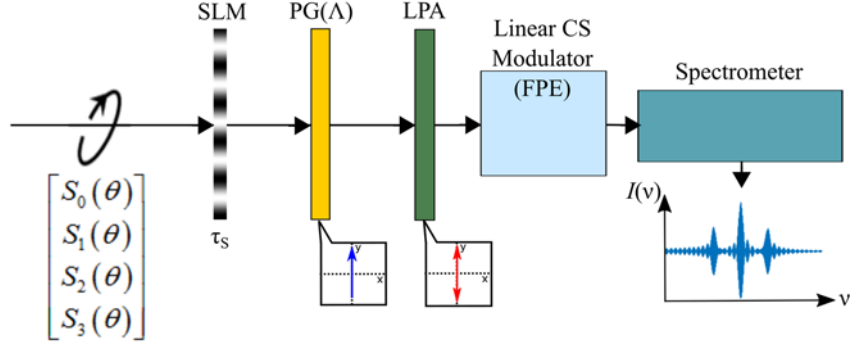


Fig. 77. Simple model of the proposed CP technique, in which angularly dependent Stokes parameters are amplitude modulated onto the source power spectrum using an SLM and sinusoidal PG. Spectrally resolving the output from a linear CS modulator generates a CS which contains polarization information of the scene.

4.2 Theory

After demonstrating successful reconstructions of both periodic and random angular spectra, the next research interest involved modulating polarization information onto channels within the measured spectrum. To accomplish this, a technique similar to the experimental design detailed in section 3.3 will be used. A schematic of the experimental setup is illustrated in Fig. 78, using a MI as the linear channeled spectrum (CS) modulator, noting that an FPE-based interferometer will be used in the interferometer's experimental validation.

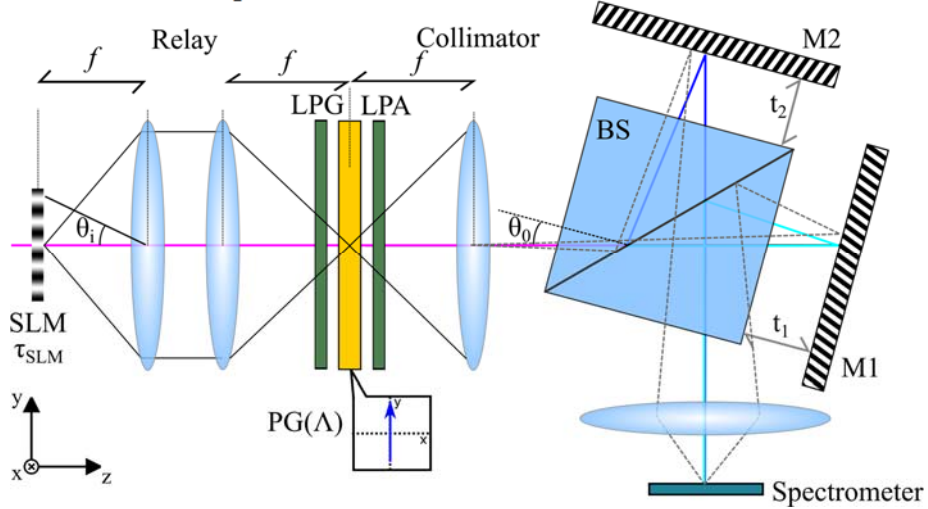


Fig. 78. Schematic of a linear channel spectrum modulator (e.g. titled MI) used to encode polarization information onto the source's power spectrum. The SLM provides the sinusoidal carrier frequency while a polarization grating (PG) of period Λ creates the sinusoidal envelope used to generate channels within the measured spectrum.

To demonstrate how polarization information is encoded onto the power spectrum, Jones calculus was used to describe the light-interaction with the polarization grating. A view of the grating's polarization behavior is illustrated in Fig. 79 from within an intermediate image plane of Fig. 78.

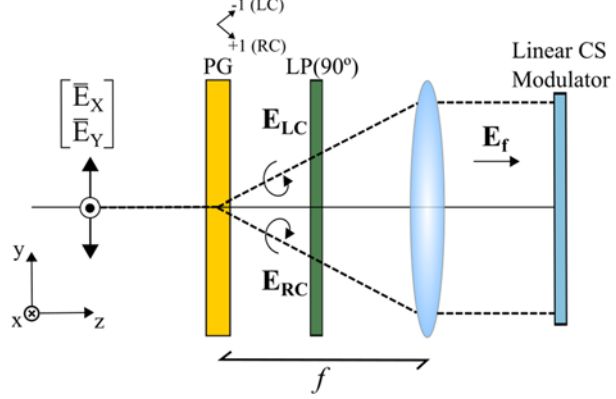


Fig. 79. Illustration of intermediate image plane of optical system in Fig. 78.

To calculate the intensity pattern that will be measured by the linear CS modulator, an arbitrarily polarized electric field was propagated from the SLM as being incident on a PG with a grating period of Λ . The incident field may be expressed as

$$\mathbf{E}_{\text{inc}} = \begin{bmatrix} \bar{E}_X \\ \bar{E}_Y \end{bmatrix} = \begin{bmatrix} E_X(x, y)e^{j\phi_x(x, y)} \\ E_Y(x, y)e^{j\phi_y(x, y)} \end{bmatrix}. \quad (132)$$

The PG's ± 1 diffraction orders may be defined by the Jones matrices for a right and left circular polarization analyzer given by

$$\mathbf{J}_{+1, \text{RC}} = \frac{1}{2} \begin{bmatrix} 1 & j \\ -j & 1 \end{bmatrix}, \text{ and} \quad (133)$$

$$\mathbf{J}_{-1, \text{LC}} = \frac{1}{2} \begin{bmatrix} 1 & -j \\ j & 1 \end{bmatrix}, \quad (134)$$

respectively. After transmitting through the PG, the electric field components for the right and left circular polarization states may be expressed as

$$\mathbf{E}_{\text{RC}} = \mathbf{J}_{+1, \text{RC}} \mathbf{E}_{\text{inc}} = \frac{1}{2} \begin{bmatrix} \bar{E}_X(x, y + \alpha) + j\bar{E}_Y(x, y + \alpha) \\ -j\bar{E}_X(x, y + \alpha) + \bar{E}_Y(x, y + \alpha) \end{bmatrix}, \text{ and} \quad (135)$$

$$\mathbf{E}_{\text{LC}} = \mathbf{J}_{-1, \text{LC}} \mathbf{E}_{\text{inc}} = \frac{1}{2} \begin{bmatrix} \bar{E}_X(x, y - \alpha) - j\bar{E}_Y(x, y - \alpha) \\ j\bar{E}_X(x, y - \alpha) + \bar{E}_Y(x, y - \alpha) \end{bmatrix}, \quad (136)$$

where α represents the angle of diffraction given by the paraxial approximation of the diffraction equation. Diffraction from a PG follows that of a standard grating, such that

$$\sin \alpha \cong \alpha = \frac{m\lambda}{\Lambda} f, \quad (137)$$

where Λ is the period of the PG and f is the focal length of the collimator. The linear polarizer, placed directly behind the PG with a transmission axis oriented at 90° , analyzes the total field at the LP interface to yield the field behind the LP given by

$$\mathbf{E}_{\text{out}} = \begin{bmatrix} 0 & 0 \\ 0 & 1 \end{bmatrix} (\mathbf{E}_{\text{RC}} + \mathbf{E}_{\text{LC}}) = \frac{1}{2} \begin{bmatrix} 0 \\ -j\bar{E}_x(x, y+\alpha) + \bar{E}_y(x, y+\alpha) + j\bar{E}_x(x, y-\alpha) + \bar{E}_y(x, y-\alpha) \end{bmatrix}. \quad (138)$$

The collimating lens creates a Fourier transform, \mathfrak{J} , on the optical field which may be expressed as

$$\mathbf{E}_f = \mathfrak{J}\{\mathbf{E}_{\text{out}}\}_{\xi=\frac{x}{\lambda f}, \eta=\frac{y}{\lambda f}} = \frac{1}{2} \begin{bmatrix} -j\bar{E}_x e^{\frac{j2\pi}{\lambda f}\alpha y} + \bar{E}_y e^{\frac{j2\pi}{\lambda f}\alpha y} + j\bar{E}_x e^{-j\frac{2\pi}{\lambda f}\alpha y} + j\bar{E}_y e^{-j\frac{2\pi}{\lambda f}\alpha y} \end{bmatrix}, \quad (139)$$

where \bar{E}_x and \bar{E}_y are defined in terms of x and y , and f is the focal length of the collimator. The total electric field intensity incident on the linear channeled spectrum modulator may then be written as

$$I = |\mathbf{E}_f|^2 = \frac{1}{2} \left(|\bar{E}_x|^2 + |\bar{E}_y|^2 \right) + \frac{1}{4} \left(\bar{E}_y \bar{E}_y^* - \bar{E}_x \bar{E}_x^* \right) e^{j\frac{2\pi}{\lambda f}\alpha y} + \frac{1}{4} \left(\bar{E}_y \bar{E}_y^* - \bar{E}_x \bar{E}_x^* \right) e^{-j\frac{2\pi}{\lambda f}\alpha y} - \frac{j}{4} \left(\bar{E}_x \bar{E}_y^* - \bar{E}_y \bar{E}_x^* \right) e^{j\frac{2\pi}{\lambda f}\alpha y} + \frac{j}{4} \left(\bar{E}_x \bar{E}_y^* - \bar{E}_y \bar{E}_x^* \right) e^{-j\frac{2\pi}{\lambda f}\alpha y}. \quad (140)$$

Substitution of the definitions for the Stokes parameters [50] allows for the simplification of the expression, such that

$$I(x, y) = \frac{1}{2} \left[S_0(x, y) - S_1(x, y) \cos\left(\frac{2\pi}{\lambda f} 2\alpha y\right) - S_2(x, y) \sin\left(\frac{2\pi}{\lambda f} 2\alpha y\right) \right]. \quad (141)$$

Finally, by substitution of $\alpha = \frac{m\lambda}{\Lambda} f$ and $\theta \equiv \frac{y}{2f}$, the final expression for the intensity incident on the linear channeled spectrum modulator, as a function of the incident angle θ , is given by

$$I(\theta) = \frac{1}{2} \left[S_0(\theta) - S_1(x, y) \cos\left(2\pi \frac{2}{\gamma} \theta\right) - S_2(\theta) \sin\left(2\pi \frac{2}{\gamma} \theta\right) \right], \quad (142)$$

where $\gamma \equiv \frac{\Lambda}{2f}$ is defined as the period of the PG in radians.

Incorporating the chirped cosinusoidal transmission function of the SLM, τ_{SLM} , as in Fig. 78 and the modulation generated by two-beam interference, the functional form of the measured interferogram may be written as

$$I(\nu, \theta) \propto \frac{\tau_{\text{SLM}}(\theta) \{1 + \cos(\phi_\nu)\}}{2} [S_0 - S_1 \cos(\phi_l) - S_2 \sin(\phi_l)], \text{ with} \quad (143)$$

$$\tau_{\text{SLM}}(\theta) = \frac{1}{2} + \frac{1}{2} \cos(\phi_{\text{SLM}}), \text{ and} \quad (144)$$

$$\phi_{\text{SLM}} = 2\pi\nu_0 q_0. \quad (145)$$

The variables S_0 , S_1 , and S_2 are the Stokes parameters related to the intensity of the source, linear 0° or 90° , and linear 45° or 135° , respectively. The variable $q_0 = \cos(\theta)$ and v_0 represents the rate of change of q_0 across the FOV. The phase terms ϕ_l and ϕ_v are representative of the angular modulation provided by the PG and two-beam interference generated by the linear CS modulator, and are given by

$$\phi_l = 2\pi \frac{2}{\gamma} \theta, \text{ and} \quad (146)$$

$$\phi_v = 2\pi v(\sigma) \cos(\theta), \text{ with} \quad (147)$$

$$v(\sigma) = \sigma OPD_0, \quad (148)$$

where OPD_0 is fixed (constant for all wavenumbers). Expansion of Eq. (143) yields

$$\begin{aligned} I(v, \theta) \propto & \frac{S_0}{2} \left\{ \cos(\phi_v - \phi_{SLM}) + \cos(\phi_v + \phi_{SLM}) \right\} \\ & - \frac{S_1}{4} \left\{ \cos(\phi_v - \phi_{SLM} - \phi_l) + \cos(\phi_v - \phi_{SLM} + \phi_l) + \cos(\phi_v + \phi_{SLM} - \phi_l) + \cos(\phi_v + \phi_{SLM} + \phi_l) \right\} \\ & - \frac{S_2}{4} \left\{ \sin(\phi_v - \phi_{SLM} - \phi_l) - \sin(\phi_v - \phi_{SLM} + \phi_l) + \sin(\phi_v + \phi_{SLM} + \phi_l) - \sin(\phi_v + \phi_{SLM} - \phi_l) \right\}. \end{aligned} \quad (149)$$

From Eq. (149) there are six distinct channels containing information related to the input polarization parameters S_0 , S_1 , and S_2 . These channels may be seen superimposed on simulated data for the experimental setup in Fig. 78. Simulation of a channeled spectrum is generated by a uniform incident angular spectrum with an 8° FOV over a spectral range of $\sigma = -2500 \text{ mm}^{-1}$ to $\sigma = +2500 \text{ mm}^{-1}$ (to illustrate channels at negative values of v) at a spectral resolution of 4 cm^{-1} . The green shaded region represents the approximate spectral response of a silicon detector ($\sigma \approx 1000-2500 \text{ mm}^{-1}$) and acts as a bandpass filter for the detectable channels present in positive values of v . The PG period is defined as $\Lambda = 2240 \mu\text{m}$ ($\gamma = 0.0448$ radians) and the SLM carrier frequency is $v = 388.02$ radians, giving $\Delta v = 0.1151$.

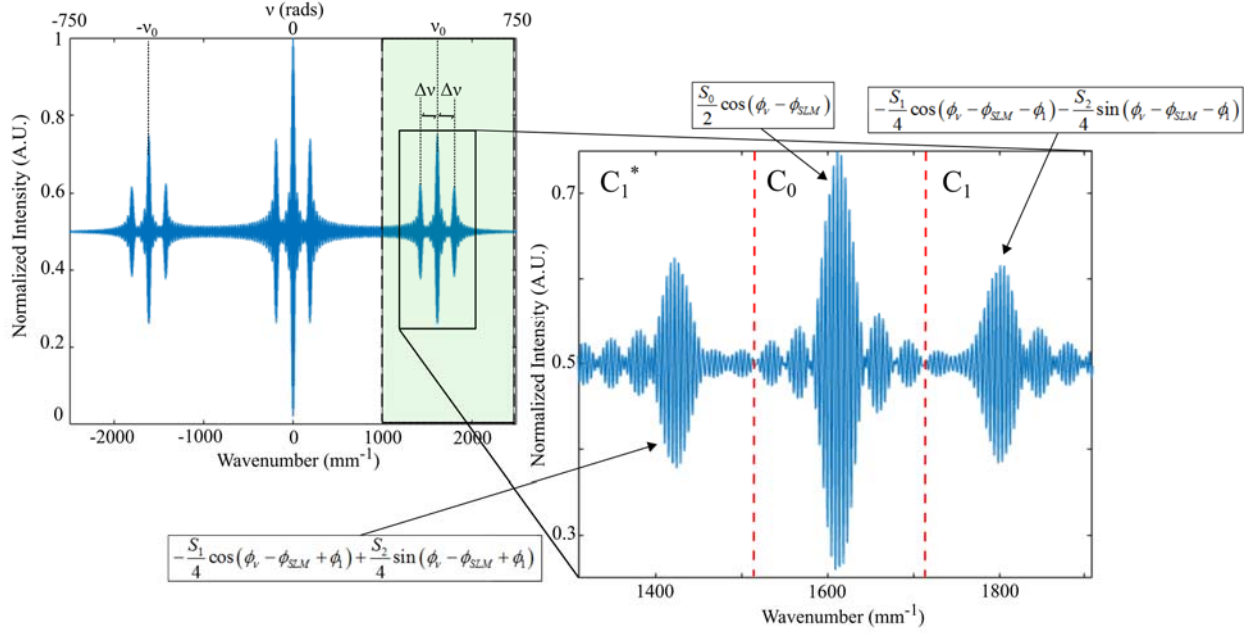


Fig. 80. Simulated channeled spectrum for system in Fig. 78 with PG period $\Lambda = 2240 \mu\text{m}$. Magnified view of the three channels separated in v space by the phase term, ϕ_1 , present within the spectral bandpass of a silicon detector.

Demodulating the Stokes parameters can be performed by direct filtering of the desired channels, followed by a Fourier transform with respect to the measurement variable v . Performing these steps on channels C_0 and C_1 as illustrated in Fig. 80 yields

$$\Im\{C_0(v)\} = \frac{1}{2} S_0(q), \text{ and} \quad (150)$$

$$\Im\{C_1(v)\} = \frac{1}{4} \{-S_1(q) - jS_2(q)\} \exp(-j\phi_1). \quad (151)$$

Thus, by measuring a known input state of polarization (SOP), the modulating phase factor ϕ_1 in channel C_1 can be calibrated out and the unknown values, S_1 and S_2 , may be reconstructed. This model demonstrates that reconstructions may be acquired directly from the measured channeled spectrum.

4.2.1 Recovery of Angularly Dependent Stokes Parameters

4.2.1.1 Reference Beam Calibration

One method to calibrate the channeled spectropolarimeter is through use of the reference beam calibration technique [51]. In this calibration technique, the modulating phase factor $\exp(-j\phi_1)$ found in channel C_1 is measured using a known reference input SOP. Unknown sample data is then divided by the reference data to recover the angular Stokes parameters per Eq. (152) through Eq. (155) below

$$S_{0,reference}(\theta) = \left| \Im\{C_{0,reference,0^\circ}(v)\} \right| \quad (152)$$

$$S_{0,sample}(\theta) = \left| \Im\{C_{0,sample}(v)\} \right| \quad (153)$$

$$S_{1,sample}(\theta) = \text{Re} \left[\frac{\Im\{C_{1,sample}(\nu)\}}{\Im\{C_{1,reference,0^\circ}(\nu)\}} \frac{S_{0,reference}}{S_{0,sample}} \right] \quad (154)$$

$$S_{2,sample}(\theta) = \text{Im} \left[\frac{\Im\{C_{1,sample}(\nu)\}}{\Im\{C_{1,reference,0^\circ}(\nu)\}} \frac{S_{0,reference}}{S_{0,sample}} \right] \quad (155)$$

For our purposes, spectral measurements were acquired with a linear polarizer generator oriented at 0° to create a sufficient reference data set.

4.2.1.2 False Signature Artifact Reduction Technique

One potential source of reconstruction error in our channeled polarimetry technique occurs if the neighboring channels are in close proximity with each other. Eqs. (151), (154), and (155) assume that the channels containing the Stokes parameters are band limited. Thus, information present in the channels is exclusively from the presence of S_1 and/or S_2 in the scene. However, higher frequency spectral variations in the source power spectrum (*i.e.* S_0) will extend the centerburst to larger values of ν , generating the false appearance of real data in the channels associated with S_1 and S_2 . An illustration of this is presented in Fig. 81, where aliasing of S_0 information is present in regions that will be Fourier filtered to extract S_1 (ignoring the S_2 component for simplicity). If the information associated with the centerburst is not removed prior to reconstruction, then the recovery of S_1 will be subject to aliasing errors.

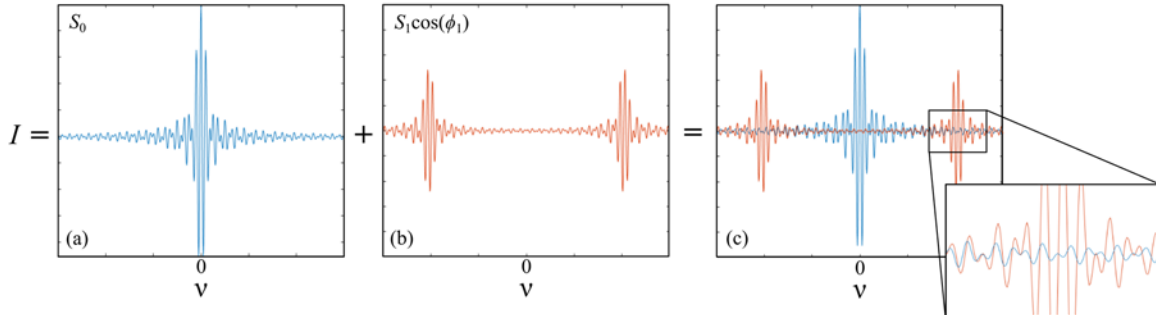


Fig. 81. In CP, (a) the S_0 component of the source is present near the centerburst, while (b) the other Stokes parameters are encoded into displaced channels. Since spectral measurements are a superposition of these components, (c) aliasing will occur when centerburst modulations are present in the side channels.

One way to remove the centerburst, or S_0 component, is to implement the false signature artifact reduction technique (ART) [49]. In the ART, two measurements of both reference and sample data are acquired with the linear polarizer analyzer oriented at 90° and 0° . For instance, if a measurement were taken with the analyzer oriented at 0° , the channeled spectrum generated by the system will be

$$I_{0^\circ}(\nu) \propto \frac{\{1 + \cos(\phi_\nu)\}}{2} [S_0 + S_1 \cos(\phi_1) + S_2 \sin(\phi_1)]. \quad (156)$$

Eq. (156) exhibits a 180-degree carrier frequency phase shift relative to Eq. (143), which was derived with an analyzer oriented at 90° . When the two measurements are weighted and summed,

the S_1 and S_2 components are removed and the result is a higher resolution channeled spectrum of the form

$$I_{90^\circ}(\nu) + \Gamma(\nu) I_{0^\circ}(\nu) \propto \{1 + \cos(\phi_\nu)\} S_0, \text{ where} \quad (157)$$

$$\Gamma(\nu) = \frac{I(\nu)_{A(90^\circ)}}{I(\nu)_{A(0^\circ)}} \quad (158)$$

is the weighting factor defined as the ratio between measurements analyzed at 90° and 0° . This term is necessary due to the Fresnel reflections at the interferometer interface, as s-polarized (90° orientation) light has a higher reflection coefficient than p-polarized (0° orientation) light at the incident angles for which the experimental system is operated.

4.3 Experimental Design and Setup

4.3.1 Longitudinal Spatial Coherence Channeled Spectropolarimeter

4.3.1.1 Experimental Design

After successful results were shown for the FTAS technique [45], we implemented the CP technique using the existing Fabry-Perot etalon (FPE) as the linear channeled spectrum modulator. The parameters of the FPE were selected such that it approximated a two-beam interferometer, with most of the power contained exclusively within the first order. A schematic of the interferometer's configuration is depicted in Fig. 82 (a). A Texas Instruments DLP LightCrafter Evaluation Module was illuminated by a xenon arc lamp after reflecting from a 25 mm dielectric mirror. The mirror's position and angle optimally couples the light into the DLP-based SLM, which contains the carrier frequency pattern associated with the scene's S_0 component. Reflected light is then relayed using two 50 mm focal length lenses and focused at an intermediate image plane, after passing through a linear polarizer generator (LPG) constructed using linear polarizer film placed in a 360° manual rotation mount. A polarization grating (PG) of period 2240 μm and aligned orthogonally with the axis of propagation is placed at the intermediate image plane. The amplitude modulated signal (*i.e.* carrier frequency pattern modulated by the sinusoidal PG) is collimated by a collimation lens (50 mm focal length) and analyzed using a linear polarizer analyzer (LPA) of the same material as the LPG. The collimated light is then propagated into a two-mirror (M2 and M3) FPE, which consists of two 10:90 (R:T) dielectric plate beamsplitters from Thorlabs (BSN16) with reflectance magnitudes of R_1 and R_2 , respectively. Mirror M3 is placed on a translation stage, which allows tuning the etalon's thickness t . A weight is placed on mirror M3's mount and coupled to mirror M2 in order to reduce vibrations that can differentially couple into the etalon. An objective lens (50 mm focal length) focuses the FPE's reflected light onto a ground glass diffuser and integrating rod, where the spatial information is homogenized. Homogenization ensures both a uniform spatial and spectral angular spectrum across the measured beam, which is often inhomogeneous due to diffraction from the SLM. Finally, the light is measured by a spectrometer at the homogenized output. An image of the proof of concept experimental setup is presented in Fig. 82 (b). A grating spectrometer using a 1200 lines/mm diffraction (Thorlabs GR50-1205) and a Thorlabs LC1-USB 3,000 pixel linear silicon CCD array was used to measure channeled spectra over wavelengths spanning 515-652 nm at a spectral resolution of $\Delta\lambda \sim 0.06$ nm. Measurements of the channeled spectra were acquired using the Thorlabs SPLICCO GUI and were calibrated in *MATLAB*.

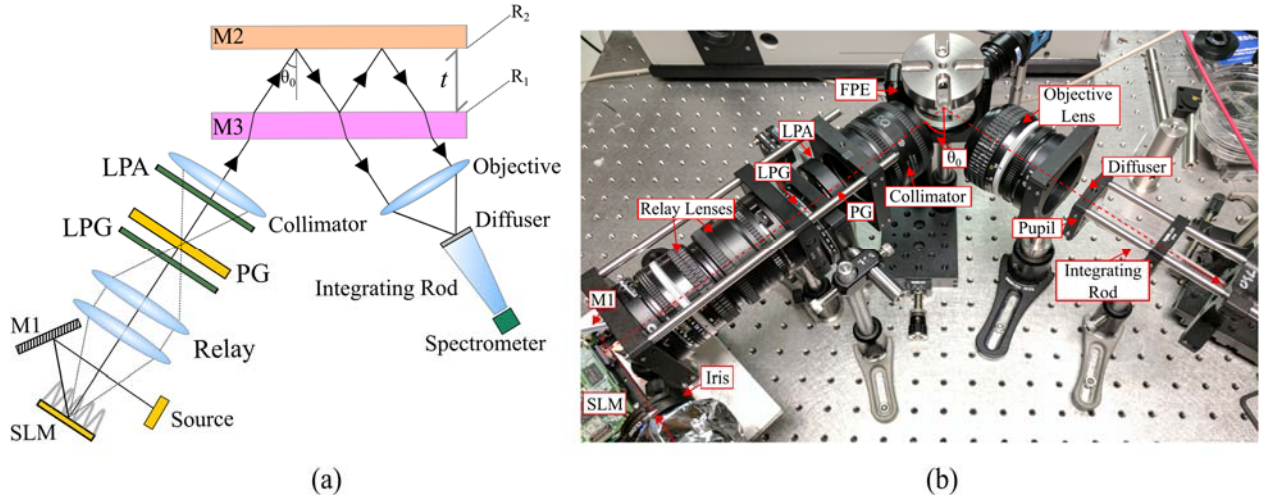


Fig. 82. (a) Schematic and (b) optical table setup of the FPE-based proof of concept system used for the channeled spectropolarimetry technique.

4.3.1.2 Alignment Procedure and Methods

High contrast of the channeled spectra's fringes is essential to maintain high signal to noise ratio (SNR) after Fourier transformation. To optimize contrast, an alignment procedure was developed. The central purpose of this procedure is to maximize the centerburst's coherence at a single wavelength within the spectrometer's spectral passband. This was achieved by tuning the etalon's thickness, such that the observed Haidinger fringes are coherently matched to the SLM's carrier frequency.

A schematic of the alignment setup is illustrated in Fig. 83 (a). While it is similar to the experimental configuration presented in Fig. 82 (a), the xenon arc lamp and spectrometer are replaced by a neon gas discharge lamp and a camera, respectively. Light from the gas lamp illuminates the SLM along the same path as the xenon arc lamp. The SLM is loaded with the desired carrier frequency, which is collimated and transmitted through the FPE. An objective (12.5 mm focal length) focuses the reflected light onto a 648x480 pixel element CCD Array, creating an image of the illuminated SLM carrier angular spectrum superimposed onto a background of neon Haidinger fringes, which is generated by the etalon. A narrowband filter, with a 633 nm center wavelength at 3 nm full-width at half maximum spectral bandwidth, is placed before the objective such that only the fringes associated with the 632.8, 633.08, and 633.44 nm transitions of the neon gas discharge lamp are transmitted to the camera [43]. Fig. 64 (b) depicts an image, measured by the camera, of the off-axis Haidinger fringes superimposed onto the SLM's carrier frequency. The carrier frequency coherently matches the Haidinger fringes transmission peaks, thus, the channeled spectrum's maximum coherence will occur at the alignment wavelength of $\lambda \sim 633$ nm. Fig. 64 (c) depicts an image (illuminated by broadband white light, rather than the monochromatic source) of the modulated carrier frequency, which would act as the channel generating scene in proof of concept experiments.

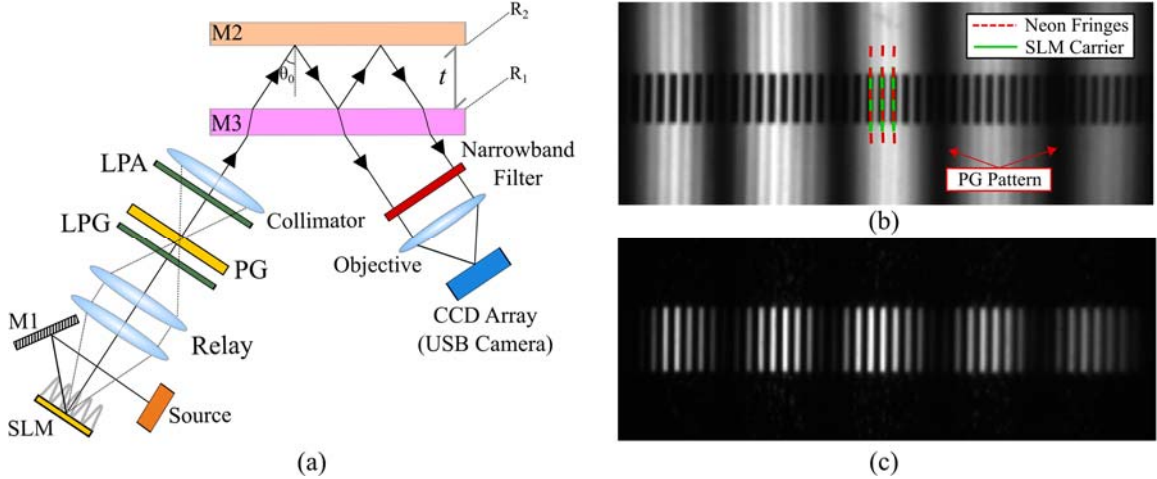


Fig. 83. (a) Schematic for FPE alignment configuration, in which the xenon arc lamp source was replaced with a low pressure neon gas discharge lamp. A camera is also used to directly observe the light from the SLM and source. (b) Image of the SLM's carrier fringe superimposed onto the fringe, observed by residual spectrally narrow band light reflected off the SLM's surface. In this aligned system case, maximum coherence would occur at a wavelength equal to the neon gas lamp's filtered emission wavelength at 633 nm. (c) Actual image of the modulated carrier frequency pattern (illuminated by white light) which would generate channels in the experimental setup.

4.4 Results

4.4.1 First order analysis

Preliminary measurements of the longitudinal spatial coherence CP technique were acquired to determine the validity of the numerical simulations. Of primary interest is the comparison between simulation and experimental data for spectral fringe frequency and contrast, spectral location of the centerburst (C_0) and channel (C_1), and phase variations in the channel generated by a polarized scene. Fig. 84 (a) plots an experimentally acquired CS generated by the experimental setup in Fig. 82 (b) for LPG(0°) and LPA(90°). The experimental data is scaled and superimposed onto a simulated CS in order to compare relative contrast between the C_0 and C_1 channels and fringe frequency across the measurement spectral range of $\lambda \sim 515\text{-}652$ nm. The scaling factor ($\times 1.7$) is attributed to differences in the transmission of the polarization optics between the ideal simulation and the experimental setup (e.g. LPG/LPA polarizing film transmission $\sim 42\%$, versus ideal 50% in simulation). Fig. 84 (b) plots an unscaled, magnified view of the C_1 channel for two different input scenes, LPG(0°) and LPA(90°). Spectral data in both plots were acquired by the grating spectrometer with 75 ms integration and 20 rolling averages. Data were background corrected and plotted versus a demodulate v' axis to reference the centerburst to $v = 0$.

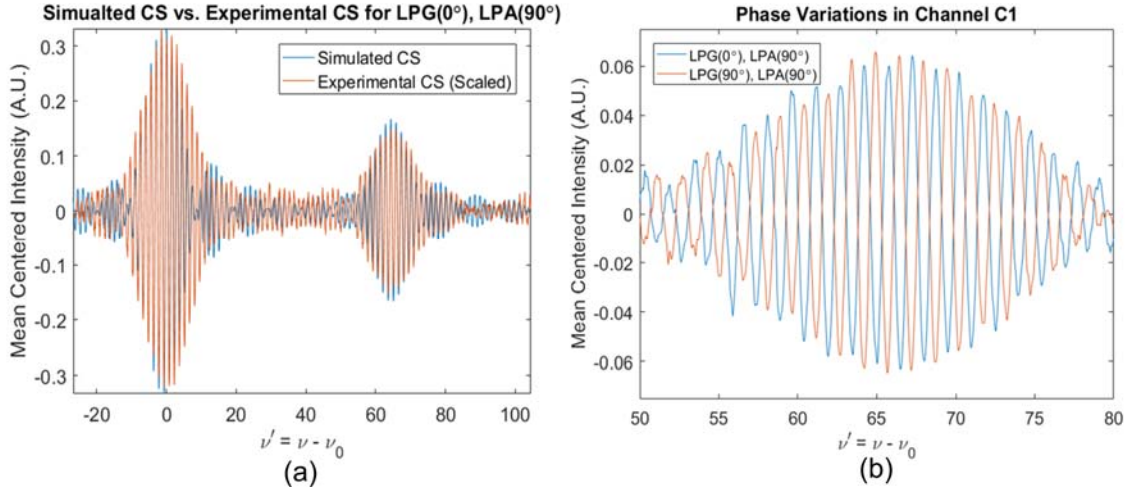


Fig. 84. (a) Scaled ($\times 1.7$) experimentally acquired CS superimposed on simulated CS for LPG(0°), LPA(90°). (b) Magnified view of channel C_1 in two experimentally acquired CS for LPG(0°) and LPG(90°).

After fitting the simulated and experimental *OPDs*, Fig. 84 (a) demonstrates strong correlation between numerical simulation and experimental CS in terms of spectral fringe contrast and frequency, and spectral location of the C_0 and C_1 channels given a PG of $\Lambda = 2240 \mu\text{m}$. Fig. 84 (b) shows the expected phase variations generated by different linearly polarized inputs, namely that orthogonal input states (e.g. LPG(0°) and LPG(90°)) create a 180° phase shift across channel C_1 . These results are promising for the CP technique and validate that the simulation matches well with reality.

4.4.2 Uniform Stokes Scenes

The first experiment to determine the validity of the CP technique for recovering angularly dependent Stokes parameters was measuring uniform linearly polarized scenes. In this experiment, an LPG polarizing film was placed before the PG ($\Lambda = 2240 \mu\text{m}$, Fig. 85 (a)) on a 360° manual rotation mount to generate uniform linearly polarized states across the FOV defined by the SLM. The LPG was aligned to a known reference linear polarizer and spectral measurements were acquired for steps of 45.0° from LPG(0°) to LPG(180°). As mentioned in section 4.2.1.2, two measurements are acquired at orthogonal analyzer orientations for both the reference and sample data to implement the ART. An image of the analyzer scheme is depicted in Fig. 85 (b), in which the analyzers are mounted onto a microscope slide, and positioned orthogonal to the optical axis during measurement. Noting that a half wave plate (HWP) film is placed behind the LPA(0°) to compensate for Fresnel reflections at the FPE surface, allowing both analyzed states to be measured by the spectrometer.

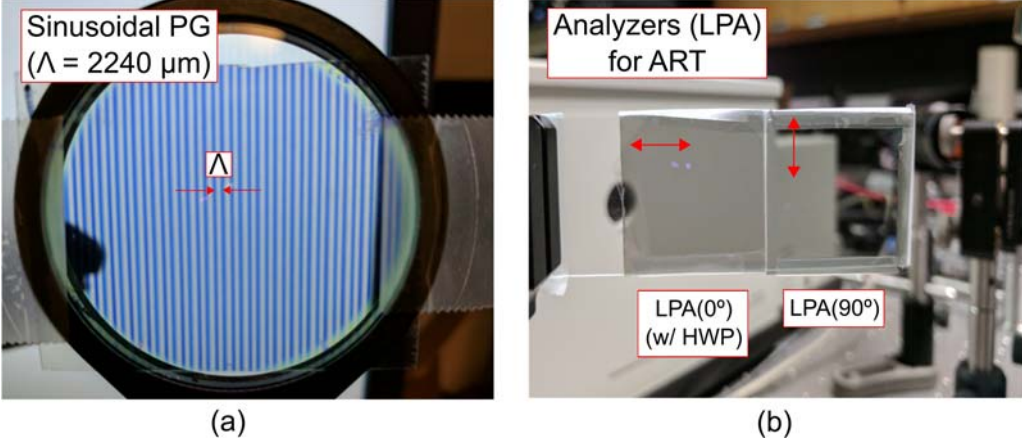


Fig. 85. (a) Image of the sinusoidal pattern of period Λ for the PG used in proof of concept experiments. (b) Image of the analyzers, LPA(0°) and LPA(90°), used to implement the ART calibration (red arrows denote orientation axis).

After light was reflected from the FPE, it was detected using the grating spectrometer ($\Delta\lambda \sim 0.06 \text{ nm}$ resolution), which measured wavelengths spanning 515-652 nm (or wavenumbers spanning $1533\text{-}1941 \text{ mm}^{-1}$). For our measurements, the centerburst wavelength was set at $\lambda = 623.5 \text{ nm}$ by varying the FPE's thickness. The raw data were processed by

$$b'(\nu) = \frac{b_M(\nu) - b_D(\nu)}{b_X(\nu)}, \quad (159)$$

where b' is the processed spectrum, b_M is the measured spectrum, b_D is a dark frame, and b_X is the spectrum of the unmodulated lamp. Note that in this case, b_X acts as a spectral ‘flat field’ for all measurements. Filtering in the Fourier domain was used to remove additional background components in the data, which exist beyond the spatial resolution of the FPE (approximately $f_c/2$). To calibrate the measurements’ ν axis, OPD_0 was calculated using Eq. (148) and a measurement of the incidence angle ($\theta_0 = 50 \pm 1^\circ$), as determined by the geometry of our experimental setup. An example of the processed CS for a reference (LPG(0°)) and uniform sample (LPG(45°)) data set is presented in Fig. 86, including the higher resolution spectrum for the ART.

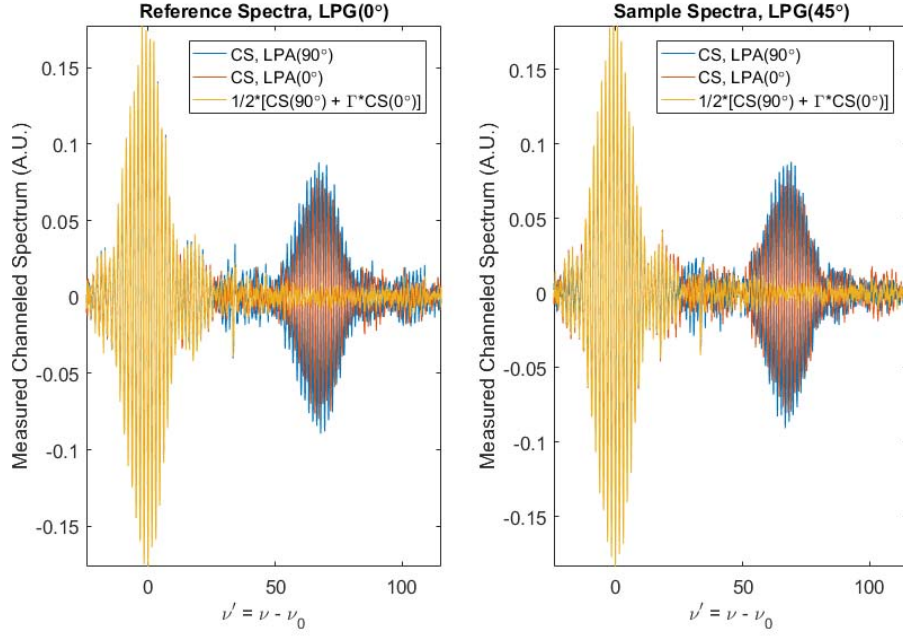


Fig. 86. Processed channeled spectra for a reference, LPG(0°), and sample, LPG(45°), data set. Blue spectra represent measurements analyzed at LPA(90°), while red spectra denote measurements for LPA(0°). The yellow spectra are the higher resolution spectrum used in the ART.

The higher resolution spectrum, CS_{HR} (yellow spectra in Fig. 86), which is subtracted from the reference and sample data before filtering channels C_0 and C_1 , is calculated as the average of the two respective analyzer measurements by

$$CS_{HR}(\nu) = \frac{1}{2} \left[CS(\nu)_{A(90^\circ)} + \Gamma(\nu) CS(\nu)_{A(0^\circ)} \right], \quad (160)$$

where the weighting factor $\Gamma(\nu)$ is defined per Eq. (158). Calculation of $\Gamma(\nu)$ is taken as the ratio of the unmodulated background (*i.e.* $b_X(\nu)$ from Eq. (159)) for the two orthogonal analyzer states. Fig. 87 plots the two unmodulated spectra versus ν' , demonstrating the need for the weighting factor $\Gamma(\nu)$.

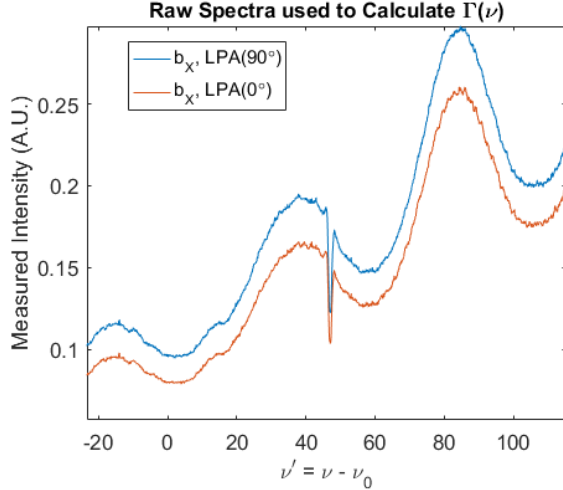


Fig. 87. Unmodulated spectra used to calculate the weighting factor $\Gamma(\nu)$.

To recover the angularly dependent Stokes parameters from the measured channeled spectra, channels C_0 and C_1 are filtered from the centerburst and the corrected reference and sample spectra become

$$CS(\nu)_{CC,reference} = CS(\nu)_{A(90^\circ),reference} - CS_{HR}(\nu), \text{ and} \quad (161)$$

$$CS(\nu)_{CC,sample} = CS(\nu)_{A(90^\circ),sample} - CS_{HR}(\nu), . \quad (162)$$

By applying the reference beam calibration using Eq. (152) through Eq. (155). The following plots in Fig. 88 compare the recovery of the uniform (normalized) Stokes parameters of S_1/S_0 and S_2/S_0 versus angle of incidence for the numerical simulations and the experimental data. The reconstruction algorithm is the same for both simulation and experiment, in that the ART is first applied, followed by the use of a Hamming filter to extract channels ($C_{0,reference}, C_{1,reference}$) and ($C_{0,sample}, C_{1,sample}$) before implementing the reference beam calibration technique.

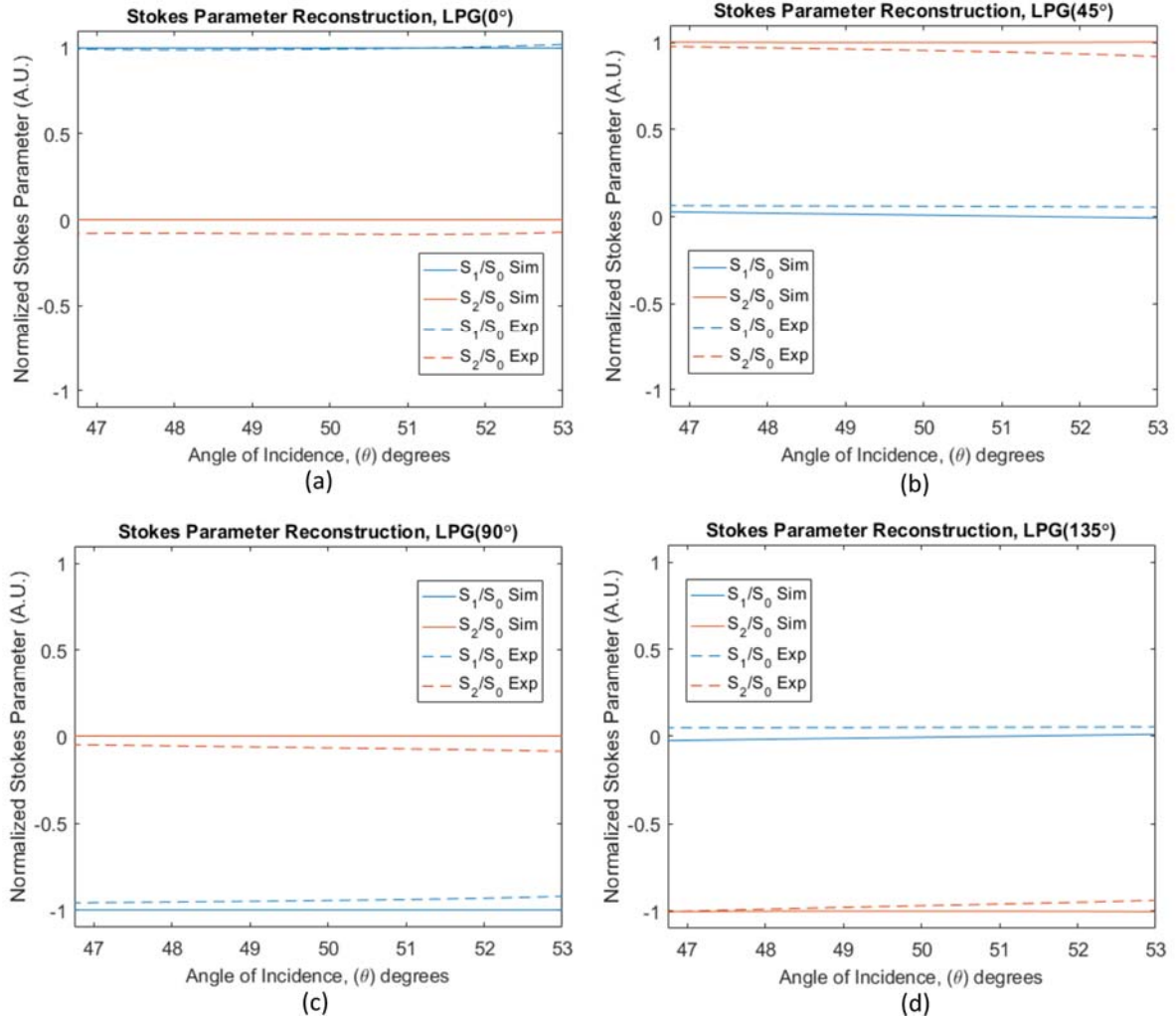


Fig. 88. Simulation (Sim, solid lines) and experimental (Exp, dashed lines) reconstruction results for the normalized angularly dependent Stokes parameters, S_1/S_0 and S_2/S_0 , versus angle of incidence for linearly polarized scenes: (a) 0° , (b) 45° , (c) 90° , and (d) 135° .

To quantify the system's accuracy, the root-mean-square (RMS) error was calculated for both the simulated and experimental reconstructions. The method used calculates error in reconstruction of the Stokes parameters of the incident range of angles, $\theta_0 \in [46.5^\circ, 53.75^\circ]$ (note: this is smaller than the full FOV due to the Gibbs phenomenon associated with the filter at the FOV's edges). Values of RMS were calculated using

$$RMS = \sqrt{\frac{\sum_{m=1}^M (\hat{y} - y)^2}{M}}, \quad (163)$$

where M is the number of samples across the field of view (*i.e.* 13 samples over the range $\theta_0 \in [46.5^\circ, 53.75^\circ]$) and \hat{y}, y represent the normalized Stokes parameters S_1/S_0 and S_2/S_0 for the simulation reconstruction and experimental reconstruction, respectively. A table of the RMS errors calculated for the plots in Fig. 88 (a) through (d) is given below.

Table 3. RMS Error calculations for reconstruction of normalized Stokes parameters for uniform, linearly polarized scenes

LPG Orientation	RMS Error	
Angle (degrees)	S_1/S_0	S_2/S_0
0	0.0196	0.0413
45	0.0502	0.0559
90	0.0569	0.0672
135	0.0652	0.0405

4.4.3 Stokes Step Function

A more complex experiment was also used to validate the CP technique's imaging capacity, in which the polarized scene was defined as a step or edge response function between two different polarization states. This 'Stokes Step Function' is created by placing two linear polarization generators (LPGs), with different transmission axis orientations. These are positioned at a slightly defocused image plane before the PG, such that half of the FOV is S_1 linearly polarized and the other S_2 linearly polarized. Note that defocus is used here in a similar capacity to a conventional channeled imaging polarimeter, in that it is a simple method to spatially band-limit a scene. Fig. 89 depicts the image of the step function generator and how the step function was modeled in numerical simulations.

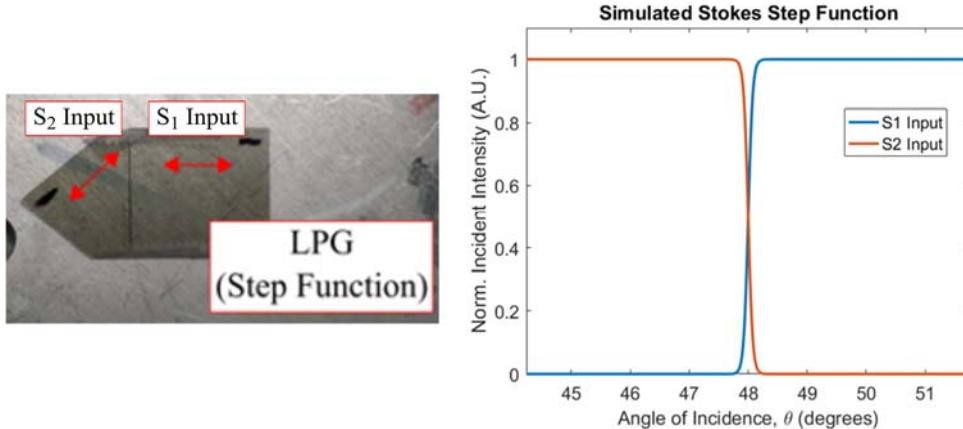


Fig. 89. (left) Image of the Stokes step function created by two linear polarizing generators oriented such that the scene is define as a step between an S_1 to S_2 polarization state. (right) Model of the Stokes step function used in numerical simulation of channeled spectra and simulated reconstructions.

As with the uniform scenes in section 4.4.2, measurements of the channeled spectra generated by the Stokes step function were acquired by the grating spectrometer for a 75 ms integration time and 20 rolling averages. The raw spectral data were processed per Eqns. (159) through (162) for flat field correction and ART. Channels ($C_{0,\text{reference}}$, $C_{1,\text{reference}}$) and ($C_{0,\text{sample}}$, $C_{1,\text{sample}}$), associated with the step function scene, were filtered from the processed CS using a rectangular filter (as opposed to the Hamming filter used previously) to increase the reconstruction's angular resolution. Once the channels were filtered, reference beam calibration was applied via Eqns. (152) through (155). Reconstruction results are presented in Fig. 90, comparing the recovered experimental Stokes parameters to simulated results.

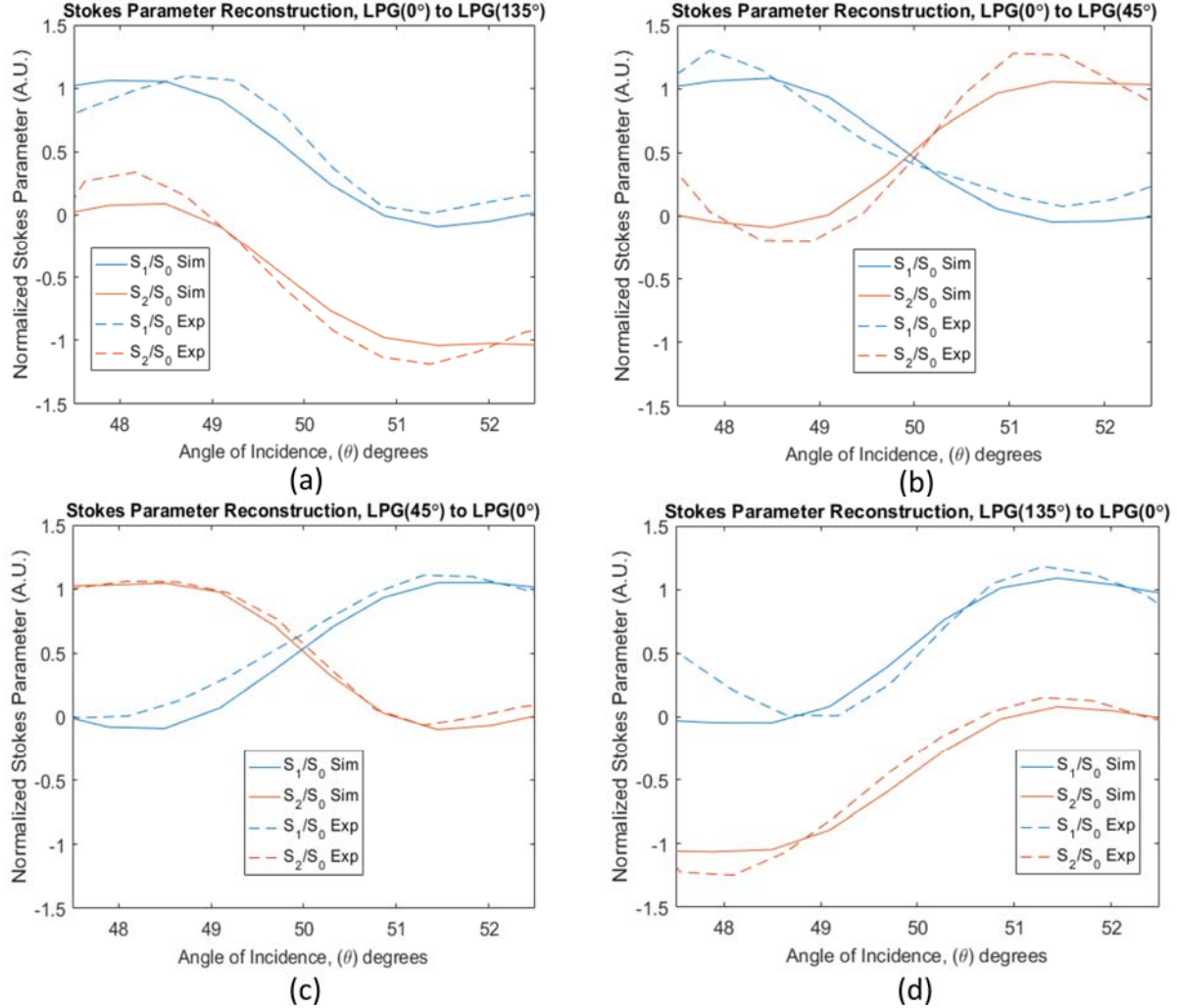


Fig. 90. Simulation (Sim, solid lines) and experimental (Exp, dashed lines) reconstruction results for the normalized angularly dependent Stokes parameters, S_1/S_0 (blue lines) and S_2/S_0 (red lines), versus angle of incidence for the Stokes step function scene. State of polarization across the FOV goes from (a) 0° to 135° , (b) 0° to 45° , (c) 45° to 0° , and from (d) 135° to 0° .

As with the uniform scenes, RMS error between the simulated and experimental reconstructions was calculated by Eq. (125). However, due to the change in the filter used to extract the channels, the Gibbs phenomenon is more prominent in the step function reconstructions and RMS error was calculated over a smaller range in incident angles (9 sampling points over $\theta_0 \in [47.5^\circ, 52.5^\circ]$). Calculated RMS error for the Stokes step function reconstructions are presented in Table 4. These are on a similar order of magnitude to our prior spatial reconstructions without polarization per Fig. 72.

Table 4. RMS Error calculations for reconstruction of normalized Stokes parameters for the step function scene

LPG Orientation		RMS Error	
θ_{\min} to θ_0	θ_0 to θ_{\max}	S_1/S_0	S_2/S_0
0	135	0.1105	0.1439
0	45	0.1497	0.1352
45	0	0.1072	0.0341
135	0	0.0945	0.0881

5.0 Four-Dimensional Object-Space Data Reconstruction Using Spatial-Spectral Multiplexing

This section investigates the data reconstruction problem of a four-dimensional scene based on the Spatial-Spectral Multiplexing (SSM) technique. The SSM technique is used in a hyperspectral imaging system for the application of passive remote sensing. The section first introduces the current development of the remote sensing field and its associated applications. The SSM technique, in particular, provides unique advantages over other systems in use for developing longitudinal spatial coherence holograms because it can enable snapshot measurements of a coherence function. Additionally, this technique can enable access to interference patterns that can be decomposed to access the phase information that is present (but inaccessible) in the pupil of a conventional lens. Finally, due to this phase-sensitivity, the technique can also enable an alternative interference-based method for passively sensing distance without the need for stereoscopic co-boresighted objectives or active illuminators. In this section, the concept is applied to the field of hyperspectral imaging because it can serve as a feasible problem to ascertain methods of data reduction and reconstruction. Since the algorithm is based on the SSM system, the section illustrates its optical model and its related modulation model. Such a model yields a challenging data reconstruction problem.

The goal of data reconstruction in the context of SSM and hyperspectral imaging is to use measurements from a given measurement matrix to recover the scene's object locations and object spectra. This can be formulated as an underdetermined linear system, thereby producing an infinite number of potential solutions. The research work in this section proposes to solve the inverse problem by incorporating several heuristic prior assumptions and formulate an optimization from a probabilistic perspective. Based on this notion, this section proposes two categories of reconstruction methods: non-parametric and parametric. In particular, the section shows that by incorporating B-splines to reparameterize the object spectra, the number of unknown variables is highly reduced in the linear system, so it can achieve a much more accurate and efficient reconstruction for large scale data.

In order to validate the algorithm, three kinds of synthetic ground truth scene objects are generated, with which the modulation model can simulate the measurements and the measurement matrix based on the SSM technique. To demonstrate the accuracy and efficiency of this algorithm, the section compares the non-parametric method and parametric method based on several reparameterization methods at various data scale. Besides, the Poisson noise with different SNRs is also added onto the measurements before optimization in order to test the algorithm's robustness. To be specific, this reconstruction algorithm is shown to be effective on both smoothly varying and point cloud objects for the SSM system. It can achieve a 0.2% overall MSE without noise, and 0.3% overall MSE with noise (SNR greater than 30). The algorithm can handle a quite large data scale with the reparameterization method. The

results of this section show the potential of applying such reconstruction methods on real-life scenes in the future.

5.1 Introduction

This section will first introduce the development, applications and current limitations of the remote sensing. Then it will analyze some hyperspectral imaging techniques that are widely used to improve remote sensing technology, and will also propose a Spatial-Spectral Multiplexing (SSM) technique, which can be used in hyperspectral imaging. Based on these theoretical backgrounds, the section will introduce the modulation model of the SSM system, which is also the optical model for this reconstruction algorithm. After that, it will briefly describe the research purpose and give an outline of the proposed methods. Additionally, an overview of the following content will be presented in the end of this chapter.

5.2 Background

5.2.1 Development in the remote sensing field

The term "remote sensing" was first used in 1960s by a scientist of U.S. Navy's Office of Naval Research [55]. There are various definitions for remote sensing. Generally speaking, remote sensing is a scientific technology of acquiring information from an object, an area or any phenomenon and analyzing the acquired data [68]. The devices or sensor systems used to obtain these useful data are not directly in contact with the objects need to be identified or measured [71].

It has been well-known that the sensors could be divided into active and passive based on the source of energy. Remote sensing that relies on solar and terrestrial energy belongs to the passive sensor systems. Taking the example of the solar energy, which accounts for the vast majority of the non-human-made sources, the sunlight is reflected, emitted or transmitted from the objects and recorded by the passive devices. There are also remote sensing systems working with active sensors [66], which emit the energy sources such as radar, sonar and laser by themselves [64]. These remote sensing systems provide human-made energy sources to scan the object then measure the returned energy [59]. According to the wavelength region, there are three categories: (1) visible and reflective infrared, (2) thermal infrared and (3) microwave remote sensing [65]. The former two types are passively detected, while the microwave type can be based on either passive or active sensors. The algorithms and techniques provided here are aimed to be applied for passive, visible and reflective infrared remote sensing.

One of the most straightforward passive sensors for remote sensing are eyes [61]. Human beings have been eager to know about the earth and space since a long time ago. Not limited to their eyes, humans began to make use of external tools, such as telescopes, to visualize the area outside the field of view. The invention of photography was another milestone in the history of remote sensing. Using the photography technology, humans tried to observe the ground and take photographs at a greater height on the mountain or in a balloon. During this initial period, remote sensing were still referred as aerial photography [73]. Afterwards, the technique of aerial photography steadily evolved due to the improvement in platforms, camera hardwares and photo interpolation techniques. The rapid growing of interests in remote sensing started after the successful launch of artificial satellites. To date, there are three main platforms in remote sensing: ground-based, airborne and space borne [65]. As the name implies, they are classified by the height from the earth's surface. The remote sensors are mounted on these platforms to detect the electromagnetic energy reflected from the earth's surface, which can be mapped to the prior knowledge of some features [67]. Multispectral images are one of the most

common images acquired by the remote sensors. In recent years, further improvement in sensors and satellites has greatly increased the quality of data and the accuracy of mapping by providing us not only multispectral images but also hyperspectral images [76].

Remote sensing has played an increasingly vital role in numerous applications fields. These include crop monitoring and type classification in the field of agriculture; flood, landslides and volcanic activity observation; geological structure mapping and natural resources exploration. There are also many promising applications in the field of hydrology, oceanography, glaciology, forest, climate, urban, military and meteorology [62]. With remotely sensed images and data, human beings have widely broadened the field of view and range of cognition.

These applications, however, can still be limited by the quality of image data, especially the image resolution and sampling frequency. There are some important properties of the remote sensing data: spatial resolution/sampling, radiometric resolution, spectral resolution/sampling and temporal resolution/sampling. Specifically, we focus on the spatial and spectral resolution/sampling, which relates to the properties of the spectrometer and the optical resolution of the SSM aperture.

5.2.2 The SSM technique

In order to surpass the limit of image quality, some new imaging techniques have been proposed to acquire a higher spectral resolution and a larger spatial coverage for remote sensing. For example, the multispectral imaging makes it possible to obtain the spectral features of many bands simultaneously [75]; hyperspectral imaging [58] makes it possible to acquire continuous and complete spectral information of each spatial location across the scene [78]. The most important part of these imaging spectroscopy methods are the imaging sensors have very high spectral resolution. Using such hyperspectral imaging techniques, a conventional way to obtain the three-dimensional (3D) spatial and spectral information of a scene is to use temporal scanning to scan the entire scene with a two-dimensional (2D) sensor. However, this method can only be applied on static objects [69]. Other non-scanning methods, such as the snapshot approach, have also achieved major advances. Snapshot spectral imaging can record a 3D object-space datacube by multiplexing the high-dimensional signal onto the 2D sensor [79].

With the same motivation, the SSM theory was also presented in [80]. The pivotal idea behind the SSM technique is that it can encode angular information of a scene onto the incident power spectrum. To be specific, the SSM technique uses the two-beam interference, generated from a spectrally-resolved interferometer, to represent every object point and to modulate the angular spectrum (incident angle) of each object point onto a spectral carrier frequency using the Fourier basis function. This means that the resultant channeled spectrum contains both phase and amplitude information, such that the spatial and spectral content of the scene can be reconstructed. Additionally, the SSM technique enables phase retrieval to be achieved from the pupil of an imaging system, without the use of a lens. Based on this SSM technique, the spatial-spectral multiplexer can be agnostic, and includes interferometers such as Fabry Perot Etalon (FPE), Michelson Interferometer (MI), MachZehnder (MZ) interferometer, etc.

Compared with the other state-of-the-art hyperspectral imaging techniques, the advantages of SSM are: first, it can encode four-dimensional(4D) scene information using 3D spectrometer measurements, which can reduce the amount of data needed during the measurement. Second, the SSM technique uses a 3D spectrometer array to sample the pupil of the spatial-spectral modulator, so that we do not need to form images before reconstruction, which provides a more computational imaging process. The limitation of

SSM is that it has not achieved much improvement in the spatial resolution in hyperspectral imaging.

5.2.3 Optical model of SSM systems

The measurements of SSM systems are simulated through modulation. The 2D modulation is needed to encode the object information onto the 2D spectrometer array for a 4D object-space data reconstruction. A 3D object can also be reconstructed by simulating the 1D modulation, because the system only need a 1D spectrometer array to sample the pupil. Since the SSM technique uses two-beam interference to modulate the spatial information onto the power spectrum, there are two point sources for each spatial location of the object in this model. As shown in Fig. 91, the red spot is one of the actual object sampling points. The blue and green ones are the two simulated point sources. Fig. 91 illustrates the modulation process for each of the y-z planes in the 2D case.

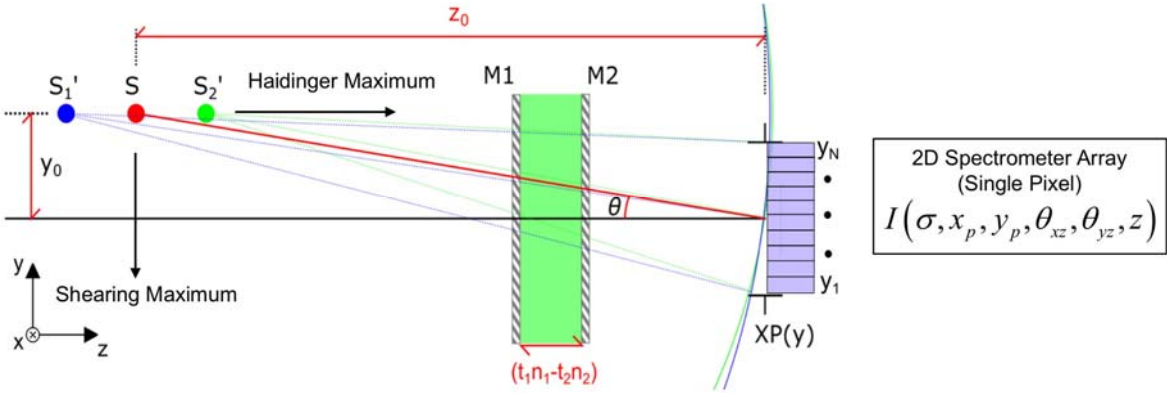


Fig. 91. Two dimensional illustration of the model used to develop the SSM technique using a two-beam interferometer and spectrometer array.

The 4D object is in the space of the Cartesian product of the 3D spatial domain and the 1D spectral domain, which can be expressed by a 4D function $f(\sigma, \theta_{xz}, \theta_{yz}, z)$. Here, σ is the wavenumber, θ_{xz} and θ_{yz} are the incident angles in x - z and y - z planes, and z is the distance from the object sampling point to the pupil plane in z direction. For notational simplicity, the following theory will also use f to denote the 4D object function $f(\sigma, \theta_{xz}, \theta_{yz}, z)$. The measurement with the 2D-spatial pupil plane $g(\sigma, x_p, y_p)$ is simulated by the dot product between the measurement matrix H and object f , as shown in Eq. (164).

$$g(\sigma, x_p^i, y_p^i) = \sum_{n=1}^N \sum_{m=1}^M \sum_{k=1}^K H(\sigma, x_p^i, y_p^i, \theta_{xz}^n, \theta_{yz}^m, z^k) \cdot f(\sigma, \theta_{xz}^n, \theta_{yz}^m, z^k), \quad (164)$$

where i, j, m, n and k are the indexes of the variables. Assuming a perfect spherical wave, the channeled spectrum $H(\sigma, x_p^i, y_p^i, \theta_{xz}^n, \theta_{yz}^m, z^k)$ is computed as follows:

$$H(\sigma, x_p^i, y_p^i, \theta_{xz}^n, \theta_{yz}^m, z^k) = \frac{1}{2} [1 + \cos(2\pi\sigma(r_1 - r_2))]. \quad (165)$$

The two beams pass through the interferometer and are combined to generate the channeled spectrum. Therefore, the measurement matrix H is made of the channeled spectra between each object point and each detector location. In Eq. (165), r_1 and r_2 are the distances from the two object point sources to the spectrometer, which can be computed by

$$r_1 = \sqrt{\left\{ \left(x_p^i - z^k \tan(\theta_{xz}^n) \right) \right\}^2 + \left\{ \left(y_p^i - z^k \tan(\theta_{xz}^m) \right) \right\}^2 + \left\{ z^k - OPD(\sigma / 2) \right\}^2}, \quad (166)$$

$$r_2 = \sqrt{\left\{ \left(x_p^i - z^k \tan(\theta_{xz}^n) \right) \right\}^2 + \left\{ \left(y_p^i - z^k \tan(\theta_{xz}^m) \right) \right\}^2 + \left\{ z^k + OPD(\sigma / 2) \right\}^2}. \quad (167)$$

Here the Optical Path Difference (OPD) has either a positive sign or a negative sign depending on which one of the two point sources is being measured. Note that the OPD can be defined differently according to the specific spatial-spectral multiplexer to be used. Details of this SSM model can also be found in [80]. Such a model motivates the need of object reconstruction; that is, given the simulated measurements g and the measurement matrix H , the goal is to estimate the object f .

This Eq. (164) is essentially a linear equation. However, the number of pupil planes is smaller than the number of sources. Therefore the SSM system is an underdetermined linear system, which means the algorithm do not have enough information to uniquely solve for the spectrum of the object f . Therefore, to optimally recover f , some additional appropriate assumptions need to be incorporated into the object scenes. These assumptions will be further described in Sec. 5.6.1.1.

5.3 Four-dimensional scene reconstruction using SSM

This section illustrates the problem going to be worked on and the research purpose. As introduced in the background section, remote sensing relies on images with very fine spatial and spectral resolutions. The hyperspectral imaging is a widely used and rapidly growing imaging technique in the remote sensing field. The problem needs to be solved is to develop an reconstruction algorithm for an optical system using a new SSM hyperspectral imaging technique. Different from other hyperspectral imaging methods, the SSM system provides a more computational way to obtain the spatial and spectral information of a scene and stores much less amount of measurements. The method that the SSM technique uses to acquire the image information is computational imaging as it encodes the scene information onto a 2D spectrometer array, which is used to sample the pupil plane. The idea is that instead of producing complete sub-images with the same level of spatial dimensions as the object, the SSM system only needs to record the multiplexed information with the same dimensions as the detector plane.

Using the SSM technique, the goal is to develop an algorithm to reconstruct 4D object-space data from the measurements acquired by the 2D pupil planes. The 4D object-space data can be a specific scene with 3D-spatial and 1D-spectral information, as what we can perceived from the world around us. In the experiments, the scenes are indicated by point clouds. The requirements of this reconstruction algorithm are: (a) to work on different realistic objects, including extended, random points and point clouds sources; (b) to deal with relative large data sets (roughly 15 Gigabytes) within an acceptable running time; (c) to achieve high accuracy in cases of both with and without Poisson noise.

5.4 Methodological design of the reconstruction algorithm

This section gives an outline of the methodologies. There are two main challenges in the reconstruction algorithm: (a) since the SSM system only stores a small amount of multiplexed information, the object from a highly underdetermined linear system (the number of unknown variables is larger than the number of linear equations) needs to be recovered, and a direct psuedo-inverse will produce meaningless results; (b) the size of the 4D object is extremely large. A

non-parametric representation of the object will lead to a large-scale linear system that is numerically difficult to solve. In the experiments, a simple $1000 \times 10 \times 10 \times 10$ object with a non-parametric representation will cost 100 Megabytes storage, and the reconstruction can be extremely time consuming.

To handle the first challenge, the algorithm proposes several heuristic prior assumptions that can adapt to the realistic 4D scenes, and with these priors the algorithm can uniquely recover the object. Moreover, an optimization model is constructed to minimize the least square reconstruction error with the constraints of the aforementioned heuristic assumptions. To deal with this second challenge, the algorithm proposes to reparameterize the 4D object data with certain basis functions to reduce the number of unknown variables in the linear system. Several parametric models based on the eigenfunctions of Gaussian kernels and basis splines are tested and compared. Additionally, a memory-efficient numerical method is also applied to accelerate the optimization process.

5.5 Experimental materials and setup

Before giving the technical details of the proposed reconstruction methods, this chapter demonstrates the experimental materials and the parameter settings of the SSM model. In this work, the experimental materials for validating the reconstruction algorithms are several synthetic scenes. The main reason for using synthetic scenes in the experiment is that the use of SSM systems, including the optical model and the reconstruction methods, is still in its preliminary stage. With the manually constructed ground truth objects in synthetic scenes, I can exactly validate the reconstruction algorithm and draw insights from the results. Therefore, a common experimental setup is to first construct a ground truth synthetic scene (a synthetic object f) and to use the SSM optical model to produce its measurements in the detector. Finally, the object will be reconstructed, denoted as f^* , from the measurements and compare the reconstructed object f^* with the ground truth object f to validate the reconstruction algorithm's accuracy.

Three kinds of objects will be designed to be recovered by the reconstruction algorithm. In order to test the generality of the algorithm, these objects have very different properties. To test the algorithm robustness, the noise will be added to the measurements before the reconstruction. Sec. 5.5.4 will describe the adding noise procedure and the associated experiment setup in detail.

5.5.1 Three-dimensional piecewise spiral curves

The first type of synthetic object is a 3D-spatial spiral curve, which is generated from the following steps:

- (a) Construct a spiral curve in the 3D-spatial space;
- (b) Randomly break the spiral curve into four intervals;
- (c) Randomly set different radii to the four spiral pieces;
- (d) Shift the four intervals apart along the z-axis;
- (e) Smooth the object using a 3D Gaussian filter.

In this way, it becomes spatially smoothed 3D spiral curves with some random radii. Fig. 92 (a) shows the piecewise spiral curve object, where x and y denotes the θ_{xz} and θ_{yz} dimension of the object $f(\sigma, \theta_{xz}, \theta_{yz}, z)$ in Eq. (164). The corresponding 3D datacube is then generated and Fig. 92 (b) shows three 2D cross-sectional slices. Each cross-sectional plane in Fig. 92 (b) is labeled as a corresponding color as in the Fig. 92 (a).

Due to the way of constructing the curve and the 3D Gaussian smoothing, the object is spatially smooth almost everywhere in the 3D-spatial space except for those breaking points (step (b)). The next chapter will show that this spatial smoothness nature plays a very important role in this reconstruction algorithm. The 3D-spatial space is known as the hyperplane, and the spectrum on every spatial hyperplane is the same, which is set to be smoothly varying from 0.1 to 1. This 1D spectrum corresponds to the a dimension in f .

5.5.2 Multiple random points

The second type of object is a random point cloud. To construct this kind of object in spatial space, it needs to define a fixed number of points in the 3D space. Assume the 3D datacube has N voxels and M points need to be generated in it, a random sample without replacement is performed to draw M positions from the N candidates.

Then different smoothly varying spectra are set to each of these points. The spectrum of a point is assumed to be one of the four functions sampled from a Gaussian Process $GP(m, K)$. A Gaussian process (GP), written as $X \sim GP(m, K)$, defines a distribution, in which the random continuous function X is distributed with mean function m and covariance function K . Since a GP defines a probability distribution on the space of continuous functions, the spectral intensity functions can be sampled from it. Here, a very important property of GP is used: every point in the continuous input space (domain of X) is associated with a normally distributed random variable; every finite collection of those random variables has a multivariate normal distribution, whose covariance matrix can be derived using the covariance function K . Therefore, if a function measured on N discrete points in a needs to be sampled, a N -dimensional multivariate Gaussian has to be defined, whose mean is the discrete realization of m . Each entry of the covariance matrix is computed by $K(x, x')$, where x and x' are two of the \underline{N} discrete points. Here, the covariance function is

$$K(x, x') = \exp\left(-\frac{\|d\|^2}{2l^2}\right), \quad (168)$$

where $d = x - x'$, l is the characteristic length-scale parameter. Finally, the functions are sampled from that multivariate Gaussian. After the four spectral intensity functions are generated, they are scaled to be positive and normalize them to the range of [0.2, 1.2]. The spectrum of each spatial location (voxel) is randomly assigned with one of the four spectral intensity functions. Fig. 93 shows four randomly generated spectral intensity functions with $l = 3 \times 10^5$. Such a large l can ensure the functions' smoothness.

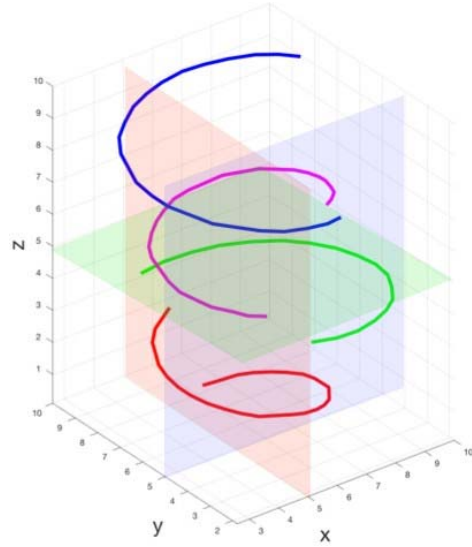


Fig. 92a. 3D-spatial spiral piecewise-smooth object

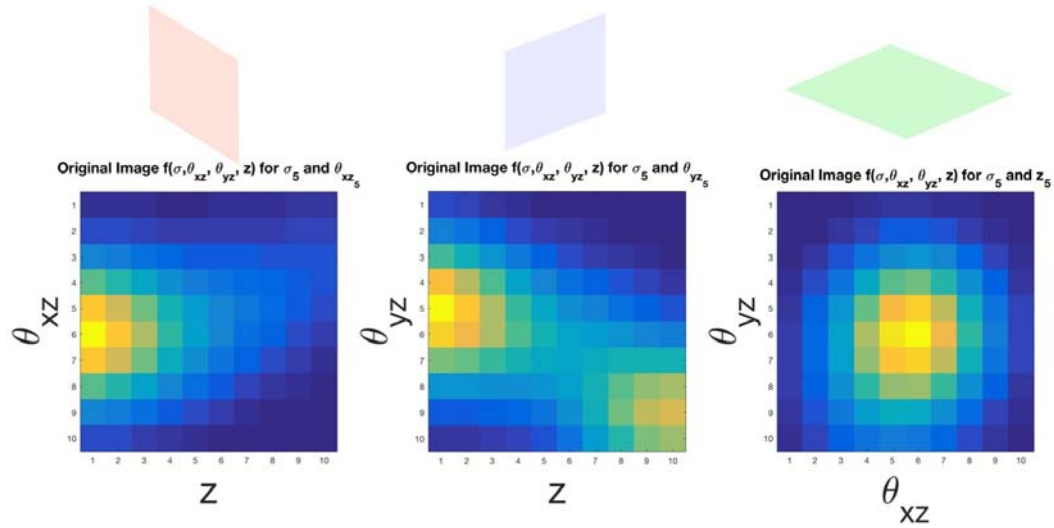


Fig. 2b. The 2D cross-sectional planes of the spatially smoothed spiral curve object associated with the fifth position in the other dimension

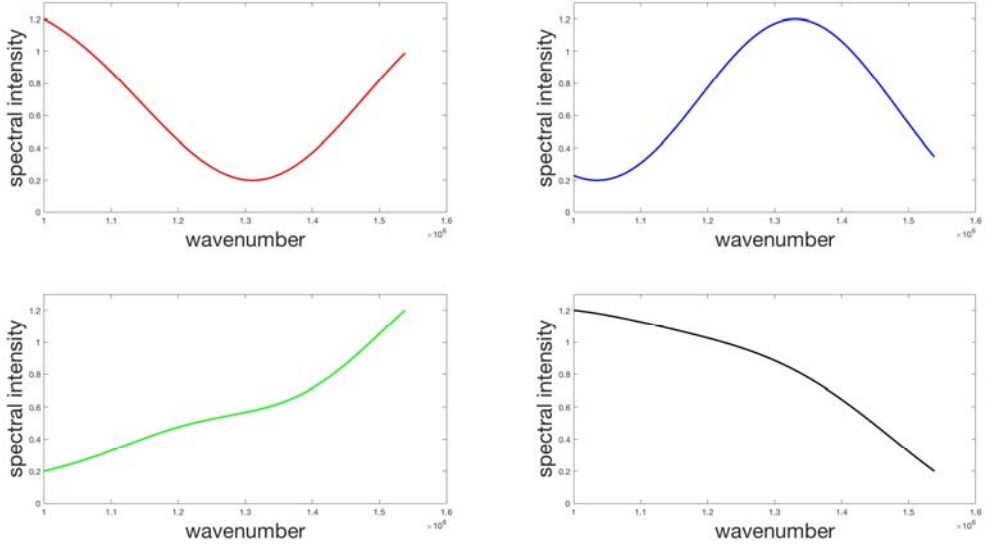


Fig. 93. Spectral intensity functions sampled from Gaussian process.

Fig. 94 shows the ground truth of three 2D cross-sectional planes of a synthetic point cloud with 100 sampled points in a 3D spatial datacube. The spectra of the points are color-coded with four different colors, corresponding to the four spectral intensity functions.

Compared to the spiral curve object, this point cloud object is more difficult to be accurately reconstructed due to the following three facts.

- (a) *The object is more complicated.* There are about 10 points in each 2D cross-sectional planes, but in previous spiral object, there are only 1 or 2 points per plane. Thus what needs to reconstruct is a mazy-like pattern.
- (b) *The object is not spatially smooth.* No Gaussian filter is applied to the point cloud object, meaning the intensity at each location is independent to others so that smoothness constraints can not be added between neighboring locations.
- (c) *The object has more complex spectra.* A randomly selected spectral intensity function is added for each spatial location, whereas in the spiral curve object, the spectral intensity on each spatial hyperplane is the same.

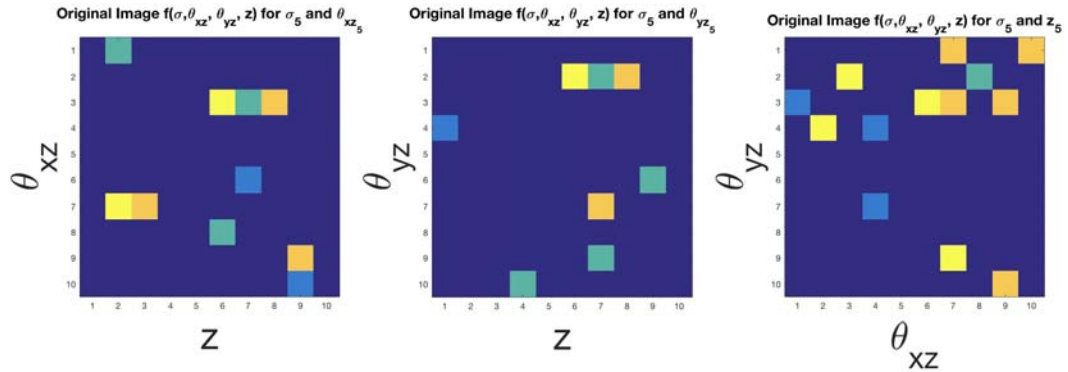


Fig. 94. Cross-sectional planes of the ground truth object with 100 random points

5.5.3 A specific scene

This section presents a further more complicated and specific object, which is a specific scene that consists of three bar objects. The shape of the bar is also represented using a point cloud. As shown in Fig. 95 (a) and (b), the three bars are placed diagonally in the spatial 3D space. Each bar contains 32 sample points divided into 4 x-y planes. The spectral intensity on each spatial location is generated using the same method as the previous point cloud object. Fig. 95 (c) shows three cross-sectional planes.

To adequately demonstrate the bar shape of the point cloud, the spatial resolution of the object needs to be increased. Moreover, the sampling points have been doubled: 288 sampling points each a in the spectrum direction compared to the previous objects (100 sampling points each a). The detector size and detector resolution are also increased to improve the condition of determination. All these facts lead to a much larger linear system with a huge number of variables to be estimated. The later chapter will show later that a simple non-parametric representation of the object will be computationally challenging, thereby motivating the parametric reconstruction methods.

5.5.4 Experimental setup

To setup the experiments, there ground truth objects $f(\sigma, \theta_{xz}, \theta_{yz}, z)$ (the object models described above) are designed. All of these three kinds of objects are put in the same spatial location in the modulation model with the incident angle from 45° to 55° and the distance of z from 1m to 4m. They have the same range of wavelength $\lambda = 1/\sigma$ from 650 nm to 1000 nm. While the object's spatial resolution and spectrometer's detector resolution are set to be different so as to adapt to each model. For the object described in Sec. 5.5.1 and Sec. 5.5.2, the object resolution is

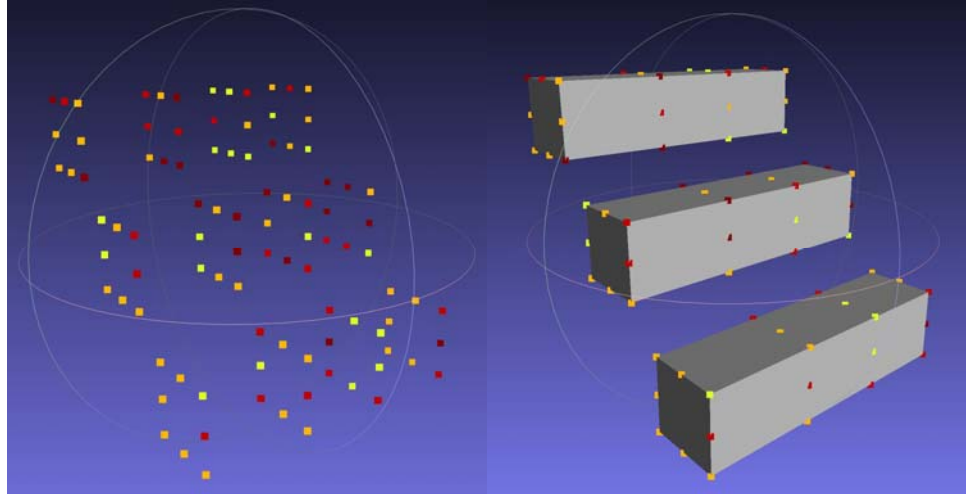


Fig. 95a. The 3-bar object shown as a point cloud. (b) The 3-bar object shown as a mesh using MeshLab (this is actual form of dataMeshLab, *i.e.* the conceptual illustration of how the algorithm deals with the object).

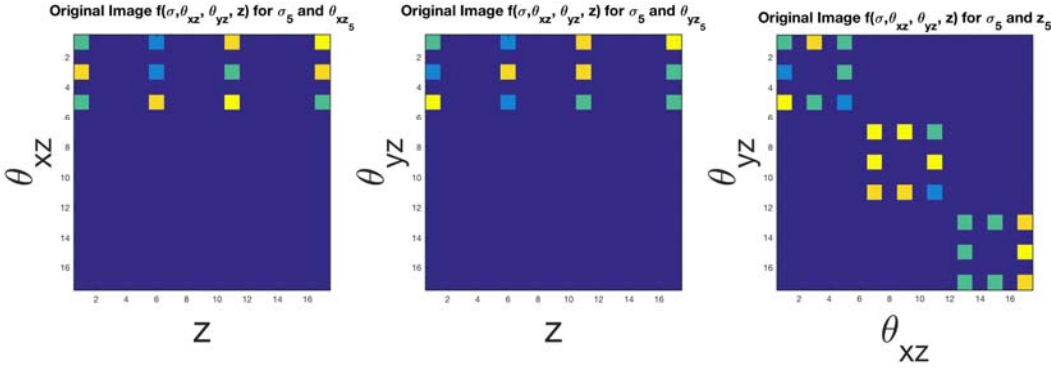


Fig. 5c. The 2D cross-sectional planes of the spatially smoothed spiral curve object associated with the fifth position in the other dimension.

1000 x 10 x 10 x 10, which means there are 1000 sampling points in σ and 10 sampling points in each spatial dimension. For the 3-bar object, the number of sampling points in σ is reduced and more points are sampled in the 3D space, so that the object resolution is 100 x 17 x 17 x 17. Then the corresponding measurements $g(\sigma, \theta_{xz}, \theta_{yz}, z)$ and the measurements matrix $H(\sigma, \theta_{xz}, \theta_{yz}, z, // \theta_{xz}, \theta_{yz}, z)$ need to be simulated. The spectrometer detector is a squared 2D plane, of which the side length varies according to the object type. The squared detector is set to be 5 cm for the spiral curve object, and 25 points are sampled within the detector (5 points for each spatial dimension), and have 25 equations for each wavelength λ . Thus the measurement resolution is 1000 x 5 x 5. The measurement matrix H is a 1000 x 5 x 5 x 10 x 10 x 10 6-dimensional matrix. Since the random point cloud object is more complex, the detector size is increased to be 10 x 10 cm², so that g has a 1000 x 10 x 10 resolution and H matrix becomes 1000 x 10 x 10 x 10 x 10 x 10. For the most challenging 3-bar scene object, the measurements g becomes 100 x 20 x 20 with a detector of 15 cm side length, so that H is 100 x 20 x 20 x 17 x 17 x 17.

There are various noise in imaging systems, including photon noise, dark noise, read noise, etc. It has been shown that the photon noise[3] accounts for the majority of the total noise. Since the Poisson distribution can best model the photon noise, Poisson noise is added onto the measurements g before the reconstruction, and compare the reconstructed result to the one without noise to test the robustness of the algorithm. The mean of the Poisson distribution, which is the square of the Signal Noise Ratio (SNR), ranges from 5 to 30 in the tests.

5.5.5 Conclusion

This section introduced three types of ground truth objects that will be used to validate the reconstruction algorithm. It described the methods to generate these objects and their characteristics respectively. The spiral curves and the random point clouds will be used in both the non-parametric and parametric data reconstruction, while the 3-bar object will only be used in the parametric model due to its large number of variables and model complexity. It also gave the parameter settings of the SSM system for generating these ground truth objects, including the detector size of the spectrometer, the range of incident angles and the range of the spatial distance from the detector. Besides, it specified the spatial and spectral resolution for each kind of objects and their corresponding measurements. Additionally, it gave the range of SNR for the Poisson noise used in the robustness tests.

5.6 Non-parametric data reconstruction

With the given optical model and the sensor measurements, the goal is to reconstruct the object scene. This chapter introduces the technical details of the data reconstruction methods. Data reconstruction is a widely studied topic in pattern recognition [53]. Methods like deep learning and Bayesian inference have achieved success in many machine learning fields to solve the reconstruction and inverse problems. Considering the fact that the reconstruction system is an ill-conditioned inverse problem, it is proposed to use two optimization-based data reconstruction approaches. This chapter will introduce the first one: non-parametric data reconstruction method, with which all of the spatial/spectral variables in the object f need to be optimized. Then this chapter will describe an iterative numerical method used for solving such a large-scale optimization problem. Finally, it will present the reconstructed results for the spiral curves and the random point cloud object and analyze the existing problems of the non-parametric optimization.

5.6.1 Posterior optimization for an underdetermined linear system

As mentioned in Sec. 5.2.3, the object to be recovered is the 4D data. In the discrete setting, the simplest way to represent such an object is to have one variable for each frequency component of each spatial location; that is, f is represented by a discrete 4D data (dimension ordered by (σ, x, y, z)) with a dimension of $M \times N \times N \times N$. In other words, f is regarded as an $M \times N \times N \times N$ dimensional variable. Such a representation is called the non-parametric representation of the 4D data.

As discussed before, the algorithm is dealing with an underdetermined linear system with more unknowns than the number of equations, so the object f cannot be uniquely computed in a closed form. Therefore, f is viewed as a high-dimensional random variable and the algorithm tries to estimate it from a probabilistic perspective. The algorithm uses an optimization-based method to estimate f instead of directly solving the linear system by matrix inverse. The method is to formulate a probability distribution on the unknown object f and perform an Maximum-a-Posteriori (MAP) analysis [72]. The measurement matrix H can be generated based on the SSM system, and the measurements \mathbf{g} can be simulated from the synthetic ground truth object. These two given data can be the entry of the optimization method to estimate the object.

To be specific, the goal is to model the probability distribution $p(f|\mathbf{g}, H)$, which indicates the probability of observing f given the measurement matrix H and the measurements \mathbf{g} . By the Bayes' rule,

$$p(f | g, H) \propto p(g, H | f) p(f) \quad (169)$$

The posterior is proportional to the product of a likelihood term $p(\mathbf{g}, H | f)$ and a prior term $p(f)$. The goal then is to find the mode (minimizer of the negative logarithm) of $p(f|\mathbf{g}, H)$. Due to the fact that the system is an under-constraint linear system, some proper prior distributions have to be imposed on the f variable.

5.6.1.1 Heuristic prior assumptions

As mentioned above, the underdetermined linear system on f may lead to an infinite number of solutions. Therefore, a key step in the Bayesian analysis is to have a proper prior distribution

$p(f)$ to regularize the recovered object. There are two heuristic assumptions to construct $p(f)$: the spatial smoothness assumption and the spectral smoothness assumption.

The *spatial smoothness* assumption refers to the fact that in almost all situations, the intensity of an object across the spatial domain tends to be smoothly varying rather than randomly changing. This idea has been extensively applied to feature detection, image segmentation tasks [57] and image denoising [74]. In this case, it is assumed that the intensity of each frequency component of the 4D object is varying smoothly in the spatial domain (x-y-z coordinates). In other words, the spectral intensities of neighboring locations have strong correlation, meaning in each spatial hyperplane (the 3D space formed by x-y-z), the spectral intensity in one location will not change too much with respect to its neighbors in any of the three spatial (x, y and z) directions. In order to model this fact, a Gaussian distribution is imposed on the object's three spatially directional derivatives:

$$p(\nabla_x f) \propto N(0, I), p(\nabla_y f) \propto N(0, I), p(\nabla_z f) \propto N(0, I), \quad (170)$$

where $\nabla_v f$ is a vector containing spatial derivatives of spectral intensities for all spatial locations and all frequency components. $\nabla_x f$, $\nabla_y f$ and $\nabla_z f$ are the three spatially directional derivative operators associated with the three orthogonal spatial directions θ_{xz} , θ_{yz} and z in the 4D space. Discrete computation of such operations will be given at the end of this section. The zero-mean Gaussian encourages small spatial derivatives, thereby allowing spatially smoothness estimation of the object.

The *spectral smoothness* assumption means that for each spatial location (discretized location of the object), its 1D spectrum should also vary smoothly across all a planes (frequency components). Similar to the spatial smoothness situation, one possible way is to impose a Gaussian distribution on the spectral derivatives of the object.

$$p(\nabla_\sigma f) \propto N(0, I), \quad (171)$$

where $\nabla_\sigma f$ is a vector containing spectral derivatives for all spatial locations. Assuming the spatial smoothness and spectral smoothness can be modeled independently, the prior distribution $p(f)$ follows

$$p(f) \propto p(\nabla_x f) p(\nabla_y f) p(\nabla_z f) p(\nabla_\sigma f). \quad (172)$$

The negative logarithm of the prior distribution $p(f)$, also known as the data regularization term, has the following form:

$$-\log(p(f)) \propto (\lambda_1 \|\nabla_x f\|^2 + \lambda_1 \|\nabla_y f\|^2 + \lambda_1 \|\nabla_z f\|^2 + \lambda_2 \|\nabla_\sigma f\|^2), \quad (173)$$

where λ_1 and λ_2 can be viewed as the weighting factors between spatial smoothness and spectral smoothness, and they are essentially related to the Gaussian distributions' standard deviations. Normally the two weighting factors should be different, because the spatial smoothness and spectral smoothness are not commensurable. The spatial smoothness priors may be disabled by setting λ_1 to zero for the random point cloud and 3-bar scene objects, because point clouds inherently do not satisfy the spatial smoothness assumption. The spectral smoothness constraint is always in use for all objects, but λ_2 may be set to different values for

different spectral smoothness levels and different spectral resolutions. For example, a larger λ_2 is needed to model a higher smoothness level of the spectral intensity function with a larger l in Eq. (168).

5.6.1.2 Likelihood

Given \mathbf{g} and H , the estimated f should satisfy the linear relationship in Eq. 1.1. This corresponds to a likelihood distribution that penalizes deviation from that linear equation. Rewriting Eq. 1.1 in a convolution format, the negative logarithm of the likelihood distribution can be defined as

$$p(g, H | f) \propto \exp \left(- \sum_{\sigma, x_p, y_p} \| g(\sigma, x_p, y_p) - H(\sigma, x_p, y_p) \otimes f(\sigma) \|^2 \right) \quad (174)$$

$$-\log(p(g, H | f)) \propto \sum_{\sigma, x_p, y_p} \| g(\sigma, x_p, y_p) - H(\sigma, x_p, y_p) \otimes f(\sigma) \|^2 + \text{constant}. \quad (175)$$

Note that this term is often referred to as the data matching term, because it encourages the estimated f to better explain the observed data \mathbf{g} and H . The following text slightly abuses this notation by denoting the linear relationship simply as $g - Hf$.

$$g(\sigma, x_p, y_p) - H(\sigma, x_p, y_p) \otimes f(\sigma) \rightarrow g - Hf \quad (176)$$

5.6.1.3 MAP analysis

Maximizing the posterior of Eq. 3.1 is equivalent to minimize its negative logarithm, which corresponds to the following objective function:

$$\arg \min f - \log(p(f | g, H)) \quad (177)$$

$$-\log(p(f | g, H)) = \|g - Hf\|^2 + (\lambda_1 \|\nabla_x f\|^2 + \lambda_1 \|\nabla_y f\|^2 + \lambda_1 \|\nabla_z f\|^2 + \lambda_2 \|\nabla_\sigma f\|^2)$$

(178)

Here only the L2 norm is used in the data matching and regularization term. This naturally corresponds to the form of the Gaussian logarithm. The Gaussian distribution is preferred in many other applications due to its many elegant properties. One particular reason is that the quadratic term of L2 norm is easy to optimize numerically. However, it is known that for some specific situation, L1 norm is more desirable due to the fact that it can induce sparse solutions, which might be a more appropriate assumption for some applications. The downside of using the L1 norm is that numerical methods for L1 optimization are generally not well developed. This application chooses to use the L2 norm instead of the L1 norm.

Discrete computation of directional derivatives.

In the discrete situation, the derivatives are approximated by computing finite difference in the four directions as illustrated in the following. Using the non-parametric presentation of the object, $\nabla_v f$ is computed by

$$\nabla_v f = [\nabla_v f(0, 0, 0, 0), \dots, \nabla_v f(i, j, k, p), \dots, \nabla_v f(M, N, N, N)], \quad (179)$$

where v can be either one of $\{\sigma, x, y, z\}$

$$\nabla_\sigma f(i, j, k, p) = f(i+1, j, k, p) - f(i, j, k, p) \quad (180)$$

$$\nabla_x f(i, j, k, p) = f(i, j+1, k, p) - f(i, j, k, p) \quad (181)$$

$$\nabla_y f(i, j, k, p) = f(i, j, k+1, p) - f(i, j, k, p) \quad (182)$$

$$\nabla_z f(i, j, k, p) = f(i, j, k, p+1) - f(i, j, k, p). \quad (183)$$

5.6.2 The L-BFGS numerical method

After having an objective function for the data reconstruction model, the next step is to find an appropriate numerical optimization method. It can be seen that the above objective function Eq. (177) is quadratic. If the data dimension is small, the optimality condition can be directly written down as another linear system with the linear matrix operator being the Hessian matrix. However, if the data dimension is large, methods that require computing or inverting the Hessian of the objective function will be too time-consuming. Since the ultimate goal is to recover a 4D point cloud dataset with more than 10GB variables, it will be too expensive to directly compute the Hessian.

There are some popular quasi-Newton methods such as symmetric rank-one (SR1), Davidon- Fletcher-Powell (DFP) and Broyden-Fletcher-Goldfarb-Shanno (BFGS) algorithm, which can approximate Hessian with faster progress [77]. An advanced BFGS algorithm, Limited-memory BFGS (L-BFGS) [70] is applied, which is especially proposed for optimizing large scale problems with only a limited computer memory. Instead of computing and storing a dense $n \times n$ approximation to the inverse Hessian (n being the number of variables in the problem), L-BFGS stores only a few vectors that represent the Hessian approximation implicitly. Thus, it can achieve fast and accurate computational results for this problem. It used to cost 1.5 hours to run a preliminary 3D object with the data scale of only 80 MB. Using L-BFGS, it can reduce the running time of 80 MB data to 5 minutes, which is a huge improvement.

5.6.3 Reconstruction results

This section presents two experimental results using the non-parametric posterior optimization method. The first experiment is to verify the necessity of both spatial and spectral smoothness assumptions using the spiral curves object with a lower spectral resolution (100 spectral sampling points per location). The second one is to analyze the reconstruction results of the spiral curves and random point clouds with a higher resolution (1000 spectral sampling points per location).

5.6.3.1 Validation test of the spatial and spectral smoothness assumptions

In order to validate the two prior assumptions, the algorithm first recovers the spiral curves without using any regularization terms, meaning that it simply perform a matrix inverse (pseudo-inverse) to the underdetermined linear system. Fig. 96 shows six cross-sectional planes (three spatial cross-sectional planes in Fig. 96 (a) and three spectral cross-sectional planes in Fig. 96 (b)) of the ground truth synthetic object for reference. Note that, Fig. 96 shows the ground truth for all the rest reconstruction results of the spiral curves object. Fig. 97 shows the reconstruction results by pseudo-inverse for the same six cross-sectional planes as in Fig. 96. It can be seen that without any spatial and spectral regularization, a direct matrix inverse

does not yield meaningful results. Neither spatial nor spectral planes can be recovered to assemble the ground truth.

Then Fig. 98 shows the reconstruction results assuming spatial smoothness only. It can be seen that the three spatial cross-sectional planes are recovered much better. However, the spectra are still problematic due to the lack of constraints.

However, when assuming spectral smoothness only, it can achieve more accurate results in both the spatial and spectral cross-sectional planes as shown in Fig. 99. That means the spectral prior alone is more effective than the spatial prior alone.

If using both spatial and spectral assumptions, the all six cross-sectional planes can be very well recovered as shown in Fig. 100, which proves the importance of the two prior assumptions used in this method. The accuracy of the algorithm is quantified with two kinds of Mean Square Errors (MSE). One MSE is the overall MSE, which is computed by averaging the squared intensity error over all spatial locations and frequency components. The other one is sparse point MSE, which is computed only on those locations with object sampling points. Besides MSEs, the running time is another important aspect needs to be investigated. The goal of this algorithm is to achieve high accuracy with limited computational time. The overall MSE of the final experiment (with both prior assumptions) is shown in Fig. 100 is 0.85% (0.85% of the maximum intensity in the normalized object). The sparse point MSE is 10.08%. Since the 4D object is extremely high-dimensional, the running time of the optimization was about 1.5 minutes on an i7-3770k 3.50GHz Intel CPU processor.

5.6.3.2 Reconstruction results of high resolution objects

When using the high resolution $1000 \times 10 \times 10 \times 10$ object, the system have much more unknown variables in spectral dimension. As shown in Fig. 101, the non-parametric method cannot reconstruct well even with both prior assumptions. The overall MSE (0.92%) and the parse point MSE (10.17%) are both larger than the low resolution results and the running time is also much longer: 6 minutes.

When it goes to the random point cloud, the object is no longer spatially smooth. Therefore, the algorithm removes the spatial smoothness constraint and only optimizes with the data matching and spectral smoothness terms. Fig. 102 shows the ground truth for the random point cloud object and Fig. 103 gives the reconstruction results. The overall MSE of this experiment is 1.73%, and it also takes nearly 15 minutes on the optimization.

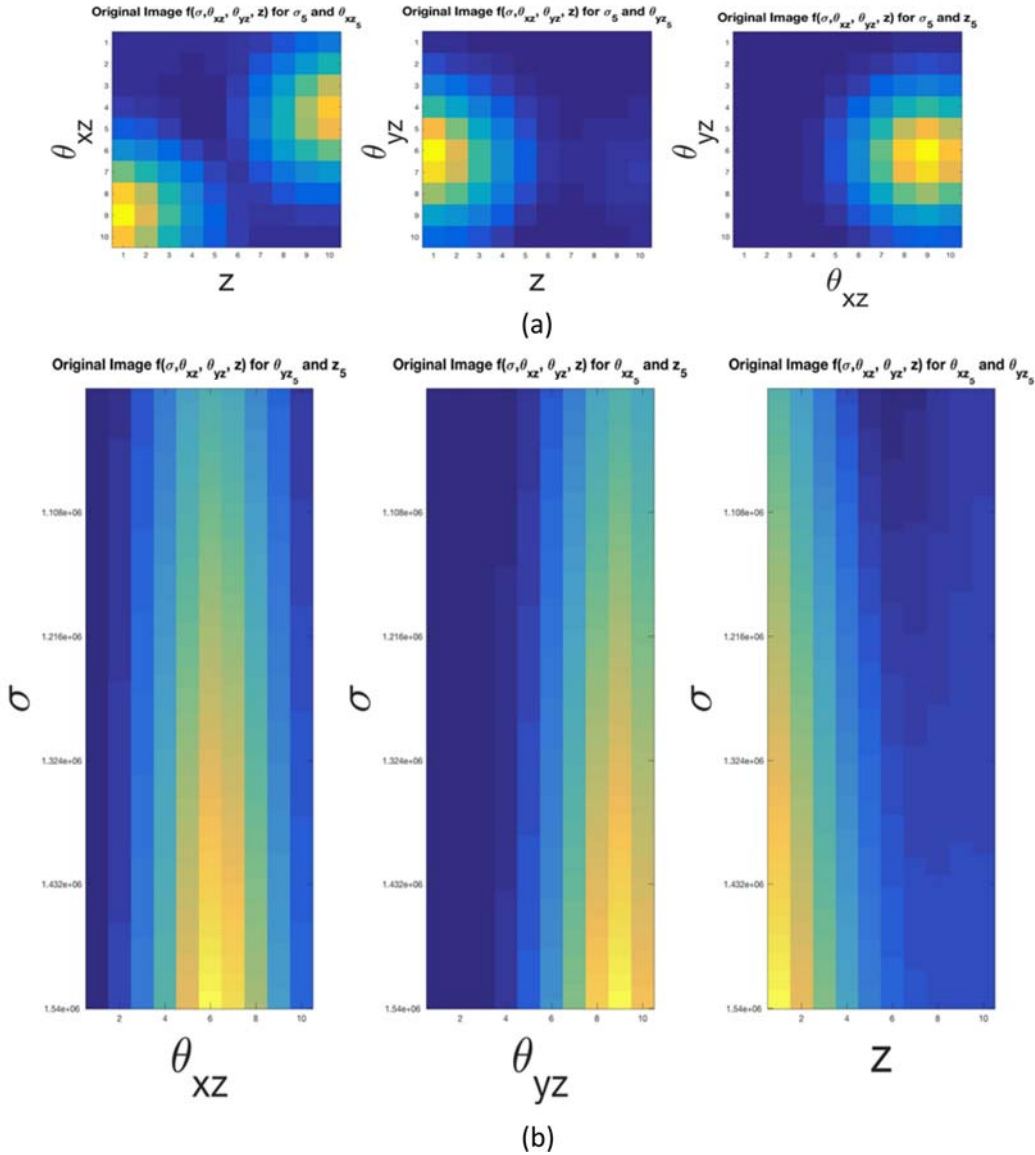


Fig. 96. Ground truth for the spiral curves object. (a) Three spatial cross-sectional planes of the ground truth spiral curves object. (b) Three spectral cross-sectional planes of the ground truth spiral curves object.

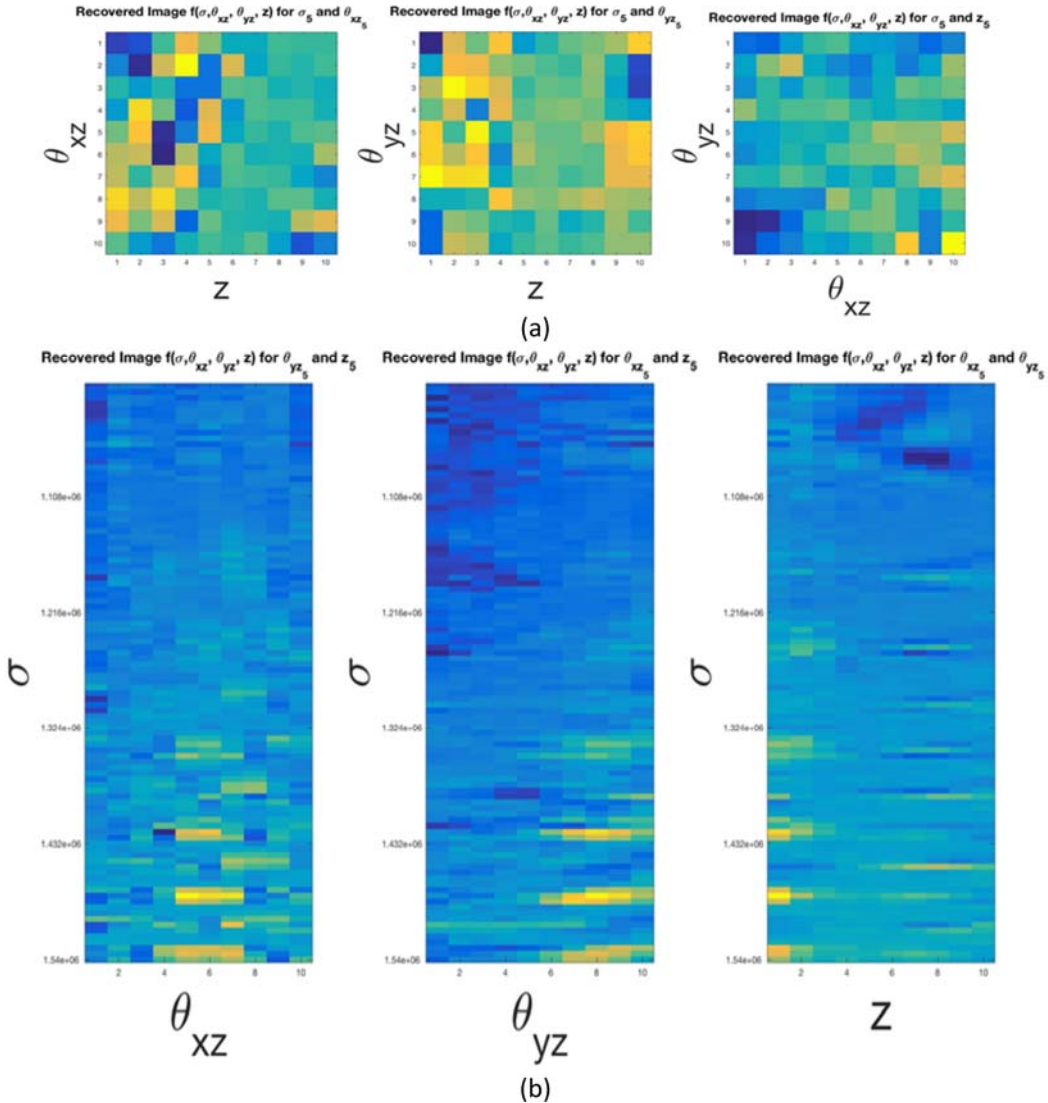


Fig. 97. Reconstruction results for the low resolution spiral curves object without using any prior assumptions. (a) Reconstruction results of the three spatial cross-sectional planes. (b) Reconstruction results for the three spectral cross-sectional planes.

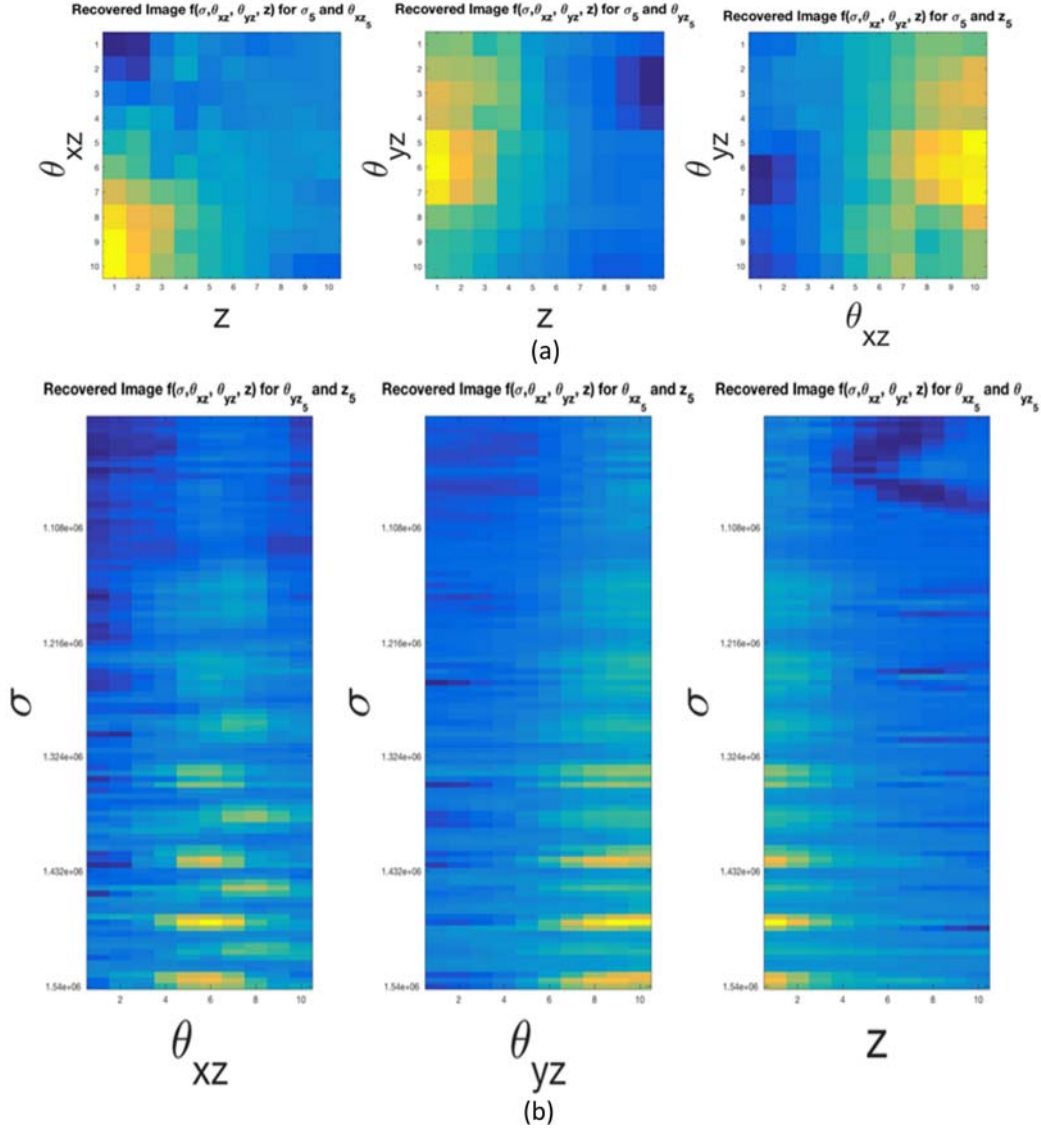


Fig. 98. Reconstruction results for the low resolution spiral curves object using the non-parametric method with the spatial smoothness assumption. (a) Reconstruction results for the three spatial cross-sectional planes. (b) Reconstruction results for the three spectral cross-sectional planes.

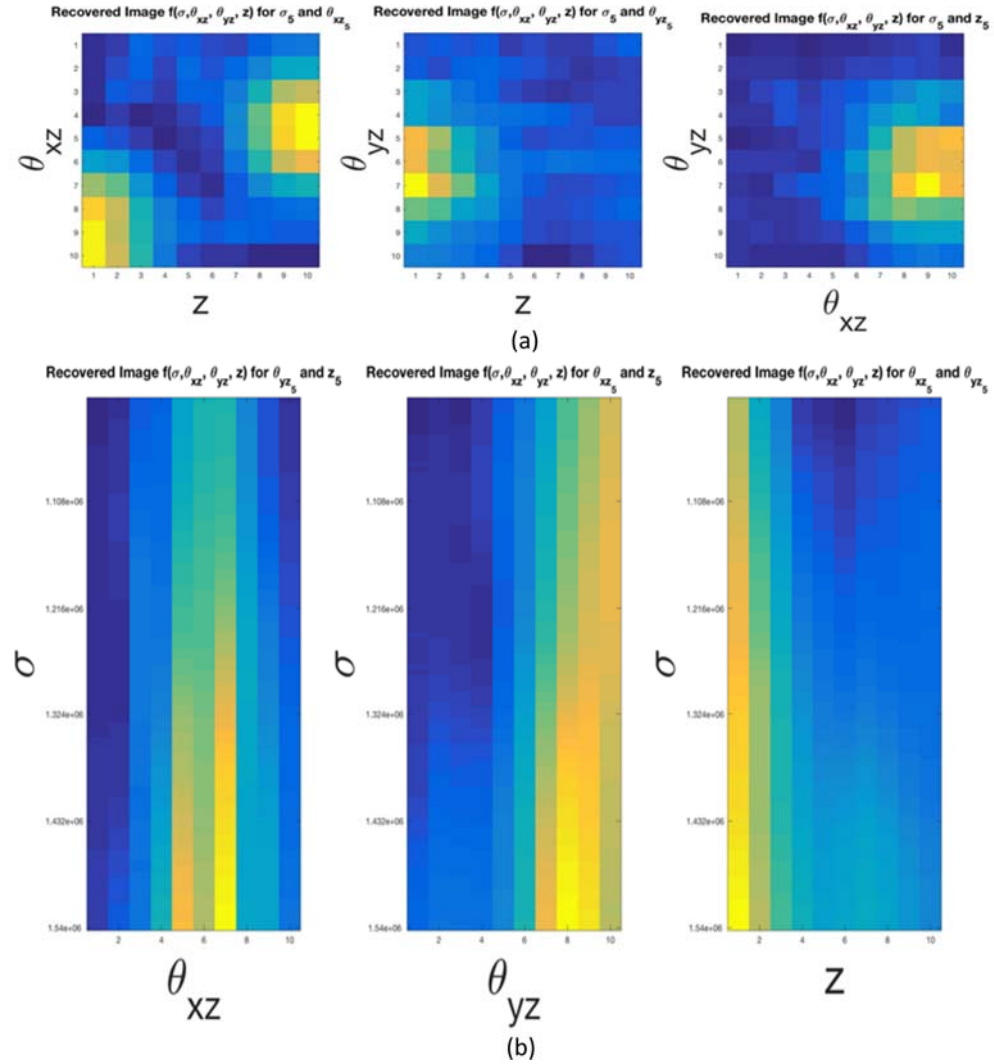


Fig. 99. Reconstruction results for the low resolution spiral curves object using the non-parametric method with the spectral smoothness assumption. (a) Reconstruction results for the three spatial cross-sectional planes. (b) Reconstruction results for the three spectral cross-sectional planes.

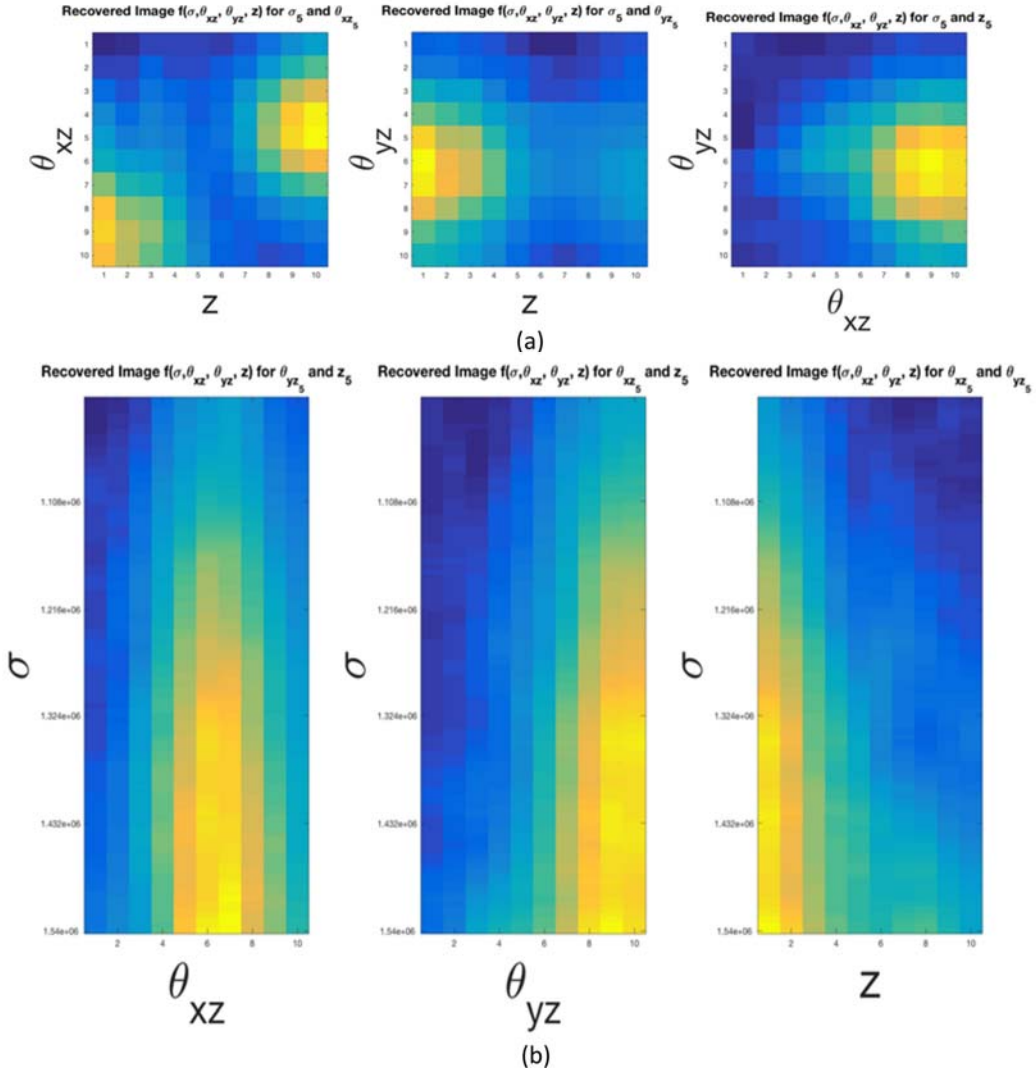


Fig. 100. Reconstruction results for the low resolution spiral curves object using the non-parametric method with both spatial and spectral smoothness assumptions. (a) Reconstruction results for the three spatial cross-sectional planes. (b) Reconstruction results for the three spectral cross-sectional planes.

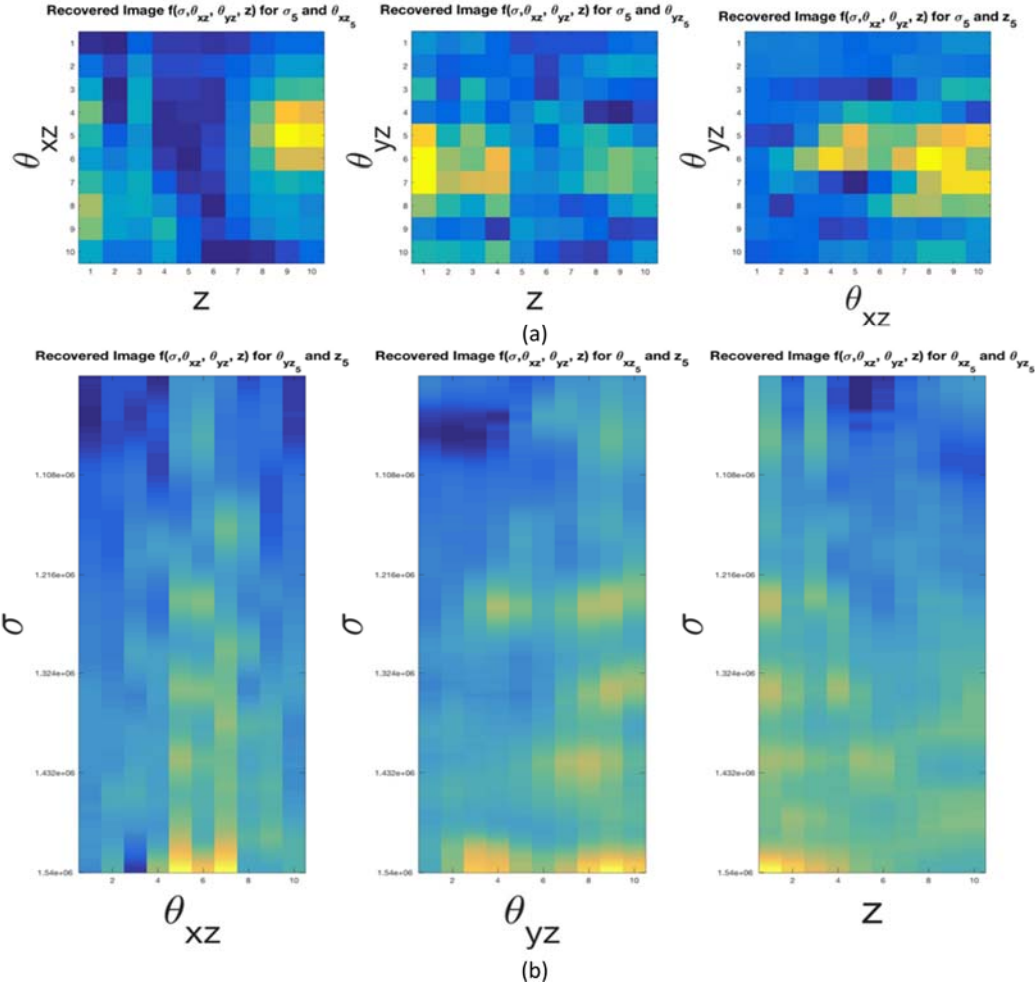


Fig. 101. Reconstruction results for the spiral curves object using the non-parametric method with both spatial and spectral smoothness assumptions. (a) Reconstruction results for the three spatial cross-sectional planes. (b) Reconstruction results for the three spectral cross-sectional planes.

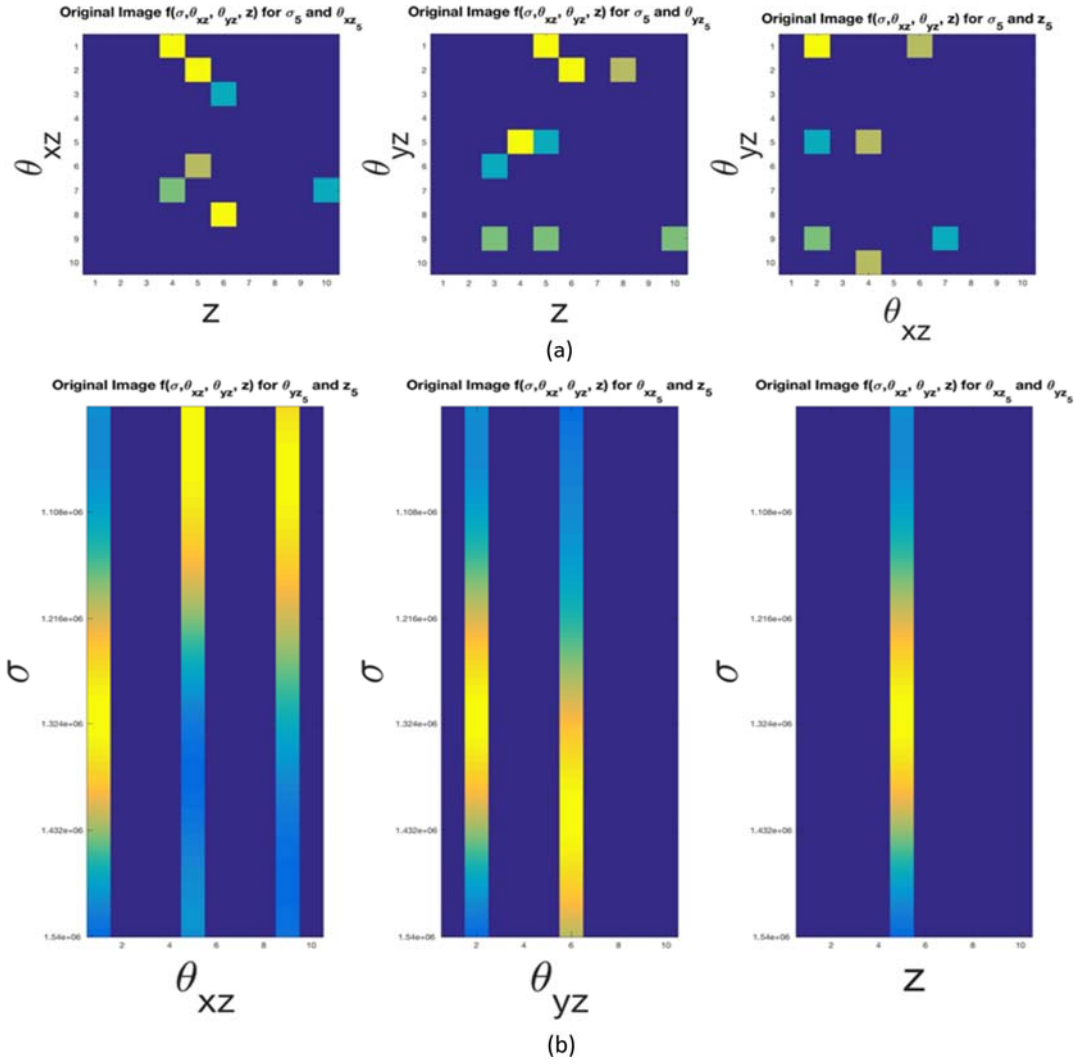


Fig. 102. Ground truth for the random point cloud object. (a) Three spatial cross-sectional planes of ground truth. (b) Three spectral cross-sectional planes of ground truth.

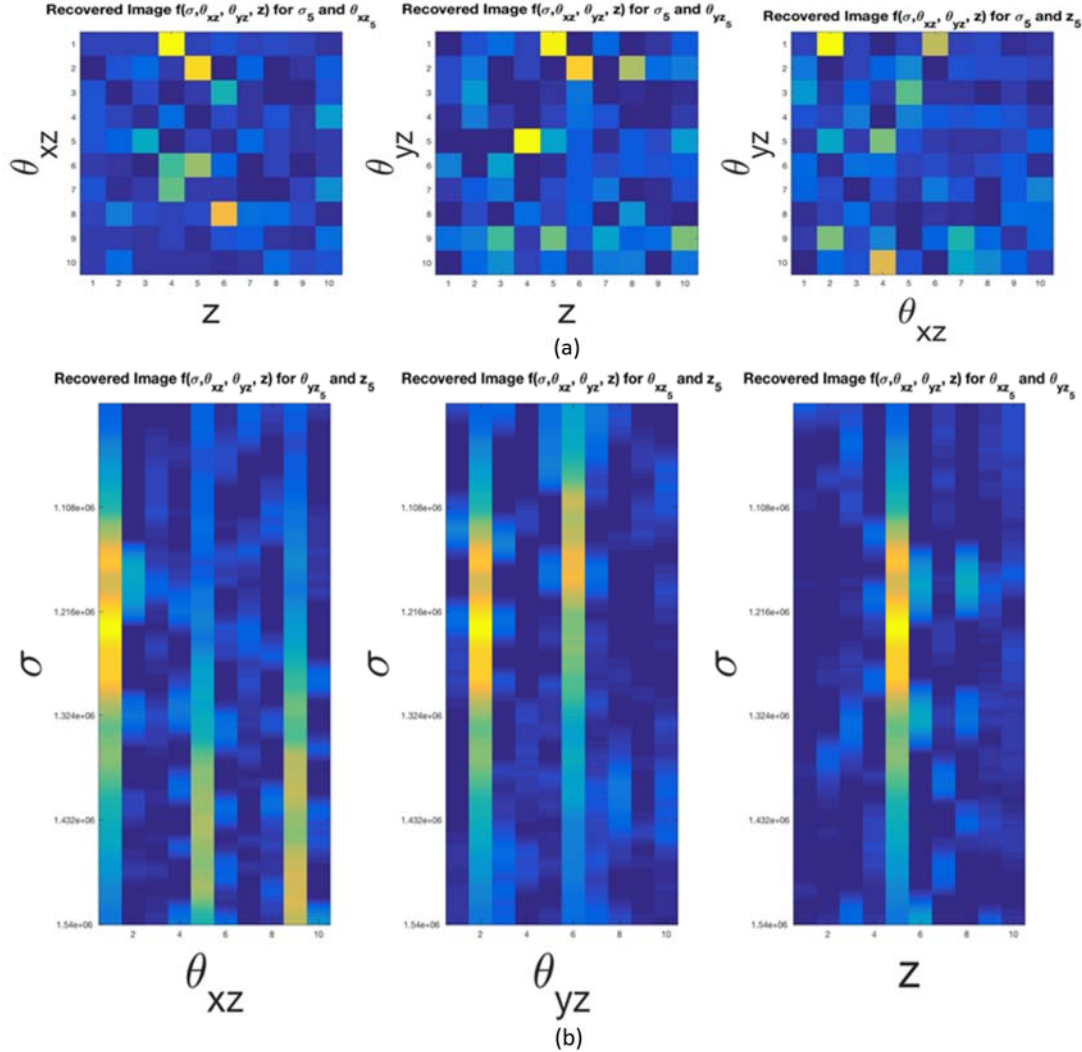


Fig. 103. Reconstruction results for the random point cloud object using the non-parametric method with the spectral smoothness assumption. (a) Reconstruction results for three spatial cross-sectional planes. (b) Reconstruction results for three spectral cross-sectional planes.

5.7 Parametric data reconstruction

It has been noticed that a non-parametric representation (one variable per frequency and per location) of f will contain a large number of variables. This leads to a high-dimensional optimization problem that is computationally intensive even with the Hessian approximation method. To handle this situation, this chapter further explores the spectral smoothness idea mentioned in Sec. 5.6.1.1 with the reparameterization trick. Given a function f represented in a canonical domain, the reparameterization of f refers to the procedure of transforming its representation in some other domains, such as the Fourier domain, the Wavelet domain [56] and the Reproducing-Kernel-Hilbert-Space (RKHS) [52]. The intention of such reparameterization tricks is that the function can be compactly represented in the new domain with much fewer coefficients; that is, after projecting f into the new coordinate system (not necessarily orthonormal), the projection coefficients are mostly zero or near-zeros. Therefore, the data components associated with the near-zero coefficients can be directly discarded, and the reconstructed function with the limited number of coefficients can still highly approximate the original f .

Therefore, given a 4D f , the idea is to reparameterize the spectrum of each spatial location to reduce the number of variables in the spectral direction. As mentioned before, in most cases, the spectra are smoothly varying and they can be compactly represented in many other domains. The reparameterize spectra are particularly chosen instead of reparameterizing spatial components because in some cases, *e.g.*, the point cloud, the spatial components are not smooth.

This chapter will investigate two reparameterization methods: RKHS and B-spline. Again, the method will still incorporate the previous prior assumptions, the posterior optimization framework and the L-BFGS numerical method. Such methods are called as parametric methods because they work with the data form after reparameterization. Besides the spiral curves and the random point cloud object, this chapter will use the parametric method to reconstruct the most challenging 3-bar object and show the effect of noise with different SNRs on all three kinds of objects. Finally, it will give a detailed comparison of the time and accuracy performance of both non-parametric and parametric methods with difference objects of different scales.

5.7.1 The RKHS reparameterization model

To reduce the number of variables, the first model applied to reparameterize the function is the RKHS space spanned by the eigenfunctions of a Gaussian kernel. The idea is that the eigenfunctions sorted by the eigenvalues show the nature of multi-scale smoothness, where the first eigenfunction is a very smooth function and the last eigenfunction is a fast oscillating function. This leads to a fact that when projecting a smooth function into the RKHS space, the projection coefficients decay very fast. In other words, it can just approximate a smooth function using the very few coefficients associated with the first few eigenfunctions [52]. The Gaussian kernel K is given in Eq. (168). By Mercer's theorem, K may be written in terms of the eigenvalues and continuous eigenfunctions as

$$K(x, x') = \sum_{i=1}^{\infty} \lambda_i \phi_i(x) \phi_i(x')^T, \quad (184)$$

where λ_i and $\phi_i(x)$ are eigenvalue and eigenfunction pairs. The RKHS is spanned by linear combinations of these eigenfunctions [63].

Therefore, for each spatial location, the spectral function $f(\cdot, x, y, z)$ can be then approximated as:

$$f(\cdot, x, y, z) \approx \Phi \alpha(x, y, z), \quad (185)$$

where the vector $\alpha(x, y, z) = [\alpha_0, \dots, \alpha_N]$ is the coefficients vector for the first N eigenfunctions, and Φ represents a matrix of the first N eigenfunctions. With this reparameterization, α is the new representation of a spectrum in the RKHS space. Typically N is much smaller than the dimension in σ , thereby enabling reduction in the number of variables. For example, Fig. 104 shows the result of projecting a simple linear function onto the first 1000 eigenfunctions. It can be seen that the projection coefficients are decaying very fast, which means the first few coefficients with their eigenvectors can precisely approximate the original function.

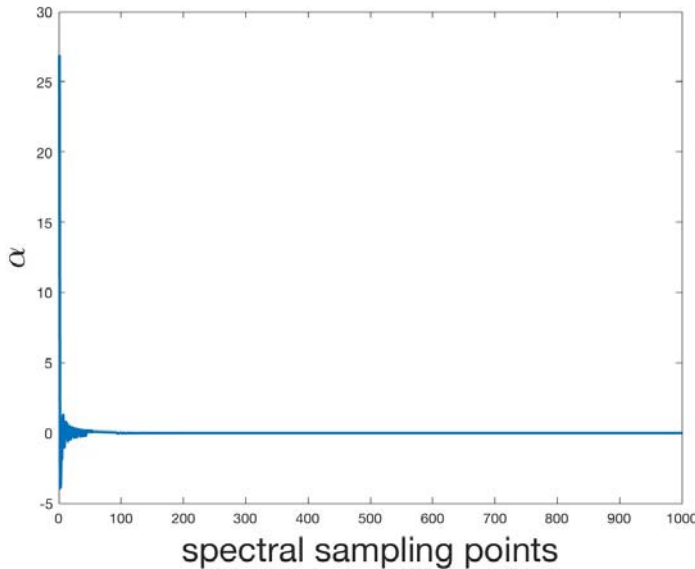


Fig. 104. A linear function is projected onto the first 1000 eigenfunctions. The projection coefficients are plotted against the number of spectral sampling points.

Therefore, if reparameterizing the spectrum of each location only using the first 50 eigenfunctions, only a 50-tuple vector for each object location needs to be recovered, whereas in the previous non-parametric representation the spectrum is a 1000-tuple vector. Now the objective function in Eq. (175) is changed to optimize the α vectors for every spatial location. With a little abuse of notation, now α is used to represent the reparameterization vectors for all spatial locations and use $\alpha(x, y, z)$ to represent the N-tuple alpha vector for a particular spatial location (x, y, z) . Therefore, $\alpha = [\alpha(0, 0, 0), \dots, \alpha(x, y, z), \dots, \alpha(N, N, N)]$. With such a reparameterization, the likelihood term becomes

$$\|g - H\Phi\alpha\|^2. \quad (186)$$

The spectral smoothness assumption is inherently given by the RKHS reparameterization: it turns out that the way for measuring a function's smoothness in the RKHS space is to use the so-called k -norm. Assume β is an RKHS reparameterization coefficient vector, its k -norm is defined as

$$\|\beta\|_k = \sum_{i=1}^N \frac{\beta_i^2}{\lambda_i}, \quad (187)$$

where the set of $\{\lambda_i\}$ is the corresponding first N eigenvalues. The spatial smoothness, on the other hand, is then measured by the k -norm of the difference between the two α vectors of neighboring spatial locations. It is defined that

$$\|\nabla\alpha(x, y, z)\| = \|\nabla_x\alpha(x, y, z)\|_k + \|\nabla_y\alpha(x, y, z)\|_k + \|\nabla_z\alpha(x, y, z)\|_k, \quad (188)$$

where $\nabla_x\alpha(x, y, z)$ is the subtraction of the two α vectors between neighboring locations in the x direction, i.e.

$$\nabla_x \alpha(x, y, z) = \alpha(x+1, y, z) - \alpha(x, y, z), \quad (189)$$

and the same rule applies for $\nabla_y \alpha(x, y, z)$ and $\nabla_z \alpha(x, y, z)$. Therefore, the overall objective function becomes

$$\arg \min_{\alpha} \|g - H\Phi\alpha\|^2 + \lambda_1 \sum_{x,y,z} \|\nabla \alpha(x, y, z)\|_k + \lambda_2 \sum_{x,y,z} \|\nabla \alpha(x, y, z)\|_k, \quad (190)$$

The same L-BFGS method can be applied here to optimize the α variables. However, the dimension of α is much smaller than that of the non-parametric form.

5.7.2 The B-spline reparameterization model

The second model used is to reparameterize the spectrum of the object using B-spline coefficients. The smooth nature of the spectrum allows us to adopt a low-order polynomial approximation with a limited number of control points (knots). Similar to the previous RKHS idea, instead of optimizing over a high-dimensional non-parametric domain associated with f , it only needs to optimize over a lower-dimensional B-spline coefficient space.

A B-spline of order n is a piecewise polynomial function of degree $< n$ [60]. The places where the pieces meet are known as knots, which can also be regarded as control points. Any spline function (piecewise polynomial) of given degree can be expressed as a linear combination of B-splines of that degree. Assume the $B(x)$ is a spline with degree n and there are K interior knots, the following equation shows the B-spline reparameterization:

$$B(x) = \sum_{i=0}^{K+n} \alpha_i B_{i,n}(x), x \in [t_0, t_{N+1}], \quad (191)$$

where n is the degree of B-spline, K is the number of interior knots, and α_i are the control point coefficients. The i^{th} B-spline basis function can be defined recursively using the Cox-deBoor recursion formula:

$$B_{i,0}(x) = \begin{cases} 1, & \text{if } t_i \leq x \leq t_{i+1} \\ 0, & \text{otherwise.} \end{cases} \quad (192)$$

$$B_{i,k}(x) = \frac{x-t_i}{t_{i+k}-t_i} B_{i,k-1}(x) + \frac{t_{i+k+1}-x}{t_{i+k+1}-t_{i+1}} B_{i,k-1}(x). \quad (193)$$

Usually, more knots should be put in regions where the functions are changing more rapidly. Since in this problem the spectrum is smoothly varying, the knots can be equidistantly placed. For any given set of knots, the B-spline is unique, Fig. 105 shows a series of B-spline functions with 10 knots and an order of 4. Each different color of the polynomial in the figure represents a different basis spline.

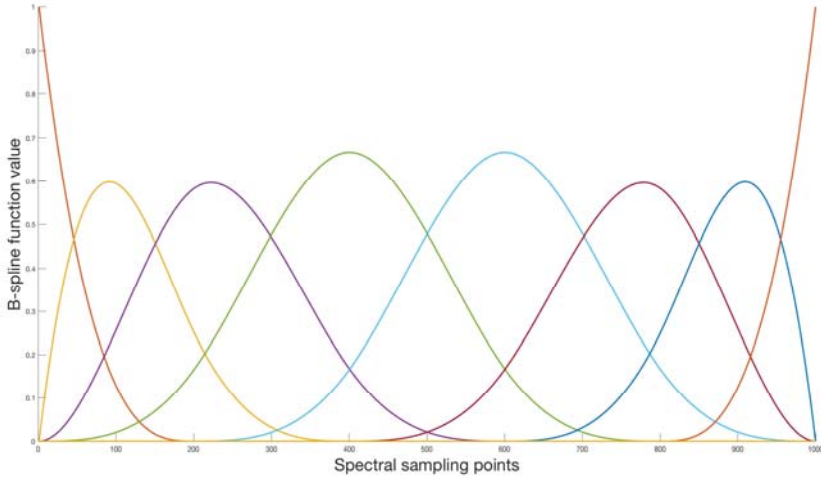


Fig. 105. B-spline functions with order 4 and 10 knots.

Therefore, for each spatial location, the 1D spectrum function of \mathbf{f} at any given local can be then approximated as a linear combination of B-splines. Similar to the previous RKHS formulation, B is used to denote a matrix storing the N B-splines and use $\alpha(x, y, z)$ to denote the B-spline coefficients of a particular spatial location (just like in the previous section $\alpha(x, y, z)$ is used to denote RKHS coefficients). Then Eq. (191) can be rewritten as

$$f(\cdot, x, y, z) \approx B\alpha(x, y, z), \quad (194)$$

Again, the following text will use α to denote the set of B-spline coefficients for all spatial locations. Since the method is using a limited number of knots for generating the B-splines, the dimension of α is much smaller than the non-parametric representation, and the number of unknown variables to be estimated is highly reduced.

Now the objective function in Eq. (178) has to be rewritten in terms of B-spline coefficients α . This part follows exactly to the previous section except that the RKHS coefficients are replaced by B-spline coefficients. For the likelihood term, it is obvious that Eq. (194) and Eq. (176) yield a composite linear relationship, which is denoted by $HB\alpha$. For the spatial smoothness term, the directional derivatives of B-spline coefficients should be penalized instead of spectral intensities. Lastly, the B-spline reparameterization already implicitly guarantees the spectral smoothness by constraining the 1D spectrum to be a low-order polynomial. However, an additional regularization $\|\alpha(x, y, z)\|^2$ is put to penalize too large B-spline coefficients to avoid overfitting. The objective function becomes

$$\arg \min_{\alpha} \|g - HB\alpha\|^2 + \lambda_1 \sum_{x,y,z} \|\nabla \alpha(x, y, z)\|^2 + \lambda_2 \sum_{x,y,z} \|\nabla^2 \alpha(x, y, z)\|^2. \quad (195)$$

5.7.3 Reconstruction results

This section will provide the reconstruction results for three different experiments with their goals being (a) to compare the RKHS and B-spline models (b) to test the robustness of the algorithm under Poisson noise and (c) to perform a thorough comparison between non-parametric and parametric methods.

5.7.3.1 Comparison tests of the RKHS and B-spline reparameterization models

Since the emphasis of this chapter is the reparameterization trick, the first validation test is to compare the performance of two parametric methods: RKHS and B-spline. Here the experiment uses the spiral curves object and assumes both spatial and spectral smoothness. The following Fig. 106 shows the reconstruction results using the RKHS reparameterization model with 10 eigenfunctions, with the overall MSE 1.33%, the sparse points MSE 10.45%, and the running time 2.5 minutes. The ground truth object can be referred to Fig. 96. It can be seen that the spatial cross-sectional planes can be almost recovered, but RKHS can not accurately represent the spectral smoothness. Therefore, RKHS is not an appropriate orthogonal basis for the reparameterization purpose.

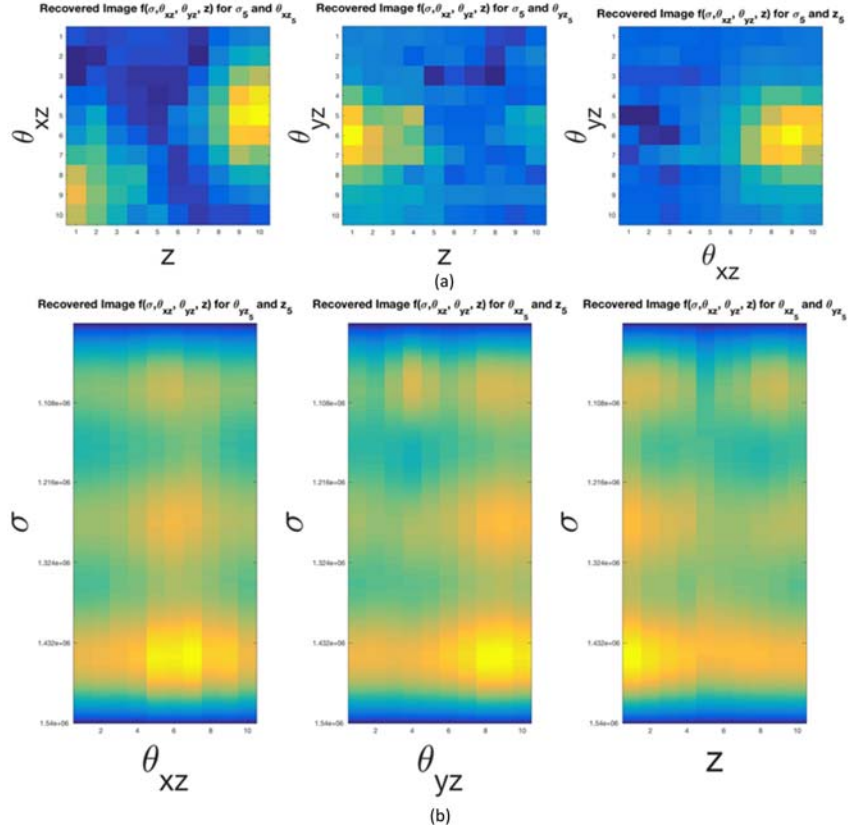


Fig. 106. Reconstruction results for spiral curves object using the RKHS parametric method. (a) Reconstruction results for the three spatial cross-sectional planes. (b) Reconstruction results for the three spectral cross-sectional planes.

While, as shown in Fig. 107, B-spline performs well in both spatial and spectral reconstruction, because the low-order polynomial functions can well represent the continuous spectral smoothness feature. The overall MSE for the results in Fig. 107 is 0.005% (sparse points MSE 7.97%), and the running time is 2 minutes for 100 L-BFGS iterations, which are all better than the results from RKHS model. Thus we use the B-spline reparameterization model for the following experiments. Then the B-spline reparameterization method is used to recover the random point cloud object. Fig. 108 shows the reconstruction results, while the ground truth can be found in Fig. 102. The overall MSE for the result without noise is 0.14% (sparse point MSE 3.62 %) and the time cost is 7 minutes.

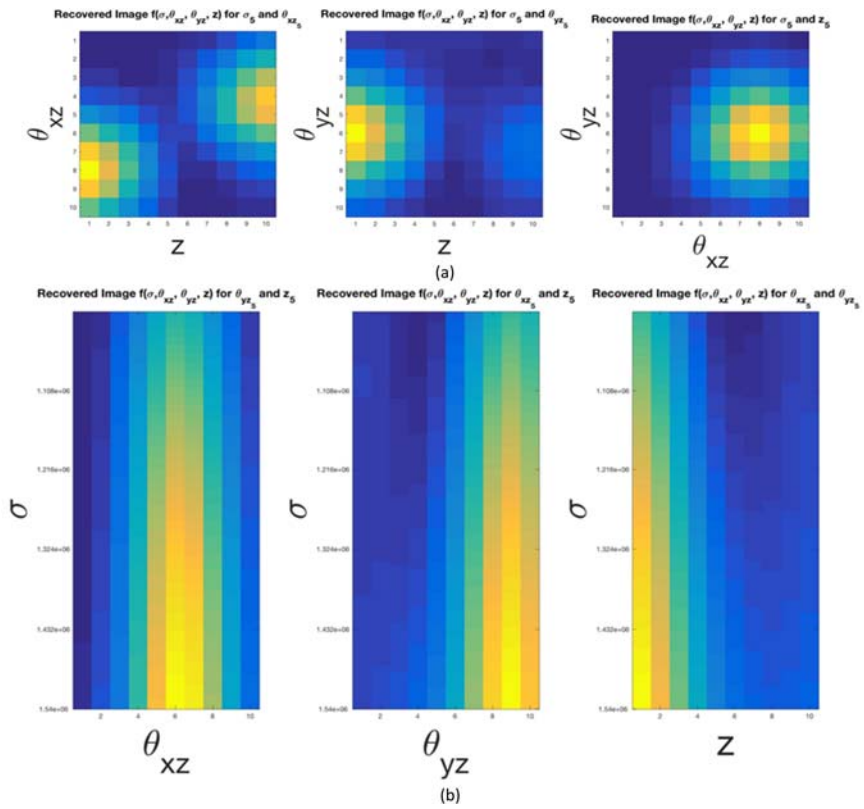


Fig. 107. Reconstruction results for spiral curves object using the B-spline parametric method. (a) Reconstruction results for the three spatial cross-sectional planes. (b) Reconstruction results for the three spectral cross-sectional planes.

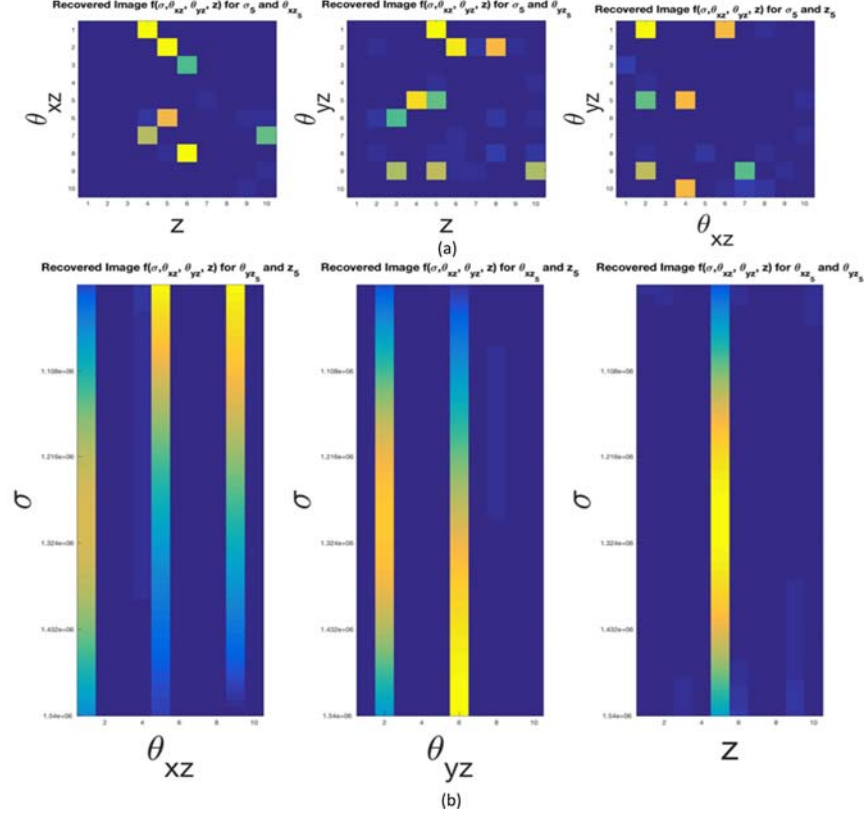


Fig. 108. Reconstruction of random point cloud object using B-spline method. (a) Reconstruction results for the three spatial cross-sectional planes. (b) Reconstruction results for the three spectral cross-sectional planes.

Due to the reduction in the number of unknown variables, the large data scale of the 3-bar scene object can be handled using the reparameterization trick. Fig. 109 gives the ground truth of the six cross-sectional planes of the 3-bar object and Fig. 110 shows the six corresponding reconstruction results. The overall MSE is 0.12% (sparse point MSE 10.82%), and running time are 40 minutes for 100 iterations.

To visualize the sparse point MSE more intuitively, the ground truth and recovered spectral intensity on one spatial location from the results in Fig. 109 and Fig. 110 are plotted in Fig. 111. The two spectral intensity functions are very close to each other, where the blue line denotes the ground truth spectrum and the green line is the recovered one.

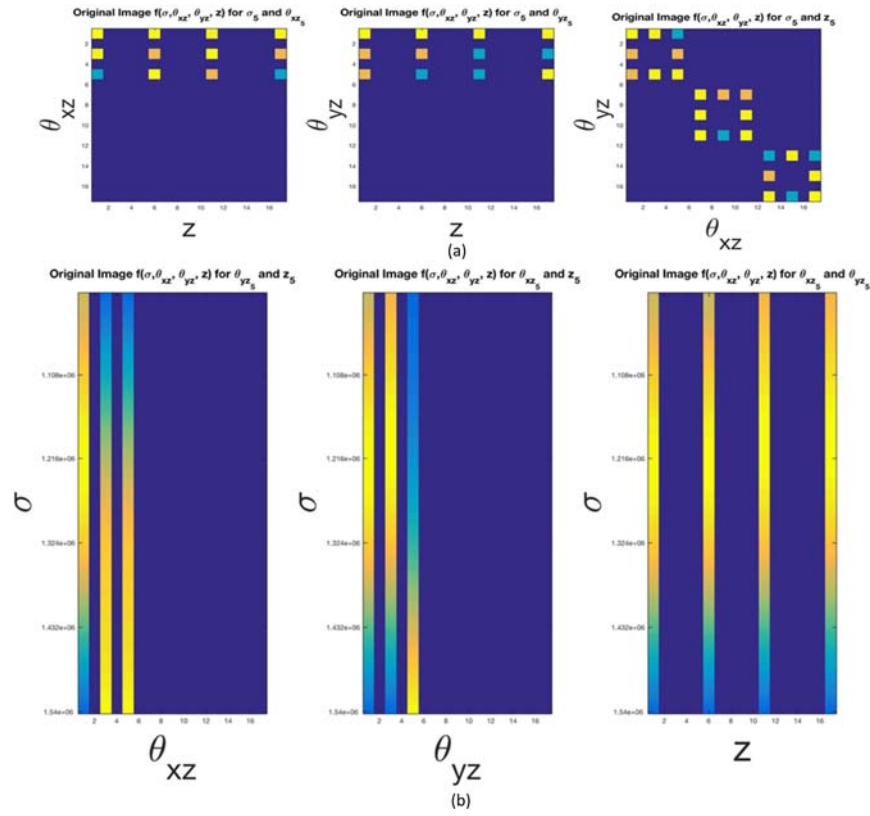


Fig. 109. Ground truth for the 3-bar object. (a) Three spatial cross-sectional planes of ground truth.
(b) Three spectral cross-sectional planes of ground truth.

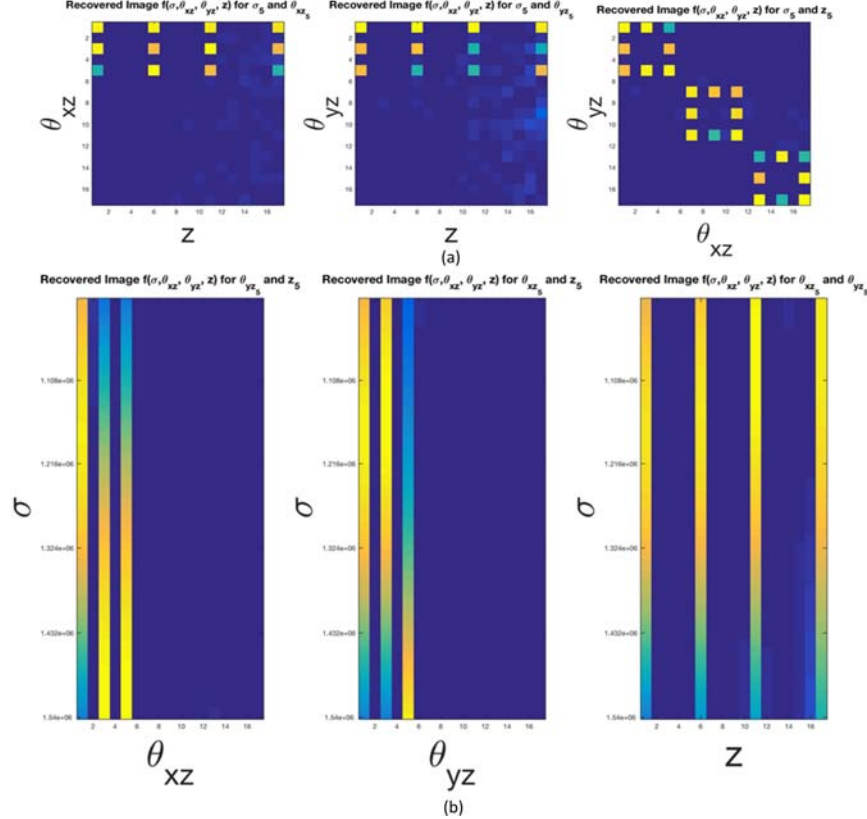


Fig. 110. Reconstruction results for the 3-bar object using the B-spline method. (a) Reconstruction results for the three spatial cross-sectional planes. (b) Reconstruction results for the three spectral cross-sectional planes.

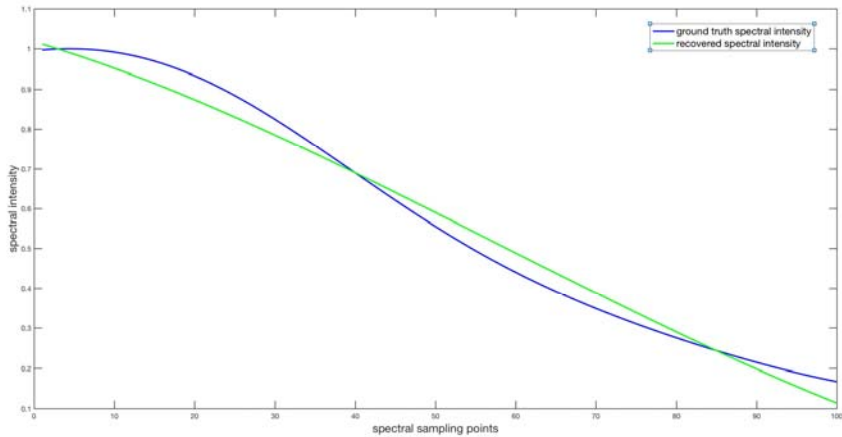


Fig. 111. The spectral intensity of 3-bar ground truth and reconstructed results using B-spline parametric method.

5.7.3.2 Robustness tests with Poisson noise

The second experiment is to validate the robustness of the B-spline-based parametric data reconstruction algorithm. As described in Sec. 5.5.4, the measurements are polluted with Poisson noise before the optimization. Taking the example of the 3-bar object, the algorithm uses the ground truth object to simulate the measurements and add Poisson noise with SNR = 30. It uses the B-spline-based parametric method to recover the 3-bar object in Fig. 109.

Ground truth for the 3-bar object. (a) Three spatial cross-sectional planes of ground truth. (b) Three spectral cross-sectional planes of ground truth. Fig. 112 shows the reconstruction results with Poisson noise (SNR = 30). The MSE for the result with noise is 0.26%. It can be seen that visually the recovered object still looks reasonable and the MSE value is only increased slightly, so it can be claimed that this algorithm gives equally reasonable results in dealing with the Poisson noise at this SNR level. The running time is also similar.

To give an overall view of the robustness tests, Fig. 113 summarizes the MSE of different SNR settings (ranging from 5 to 30) for all three objects using the B-spline-based parametric optimization. It can be seen that the performance of the method drops with lower SNR. However, but the algorithm can still achieve reasonably good MSE at the level of SNR = 30.

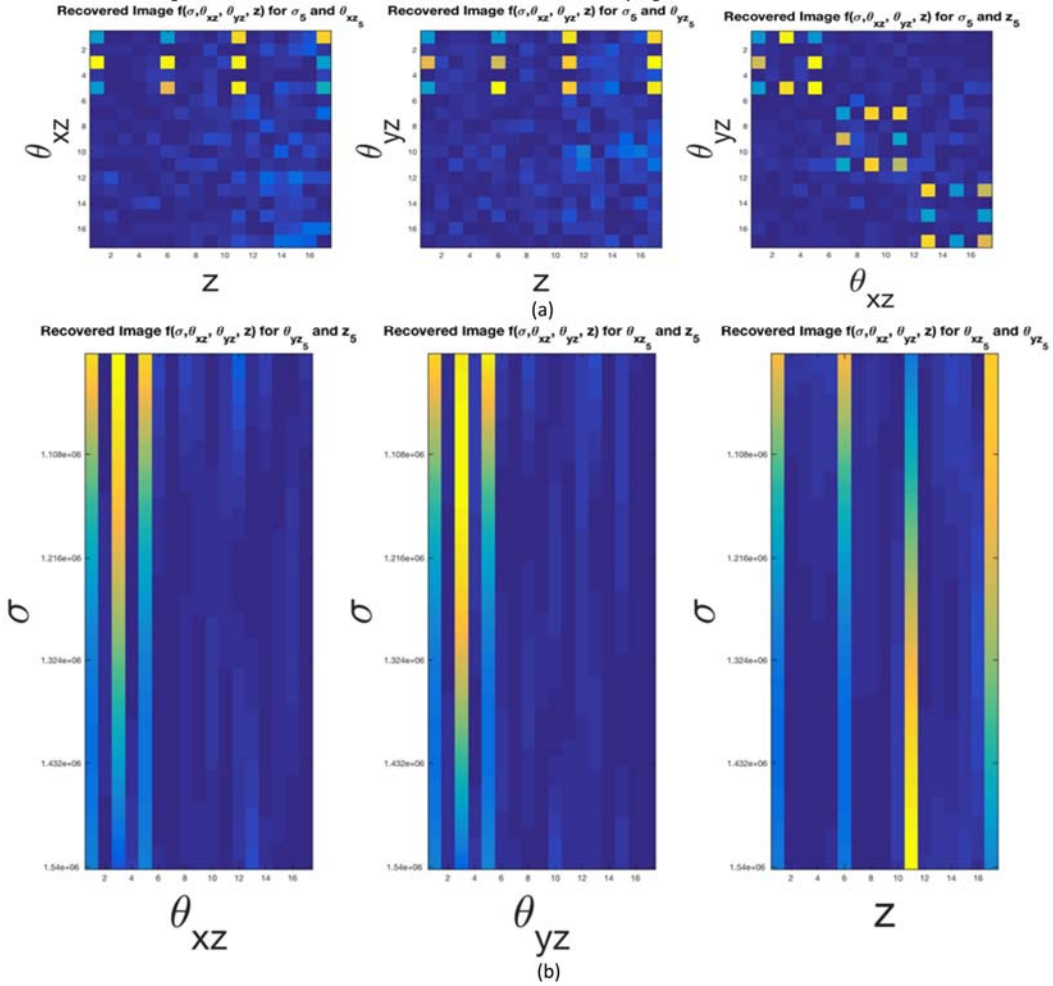


Fig. 112. Reconstruction results for the 3-bar object using the B-spline parametric method with Poisson noise. (a) Reconstruction results for the three spatial cross-sectional planes. (b) Reconstruction results for the three spectral cross-sectional planes.

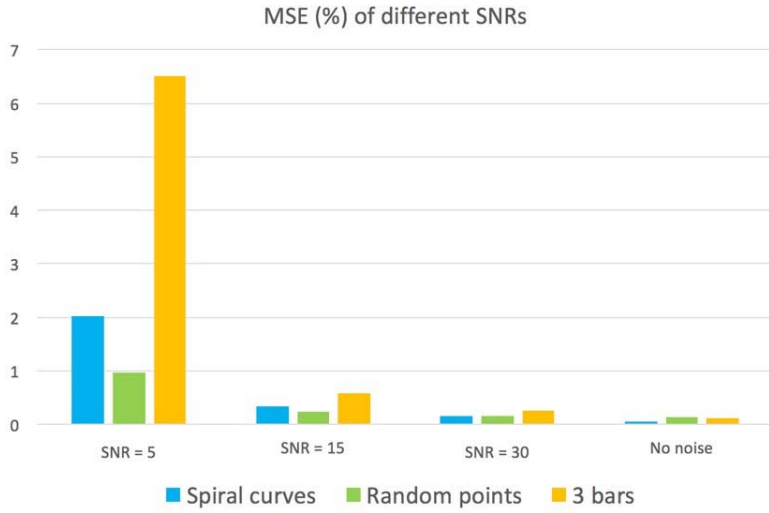


Fig. 113. The overall MSEs of recovering three objects from noisy measurements (Poisson noise) with different SNRs using the B-spline parametric method.

5.7.3.3 Comparison tests of non-parametric and parametric method

Finally, this section will illustrate the advantages of the B-spline-based data reconstruction method by comparing the accuracy and efficiency with the non-parametric method. The above reconstruction figures can give us a qualitative comparison, while the following figures and tables will provide a quantitative results.

Besides the fact that the reparameterization trick can save more computer memory, the most critical advantage is its higher computational efficiency. The parametric method can be much more time-consuming at any data scale level as shown in Fig. 114. The vertical axis means the running time with the unit of seconds and the horizontal axis represents different data scales. The gap between the running time becomes even larger when the data scales up.

Although the parametric method costs less running time and saves memory, it can provide even better reconstruction results as the non-parametric method. Fig. 115 shows the overall MSEs for different data scales using these two methods.

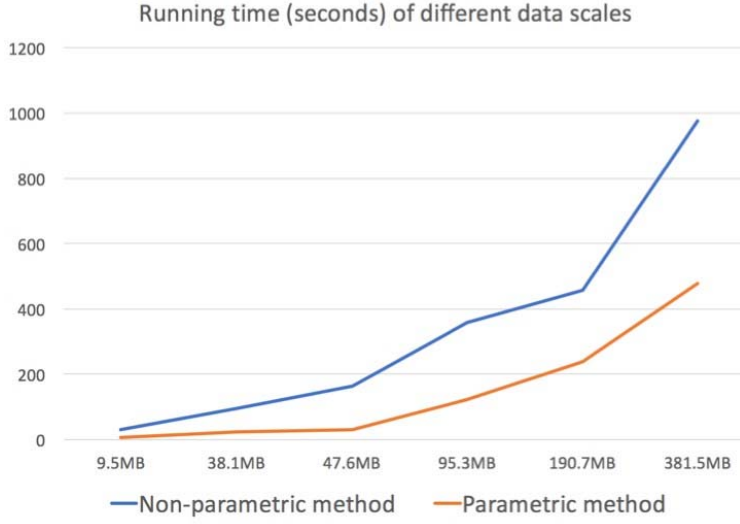


Fig. 114. The time costs of recovering object with different data scales using the non-parametric and parametric methods.

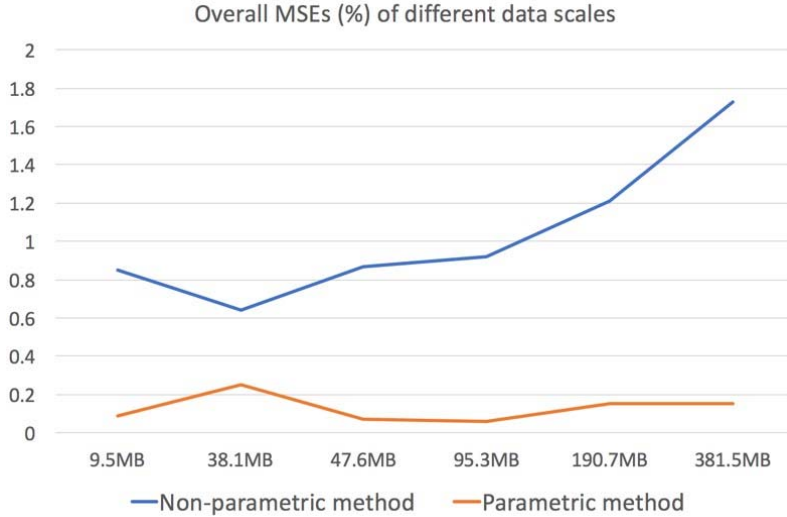


Fig. 115. The overall MSEs of recovering objects with different data scales using the non-parametric and parametric methods.

5.7.4 Conclusion

Considering both of the limited computer memory and high-dimension object datasets, the algorithm proposed two reparameterization methods to reduce the number of variables in the posterior optimization. One is the RKHS model, which uses the first few eigenfunctions of a Gaussian kernel to approximate a smooth function. The other one is the B-spline model, which reparameterizes a function by some low-order polynomials. According to the experiment results, the B-spline model is better at modeling the continuous spectra. Then it demonstrated the reconstruction results of three kinds of objects using this B-spline-based method with and without the Poisson noise. In the end, it compared the parametric method with the non-parametric method from the aspects of accuracy and efficiency to prove the advantage of using reparameterization.

5.8 Conclusion and Discussion

We investigated a reconstruction algorithm for 4D object-space data using the SSM technique and validated the algorithm using synthetic ground truth objects. The SSM technique is a hyperspectral imaging technique applied for far-field target detection in passive remote sensing systems.

The first problem encountered is that the SSM system is an underdetermined linear system. The system has much fewer number of equations from the optical and modulation model than the number of unknown variables in the scene object, so it cannot uniquely compute the unknown variables in a closed form. Therefore, the algorithm models the problem from a probabilistic point of view. The algorithm has proposed two proper prior distributions on the object scene and formulated a posterior optimization to solve the inverse problem. The second challenge is the optimization efficiency. When trying to reconstruct the 4D scene with much larger data scale (more than 10 GB), one problem is the computer memory is not large enough to handle the optimization, and the computational time is also too slow; the other problem is that with limited detector size this system becomes further ill-posed for such a large-scale object scene. Thus, the data is reparameterized by projecting it into some other domain and using only a few projection coefficients. In particular, fewer variables are used to represent the continuous spectra of the object. Such a reparameterization trick can reduce the optimization memory consumption by 95%. Through the experiments on several different reparameterization models, it proves that the B-spline reparameterization can best reconstruct the object with efficient computation.

The novelty of the algorithm includes: (a) it proposes to incorporate proper prior assumptions to the object scene so that it can solve effectively the underdetermined linear system by an inverse optimization (b) it proposes to use RKHS basis functions and B-spline polynomials to represent the continuous frequency components of the highly sampled spectra, thereby producing more efficient and accurate reconstruction.

Based on the optical model of the SSM system, the ground truth 4D object-space data used to validate the algorithm are three kinds of synthetic scenes: smooth spiral curves, random point clouds and a specific 3-bar point cloud. The performance of this algorithm should be tested from three aspects: accuracy (overall MSE and sparse point MSE), efficiency (optimization time) and robustness (with Poisson noise). The overall MSE is less than 0.3%, which means it can reasonably determine the location and the general shape of the objects. While the relatively higher sparse point MSE (about 11%) means that it is still needed to further improve the object intensity estimation on those specific point locations. Using the parametric method, the algorithm can reduce the optimization memory by 95% with respect to the non-parametric method, which gives more possibilities to the reconstruction of more complex real-life scenes with larger data scale in the future work. Besides, the experiments have shown that our algorithm can handle Poisson Noise effectively.

To conclude, this data reconstruction algorithm can perform well for the SSM hyperspectral imaging system. It has potential to be applied to other optical systems that can be formulated as an underdetermined system with given measurements and measurement matrices. The future work mainly includes: (a) to investigate more on the sparse point cloud object to increase the reconstruction accuracy on the point locations; (b) to apply this method on more complex point cloud objects; (c) to extend our method to other image compression inverse problems.

6.0 Alternative Imaging Methods

Alternative angular filtering methods were also investigated during the period of performance. Other non-interferometric methods were studied in which angular cutoffs, created by plasmonic effects, were investigated. Plasmonic waves typically have much shorter propagation distances (~ 300 microns) before they encounter diffraction limited effects.

6.1 Total Internal Reflection Tradespace

Exploiting near-field effects for creating an angular filter, which can define the transfer function of an imaging system, may enable higher resolution far-field imaging. For instance, total internal reflection (TIR) can be used to produce an angular filter, and multiple dimensions can be simultaneously filtered by stacking several prisms together. This concept is illustrated in Fig. 116 (a) in which air gaps are included between two sets of prisms. Here, prisms 1 and 2 reflect light exceeding a cutoff angle θ_{xz} in the xz plane, in which angles spanning $-\Delta\theta < \theta_{xz} < \Delta\theta$ are allowed to transmit. Similarly, prisms 3 and 4 are rotated by 90 degrees in the xy plane, and transmit light spanning $-\Delta\theta < \theta_{yz} < \Delta\theta$. A magnified view of a single prism is illustrated in Fig. 116 (b), in which the angle θ_1 is indicated, relative to the normal $\hat{\mathbf{n}}_1$, of the tilted prism interface. Meanwhile, the angle of incidence onto prism, from air, is defined relative to the normal $\hat{\mathbf{n}}_i$ of the flat surface and is related to the wedge angle by

$$\theta_{air} = \theta_1 n_1 / n_2 , \quad (196)$$

where n_1 is the prism's refractive index and n_2 is the refractive index of the incident medium (air). In this case, the small angle approximation is used and is valid since θ_{air} is small relative to $\hat{\mathbf{n}}_i$. Ultimately, these TIR interfaces reject light from the optical system beyond the critical angle.

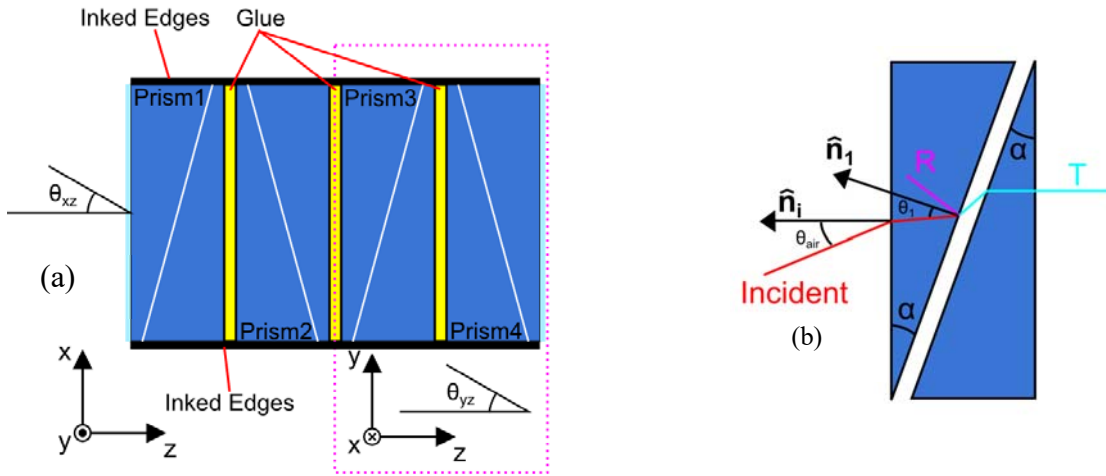


Fig. 116. (a) Optical schematic for a total internal reflection-based angular filter for two dimensions and (b) magnified view with exaggerated air gap indicating the plane of the prism where the angular filtering occurs.

Due to the air-gaps, this angular filter preferentially transmits p polarized light, and preferentially rejects s polarizations. Additionally, due to the nature of TIR, the transmittance of this structure is also low when all 8 air-to-glass or glass-to-air interfaces are present. The plane of incidence, defined by the normal vector and the refracted ray, is illustrated in Fig. 117.

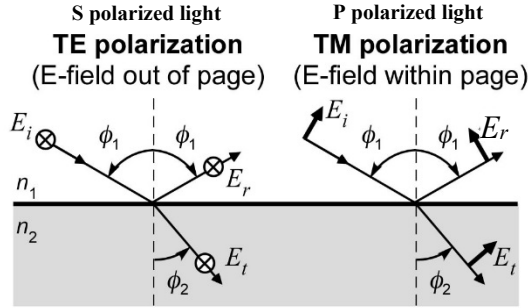


Fig. 117. (Left) S polarized light and (right) P polarized light within the plane of incidence.

The Fresnel reflection coefficients, r_p and r_s , are expressed as a function of the refractive index of the prism material and the angle relative to the normal vector, defining the plane of incidence, as

$$r_p = \frac{E_r^p}{E_i^p} = \frac{-n_2^2 \cos \phi_1 + n_1 \sqrt{n_2^2 - n_1^2 \sin^2 \phi_1}}{n_2^2 \cos \phi_1 + n_1 \sqrt{n_2^2 - n_1^2 \sin^2 \phi_1}}, \text{ and} \quad (197)$$

$$r_s = \frac{E_r^s}{E_i^s} = \frac{n_1 \cos \phi_1 - \sqrt{n_2^2 - n_1^2 \sin^2 \phi_1}}{n_1 \cos \phi_1 + \sqrt{n_2^2 - n_1^2 \sin^2 \phi_1}}, \quad (198)$$

where ϕ_1 is the incidence angle, n_1 is the refractive index of the incident material, and n_2 is the refractive index of the subsequent material. Meanwhile, superscripts s or p represent s or p polarized light, respectively, and subscripts r or i represent incident or reflected values of the complex electric field vector E , respectively. The Fresnel reflection coefficients are illustrated in Fig. 118 versus incidence angle ϕ_1 (or θ_1 per Fig. 116 (b)) where reflectance is calculated as

$$R_p = |r_p|^2, \text{ and } R_s = |r_s|^2. \quad (199)$$

In this case, three refractive indices are plotted corresponding to $n_1 = 4, 2.5$, and 1.5 with $n_2 = 1.0$. Notable is the decreased “sharpness” of R_p as the refractive index is increased.

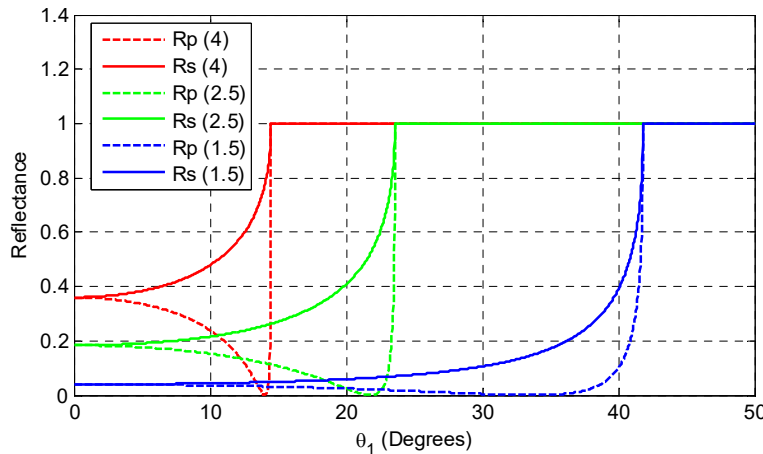


Fig. 118. Fresnel reflectance vs. angle of incidence, relative to the TIR surface’s normal, for three refractive indices: $n = 4, 2.5$, and 1.5 where $\phi_1 = \theta_1$ represents the angle inside the glass.

The transmittance of one half of the TIR filter (*e.g.*, prisms 1 and 2) are plotted versus incidence angle per Fig. 119. Note that in Fig. 118, the angle of incidence on the interface was plotted from inside the glass, whereas in Fig. 119, this angle has been related to object space by use of Eq. (196). Note that Eq. (196) dictates that the angular resolution in object space is worse by a factor of the refractive index n_1 . For Fig. 119 (a-c), the transmittance for prisms with apex angles $\alpha = 14.1880^\circ$, $\alpha = 14.3327^\circ$, and $\alpha = 14.4630^\circ$ are provided, respectively, and demonstrate an increasing angular full-width (FW) resolution and a corresponding decrease in the transmitted light intensity.

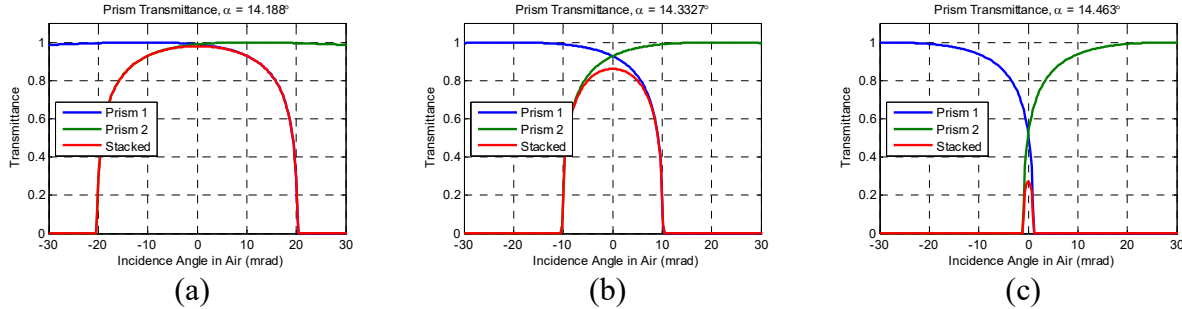


Fig. 119. Transmittance of two stacked prisms (*e.g.*, prisms 1 and 2 per Fig. 116), as a function of angle of incidence in the xz plane. Three apex angles are provided: (a) $\alpha = 14.1880^\circ$; (b) $\alpha = 14.3327^\circ$; and (c) $\alpha = 14.4630^\circ$

This analysis can be further extended to plot the angular full width resolution as a function of the prism apex angle α and peak transmittance of a two-prism system. In this case, since a higher refractive index corresponds to a sharper transition for p polarized light, a higher angular resolution can be obtained with less tradeoff against the filter's efficiency. A view of this analysis is illustrated in Fig. 120 and shows the peak transmittance, in percent, plotted versus the prism apex angle α and the FW angular resolution in mrad. Also shown are two equivalent lens diameters. These correspond to an angular resolution, in air ($n = 1$) at which the transmission of the prisms equals 100% (*e.g.*, Brewster's angle) and when the transmission of the prisms equals 50%. The lens diameter D , as a function of angular resolution, is calculated as

$$D = \lambda_0 n_2 / (2.44 n_1 d\theta), \quad (200)$$

where $\lambda_0 = 10 \mu\text{m}$ and the angular resolution $d\theta$ is first calculated within the prism material of refractive index $n_1 = 4$ and has been related to the angular resolution outside the prism, within refractive index $n_2 = 1$. At a transmittance of 100%, the angular resolution is approximately 62 mrad, which corresponds to a lens diameter $D = 0.4 \text{ mm}$. Meanwhile, at a 50% transmittance, the resolution increases to approximately 10 mrad, which corresponds to a lens diameter $D = 2.3 \text{ mm}$.

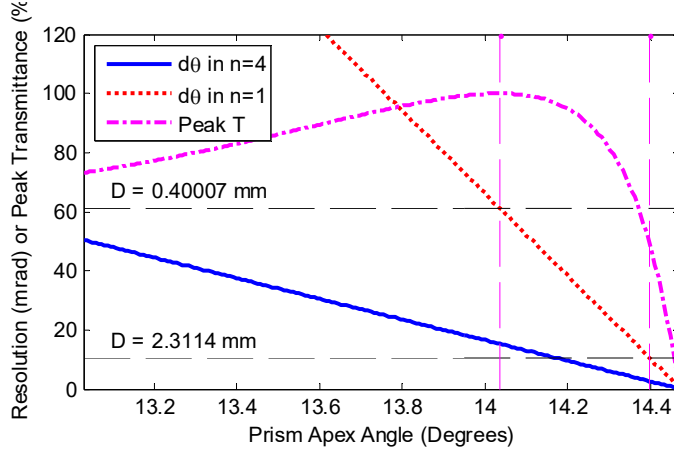


Fig. 120. Plot of FW resolution versus prism apex angle α , plotted alongside peak transmittance versus α , calculated at a wavelength of 10 microns, for an index $n_1 = 4$ prism pair.

For an index $n_1 = 4$ prism, the resolution tradespace when compared to a conventional lens is not competitive. In order to start being competitive with a lens, the refractive index would need to increase to a value closer to $n_1 = 10$ for the TIR effect to approach the angular resolution of a typical lens system. A similar series of plots for this higher index case are illustrated below in Fig. 121 (a-c). Compared to the $n_1 = 4$ material, the improved transmittance versus spatial resolution tradespace is most noticeable when comparing Fig. 121 (c) to Fig. 119 (c). In this case, the spatial FW resolution is approximately 2.5 mrad while the peak transmittance of the higher index material is nearly 3 times higher.

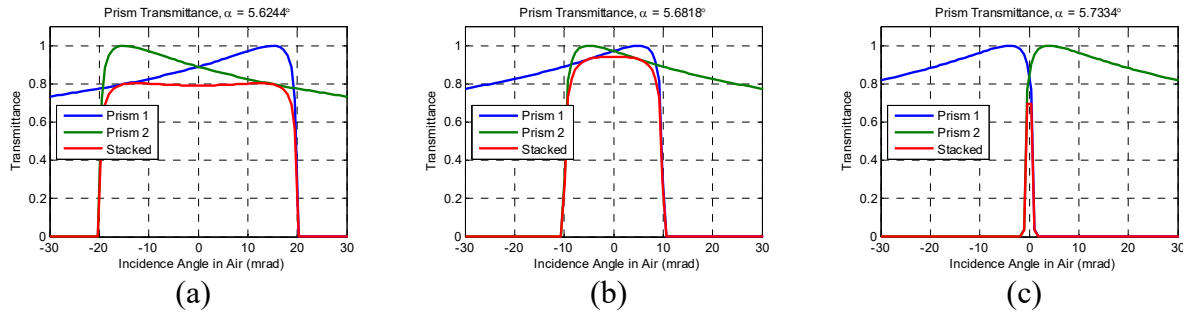


Fig. 121. Transmittance of two stacked prisms for a higher refractive index material $n_1 = 10$. Three apex angles are provided: (a) $\alpha = 5.6244^\circ$; (b) $\alpha = 5.6818^\circ$; and (c) $\alpha = 5.7334^\circ$

The spatial resolution tradespace for the $n_1 = 10$ prism is depicted in Fig. 122, and demonstrates that for a peak transmission of 100%, the spatial resolution matches that of a 2.5 mm lens while at 50% transmission, the spatial resolution matches that of a larger 14 mm lens. Still, this resolution tradespace is not ideal when considering the reduced transmittance; thus, a method of increasing the sharpness of this resonance is needed in order to formalize a realistic method of implementing this kind of imaging filter.

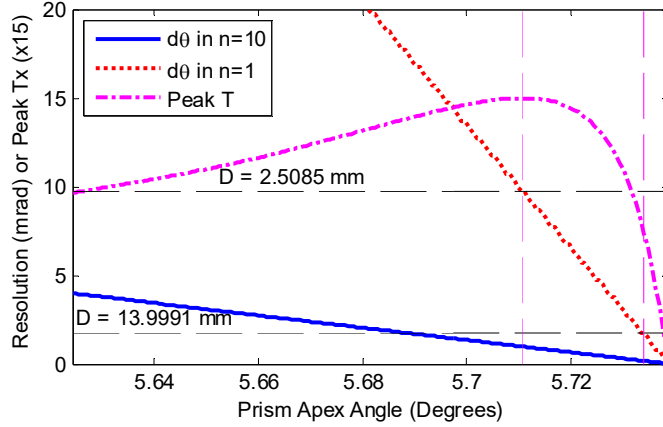


Fig. 122. Plot of FW resolution versus prism apex angle α , plotted alongside peak transmittance versus α , calculated at a wavelength of 10 microns, for an index $n_1 = 10$ prism pair.

6.2 Plasmonic Angular Transmission Filter

The concept of using plasmonic filters to perform spatial-spectral modulation has been implemented by other researchers for near field lensless imaging. In this case, a spatially patterned 2D plasmonic filter mask was placed close to the object under measurement. By modulating the spatial period of an array of nanoholes in a gold film, the surface plasmon resonance wavelength was also spatially modulated. This meant that information about the object could be inferred at a distance away from the target by performing a matrix inversion. However, this would not be appropriate for standoff imaging since there is no feasible way to modulate the scene directly. Instead, a similar effect would need to be created in the pupil of an imaging system. Such a modulation scheme would need to be implemented so that the surface plasmon resonance (SPR) wavelength would change as a function of incidence angle. For a surface plasmon, the resonance wavelength can be calculated using the matrix method of thin film interference, as well as by calculating the 1st order from a rigorous coupled wave analysis (RCWA) simulator. A view of the geometry for a homogeneous metal film is illustrated in Fig. 123 in which a glass substrate is used to couple light, near the critical angle, into a surface plasmon within a metal film. The metal film's thickness, h , can be varied, as well as the refractive index of the substrate and the transmitted medium. In this case, the medium is shown as air; however, this can be changed according to the needs of the simulation.

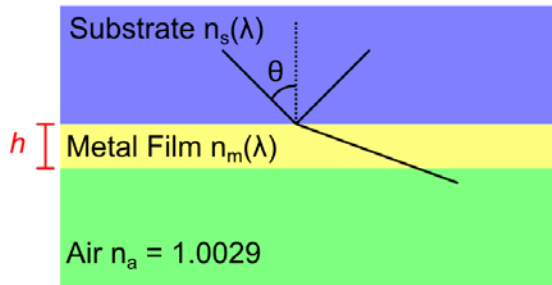


Fig. 123. Geometry for plasmon resonance simulations of a homogeneous thin film.

In order to validate the simulation's performance, comparisons were made between the RCWA simulator. The reflectance of this plasmonic effect, per. [81], is illustrated in Fig. 124 (a). In this case, the glass substrate was simulated using a boro silicate material with a refractive index of

1.514 and a gold layer refractive index of $0.1726 + j3.4218$ at a wavelength of 633 nm. Finally, the refractive index of the transitional media (in Fig. 123, this is shown as being air) was modeled using the refractive index of the aqueous and vitreous humor, or 1.336. Results from our RCWA simulations are illustrated in Fig. 124 (b).

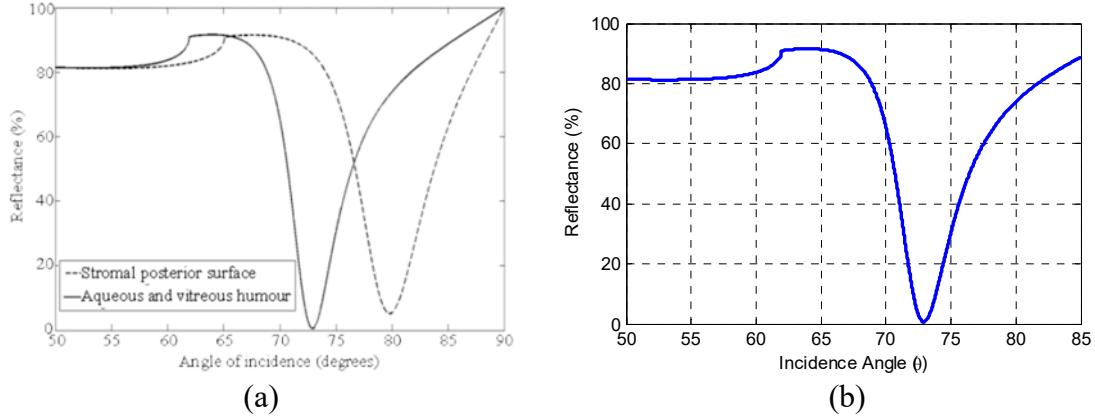


Fig. 124. Reflectance of a Boro silicate glass prism and gold film interface, with a thickness of 50 nm, in (a) and per our calculations of the same geometry per (b) for the aqueous and vitreous humor.

Extending these simulations to a gold film on a germanium substrate ($n_s = 4.005$), with a transmission medium of air ($n_a = 1.0029$) as shown previously in Fig. 123, yields the results depicted in Fig. 125 below. In this figure, the transmittance is provided for five metal film thicknesses of 0, 5, 10, 15, and 20 nm. Transmission is plotted versus angle of incidence, where the incidence angle has been extended to that in air using Eq. (196). Shown in Fig. 125 (a) is the absolute transmittance versus incidence angle for a solid metal film, as compared to the “standard” TIR transmittance. Notable is the markedly reduced transmission of the structure as the film thickness is increased. However, the “sharpness” of the edge – e.g., the resolution of the low pass angular filter – is correspondingly increased. This is illustrated in Fig. 125 (b), in which each of the transmittance plots shown in Fig. 125 (a) are normalized to their maximum value. Here, the sharpness of the transition from the transmitting to the blocking state has been enhanced by the plasmon and the presence of the metallic film.

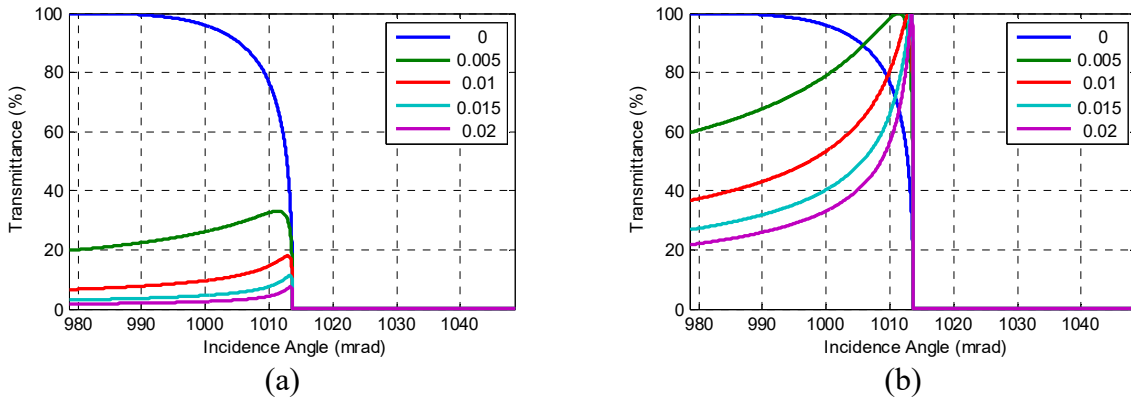


Fig. 125. Plasmonic filter transmission versus incidence angle and gold film thickness, in microns.
(a) Absolute transmission and (b) normalized transmission.

Ultimately, the efficiency of these plasmonic structures, in transmission, can be enhanced by patterning a small array of holes (or grating grooves) into the metallic film. This is where RCWA simulations are extended to 2-dimensional (2D) patterned structures. It should be noted here that one caveat of RCWA is the assumption of gratings with an “infinite extent”. Thus, these simulations will be followed up by COMSOL simulations to demonstrate the effect of finite aperture size on the angular filter.

6.2.1 RCWA Simulations of 2D Patterned Sub-wavelength Gratings

RCWA simulations were performed on 2D grating structures to investigate how the layer’s transmission could be enhanced while preserving the sharpness of the angular transition. RCWA is a rigorous harmonic-based method of calculating the exact solution to Maxwell’s equations, provided a sufficient number of harmonics are included in the analysis. For this study, the RCWA module in OptiScan was used within a Matlab environment. A side profile of the general grating structure that was investigated is depicted in Fig. 126 (a) with the incident, reflected, and transmitted electric field components detailed in Fig. 126 (b). Note that for the purposes of our simulation, light is incident from the higher index substrate, interacts with the grating, and then transmits into air. To prevent simulation instabilities, the refractive index of air ($1.0029+j*1E-8$) was assumed. Note that a small imaginary component must be added in some cases to stabilize the RCWA simulation result. This yields negligible electric field coupling into the incident medium, due to the presence of a small evanescent wave just beyond the grating.

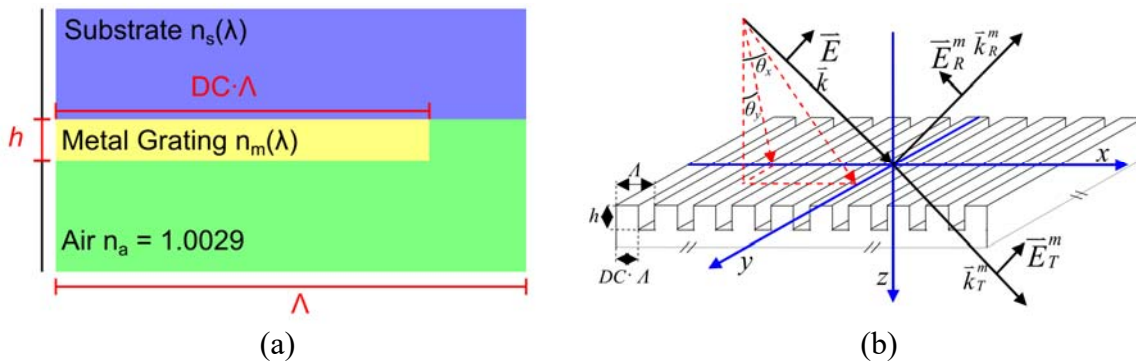


Fig. 126. (a) Side profile of one grating period and (b) grating geometry for the RCWA calculation. Coordinate system for the RCWA simulations of the WGBS and WP where \bar{E} denotes the electric field vector. θ_x and θ_y are angles that the propagation vector (\bar{k}) makes from the z axis in the xz and yz planes, respectively, while Λ , h and DC are the respective period, height and duty cycle of the grating.

For the purposes of this simulation, the transmitted diffraction efficiencies were calculated for incident p polarized light. A view of the transmitted diffraction efficiency versus wavelength and angle of incidence is illustrated in Fig. 127 for a period of 2 microns, metal grating thickness of 0.5 microns, and duty cycle of 80%. With these grating parameters, the aspect ratio (height/depth) is approximately 0.9 with a minimum feature size of 400 nm, making it feasible for fabrication.

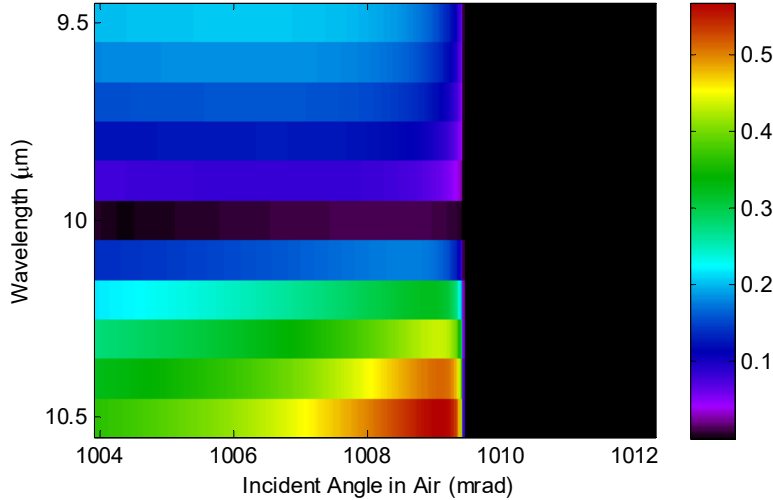


Fig. 127. Diffraction efficiency (DE) versus wavelength and angle of incidence for a gold grating on germanium. The grating has a duty cycle of 80%, depth of 0.5 microns, and period of 2 microns.

For these parameters, the angular filter's sharpness is increased at longer wavelengths, to a maximum (in the range of this simulation) at 10.5 microns. Generally, the ideal grating configuration should (a) maximize transmitted light; and (b) have the sharpest possible transition versus angle.

6.2.1.1 Order Stability Analysis

For an aluminum grating, the diffraction efficiency versus incidence angle is plotted below in Fig. 128. In this simulation, the stability of the 0th order transmitted diffraction efficiency (DE) for *p* polarized light was investigated at a single angle of incidence near the grating's resonance. A duty cycle of 80%, period of 2 microns, wavelength of 10.4 microns, and incident angle of 14.5 degrees were used in the simulation of an aluminum grating with a thickness that spanned 0 to 0.5 microns thick. The calculation of the diffraction efficiency was conducted several times for different orders M. In this case, the number of orders kept influences the simulation's accuracy, where higher accuracy is achieved keeping more diffraction orders at the cost of longer simulation time. From this analysis, an order *M* = 26 was used for preliminary calculations, as it is representative of relatively stable operation. Simulations were then verified at an order setting of *M* = 60 to validate the accuracy and to confirm that the simulation was stable.

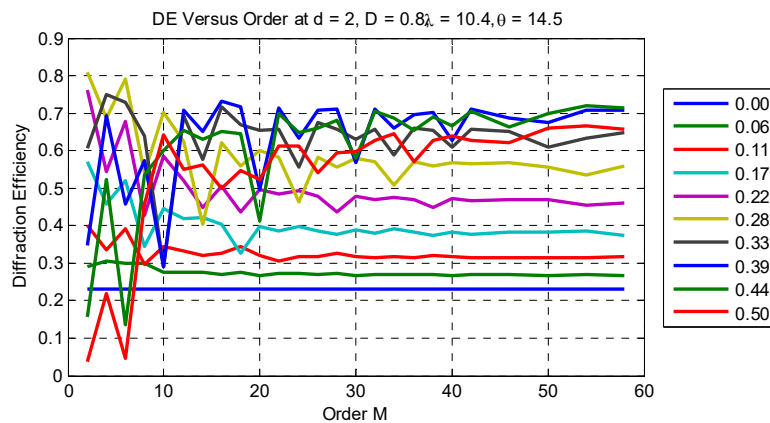


Fig. 128. (a) Side profile of one grating period and (b) grating geometry for the RCWA calculation.

Parameter sweeps across grating thickness, duty cycle, wavelength, period, and incident angle were simulated for various metals that can be deposited via lithography and patterned via photoresist. Results of these parameter sweeps were calculated for copper, gold, aluminum, and silver. For each metal, the derivative of the *p*-polarized transmittance was calculated, which yields a measure of the rate of change in the transmission versus the rate of change in angle. In this case, larger values are indicative of higher spatial resolution. From this analysis, the metal type is relatively independent of the grating parameters and nearly all of the metals simulated perform similarly. Ultimately, the choice of metal is also limited to lithographic processing options. For instance, gold is often deposited with an adhesion layer of titanium, which could interfere with the surface plasmon coupling. Additionally, copper oxidizes easily and also (generally) must have an adhesion layer. Ultimately, aluminum is the most likely candidate due to its low rate of oxidization in the atmosphere and high adhesion without the need of an adhesion layer. Thus, aluminum is the likely candidate moving forward for fabrication and testing.

6.3 Merit Function and Optimization (Germanium, No Dispersion)

Selection of the optimal grating configuration was conducted by maximizing both the transmitted intensity at resonance, as well as the maximum value of the derivative. This created a merit function M_E such that

$$M_E = \max \left[DE_{PT} (\Lambda, DC, h, \lambda, \theta_{air}) \right]^{w_1} \times \left[dDE_{PT} (\Lambda, DC, h, \lambda, \theta_{air}) / d\theta_{air} \right]^{w_2}, \quad (201)$$

where w_1 and w_2 are weighting parameters and DE_{PT} is the transmitted *p*-polarized diffraction efficiency. It should be mentioned that DE_{PT} is, per the parameter sweep, a function of the grating period, duty cycle, grating height, wavelength, and incidence angle on the interface (note that the derivative is taken again with respect to the angle of incidence in air). Choosing the largest value of M_E produces a grating with a simultaneously high derivative and high transmittance given appropriate weighting factors w_1 and w_2 . To observe the influence of these weighting factors, three combinations of values were chosen with a fixed $w_1 = 1$ and $w_2 = 0.5, 0.75$, and 1 . These are shown in Fig. 129 through Fig. 131 below, while the optimal results are summarized in Table 1.

Table 1. Optimal solutions for different combinations of the weighting coefficients and their performance.

w_1	w_2	λ (μm)	DC (%)	Λ (μm)	h (μm)	DE (%)	Derivative
1	0.2	10.6	77	1.975	0.5	82	10.79
1	0.75	10.7	77	2.05	0.44	78	12.28
1	1	10.5	85	1.975	0.5	71.6	13.75

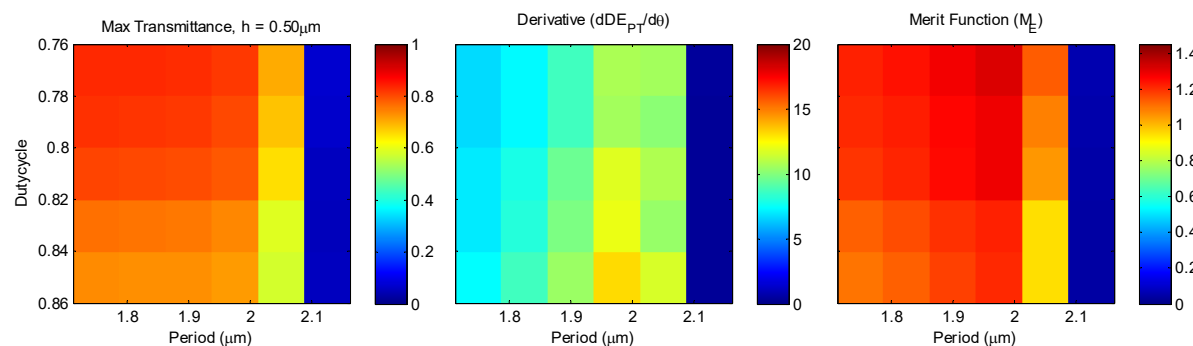


Fig. 129. Merit function optimization space for $w_1 = 1$ and $w_2 = 0.2$.

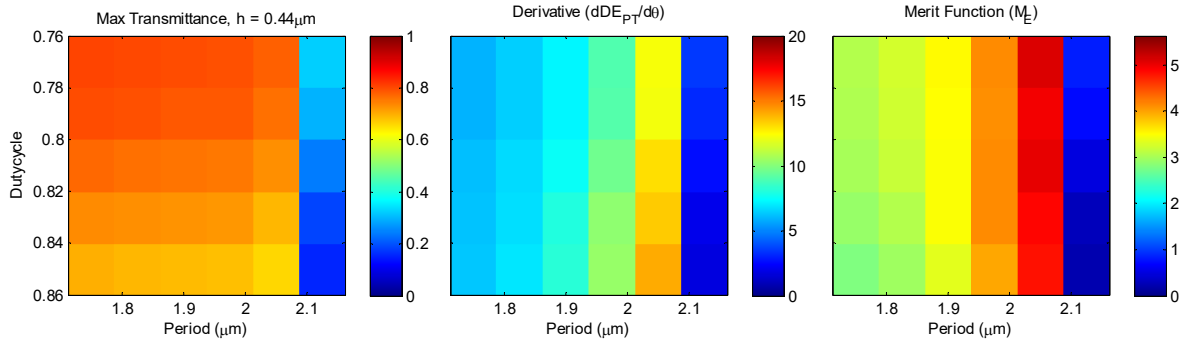


Fig. 130. Merit function optimization space for $w_1 = 1$ and $w_2 = 0.75$.

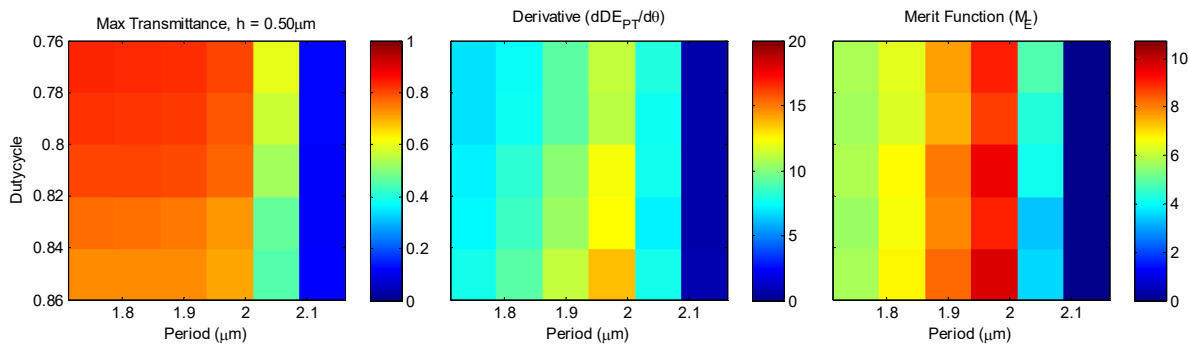


Fig. 131. Merit function optimization space for $w_1 = 1$ and $w_2 = 1$.

When two prisms are combined together with the parameters in Table 1, their spatial transmittance functions can be visualized as previously with the case of TIR shown in Fig. 121. These results are depicted in Fig. 132 for the condition such that the maximum transmittance of each prism overlaps with the next, ensuring that the maximum power is transmitted by the prism.

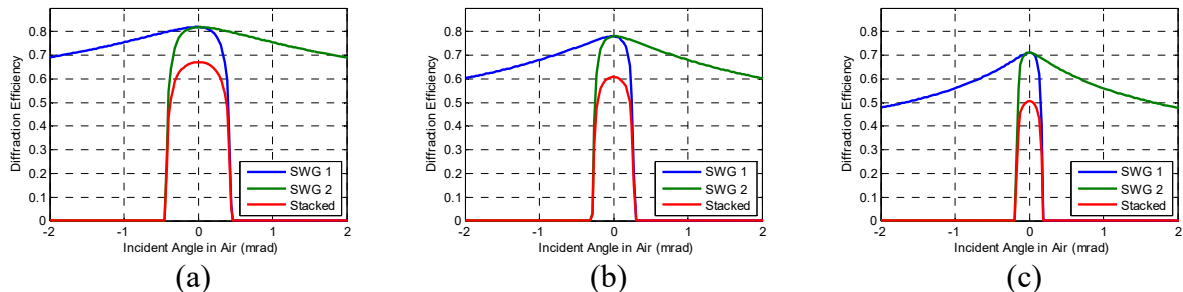


Fig. 132. Diffraction efficiencies of two “stacked” subwavelength gratings (SWGs) on prisms 1 and 2, as well as the stacked transmittance. The FW resolution is (a) 0.7 mrad; (b) 0.5 mrad; and (c) 0.4 mrad for $w_2 = 0.2, 0.75$, and 1, respectively.

However, the resolution can be increased further by placing the curves closer together. In this simulation, the transmission peaks of the subwavelength gratings were translated such that the maximum diffraction efficiency is 0.4. These plots appear in Fig. 133 (a-c) and yields the FW resolution of (a) 0.178 mrad; (b) 0.167 mrad; and (c) 0.120 mrad. Thus, systems with a larger maximum derivative do have higher spatial resolution potential with this form of adjustment.

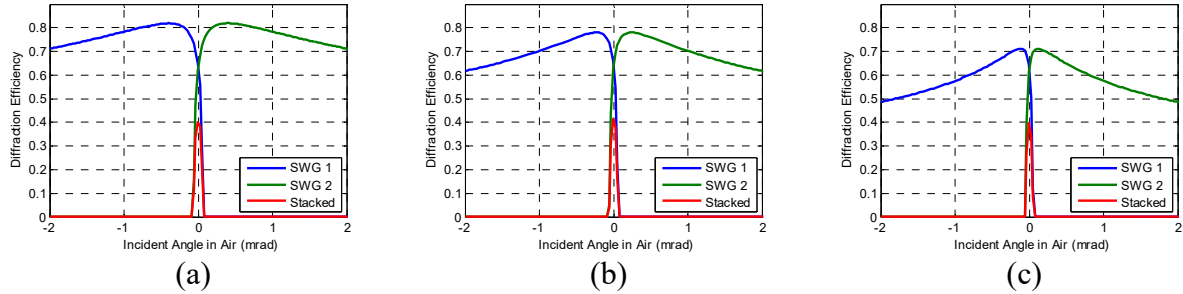


Fig. 133. Diffraction efficiencies of two stacked subwavelength grating (SWG) on prisms 1 and 2, as well as the stacked transmittance. The FW resolution is (a) 0.178 mrad, (b) 0.167 mrad, and (c) 0.120 mrad for $w_2 = 0.2, 0.75$, and 1, respectively.

6.3.1 Evanescent Field Interaction with Direct Vision Prism

One issue with the aforementioned approach is to couple the light through the prism in a “direct vision” capacity. This means that the light, transmitted by the grating interface, must be refracted back into a subsequent prism placed behind it. In the previous simulations per Fig. 132 and Fig. 133, it was assumed that placing this prism close to the subwavelength diffraction grating (SDG) does not interfere with the resonance’s sharpness. However, placing this interface close to the SDG will cause a perturbation to the evanescent field, thereby degrading the resonance’s sharpness. A view of this configuration is illustrated, per an RCWA simulation, in Fig. 134 (a-c) for separations, between the grating and the subsequent surface, of 10, 20, and 50 microns, respectively. Notable is the reduced sharpness of the resonance when compared to the original grating in which a “near infinite” air substrate existed. This is likely a result of the interference that is setup within the cavity between the two prisms and the close proximity of the surface to the evanescent field exiting the grating interface.

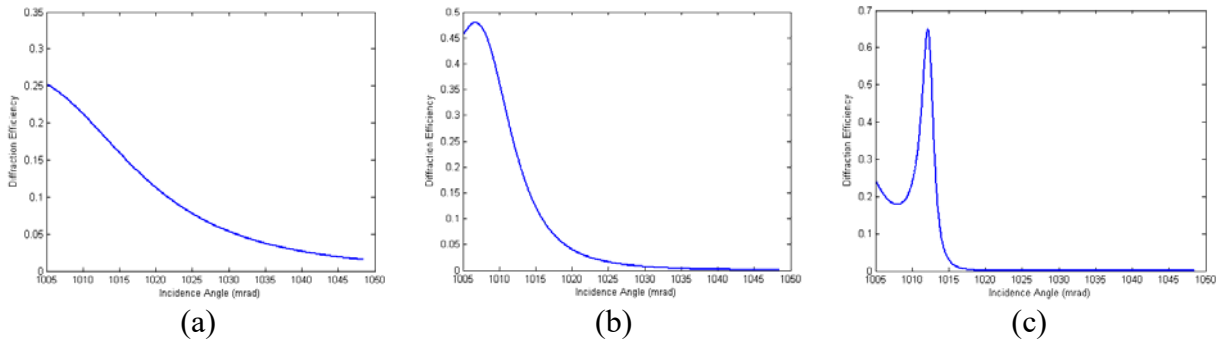


Fig. 134. Diffraction efficiency when second surface perturbs the evanescent field close to the SDG. Illustrated are efficiencies for a (a) 10; (b) 20; and (c) 50 micron thick airgap.

6.4 Prism Specifications for Single “Knife Edge” Filter

6.4.1 Grating

A side profile of the diffraction grating is depicted in Fig. 135 with important parameters summarized. Λ , h and DC are the period, height and duty cycle of the grating, respectively.

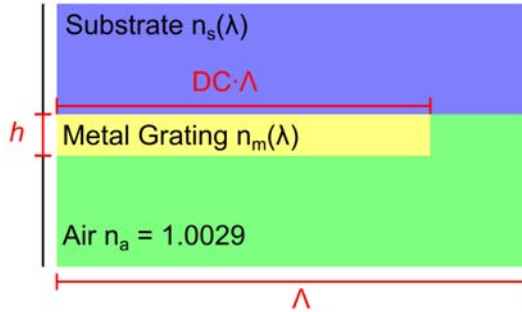


Fig. 135. Side profile of one grating period.

The optimal performance is obtained with an aluminum metal grating with the following parameters per Table 1.

Table 1. Grating parameters for aluminum on the backside of a Germanium prism.

λ (μm)	DC (%)	Λ (μm)	h (μm)
10.5	85 +/- 1	1.975 +/- 0.02	0.5 +/- 0.025

6.4.2 Prism

The prism dimensions and specifications are provided below. Note that for each prism that requires a grating, a “bare” prism can be provided. This could be used for leveling the prism during lithography if needed.

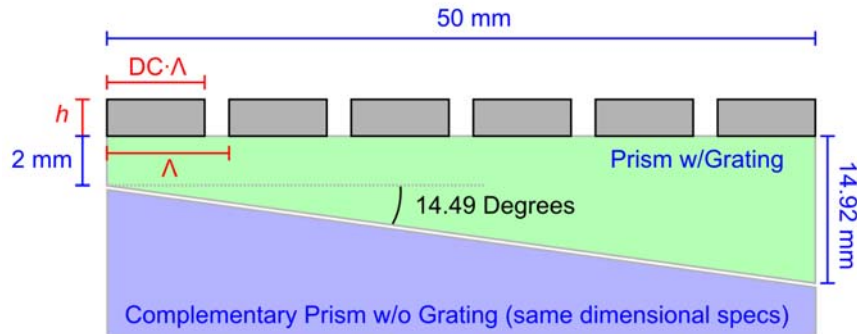


Fig. 136. Angular filter schematic.

6.4.3 COMSOL Simulations

COMSOL was utilized to simulate the grating. However, results indicated a poor tradespace for the angular filter, even when using plasmonic effects.

7.0 Publications and Products

Publications and conference proceedings, produced under funding from this work, includes:

- [1] E. R. Woodard and M. W. Kudenov, "Snapshot spectrally resolved longitudinal spatial coherence interferometry," Opt. Eng. 56(6), 064104 (2017).
- [2] Z. Wu, "Four-dimensional object-space data reconstruction using spatial-spectral multiplexing", Master's thesis, North Carolina State University, Raleigh, NC (2017).
- [3] E. R. Woodard and M. W. Kudenov, "Spectrally resolved longitudinal spatial coherence interferometry", Proc. SPIE, Algorithms and Technologies for Multispectral, Hyperspectral, and Ultraspectral Imagery XXIII, 1019806 (2017).

[4] Z. Wu and M. W. Kudenov, "A reconstruction algorithm for three-dimensional object-space data using spatial-spectral multiplexing," Proc. SPIE, Algorithms and Technologies for Multispectral, Hyperspectral, and Ultraspectral Imagery XXIII, 1019812 (2017).

[5] E. R. Woodard and M. W. Kudenov, "Passive standoff imaging using spatial-spectral multiplexing", Proc. SPIE, Algorithms and Technologies for Multispectral, Hyperspectral, and Ultraspectral Imagery XXI, 94721A (2015).

Pending Publications that are in the process of being finalized and submitted include:

[1] E. R. Woodard, "Spectrally Resolved Longitudinal Spatial Coherence Interferometry", PhD Thesis, North Carolina State University, Raleigh, NC (Pending, 2018).

[2] E. R. Woodard and M. W. Kudenov, "Spectrally Resolved Longitudinal Spatial Coherence Interferometry for Channeled Imaging Polarimetry", Opt. Eng. (Pending, 2017).

Presentation Listing:

[1] E. R. Woodard and M. W. Kudenov, "Spectrally resolved longitudinal spatial coherence interferometry", SPIE Defense + Commercial Sensing Conference, Anaheim, CA (April 2017).

[2] Z. Wu and M. W. Kudenov, "A reconstruction algorithm for three-dimensional object-space data using spatial-spectral multiplexing", SPIE Defense + Commercial Sensing Conference, Anaheim, CA (April 2017).

[3] E. R. Woodard and M. W. Kudenov, "Passive standoff imaging using spatial-spectral multiplexing", SPIE Defense + Security Conference, Baltimore, MD (April 2015).

8.0 References

1. E. R. Woodard and M. W. Kudenov, "Passive standoff imaging using spatial-spectral multiplexing," Proc. SPIE **9472**, 94721A–94721A–10 (2015).
2. SCHOTT North America, Inc. "Optical Glass Data Sheets," Duryea, PA (2013).
3. D. Liu, C. Hostetler, I. Miller, A. Cook, and J. Hair, "System analysis of a tilted field-widened Michelson interferometer for high spectral resolution lidar", Opt. Expr. Vol. 20, No. 2 (2012).
4. G. Shepherd et al., "WAMDII: wide-angle Michelson Doppler imaging interferometer for Spacelab", Appl. Opt., Vol. 24, No. 11, (1985).
5. P. Yeh, "Zero Crossing Birefringent Filters", Vol 35. No. 1, Opt. Commun (1980).
6. Z. Wang, H. Ma, "Advanced continuous wavelet transform algorithm for digital interferogram analysis and processing" in *Opt. Eng.*, Vol. 45. Issue 4. (2006).
7. C. J. Tay et al., "Demodulation of a single interferogram based on continuous wavelet transform and phase derivative", in *Optics Communications*, Vol. 280, Issue 2, pp. 327-336. (2007).
8. P. J. de Groot, L. Deck, "Surface profiling by frequency-domain analysis of white light interferograms" in *SPIE*, Vo.1 2248, pp. 101-104. (1994).
9. P. Hlubina et. Al., "Windowed Fourier transform applied in the wavelength domain to process the spectral interference signals", in *Optics Communications*, Vol. 281, Issue 9, pp. 2349-2354. (2008).
10. J. Proakis, D. Manolakis, "Efficient Computation of the DFT: Fast Fourier Transform Algorithms" in *Digital Signal Processing: Principles, Algorithms and Applications*, 4th ed. (Pearson, 1994), Chapter. 8.
11. Griffiths, P. M. and de Haseth, J. A., [Fourier Transform Infrared Spectrometry], Wiley-Interscience, Ch. 1-3 (1986).
12. Hilliard, R. L. and Shepherd, G. G., "Wide-Angle Michelson Interferometer for Measuring Doppler Line Widths," J. Opt. Soc. Am., 56(3), 362-369 (1966).
13. Born, M. and Wolf, E., [Principles of Optics], Cambridge University Press, Cambridge & New York, Ch. 7-8 (1999).
14. A. I. Kartashev, "Optical Systems with Enhanced Resolving Power," Opt. Spectrosc+ **9**, 204 (1960).
15. J. D. Armitage, A. Lohmann, and D. P. Paris, "Superresolution Image-Forming Systems for Objects with Restricted Lambda Dependence," Jpn. J. Appl. Phys. **3**, 273 (1964).
16. H. O. Bartelt, "Wavelength multiplexing for information transmission," Opt. Commun. **27**, 365–368 (1978).
17. A. A. Friesem, U. Levy, and Y. Silberberg, "Parallel transmission of images through single optical fibers," *Proceedings of the IEEE* (IEEE, 1983), pp. 208–221.
18. D. Mendlovic, J. Garcia, Z. Zalevsky, E. Marom, D. Mas, C. Ferreira, and A. W. Lohmann, "Wavelength-multiplexing system for single-mode image transmission," Appl. Optics **36**, 8474–8480 (1997).
19. A. Abramov, L. Minai, and D. Yelin, "Multiple-channel spectrally encoded imaging," Opt. Express **18**, 14745 (2010).
20. R. Barankov and J. Mertz, "High-throughput imaging of self-luminous objects through a single optical fibre," Nat. Commun. **5**, 5581 (2014).

21. G. J. Tearney, R. H. Webb, and B. E. Bouma, "Spectrally encoded confocal microscopy," *Opt. Lett.* **23**, 1152 (1998).
22. D. Fixler, A. Schwarz, J. Garcia, and Z. Zalevsky, "Lensless microscope using wavelength multiplexing," *Proc. SPIE* **7365**, 73650J–73650J–11 (2009).
23. A. Gur, R. Aharoni, Z. Zalevsky, V. G. Kutchoukov, V. Mico, J. Garcia, and Y. Garini, "Sub-wavelength and non-periodic holes array based fully lensless imager," *Opt. Commun.* **284**, 3509–3517 (2011).
24. K. Oka and T. Kato, "Spectroscopic polarimetry with a channeled spectrum," *Optics Letters* **24**, 1475 (1999).
25. M. W. Kudenov, N. A. Hagen, E. L. Dereniak, and G. R. Gerhart, "Fourier transform channeled spectropolarimetry in the MWIR," *Opt. Express* **15**, 12792–12805 (2007).
26. K. H. Nordsieck, "A Simple Polarimetric System for the Lick Observatory Image-Tube Scanner," *Publ. Astron. Soc. Pac.* **86**, 324 (1974).
27. P. R. Griffiths, J. A. de Haseth, *Fourier Transform Infrared Spectrometry* (Wiley, 1986).
28. C. W. McCutchen, "Generalized Source and the van Cittert–Zernike Theorem: A Study of the Spatial Coherence Required for Interferometry," *J. Opt. Soc. Am.* **56**, 727 (1966).
29. J. Rosen and A. Yariv, "General theorem of spatial coherence: application to three-dimensional imaging," *J. Opt. Soc. Am.* **13**, 2091 (1996).
30. J. Rosen and M. Takeda, "Longitudinal spatial coherence applied for surface profilometry," *Appl. Optics* **39**, 4107 (2000).
31. W. Wang, H. Kozaki, J. Rosen, and M. Takeda, "Synthesis of longitudinal coherence functions by spatial modulation of an extended light source: a new interpretation and experimental verifications," *Appl. Optics* **41**, 1962 (2002).
32. V. Ryabukho, D. Lyakin, and M. Lobachev, "Influence of longitudinal spatial coherence on the signal of a scanning interferometer," *Opt. Lett.* **29**, 667 (2004).
33. V. Ryabukho, D. Lyakin, and M. Lobachev, "Longitudinal pure spatial coherence of a light field with wide frequency and angular spectra," *Opt. Lett.* **30**, 224 (2005).
34. A. Hirai, T. Inoue, K. Itoh, and Y. Ichioka, "Application of Measurement multiple-image fourier of fast phenomena transform spectral imaging to measurement of fast phenomena," *Optical Review* **1**, 205–207 (1994).
35. A. R. Harvey and D. W. Fletcher-Holmes, "Birefringent Fourier-transform imaging spectrometer," *Optics Express* **12**, 5368 (2004).
36. J. D. Gaskill, *Linear Systems, Fourier Transforms, and Optics* (Wiley, 1978).
37. Y. Ferrec, N. Ayari-Matallah, P. Chavel, F. Goudail, H. Sauer, J. Taboury, J.-C. Fontanella, C. Coudrain, and J. Primot, "Noise sources in imaging static Fourier transform spectrometers," *Opt. Eng.* **51**, 111716–1 (2012).
38. G. G. Shepherd, W. A. Gault, D. W. Miller, Z. Pasturczyk, S. F. Johnston, P. R. Kosteniuk, J. W. Haslett, D. J. W. Kendall, and J. R. Wimperis, "WAMDII: wide-angle Michelson Doppler imaging interferometer for Spacelab," *Appl. Optics* **24**, 1571–1584 (1985).
39. J. Craven and M. W. Kudenov, "False signature reduction in channeled spectropolarimetry," *Opt. Eng.* **49**, 053602–053602 (2010).
40. F. Snik, T. Karalidi, and C. U. Keller, "Spectral modulation for full linear polarimetry," *Appl. Optics* **48**, 1337–1346 (2009).

41. E. R. Woodard and M. W. Kudenov, "Passive standoff imaging using spatial-spectral multiplexing," Proc. SPIE **9472**, 94721A–94721A–10 (2015).
42. Reflection and Transmission Data, "Thorlabs - BSN16 UVFS Plate Beamsplitter" <https://www.thorlabs.com/thorproduct.cfm?partnumber=BSN16>. Accessed 6/10/2016.
43. United States Department of Commerce, "NIST Atomic Spectra Database," <http://www.nist.gov/pml/data/asd.cfm>. Accessed 6/23/2016.
44. L. Mertz, "Auxiliary computation for Fourier spectrometry," Infrared Phys. **7**, 17-23 (1967). Photon Technologies International, "PTI Technical Notes: Lamp Emission Spectra," <http://www.pti-nj.com/TechnicalNotes/Lamp-Emission-Spectra.pdf>.
45. E. Woodard, Michael W. Kudenov, "Snapshot spectrally resolved longitudinal spatial coherence interferometry," Opt. Eng. **56**(6), 064104 (2017).
46. K. Oka and T. Kato, "Spectroscopic polarimetry with a channeled spectrum," Optics Letters **24**, 1475 (1999).
47. M. W. Kudenov, M. J. Escuti, E. L. Dereniak, and K. Oka, "White-light channeled imaging polarimeter using broadband polarization gratings," Appl. Opt., AO **50**, 2283–2293 (2011).
48. M. W. Kudenov, N. A. Hagen, E. L. Dereniak, and G. R. Gerhart, "Fourier transform channeled spectropolarimetry in the MWIR," Opt. Express, OE **15**, 12792–12805 (2007).
49. J. Craven and M. W. Kudenov, "False signature reduction in channeled spectropolarimetry," Opt. Eng **49**, 053602-053602-10 (2010).
50. D. Goldstein, "Polarized Light", (Marcel Dekker, 2003).
51. A. Taniguchi, K. Oka, H. Okabe, and M. Hayakawa, "Stabilization of a channeled spectropolarimeter by self-calibration," Opt. Lett., OL **31**, 3279–3281 (2006).
52. Alain Berlinet and Christine Thomas-Agnan. Reproducing kernel Hilbert spaces in probability and statistics. Springer Science & Business Media, 2011.
53. Christopher M Bishop. Pattern recognition. Machine Learning, 128:1-58, 2006.
54. Ya M Blanter and Markus Büttiker. Shot noise in mesoscopic conductors. Physics reports, 336(1):1-166, 2000.
55. J.B. Campbell and R.H. Wynne. Introduction to Remote Sensing, Fifth Edition. Guilford Publications, 2011.
56. Raymond H Chan, Tony F Chan, Lixin Shen, and Zuowei Shen. Wavelet algorithms for high-resolution image reconstruction. SIAM Journal on Scientific Computing, 24(4):1408-1432, 2003.
57. Tony F Chan and Luminita A Vese. Active contours without edges. IEEE Transactions on image processing, 10(2):266-277, 2001.
58. C.I. Chang. Hyperspectral Imaging: Techniques for Spectral Detection and Classification. Number v. 1 in Hyperspectral Imaging: Techniques for Spectral Detection and Classification. Springer US, 2003.
59. A.A. Daptardar and Vishal J. Kesti. Introduction to Remote Sensors and Image Processing and its Applications. International Journal of Latest Trends in Engineering and Technology (IJLTET), pages 107-114, 2013.
60. Carl De Boor, Carl De Boor, Etats-Unis Mathématicien, Carl De Boor, and Carl De Boor. A practical guide to splines, volume 27. Springer-Verlag New York, 1978.

61. J.R. Eastman and Clark Labs. IDRISI Kilimanjaro: Guide to GIS and Image Processing. Clark Labs, Clark University, 2003

62. C. Elachi and J.J. van Zyl. Introduction To The Physics and Techniques of Remote Sensing. Wiley Series in Remote Sensing and Image Processing, Wiley, 2006.

63. Thomas Gerig, Kamal Shahim, Mauricio Reyes, Thomas Vetter, and Marcel Lüthi. Spatially varying registration using gaussian processes. In MICCAI (2), pages 413-420, 2014.

64. Shakti Goap. Remote Sensing and Image Analysis, 2015.

65. Kumar Singh Jitendra, Kumar Yadav Krishna, Neha Gupta, and Vinit Kumar. Remote sensing and geographical information system (gis) and its applicationn in various fields). In National Conference on Energy and Environment: Threats and Remedies, 2016.

66. N. Kerle and W.H. Bakker. Principles of Remote Sensing: An Introductory Textbook. ITC educational textbook series. Internat. Inst. for Geo-Information Science and Earth observation, 2004.

67. S Lee. Application of logistic regression model and its validation for landslide susceptibility mapping using gis and remote sensing data. International Journal of Remote Sensing, 26(7):1477-1491, 2005.

68. T. Lillesand, R.W. Kiefer, and J. Chipman. Remote Sensing and Image Interpretation. John Wiley & Sons, 2014.

69. Xing Lin, Yebin Liu, Jiamin Wu, and Qionghai Dai. Spatial-spectral encoded compressive hyperspectral imaging. ACM Transactions on Graphics (TOG), 33(6):233, 2014.

70. Dong C Liu and Jorge Nocedal. On the limited memory bfgs method for large scale optimization. Mathematical programming, 45(1):503-528, 1989.

71. P.M. Mather and M. Koch. Computer Processing of Remotely-Sensed Images: An Introduction. John Wiley & Sons, 2011.

72. Kevin P Murphy. Machine learning: a probabilistic perspective. MIT press, 2012.

73. Punyatoya Patra. Remote sensing and geographical information system (gis). The Association for Geographical studies, 2010.

74. Leonid I Rudin, Stanley Osher, and Emad Fatemi. Nonlinear total variation based noise removal algorithms. Physica D: Nonlinear Phenomena, 60(1-4):259-268, 1992.

75. J Solomon and B Rock. Imaging spectrometry for earth remote sensing. Science, 228(4704):1147-1152, 1985.

76. P.H. Swain and S.M. Davis. Remote Sensing: The Quantitative Approach. Advanced book program. McGraw-Hill International Book Company, 1978.

77. Min-Jea Tahk, Moon-Su Park, Hyun-Wook Woo, and Hyoun-Jin Kim. Hessian approximation algorithms for hybrid optimization methods. Engineering Optimization, 41(7):609-633, 2009.

78. J Scott Tyo, Dennis L Goldstein, David B Chenault, and Joseph A Shaw. Review of passive imaging polarimetry for remote sensing applications. Applied optics, 45(22):5453-5469, 2006.

79. Ashwin Wagadarikar, Renu John, Rebecca Willett, and David Brady. Single disperser design for coded aperture snapshot spectral imaging. Applied optics, 47(10):B44-B51, 2008.

80. Ethan R Woodard and Michael W Kudenov. Passive standoff imaging using spatial-spectral multiplexing. In SPIE Defense+ Security, pages 94721A-94721A. International Society for Optics and Photonics, 2015
81. K. Brahmachari, S. Ghosh, and M. Ray, "Surface plasmon resonance based sensing of different chemical and biological samples using admittance loci method," Photonic Sens 3, 159–167 (2012)